Identication of trapped electron modes in frequency fluctuation spectra of fusion plasmas

Hugo Arnichand

Energy, Radiation and Plasma

Engineering Physics

DOCTORAL THESIS

Identification of Trapped Electron Modes in Frequency Fluctuation Spectra of fusion plasmas

by:

Hugo Arnichand

Board of examiners for public Ph.D. defense on October, 26th 2015:

Dr. John E. RICE	Referee – MIT
Dr. Stefano CODA	Referee – EPFL
Dr. Pascale HENNEQUIN (chair)	Examiner – CNRS/École Polytechnique
Dr. Yann CAMENEN	Examiner - AMU
Dr. Roland SABOT	Thesis director – CEA
Dr. Sébastien HACQUIN	Supervisor – CEA
Dr. Andreas KRÄMER-FLECKEN	Supervisor – FZ-Jülich
Prof. Guido VAN OOST	Thesis promotor - UGent

Main laboratory (Oct 2012 – Oct 2015):
Institut de **R**echerche sur la **F**usion par confinement **M**agnétique
CEA Cadarache 13108 Saint-Paul-lez-Durance, France

Contents

Abstract

Turbulence is responsible for anomalous transport, which lowers the particle and energy confinement, and degrades the performance of fusion devices. Several types of instabilities can induce turbulent phenomena. In toroidal magnetized plasmas, turbulence is triggered by micro-instabilities. At low wave-numbers $k_\perp$ normalized to the Larmor radius ρ_i ($0.1 < k_\perp \rho_i < 1$), the dominant micro-instabilities are the Ion Temperature Gradient (ITG) modes and the Trapped Electron Modes (TEM).

An important property of these electrostatic modes is that they both exhibit a threshold above which they are unstable. As ITG and TEM are driven by different temperature and density gradients, they can either (i) both be stable, (ii) both coexist or (iii) give way to a single dominant mode (ITG or TEM).

The heat and particle transport induced by ITG and TEM are noticeably different. First the sign of their convection velocity can be opposite, leading to an outward/inward particle pinch, which tends to flatten/peak the density profiles, respectively. ITG and TEM can also influence the intrinsic toroidal velocity in a different way via the residual stress mechanisms. Additionally, ITG and TEM show distinct dependencies on plasma parameters (magnetic shear, T_i/T_e, collisionality, etc.). Therefore changes in these parameters can have different effects whether ITG or TEM dominates. For these reasons it is important to be able to discriminate experimentally the regimes dominated by TEM and ITG.

These modes can be distinguished via their phase velocity at a given wave-number in the plasma frame, which is in opposite directions. However this is challenging since the $E \times B$ drift of the plasma frame is expected at much higher values than the phase velocity which is not directly measurable. Alternatively, transport studies can help discriminate ITG from TEM dominated regimes, but it requires perturbation experiments to get a precise estimation of the diffusion coefficients and the convection velocities.

This thesis shows that the analysis of frequency fluctuation spectra can provide an additional experimental indication of the dominant mode. Depending on the plasma scenario, fluctuation spectra can display different frequency components:

- Broadband spectra ($\Delta f \approx$ hundreds of kHz) which are always observed. Their amplitude is maximum at the zero frequency and they are attributed to turbulence.
- Coherent modes ($\Delta f \approx 1$ kHz) which oscillate at a very well defined frequency. They can for example be due to geodesic acoustic or magnetohydrodynamic (MHD) modes
- Quasi-Coherent (QC) modes ($\Delta f \approx$ tens of kHz) which oscillate at a rather well defined frequency but which are reminiscent of broadband fluctuations.

The fluctuation study performed in the plasma core region shows that the fluctuation spectra in TEM-dominated regimes can be noticeably different from the ones in ITG-dominated regimes, as only TEM can induce QC modes. Such a finding has been achieved by comparing fluctuations measurements with simulations.

Measurements are made with a reflectometry diagnostic, a radar-like technique able to provide local indications of the density fluctuations occurring in the vicinity of the reflection layer. Frequency fluctuation spectra are inferred from a Fourier analysis of the reflectometry signal.

First, the main properties of QC modes are characterized experimentally. Their normalized scale is estimated to $k_\perp \rho_i \leq 1$, their amplitude is ballooned on the low field side mid-plane and they can be observed at many different radii. These indications are in agreement with what could be expected for ITG/TEM instabilities.

Then reflectometry measurements are analyzed in Ohmic plasmas. QC modes are observed in the Linear Ohmic Confinement (LOC) regime dominated by TEM whereas only broadband spectra are seen in the Saturated Ohmic Confinement (SOC) regime dominated by ITG. Frequency spectra from nonlinear gyrokinetic simulations show that TEM induce a narrow frequency spectra responsible for the QC modes observed experimentally. This interpretation of the measured spectra is made via a synthetic reflectometer diagnostic using the gyrokinetic simulations as an input. The QC modes observed in the plasma core have then been renamed QC-TEM as a reference of their TEM origins.

Thereafter, the first applications of the knowledge of QC-TEM properties are made in Ohmic plasmas of Tore Supra, TEXTOR, JET and ASDEX-Upgrade. The global disappearance of QC-TEM simultaneously with the LOC-SOC transition suggests that the stabilization of TEM plays an important role in the change of Ohmic regime. The disappearance of QC-TEM can also be correlated to intrinsic toroidal velocity bifurcation, which is not explained by neoclassical predictions.

Another application using the QC signature of TEM has been done in Tore Supra ECRH plasmas. A previous study found an increase of the diffusion coefficient with the electron temperature gradient in a region predicted to be dominated by electron modes ($r/a < 0.2$). Further out ($r/a > 0.2$), the diffusion was independent of the electron temperature gradient in a region dominated by ion turbulence. Reflectometry measurements brought an additional indication by showing the presence of QC-TEM at $r/a < 0.2$ and a broadband spectrum at $r/a > 0.2$, supporting the previous investigations.

Finally, transitions between electrostatic fluctuations (QC-TEM) and electromagnetic MHD modes have been observed.

Spatial transitions from TEM toward MHD modes are reported in Ohmic ASDEX-Upgrade plasmas and Tore Supra plasmas heated with Lower Hybrid (LH) waves. They may contribute to the sudden stabilization of TEM observed toward the plasma center.

Temporal interplay between QC-TEM and MHD modes has also been observed with various heating schemes in Tore Supra plasmas (LH and electron cyclotron resonance heating), and in JET with neutral beam injection heating. This interplay which may have different drives (sawtooth, magnetic shear) indicates that QC-TEM and MHD are anti-correlated, QC-TEM fluctuations showing a delay of the order of ms compared to the MHD modes.

These multiple observations suggest that spatial and temporal interactions between MHD and turbulent instabilities may be at play in the plasma core region.

Résumé

La turbulence est responsable du transport anormal qui diminue le confinement du plasma et par conséquent dégrade les performances des réacteurs à fusion. Différents types d'instabilités peuvent induire de la turbulence. Dans les plasmas magnétisés toroïdaux, la turbulence est déclenchée par des micro-instabilités. A faibles nombres d'ondes $k_\perp$ normalisés au rayon de Larmor ρ_i ($0.1 < k_\perp \rho_i < 1$), les micro-instabilités dominantes sont les "Ion Temperature Gradient" (ITG) et les "Trapped Electron Modes" (TEM).

Ces modes ont un seuil au-delà duquel ils sont instables. Comme les ITG et les TEM sont déstabilisés par différents gradients, ils peuvent tous les deux être (i) stables, (ii) instables, ou (iii) donner un seul mode dominant (ITG ou TEM).

Le transport de chaleur et de particules induit par les ITG et les TEM est sensiblement différent. Tout d'abord, le signe de leur vitesse de convection peut-être opposé, contribuant à piquer ou aplatir les profils de densité. Les ITG et les TEM peuvent aussi influencer la vitesse de rotation toroïdale intrinsèque de manière différente. De plus, les ITG et les TEM dépendent différemment de plusieurs paramètres du plasma, des modifications de ces paramètres peuvent avoir des effets différents si les ITG ou les TEM dominent. Pour ces raisons, il est important d'être capable de discriminer expérimentalement les régimes dominés par les TEM ou les ITG.

Ces modes peuvent être distingués par leur vitesse de phase à un nombre d'onde donné dans le référentiel du plasma, car elles sont opposées. Cependant, cela est difficile car la dérive $E \times B$ du référentiel du plasma est nettement supérieure à la vitesse de phase qui ne peut pas être mesurée directement. Alternativement, l'étude du transport peut permettre de discriminer les régimes dominés par les TEM de ceux dominés par les ITG, mais cela nécessite des expériences de perturbation pour avoir une estimation précise des coefficients de diffusion et de convection.

Cette thèse montre qu'une analyse des spectres fréquentiels de fluctuation peut fournir une indication expérimentale du mode dominant. En fonction du scénario de plasma, les spectres fréquentiels de fluctuation peuvent exhiber différentes composantes :

- Les spectres à large-bande ($\Delta f \approx$ quelques centaines de kHz) ont une amplitude maximum à la fréquence zéro et sont atribués à la turbulence
- Les modes cohérents ($\Delta f \approx 1$ kHz) qui oscillent à une fréquence bien définie peuvent par exemple être dus aux modes magnétohydrodynamiques (MHD).
- Les modes Quasi-Cohérents (QC) ($\Delta f \approx$ quelques dizaines de kHz) qui oscillent à une fréquence plutôt bien définie mais qui rappellent les spectres à large-bande de par leur large bande spectrale.

Cette étude des fluctuations menée dans le plasma de cœur montre que contrairement aux spectres des ITG, les spectres des TEM peuvent induire des modes QC. Cette découverte a été faite en comparant les fluctuations mesurées avec celles fournies par des simulations.

Les mesures ont été faites par réflectométrie, un diagnostic de type radar capable de fournir des indications locales sur les fluctuations de densité dans la région de la couche de

coupure. Les spectres fréquentiels de fluctuation sont obtenus par une analyse de Fourier des signaux de réflectométrie. Les principales propriétés des modes QC ont tout d'abord été caractérisées expérimentalement. Leur échelle normalisée est estimée à $k_\perp \rho_i \leq 1$, leur amplitude est ballonnée côté faible champ et ils peuvent être observés à de nombreux rayons différents. Ces indications sont en accord avec ce que l'on peut attendre pour les instabilités de type ITG/TEM.

Puis, les mesures de réflectométrie ont été analysées dans les régimes de Confinement Ohmique Linéaire (LOC) dominé par les TEM et de Confinement Ohmique Saturé (SOC) dominé par les ITG. Les modes QC ont été observés seulement en régime LOC alors qu'un spectre à bande large a été observé en régime SOC. Les simulations gyrocinétiques non-linéaires montrent que les TEM induisent des spectres fréquentiels étroits responsables des modes QC observés expérimentalement. Cette interprétation a été faite via un réflectomètre synthétique utilisant les simulations gyrocinétiques. Les modes QC observés dans le cœur du plasma ont été renommés QC-TEM en référence à leur lien avec les TEM.

Les premières applications de la connaissance des QC-TEM ont été faites dans les régimes Ohmiques de Tore Supra, TEXTOR, JET et ASDEX-Upgrade. Ils indiquent que la disparition des QC-TEM est globale et simultanée à la transition LOC-SOC, suggérant que la stabilisation des TEM joue un rôle important dans le changement de régime Ohmique. La disparition des QC-TEM peut être aussi corrélée à des bifurcations de la vitesse toroïdale intrinsèque qui ne sont pas expliquées par des prédictions néoclassiques.

Un autre application de la connaissance des QC-TEM a été faite dans les plasmas de Tore Supra chauffés par ECRH. Une étude précédente avait montré que dans une région dominée par une turbulence électronique ($r/a < 0.2$), une augmentation du coefficient de diffusion était observée lorsque le gradient de température électronique normalisé augmentait. Plus vers l'extérieur ($r/a > 0.2$), une diffusion indépendante du gradient de température électronique normalisé avait été observée alors qu'une turbulence ionique dominait. Les mesures de réflectométrie ont amené une indication supplémentaire en montrant des QC-TEM seulement pour $r/a < 0.2$ et un spectre à bande large pour $r/a > 0.2$, appuyant les précédentes études.

Finalement, des transitions entre des fluctuations électrostatiques (QC-TEM) et électromagnétiques (MHD) sont rapportées. Radialement, les TEM peuvent disparaitrent au profit de modes MHD dans des plasmas Ohmiques d'ASDEX-Upgrade et dans les plasmas de Tore Supra utilisant le chauffage hybride. Temporellement, des interactions entre des modes MHD et des TEM ont aussi été rapportées dans divers régimes de chauffages électroniques de Tore Supra et dans des plasmas de JET chauffés par injection de neutres. Ces observations suggèrent que des interactions spatiales et temporelles peuvent avoir lieu entre des instabilités turbulentes et des modes MHD dans le cœur du plasma.

Overzicht

Turbulentie is verantwoordelijk voor het anomalous transport dat de deeltjes- en energieconfinement vermindert en de performantie van fusie-reactoren verslechtert. Ver-

scheidende types van onstabiliteiten kunnen turbulente fenomenen induceren. In toroïdale magnetische geometrieëen wordt turbulentie getriggerd door micro-onstabiliteiten. Voor lage waardes voor de wave numbers $k_\perp$, genormalizeerd tot de Larmor-straal ρ_i ($0.1 < k_\perp \rho_i < 1$), is de dominante micro-onstabiliteit de Ion Temperature Gradient Mode (ITG) en de Trapped Electron Mode (TEM). Een belangrijke eigenschap van deze electrostatische modes is dat beide een grenswaarde hebben waarboven ze onstabiel worden. Daar ITG en TEM gedreven worden door verschillende gradiënten kunnen ze ofwel (i) allebei stabiel zijn, (ii) beide bestaan of (iii) resulteren in één enkele dominante mode.

Het warmte- en deeltjestransport geïnduceerd door ITG en TEM is erg verschillend. Ten eerste kan het teken van de convectiesnelheid omgekeerd zijn, wat tot een outward/inward particle pinch kan leiden wat op zijn beurt een vlak of gepiekt dichtheidsprofiel kan veroorzaken. ITG en TEM kunnen ook de intrensieke toroïdale snelheid op een verschillende manier beïnvloeden via residuele spanningsmechanismen. Bovendien kunnen ITG en TEM verschillende afhankelijkheden vertonen van de plasmaparameters (magnetische shear, T_i/T_e, collisionality, etc.). Daarvoor kunnen veranderingen in deze parameters verschillende effecten hebben naargelang ITG of TEM domineert. Omwille van al deze redenen is het belangrijk om experimenteel te kunnen bepalen welke regimes gedomineerd worden door TEM en ITG.

De modes kunnen worden ondersheiden met behulp van hun fasesnelheden voor een gegeven golfgetal in het plasma frame, die in verschillende richtingen georiënteerd zijn. Maar dit is een uitdaging omdat de $E \times B$ drift van het plasma frame verwacht wordt bij veel grotere waardes van de fasesnelheid die niet direct meetbaar is. Als een alternatief kunnen transportstudies helpen om te discrimeneren tussen ITG- en TEM-gedomineerde regimes, maar hiervoor zijn perturbatieëxperimenten noodzakelijk om een goede schatting te kunnen geven van de diffusiecoefficiënten en de convectiesnelheden.

Deze thesis illustreert dat de analyse van de spectra van de frequentiefluctuaties een verdere experimentele indicatie kan geven van de dominante mode. Afhankelijk van het scenario kunnen deze spectra verschillende componenten vertonen:

- Breedbandige spectra ($\Delta f \approx$ honderden kHz) worden altijd geobserveerd. Hun amplitude is maximimaal voor de nulfrequentie en ze worden veroorzaakt door turbulentie.

- Coherente modes ($\Delta f \approx 1$ kHz) oscilleren met een scherp gedefinieerde frequentie. Ze kunnen bijvoorbeeld het gevolg zijn van een geodesische acoustische mode of mangetohydrodynamische modes.

- Quasi-Coherente (QC) modes ($\Delta f \approx$ tientallen kHz) oscilleren met een nauwkeurig gedefinieerde frequentie maar ze zijn reminiscent of the broadband fluctuations (?).

Het toepassen van deze fluctuatiestudie in de plasma core leidt tot de vaststelling dat de spectra van TEM modes zeer verschillend kunnen zijn van een ITG mode, omdat enkel TEM QC modes kan induceren. Deze ontdekking wordt gedaan door het vergelijken van fluctuatiemetingen met simulaties. Metingen worden gedaan met behulp van

reflectometrie, een techniek die op radar lijkt en locale indicaties geeft over de dichtheidsfluctuaties dichtbij de reflectielaag. Frequentiefluctuatiespectra worden dan afgeleid door een analyse van Fourier van het reflectometriesignaal.

De voornaamste kenmerken van QC modes worden eerst experimenteel bestudeerd. Hun genormalizeerde schaal wordt geschat op $k_\perp \rho_i \leq 1$, hun amplitude balloont in de low-field side midplane en ze kunnen worden geobserveerd op verscheidende radii. Deze aanwijzingen zijn coherent met wat verwacht kan worden voor ITG/TEM instabiliteiten.

Daarna worden reflectometriemetingen geanalyzeerd in Ohmische plasmas. QC modes worden geobserveerd bij Linear Ohmic Confinement (LOC), gedomineerd door TEM, maar enkel een breedband spectrum wordt gezien in bij Saturated Ohmic Confiment (SOC), gedomineerd door ITG. Frequentiespectra van niet-lineaire gyrokinetische simulaties tonen aan dat TEM het smal frequentiespectrum kan induceren dat verantwoordelijk kan zijn voor de QC modes die experimenteel worden geobserveerd. Deze interpretatie van de gemeten spectra gebeurt via een synethetische reflectometer dat de gyrokinetische simulaties als input heeft. De QC modes die geobserveerd worden in de plasma core worden dan QC-TEM modes genoemd, met de referentie naar hun TEM-oorsprong. Dan worden de eerste toepassingen van de kennis over QC-TEM gedaan in de Ohmische plasmas van de Tore Supra, TEXTOR, JET en ASDEX-Upgrade. De globale verdwijning van QC-TEM gelijktijdig met de LOC-SOC transitie suggereert dat de stabilizatie van de TEM een grote rol speelt in de verandering van het Ohmische regime. De verdwijning van de QC-TEM kan ook gecorreleerd zijn met de intrinsieke toroïdale snelheidsbifurcatie die niet worden verklaard met neoklassieke voorspellingen.

Een andere toepassing die gebruik maakt van de QC-natuur van TEM wordt gedaan in Tore Supra ECRH plasmas. Een vorige studie toonde aan dat de diffusiecoefficiënt stijgt als functie van de electrontemperatuursgradiënt in een regio die wordt voorspeld gedomineerd te zijn door electron modes ($r/a < 0.2$). Verder naar buiten ($r/a > 0.2$) was de diffusie onafhankelijk van de electrontemperatuursgradiënt in een regio die gedomineerd werd door ion turbulence. Reflectometrie metingen geven een bijkomende indicatie door aanwezigheid aan te tonen van QC-TEM in $r/a < 0.2$ en een breedbandspectrum voor $r/a > 0.2$, wat de resultaten van eerdere onderzoeken steunt.

Uiteindelijk werden transities tussen electrostatische turbulentie (QC-TEM) en electromagnetische MHD modes geobserveerd.

Ruimtelijke transities van TEM naar MHD modes werden gereporteerd voor Ohmische ADEX-Upgrade plasmas en Tore Supra plasmas die werden verwarmd door lower hybrid (LH) waves. Deze zouden kunnen bijdragen tot de plotse stabilizatie van TEM die wordt geobserveerd dicht bij het centrum van het plasma. Tijdelijke interplays tussen QC-TEM en MHD modes werden ook geobserveerd met meerdere verwarmingsschemas in Tore Supra plasmas (LH en electron cyclotron resonance heating) en JET (NBI). Deze interplays, die verschillende drives kunnen hebben (sawtooth, magnetic shear) tonen aan dat QC-TEM en MHD anti-gecorreleerd zijn, waarbij QC-TEM fluctuaties een vertraging van de orde van ms vertoont vergeleken met MHD modes.

Dit veelvoud van observaties suggereert dat ruimtelijke en tijdelijke interacties tussen MHD en turbulente onstabiliteiten van belang zijn in de plasma core region.

Acknowledgments

There are many persons that I would like to thank for their involvement in this thesis. First and foremost, I gratefully acknowledge Sébastien Hacquin and Roland Sabot, my thesis supervisor and director in the Cadarache research center. They have continuously and with a great rigor followed my work during these three years and a half, since the master until the Ph.D. thesis. For the same reasons, I am also very grateful to Andreas Krämer-Flecken from the Jülich research center. Thanks to their scientific and human qualities, it has been a real pleasure to work with them.

I would also like to strongly acknowledge all the members of my thesis committee. I am grateful to John Rice for his early interest in this work and his availability to stay in Europe for the defense as a rapporteur. As some of his previous studies were among the foundations of the results I have obtained, one can understand how important his participation was. I would also like to acknowledge Stefano Coda for having accepted to be rapporteur and for having taken the time to read the manuscript and for having attended to the defense. I hope that these results can have some interesting applications to future studies in the TCV tokamak. I also owe acknowledgments to Pascale Hennequin for the multiple tasks she has achieved in this thesis as president of the jury, examiner and member of the UGent reading committee. I thank Yann Camenen, who has accepted to be examiner of this thesis and who has contributed to initiate a collaboration between theoreticians from AMU and experimentalists from CEA on the topic preliminary investigated in the section 6 of this manuscript. I am very grateful to Guido Van Oost for being my thesis promotor and for having created the European Master of Science in nuclear fusion and engineering physics. I acknowledge Kathleen Van Oost who helped me to solve the issues related to the cotutelle, UGent and Fusion-DC. Jean-Marie Noterdaeme who became my thesis promotor at the end of the thesis and Daniel De Zutter who was involved in the UGent reading committee.

Besides the members of the jury, there are numerous colleagues from various research centers that I would like to thank: Luis Meneses, Jon Hillesheim and João Bernardo from the Culham research center, Anna Medvedeva, Alexander Lebschy, Dmitrii Prisiazhniuk, Valentina Nikolaeva from the Garching research center, Antoine Sirinelli from ITER who contributed to the development of two reflectometer systems that I have used, and Luxherta Busy and Jorge Martín Hernandez that were my master thesis colleagues in the Jülich research center. I am grateful to all the other former students of the fusion-EP master and to those of the fusion-DC program with a special thanks to Hugo Peraza Rodriguez, Toon Weyens, Masa Scepanovic, William Gracias and Kostiantyn Achkasov. More generally, I would like to thank all those who have contributed to the set-up and the operation of Tore Supra, TEXTOR, JET and ASDEX-Upgrade, and all the individuals who make possible a thesis work by taking care of the administrative, management, logistical, security and maintenance services. To conclude these acknowledgments in English, I would also like to thank the members of the ITPA, TTF and EPS committees who gave me the opportunity to communicate my these results.

En Français maintenant, je voudrais aussi remercier un grand nombre de collègues de l'IRFM: Jean-Claude Giacalone un des pères du réflectomètre que j'ai le plus utilisé durant cette thèse. Christine Bottereau, Frédérique Clairet et Diego Molina qui ont contribués à la conception, l'installation et la mise en service des réflectomètres à balayage ultra-rapide sur Tore Supra puis ASDEX-Upgrade. Rémy Guirlet voisin de bureau dont les précédentes études sur le transport d'impuretés ont permis d'intéressantes applications de mes résultats. Cassio Amador à qui je souhaite bonne chance dans l'étude des interactions entre modes turbulents et MHD. Jonathan Citrin avec qui j'ai eu la chance de collaborer et dont les simulations non-linéaires ont jouées un rôle clef dans la compréhension des observations expérimentales que j'avais réalisées. Même si ses qualités de skieur n'égalent pas encore ses qualités humaines et ses connaissances en physique, la passion est là, et c'est le plus important. Clarisse Bourdelle qui fait partie de celles et ceux qui s'efforcent de faire le lien entre simulations et mesures, avec les résultats que l'on connait. Xavier Garbet, véritable "Paulo la science" de l'institut, toujours intéressé par des mesures et intéressant lors des discutions qui en découlent, théoricien dont la gentillesse et la pédagogie a je pense été démontré expérimentalement par bon nombre de thésards. Son large spectre de connaissances (de la MHD à la turbulence) a été une grande aide dans ces travaux portant sur des modes turbulents à spectres étroits... Je remercie également Valérie Icard et Nathalie Borio pour le travail qu'elles accomplissent au SCCP, Yanick Sarazin pour son implication dans la formation en amont et aval de bon nombre de thèses. Sophie Salasca avec qui j'ai découvert la fusion, ainsi que Guido Ciraolo fidèle co-voitureur entre Montpellier et Aix-en-Provence, Hugo-Georges Bufferand et Nicolas Fedorzack pour toutes les pauses café partagées au 508.

Je voudrais aussi remercier les personnes impliquées dans la direction de l'institut de la recherche sur la fusion magnétique et de son service chauffage et confinement du plasma: Alain Bécoulet, Tuong Hoang, Jean-Michel Bernard, Frédéric Imbeaux, Clément Laviron, et tout particulièrement Xavier Lithaudon qui a accepté de financer la moitié du coût de ma thèse. Merci également aux élus de la région Provence-Alpes-Côte-D'azur d'en avoir financé une autre moitié, et à Arnaud Sakda de l'entreprise ATEM, pour avoir établi un partenariat avec le CEA pour ma thèse.

Je souhaite aussi remercier toutes les perpanents du CEA avec qui j'ai travaillé ou simplement discuté durant ces trois années de thèse et dans les stages précédents: Guilhem Dif-Pradalier, Patrick Tamain, Didier Elbeze, Laurent Manenc, Gilles Moureau, Christophe Bouchand, Laurent Colas, Pascale Monier-Garbet, Marc Goniche, Patrick Maget, Rémi Dumont, Gloria Falchetto, Alain Simonin, Cedric Reux, Jeronimo Garcia et tous ceux que j'aurais pu oublier.

Impossible de ne pas remercier mes collègues thésards de l'IRFM, en commençant par les déjà docteurs (par respect pour les anciens): Thomas Cartier-Michaud dont la qualité du travail n'a d'égal que la qualité de sa barbe, même si il lui reste encore du chemin avant d'égaler celle de son mentor Philippe. Grégoire Hornung dont j'ai apprécié la présence durant la première partie de ma thèse et avec qui ça a toujours été un plaisir de discuter de réflectométrie et de sujets plus sérieux. Timothee Nicolas que j'ai eu le plaisir de

voir de d'Aubenas jusqu'à Kyoto. François Orain au mauvais goût légendaire, que je ne remercierai jamais assez de m'avoir fait découvrir Claude Barzotti. Je remercie au passage sa copine (Capucine) et son sanglier (Johnny) qui je l'espère, sont heureux de cohabiter en Germanie. Je remercie aussi Didier Vezinet, marin/géopolitologue de renom et physicien à ses heures perdues, Fabien Rozar qui détient probablement le record Cadarachien de la fréquence de ratage de bus du CEA pour encore de longues années. Jean-Baptiste Girardo qui est passé de l'autre côté du mur et à qui je souhaite bien du courage. Alexandre Fil, qui lui est passé de l'autre côté de l'atlantique pour de nouvelles aventures. Capitaine d'une équipe de foot qui ne rentrera pas dans la légende mais qui a vaillamment gagné la consolante de la consolante du tournois de Cadarache. Il a magnifiquement coaché des talents en devenir que je remercie pour ces moments passés ensemble: Jorge Morales notre "Valdérama", Charles Ehrlacher qui va mettre les électrons de Gyséla au régime, ainsi que d'autres dont le talent footballistique a déjà été confirmé : Jae-Heon que je suis heureux de compter parmi mes nouveaux compatriotes et Nicolas Nace supporteur inconditionnel du PSG. Je remercie aussi Olivier Février le plus grand sportif et le plus grand routier d'entre nous. Damien Esteve dit "Super Normand" avec qui j'ai (sur)vécu pendant une année intense, j'en profite pour également remercier sa mère. Claudia Norcini ainsi que ses deux fidèles compagnons: Unkyu Lee and Sptizi (ce dernier me pardonnera une éventuelle faute d'orthographe à son nom). Laurent Valade ou plutôt "l'eau rend malade" et sa laurent-mobile, qui fut un très bon compagnon de route pendant près de deux ans au 508, ainsi que Ling-Feng Lu que j'ai eu le plaisir de connaitre en France et que je reverrai bientôt en Chine. Je remercie aussi Renan Morales, Alberto Gallo, Camille Baudoin, Clothilde Colin, Julien Denis, Romain Futtersack, Laurent Chôné, Cristian Sommariva, Axel Jardin, Nicolas Fil, Walid Hélou, Francisco Guzmán, Shimpei Futatani, Farah Hariri, Etienne Hodille, Sarah Breton, Emelie Nilsson, Sabine Cockenpot, et bien sur mes anciens collocs avec qui j'ai vécu pendant ces trois années, notamment Davide Galassi, Camille Bouriane et Clément Nguyen Thanh Dao pour tout les bons moments passés ensemble.

Enfin, je dois un grand merci à ma compagne, mes parents, ma sœur, ma grand-mère, le reste de ma famille, et mes amis, mais un tels remerciements seraient bien trop grand pour rentrer dans un format A4.

Acronyms

- **AUG**: Axially Symmetric Divertor EXperiment (ASDEX) Upgrade
- **BB**: BroadBand
- **CXRS**: Charge eXchange Recombination Spectroscopy
- **DBS**: Doppler Backscattered Signal
- **DIII-D**: Doublet III–D
- **ECRH**: Electron Cyclotron Resonance Heating
- **ECE**: Electron Cyclotron Emission
- **E-fishbone**: Electron fishbone
- **ETG**: Electron Temperature Gradient
- **FDTD**: Finite Difference Time Domain
- **FFT**: Fast Fourrier Transform
- **FWHM**: Full Width at Half of the Maximum
- **GAMs**: Geodesic Acoustic Modes
- **GENE**: Gyrokinetic Electromagnetic Numerical Experiment
- **HFS**: High Field Side
- **ICRH**: Ion Cyclotron Resonance Heating
- **ITG**: Ion Temperature Gradient
- **JET**: Joint European Torus
- **LF**: Low Frequencies
- **LFS**: Low Field Side
- **LHCD**: Lower Hybrid Current Drive
- **LNA**: Low Noise Amplifier
- **LOC**: Linear Ohmic Confinement
- **MHD**: Magnetohydrodynamics
- **MSC**: Magnitude Squared Coherence
- **NBI**: Neutral Beam Injection
- **O-mode**: Ordinary mode
- **PCR**: Poloidal Correlation Reflectometry
- **QC**: Quasi-Coherent
- **QC-TEM**: Quasi-Coherent modes due to Trapped Electron Modes
- **SOC**: Saturated Ohmic Confinement
- **SSBM**: Single SideBand Modulator
- **SXR**: Soft X-rays
- **TEM**: Trapped Electron Modes
- **TEXTOR**: Tokamak EXperiment for Technology Oriented Research
- **TIM**: Trapped Ion Modes
- **VCO**: Voltage Controlled Oscillator
- **X-mode**: eXtraordinary mode
- **ZFs**: Zonal Flows

Chapter 1

Introduction

Contents

1.1 Issue of the energy needs & nuclear fusion

1.1.1 State & perspectives of the world energy consumption

Energy needs together with the connected environmental issues are expected to be one of the major challenges humanity will have to face in the coming centuries. As shown in figure 1.1, fossil fuel (Oil, Gas and Coal) represented in 2013 most of the total primary energy consumption. At the current extraction rate, reserves of fossil fuels were estimated in 2013 to be 54, 55 and 115 years for oil, gas and coal respectively [WEC 2013]. The term "nuclear" mentioned in figure 1.1 refers to nuclear power plants which produce electricity by fission reactions using uranium 235. The reserves of uranium are estimated to 150 years at the current reactor requirements [IAE 2014]. However, if the predicted scenario of high demand occurred, almost half of these resources would be consumed in 2035.

Resources providing more than 90% of our primary energy consumption will become economically non exploitable on the century time scale. This assessment implies that

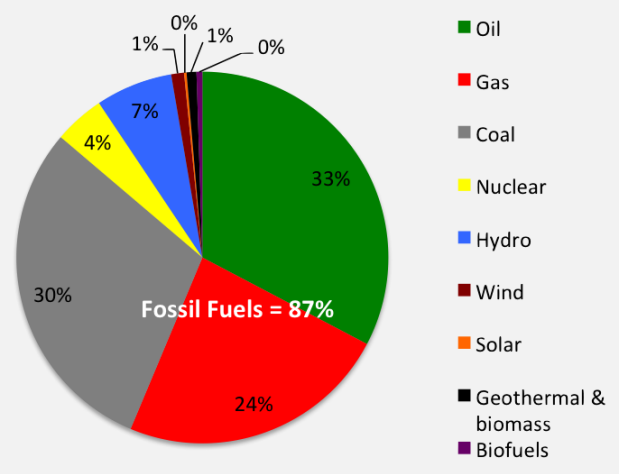

Figure 1.1: Global primary energy consumption in 2013 [BP 2014].

solutions have to be found either to produce a massive amount of energy and/or to strongly reduce its consumption.

A decrease of the energy consumption appears probable in developed countries where the energy consumption per person is currently very high and where the economical growth is rather low. However, such a scenario seems unrealistic for developing countries, which experience a strong and sustained economical development. Additionally, a drastic reduction of the global energy demand is unlikely in view of the global population growth. Indeed a stabilization of the world population is not expected below 10 billion according to the medium scenario of the United Nations [UN 2003].

An increase of the current energy sources, which will not suffer from a shortage of reserves, has to be considered. This is the case of renewable energies which represent nowadays almost 10% of the world primary energy consumption. Nevertheless, most of these energy sources do not work in a continuous way which can limit their contribution to the global energetic mix as long as the possibility for energy storage remains limited.

The discovery of new techniques is the last possibility to answer to the future needs of energy. Several new ways of renewable energy production are currently investigated. Nuclear fission of 4^{th} generation using not only the uranium 235 is also considered. This thesis has been carried out in the framework of research dedicated to nuclear fusion, another potential new energy source.

1.1.2 Main principles of energy release by nuclear reactions

In the nuclei, protons and neutrons are not held together with the same strength, but this property depends on their mass number [Figure 1.2]. This results from a competition between two forces acting on the protons: the attractive strong interaction acting at short distances and the repulsive electromagnetic force acting at larger distances.

- For small elements the binding energy per nucleon generally increases with the mass. Due to the dominant strong interaction, each additional nucleon induces that the whole is more tightly bound.

- Around the atomic mass of iron, the attractive strong force is balanced by the repellent electromagnetic forces. Nuclei are large enough so that the strong interaction no longer acts across its entire width.

- For heavier elements, the binding energy per nucleon decreases as the atomic number increases. This results from the electromagnetic repulsive force which progressively overcomes the strong nuclear force attraction.

Generally, to loosen a system requires energy while going toward a more tightly bound system releases energy. Therefore, energy can be released when a nuclear reaction produces nuclei whose the total mass gets closer to the iron mass. This is the case for fission of massive nuclei (such as uranium) or for fusion of small nuclei (such as hydrogen isotopes).

For both nuclear fusion and fission, the mass of the original nuclei/nucleus is larger than the mass of the final one(s). The mass difference is transformed in energy following the well-know Einstein formula:

$$\triangle E = \Delta m c^2 \tag{1.1}$$

with Δm the mass difference, c the light velocity in vacuum and ΔE the energy released by the reaction.

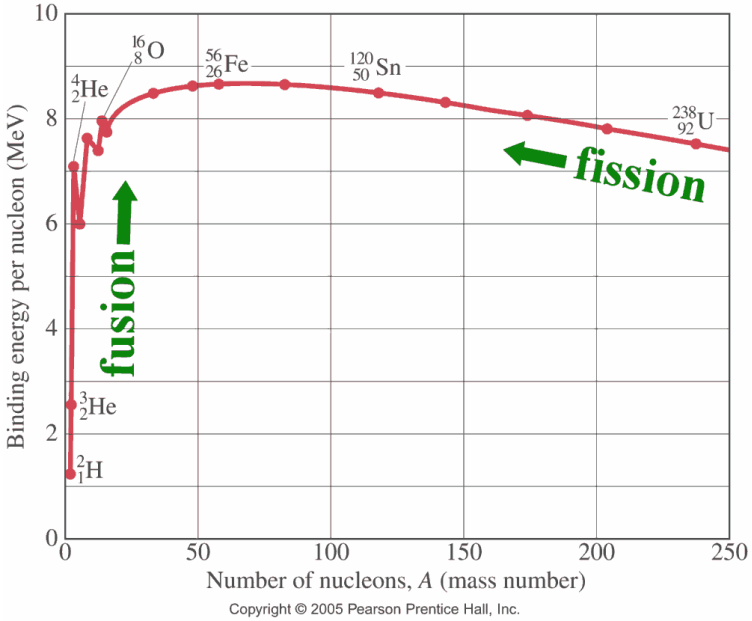

Figure 1.2: Binding energy per nucleon as a function of the mass number.

1.1.3 Nuclear fusion on earth

To fuse two positively charged nuclei, the repulsive coulomb barrier has to be overtaken at very high temperature. This occurs in a state called plasma which represents more than 99% of the known matter of the universe. Plasma is a gas in which electrons and nuclei are separated (i.e. an ionized gas) which is quasi-neutral and suffers collisions and interactions between its particles.

Such conditions are fulfilled in the sun, where the plasma is confined by gravity and the high temperatures are reached due to the fusion energy released. On earth, nuclear reactions were first triggered in thermonuclear weapons to obtained energy (H-bomb). In parallel, the research dedicated to energy production in fusion power plants has led to the first significant concept at the end of the sixties: the tokamak.

1.1.3.1 Nuclear fusion, one of the possible future solutions ?

Nuclear fusion is a potential way of electricity production offering many advantages:

- No greenhouse gases would be produced in a fusion reactor. This is an important aspect as the impact of greenhouse gases emitted by human activities on the current climate change is considered as "extremely probable" ($> 95\%$) by the Intergovernmental Panel on Climate Change [IPC 2014].

- There is no risk of uncontrolled chain reactions in a fusion reactor because the fusion of nuclei is not due to chain reactions.

- Radioactive wastes would mainly come from the activation of the reactor walls which would represent a smaller quantity than in fission reactors. Additionally, their lifetime would not be longer than a century.

- The electricity would be produced in large quantities and in a continuous way, independently from external parameters (sun, wind, etc.). One can note that alternative fusion research is focused on small, pulsed energy production [Lerner 2012].

Currently such a reactor is not feasible due to many complex technological challenges which still have to be overcome. In addition, fusion reactors would have to be efficient and reliable enough to provide energy at a competitive price. In the most optimistic case fusion power plants will probably not appear before the end of the 21^{th} century. Such long time scale combined with the uncertainties in the realization are major limitations to find investors.

In this context, several countries have launched a common project of research called Iter, currently under construction in Cadarache. The goal of this tokamak is to demonstrate that nuclear fusion devices can be energetically profitable. This fusion device will start during the 2020's and will remain an experimental device that will not produce electricity.

1.1.3.2 Conditions required to obtain fusion energy on earth

To achieve fusion in a power plant, tritium and deuterium have been selected because their fusion presents the most optimum reaction rate at the lowest temperature (on the order of 100-150 millions degrees). The fusion of these two isotopes of hydrogen releases 17.6 MeV of energy and creates a neutron and an alpha particle (i.e. a fully ionized helium atom). The energy obtained from fusion reactions could be used to warm up water, to obtain vapor acting on a turbine, and to produce electricity as in any other power plant.

The high temperature needed to achieve fusion requires initially an input of energy from additional heating systems [for more detail see section 1.2.3]. A fusion reaction is therefore energetically profitable only if a condition called the Lawson criterion is satisfied: $n\tau_E > 1.5 \times 10^{20}$ s/m^3 for a deuterium-tritium fusion at the optimum temperature mentioned above, with n in m^{-3} the plasma density and τ_E in s the energy confinement time. The confinement time is a global quantity which corresponds to the time taken by the plasma to lose all its energy content after the sources sustaining it are switched off:

$$\tau_E = \frac{W}{\sum P_{ext} - \frac{\partial W}{\partial t}} \tag{1.2}$$

with W is the plasma energy content[1] and P_{ext} the external heat source.

1.1.3.3 Two main approaches to achieve fusion on earth

On earth, the two main ways considered to satisfy the Lawson criterion are:

- **Inertial confinement** uses high plasma density and short energy confinement time. A micro sphere contains the fuel which is targeted by high-energy lasers on the order of a mega joule. The two most significant fusion devices by inertial confinement are the National Ignition Facility (NIF) [Hurricane 2014] and the Laser Mega Joule (LMJ) [Besnard 2007].
- **Magnetic confinement** uses low plasma density with long energy confinement time. Charged particles describe an helical motion along magnetic field lines used to confine them in a toroidal vacuum chamber. The magnetic field lines have to be helical to balance the effect of particle drifts [see section 2.2.1] which would lead to a loss of confinement otherwise. The main types of devices are stellarators, tokamaks and Reversed-Field Pinch (RFP). In stellarators, twisted coils are used to produce the helical magnetic field whereas it is obtained indirectly in tokamaks and RFPs by the combination of two magnetic fields. The main differences between tokamaks and RFPs is that in a RFP the magnetic field direction reverses at some radius.

[1] With s applied to each species contained in the plasma, the energy content is defined by:

$$W = \frac{3}{2} \sum_s \int n_s T_s d^3\boldsymbol{x}$$

1.2 Tokamaks

This thesis focuses on plasmas magnetically confined in tokamaks. Such a device is so far the most advanced in term of fusion performance [Keilhacker 2001].

1.2.1 Geometry

A tokamak is a toroidal vacuum chamber, in which a high temperature plasma is confined by magnetic fields. Two directions can be defined in a tokamak: the toroidal direction ϕ, and the poloidal direction θ. A schematic poloidal cut of a tokamak is shown in figure 1.3(a) with the main torus parameters and its two directions.

The size of a tokamak is defined with the major radius R_0 and the minor radius a, thus fixing ε the inverse of the aspect ratio defined by $\varepsilon = a/R_0$. Besides θ and ϕ, the position of a point in a tokamak can then be described by the parameters R (the distance from the axis of revolution), and r (the distance from the center of the plasma). The normalized radius r/a is often used to localize measurements into the torus. One can note that this schematic representation is valid for tokamaks with circular plasmas. The elongation is additionally required to properly define D-shape plasmas.

1.2.2 Magnetic configuration

Magnetic fields are required to confine a hot plasma. In a tokamak, the field lines are twisted around the torus [see figure 1.3(d)]. The helical magnetic field is obtained with the combination of a toroidal B_ϕ [see figure 1.3(b)] and a poloidal magnetic field B_θ [see figure 1.3(c)]. Toroidal coils produce B_ϕ while B_θ is produced by I_p, a current flowing in the plasma induced by a central solenoid, equivalent of a transformer.

Due to the toroidal coil configuration, B_ϕ decreases with the major radius $B_\phi \propto 1/R$. Therefore the magnetic field always has a gradient ∇B directed toward the axis of revolution. For this reason the outer part of the torus is called Low Field Side (LFS) and the inner part of the torus is called High Field Side (HFS).

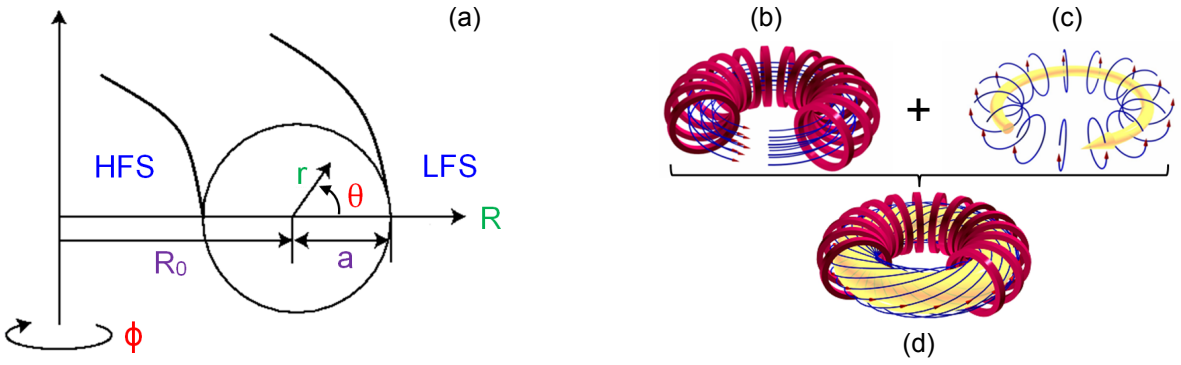

Figure 1.3: Schematic representation of (a) the main torus geometric parameters, (b) the toroidal field, (c) the poloidal field, (d) the total helical field. The magnetic field lines are shown in blue.

1.2.3 Heating systems

Once a plasma is magnetically confined, heating systems are needed to reach the high temperature required for fusion reactions. Historically, the first heating method used in tokamaks was the Joule effect. As it will be described, scientists found out that external plasma heating was necessary to reach the temperature needed. Therefore, different ways of heating the plasma are currently used in tokamaks:

- **Ohmic heating:** The current flowing in the plasma heats it by Joule effect. As the Joule effect depends on the resistivity which decreases when the temperature increases, it is efficient only at "low" temperatures. Once the temperature has reached a certain value (around 10 millions degrees), it saturates. Plasmas heated only by the Joule effect are called "Ohmic".
- **Neutral beam injection (NBI) heating:** A NBI system first accelerates charged nuclei, then they are neutralized to allow their penetration into the plasma. This would be impossible otherwise due to the magnetic field configuration of the tokamaks. The neutral particles enter the plasma with a given velocity and collide with the particles already present in the plasma, increasing the global temperature.
- **Radio frequency heating:** Electron/Ion Cyclotron Resonance Heating (ECRH/ICRH) use electromagnetic waves launched with the frequency of the electron/ion cyclotron resonances and absorbed by the plasma whose temperature increases. Lower Hybrid (LH) heating is another system launching electromagnetic waves into the plasma to achieve Landau absorption. Since its efficiency is rather moderate, it is mainly used for plasma current generation.

As it can be noticed, these heating systems use significant different processes. Therefore they will affect differently many plasma properties such as its rotation, its confinement, its turbulent aspect, etc. It is in the perspective of studying these plasma properties that different heating schemes have been analyzed in this thesis.

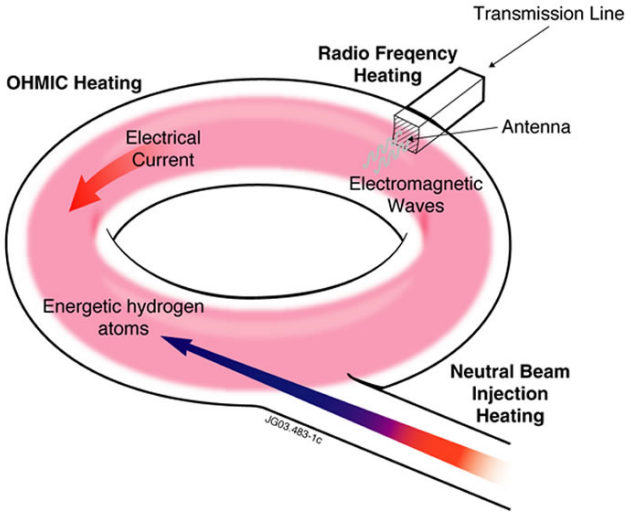

Figure 1.4: Three types of heating systems of tokamak plasmas.

1.2.4 Diagnostics

Once a plasma is confined and heated, it has to be controlled and investigated. To this end, measurement tools called diagnostics are used. Diagnostics are installed around the vacuum chamber within the port-plugs which provide access to the plasma across the first wall. This is illustrated in figure 1.5 where the port-plugs are shown in red for the Iter tokamak. The space available in the port-plug is limited and the number of diagnostics required is important. As an example more than 40 diagnostics are installed in Tore Supra. This makes the issue of the plasma accessibility and the diagnostic size essential.

The diagnostics also have to work properly in the tokamak environment (high temperatures, vacuum, radiation, strong magnetic field, neutron fluxes, etc.). Thus their design and their operation are challenging. However, they are essential to determine plasma parameters, which are critical for machine protection, plasma control and physics studies:

- First, they ensure the safe operation of the device, to prevent physical phenomena which can damage the internal walls and other components of the torus. The diagnostic systems provide data allowing to predict and mitigate such damage.
- Secondly, diagnostics also allow an efficient operation of the device by controlling its main parameters. Indeed, due to extreme conditions, the plasma of a tokamak is very unstable. Thus it is crucial to well control its parameters (position, shape, current, density, etc.).
- Finally, they allow to increase performance of tokamaks studying for example turbulence. Turbulence degrades plasma confinement which limits the performance of the fusion devices like tokamaks. A better control of turbulence implies a clearer understanding of both the physical mechanisms of turbulence and the conditions of stabilization. For this purpose, diagnostics can measure the fluctuations of the main plasma parameters (temperature, density, etc.).

Therefore diagnostics have a crucial role in the operation of fusion devices. The diagnostics used for this thesis can be classified in this third category. They are named reflectometers and will be presented in chapter 3.

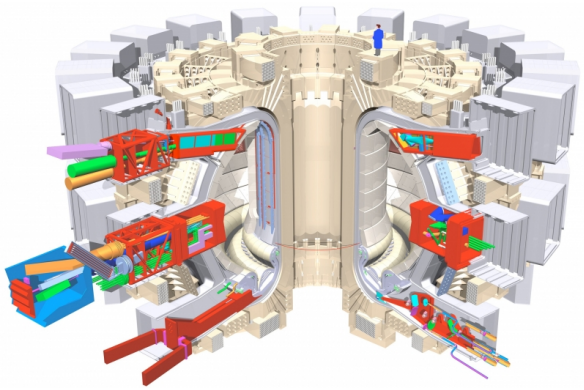

Figure 1.5: Iter tokamak with its port-plugs (in red) where the diagnostics are installed.

1.3 Particles motions

1.3.1 Gyro-motion

A plasma can be magnetically confined because its charged particles follow the magnetic field lines by describing the so-called gyro-motion (see figure 1.6). For a species s, we can define the gyro radius ρ_s (also named Larmor radius) and the gyro frequency ω_{cs}:

$$\rho_s = m_s V_\perp / e_s B \tag{1.3}$$

$$\omega_{cs} = e_s B / m_s \tag{1.4}$$

With e_s the charge, B the magnetic field, m_s the mass, $V_\perp$ the velocity perpendicular to the magnetic field lines.

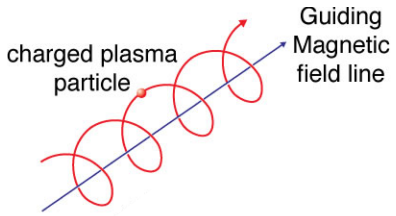

Figure 1.6: Gyro-motion of a charge particle in the presence of a magnetic field line.

1.3.2 Trapped and passing particles

In addition to the fast gyro-motion described above, the particles can follow two types of trajectories on the scale of the torus: the passing and the trapped particles.

1.3.2.1 Passing particles

As shown in blue in figure 1.7, the condition for a particle to be passing depends on the ratio of the velocity perpendicular $v_\perp$ and parallel $v_\parallel$ to the magnetic field lines. The passing particles follow the magnetic field lines as described in figure 1.8(left). In case of rational flux surface $q = m/n$ with q the safety factor, they achieve along the field line m toroidal and n poloidal revolutions before coming back to their initial position.

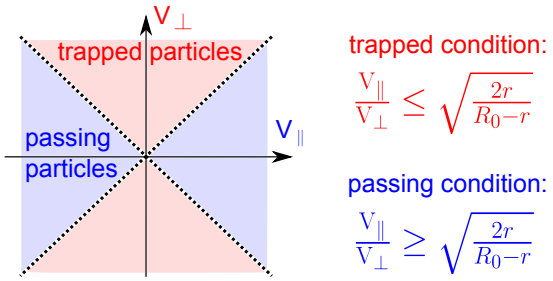

Figure 1.7: Schematic plot of the passing and trapping conditions for $\theta = 0°$ as a function of the perpendicular and parallel velocities.

1.3.2.2 Trapped particles

The trapped particles have a trajectory whose poloidal projection describes a "banana shape" [see figure 1.8(center)]. The trapped particles which are close to the passing limit are named barely trapped particles. Toroidally, the trapped particles have a slow toroidal precession [see figure 1.8(right)]. The quantities which define the properties of trapped particles are the banana width δ_b and the precession frequency ω_d:

$$\delta_b = \frac{2q\rho_s}{\sqrt{r/R}} \tag{1.5}$$

$$\omega_d \approx q\frac{\rho_s^2}{rR}\omega_{cs} \tag{1.6}$$

Trapped particles are due to ∇B, and their occurrence can be explained by the conservation of the magnetic moment $\mu = mv_\perp^2/2B$. When a particle on the LFS goes toward the HFS, B increases thus $v_\perp$ increases to keep μ constant. As the energy is conserved, $v_\parallel$ decreases and becomes zero at a given point where the particle turns around. The particle is therefore "trapped" on the LFS, with $v_\parallel \ll v_\perp$. The trapped particles which fulfill the trapped condition shown in blue in figure 1.7 can be untrapped by collisions and move to the so-called "loss cone" (in blue in figure 1.7), as a reference to the magnetic mirrors. The fraction of trapped particles is defined by:

$$f_t = \sqrt{\frac{2r}{R_0 + r}} \tag{1.7}$$

The fraction of trapped particles can be significant, as for example in Iter ($a = 2$m and $R_0 = 6.2$m) where half of the particles are expected to be trapped at mid-radius [Sarazin]. If the particles followed only the gyro-motion and these two types of trajectories, they would remain well confined. Unfortunately their dynamics are not fully explained by these motions because they also suffer collisional and turbulent transport. The transport is usually dominated by turbulent transport (also named anomalous transport). The latter is responsible of the degraded performance observed in tokamaks with respect to the first optimistic predictions made during the earlier fusion research, which were restricted to collisional transport.

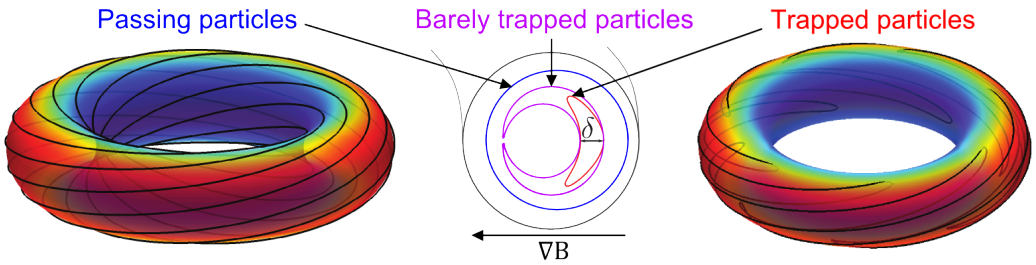

Figure 1.8: Schematic view of the toroidal trajectories of passing (left) and trappped particles (right) adapted from [Villegas 2010a]. In the middle is shown a poloidal projection of passing (blue), barely trapped (magenta) and trapped (red) particle trajectories.

1.4 Outline of the thesis

This thesis is focused on the study of density fluctuations induced by turbulence in tokamak plasmas.

Chapter 2 describes the theory of turbulence and transport. We will see that turbulence is in fact induced by several instabilities which can have different impacts. Thus it is important to be able to discriminate the regimes where the different instabilities dominate. This can be easily done in simulations but there remains one experimental issue that this thesis aims to address for one instability, the trapped electron modes.

Chapter 3 is dedicated to reflectometry, a diagnostic which allows to investigate local density fluctuations in the plasma core region. As turbulence induces fluctuating quantities, their study allows to infer information on the nature of turbulence. For this purpose, spectral analysis is used as a tool to analyze the reflectometry signal.

Chapter 4 shows the main results of this thesis: the identification of a spectral signature of a turbulent phenomena, the Trapped Electron Modes (TEM).

Chapter 5 presents the first applications of the spectral identification of TEM to the analysis of ECRH and Ohmic plasmas.

Finally, chapter 6 reports interplay observed between electrostatic instabilities (TEM) and electromagnetic fluctuations (magnetohydrodynamics modes), two families of plasma instabilities.

The experimental data analyzed in this thesis were measured in the four following tokamaks [see table 1.1 for more details]:

- **Tore Supra** is installed in the CEA Cadarache research center (France) and managed by IRFM. Due to an unexpected power supply failure, Tore Supra shut down in 2012. Currently, an upgrade of this tokamak is in progress: the WEST project for Tungsten (W) Environment in Steady-state Tokamak.
- **TEXTOR** (Tokamak EXperiment for Technology Oriented Research) operated in the Forschungszentrum-Jülich research center until 2013. It was managed by the Trilateral Euregio Cluster (TEC) which includes the following institutes: IPP-FZJ (Jülich, Germany), FOM-DIFFER (Nieuwegein, the Netherlands), ERM/KMS and SCK-CEN (Brussels and Mol, Belgium).
- **JET** (Joint European Torus) is an European tokamak located in the Culham research center (United Kingdom). It is currently the world largest tokamak.
- **ASDEX-Upgrade** (Axially Symmetric Divertor EXperiment) is installed in the Garching research center (Germany) managed by the Max-Planck-Institut für Plasmaphysik (IPP).

Almost all the results obtained in this thesis come from the analysis of databases. Following the exploration of the Tore Supra and TEXTOR databases, non-dedicated experiments from JET and ASDEX-Upgrade were analyzed. The drawback is that the experimental conditions were not always optimal because the settled parameters were not chosen (diagnostics, heating schemes, plasmas parameters, etc.).

Tokamaks	Tore Supra	TEXTOR	JET	ASDEX-Upgrade
Central B_t [T]	4.2	2.7	3.45	3.1
I_p [MA]	1.5	0.6	4.8	1.6
Minor radius [m]	0.7	0.5	1.25-2.1	0.5-0.8
Major radius [m]	2.4	1.75	3	1.65
Plasma volume [m^3]	25	7	100	13
Pulse duration [s]	$<$400	$<$10	$<$30	$<$10
Cross-section	circular	circular	D-shape	D-shape
Plasma facing materials	Carbon	Carbon	Tungsten, Beryllium	Tungsten
Heating systems	LH, ECRH, ICRH	NBI, ICRH	NBI, ICRH	NBI, ICRH, ECRH

Table 1.1: Main characteristics of the tokamaks providing data for this thesis.

The hardware tools that I have used were operating prior to my thesis. As I performed mainly database analysis, I had no need to contribute to their development.

The experimental results that I have obtained have then motivated our team to perform gyrokinetic simulations presented in section 4.3.2. Even though I have run some linear simulations during my thesis, my contribution to the nonlinear simulations was restricted to raise awareness among specialists (J. Citrin, C. Bourdelle), and to discuss their results. These experimental observations have also motivated the development of a synthetic diagnostic by one of my supervisor (S. Hacquin).

Regarding the experimental work, most of it is dedicated to reflectometry data analysis and has been carried out by myself. Collaborations on specific points not always presented in this thesis manuscript were also made with some colleagues for the data of Tore Supra (G. Hornung), TEXTOR (A. Krämer-Flecken), JET (J. Hillesheim, J.C. Giacalone) and ASDEX-Upgrade (D. Prisiazhniuk, A. Lebschy, A. Medvedeva, F. Clairet, V. Nikolaeva). Some of my work has been motivated by results obtained in other fields (intrinsic toroidal rotation in section 5.1.3 by J. Bernardo, transport studies in section 5.2.2 by D. Villegas and R. Guirlet). They are shown when it is required for the understanding of my results, and the contribution of my colleagues are highlighted.

Chapter 2

Transport and turbulence

Contents

To fulfill the Lawson criterion without damaging the devices, all the fusion plasmas should satisfy the following boundary conditions:

- In the plasma center where the fusion reactions occur, we want $T > 10$ keV and $n > 10^{20}$ particles/m^3.
- Close to the first wall, n and T have to be maintained at low values to not damage the material (in the order of several hundred degrees).

Strong gradients (∇n, ∇p, ∇T) are therefore created, and the system naturally tends to flatten these profiles with turbulent phenomena. Turbulence [George , Frish 1995] is a state of motion, apparently random and chaotic, strongly non linear which mixes, drags, increasing heat and particle transfer. It has multiple drivers and acts on multiple scales. Turbulence generally lowers the particle and energy confinement, thus degrading the performance of fusion devices.

This chapter is dedicated to turbulence and transport in tokamaks. In section 2.1, the main transport parameters are described together with the main types of transport, including anomalous turbulent transport. Section 2.2 is dedicated to turbulence. The

drift motions and the two main turbulent mechanisms they induced are explained together with the important micro-instabilities which result in tokamak plasmas. Section 2.3 is dedicated to gyrokinetic simulations, a computational tool to investigate turbulence which has been used in this thesis. Finally, section 2.4 describes the motivations of this thesis which are the experimental differentiation of turbulent phenomena.

The descriptions made in this chapter are succinct and focused on the subjects relevant for this thesis. More detailed explanations of the different transport mechanisms can be found in [Guirlet , Helander , Hogeweij]. The link between turbulence and transport is detailed in [Bourdelle 2005, Bourdelle 2007, Angioni 2009, Angioni 2012], the turbulence mechanisms and the micro-instabilities are detailed in [Garbet 2004, Sarazin , Bourdelle 2015a], an overview of gyrokinetic simulations is provided by [Garbet 2010b] and a review on zonal flows and their link with turbulence can be found in [Diamond 2005].

2.1 Transport in tokamak plasmas

2.1.1 Generalities on transport

During a plasma discharge, particles are injected in the vacuum vessel and become more energetic due to the heating systems. The performance of the discharge will then depend on the transport that will occur in the tokamak. Let's consider the particle and heat transport of a species s. The particle source is due to convection and diffusion with $V_s(r)$ and $D_s(r)$ their respective coefficients. The heat diffusion coefficient is written $\chi_s(r)$ (also named diffusivity). Then, the following equations define the particle $\boldsymbol{\Gamma}_s(r)$ and heat $\boldsymbol{q}_s(r)$ fluxes (the momentum flux is not described here):

$$\boldsymbol{\Gamma}_s(r) = -D_s(r)\boldsymbol{\nabla} n_s(r) + \boldsymbol{V}_s(r) n_s(r) \tag{2.1}$$

$$\boldsymbol{q}_s(r) = -\chi_s(r) n_s(r) \boldsymbol{\nabla} T_s(r) \tag{2.2}$$

Where $n_s(r)$, $T_s(r)$ are the density and the temperature of the species s. The convection (or pinch velocity), is by convention directed toward the plasma edge when its value is negative. Several transport mechanisms are described in the following sections by increasing order of importance for electrons and ions: classical, neoclassical and anomalous transport. Equations 2.1 and 2.2 are valid for these different transport mechanisms, with each of them providing a set of transport coefficients. Table 2.1 shows an example of the estimation of the diffusion coefficients χ and D in the Tore Supra tokamak.

Diffusion coefficients	classical	neoclassical	experimental
D [m^2/s]	$\approx 4 \times 10^{-5}$	$\approx 2.4 \times 10^{-3}$	≈ 0.25
χ_e [m^2/s]	$\approx 1 \times 10^{-4}$	$\approx 3 \times 10^{-3}$	≈ 1
χ_i [m^2/s]	$\approx 2 \times 10^{-3}$	$\approx 4 \times 10^{-2}$	≈ 1

Table 2.1: Orders of magnitude of χ and D in the Tore Supra plasma core [Gerbaud 2006]

2.1.2 Classical and neoclassical transport

2.1.2.1 Classical transport

Classical theory takes into account Coulomb interactions and is based on a simple cylindrical geometry. A quiescent plasma is assumed, therefore the transport due to fluctuations is not taken into account. Classical transport usually dominates along the field lines (i.e. $\parallel B_0$) but is small toward the edge (i.e. $\perp B_0$) [see figure 2.1]. Therefore it is not appropriate to describe the perpendicular transport of interest, related to the confinement losses in the perpendicular direction.

2.1.2.2 Neoclassical transport

Neoclassical theory is an extension of the classical theory toward the toroidal geometry which implies the existence of trapped particles [see section 1.3.2]. It takes into account the transport due to collisions between particles. Figure 2.1 show that neoclassical transport coefficients show three regimes, which depend on the normalized collisionality defined by $\nu^\star = \equiv \nu_{ei} Z_{eff}^2 qR/\varepsilon^{1.5} v_{te}$ with $\varepsilon = a/R$ and $v_{\rm te} \equiv \sqrt{T_e/m_e}$:

- **In the banana regime** ($\nu^\star \leq 1$), the trapped particles determine the transport coefficients. In the plasma core, the banana regime always includes the electrons, possibly the main ions and the light impurities.
- **In the plateau regime** ($1 \leq \nu^\star \leq \varepsilon^{-3/2}$) the transport is independent of $\nu^\star$. The main ions and the light impurities of the plasma core can be in the plateau regime, which may also include the heavy impurities in very hot plasmas.
- **The Pfirsch-Schlüter** regime ($\varepsilon^{-3/2} \leq \nu^\star$) shows the higher transport coefficients and usually includes only the heavy impurities in the plasma core. In fact it is more generally a typical regime in the plasma edge.

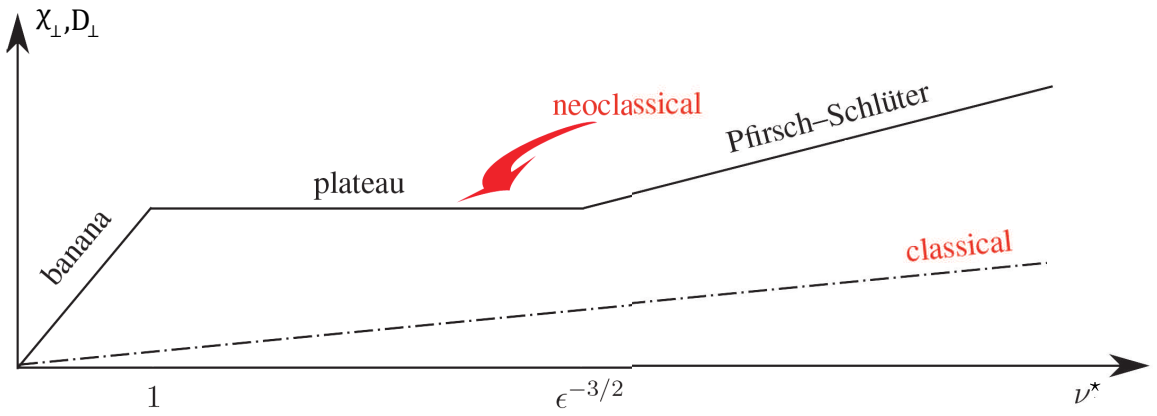

Figure 2.1: Heat χ and particle D diffusion coefficients as a function of collisionality $\nu_\star$, for the classical and the neoclassical regimes. Adapted from [Dif-Pradalier 2008].

2.1.3 Anomalous transport

The classical and neoclassical effects usually[1] do not predict the degraded confinement observed in tokamaks. Indeed the measured transport coefficients are much larger than the classical and neoclassical predictions [see table 2.1]. It is now recognized that turbulence is responsible for this so-called anomalous transport.

Fluctuations of plasma parameters are responsible of the anomalous transport observed [Ritz 1989, Colas 1998]. Among the fluctuations, two cases can be considered: electrostatic turbulence $\widetilde{\phi}$ and magnetic turbulence $\widetilde{B}$. A rough estimate of the diffusion coefficient D using a random walk model shows that $\delta\phi \approx 1\%$ or $\delta B \approx 0.01\%$ are enough to produce a $D \approx 1$ m^{2}s^{-1} [Bourdelle 2000], which is compatible with the measurements. Thus the study of the fluctuating plasma parameters is of interest to investigate transport.

For electrostatic turbulence, figure 2.2 shows schematically the processes which lead the local fluctuating quantities to act on the global confinement parameters (such as τ_E discussed in section 1.1.3 or τ_P its equivalent for particles[2]). First, the combination of a pressure gradient ∇p with local fluctuations and perpendicular drifts induces drift-waves and interchange modes. Then these mechanisms trigger different types of micro-instabilities. As a consequence, the transport coefficients are increased. In the end, the local transport coefficients decrease the values of the global confinement parameters (τ_E, τ_P) and the performance of the fusion devices are degraded.

Section 2.4.1 will show that the picture is in fact more complex. Indeed the various turbulent phenomena (ITG, TEM) can have different impact on the transport coefficients, depending also on the plasma components (electrons, ions). Additionally, the evolution of the transport coefficients also influences back the micro-instabilities via modifications of the gradients which drive them.

Thus, the study of local fluctuations is of interest to identify the underlying dominant turbulent instabilities and better understand the behavior of the global confinement parameters.

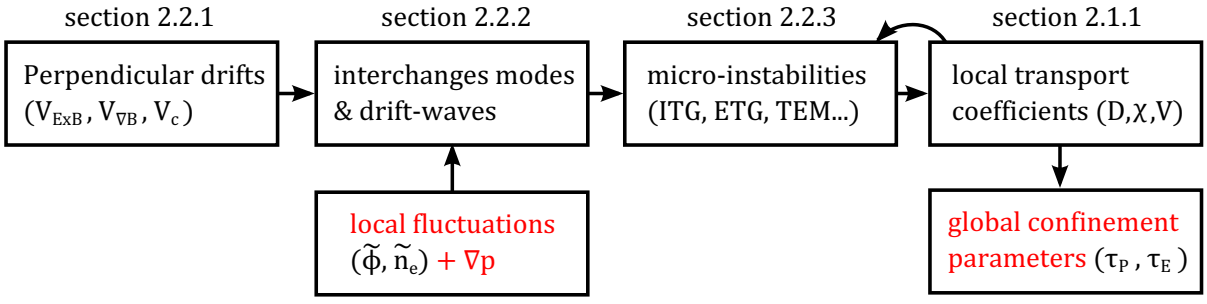

Figure 2.2: Schematic view of the anomalous transport processes showing the effect of local fluctuations on global confinement parameters via electrostatic turbulence.

[1] neoclassical effects can dominate when turbulence reduction occurs in internal transport barrier [Efthimion 1999, Takenaga 2003] or in case of heavy impurities [Casson 2015]

[2] The particle confinement time is defined by $\tau_P = N/\left(\sum \Phi_{ext} - \partial N/\partial t\right)$ with N the number of particles and Φ_{ext} the external particle source

2.2 Turbulence in tokamak plasmas

2.2.1 Drift motions

We consider the spatial and the temporal scales of the electromagnetic field variations large compared to ρ_s [see equation 1.3] and ω_{cs} [see equation 1.4], respectively. In that case, the total velocity $\mathbf{v}_{tot}$ of a plasma particle can be decomposed as:

$$\mathbf{v}_{tot} = \underbrace{\mathbf{v}_{gyro}}_{\substack{\text{Gyro-}\\\text{motion}}} + \underbrace{\mathbf{v}_{\parallel}}_{\substack{\text{Parallel}\\\text{motion}}} + \underbrace{\mathbf{v}_{GC}}_{\substack{\text{Guiding-center}\\\text{motion}}} \tag{2.3}$$

With $\mathbf{v}_{gyro}$ the gyro-motion [see section 1.3.1], $\mathbf{v}_{\parallel}$ the parallel motion of the particles along the magnetic field lines and $\mathbf{v}_{GC}$ the guiding center motion. For this study $\mathbf{v}_{GC}$ is of interest because it is responsible for the perpendicular transport, which leads to a loss of confinement. The main drifts which compose $\mathbf{v}_{GC}$ are:

$$\mathbf{v}_{GC} = \underbrace{\mathbf{v}_{E\times B}}_{\substack{E\times B\\\text{drift}}} + \underbrace{\mathbf{v}_{\nabla B}}_{\substack{\nabla B\\\text{drift}}} + \underbrace{\mathbf{v}_{c}}_{\substack{\text{Curvature}\\\text{drift}}} \tag{2.4}$$

$\mathbf{v}_{E\times B}$ is the $E\times B$ drift, $\mathbf{v}_{\nabla B}$ the grad-B drift and $\mathbf{v}_c$ the drift curvature defined by:

$$\mathbf{v}_{E\times B} = \frac{\boldsymbol{E}\times\boldsymbol{B}}{B^2} \tag{2.5}$$

$$\mathbf{v}_{\nabla B} = \frac{\mu_s \boldsymbol{B}\times\boldsymbol{\nabla} B}{e_s B^2} \tag{2.6}$$

$$\mathbf{v}_{c} = \frac{m_s v_{\parallel}^2 \boldsymbol{B}\times\boldsymbol{N}}{e_s B^2 R} \tag{2.7}$$

with $\boldsymbol{N}$ the unit vector normal to the magnetic field lines, and μ_s, e_s and m_s the magnetic moment, electric charge and mass of the particle s. We will see in section 2.2.2 that these drifts play a fundamental role in the mechanisms leading to the turbulent instabilities.

Contrary to $\mathbf{v}_{E\times B}$, both $\mathbf{v}_{\nabla B}$ and $\mathbf{v}_c$ depend on the charge thus are in opposite directions for ions and electrons, and lead to charge separations. Additionally, $\mathbf{v}_{\nabla B}$ and $\mathbf{v}_c$ do not depend on the electric field, thus they are not at the origin of the transport in case of electrostatic turbulence which arises from $\mathbf{v}_{E\times B}$ ($\mathbf{E} = -\boldsymbol{\nabla}\phi$):

$$\widetilde{\mathbf{v}}_{E\times B} = \frac{\boldsymbol{B}\times\boldsymbol{\nabla}\widetilde{\phi}}{B^2} \tag{2.8}$$

The transport in case of electrostatic turbulence will then occur via $\widetilde{\mathbf{v}}_{E\times B}$, inducing a convection rotating around the local potential maximum.

2.2.2 Main turbulent mechanisms

2.2.2.1 Drift-wave mechanism

Drift-waves arise when a homogeneous magnetic field is combined with a density gradient, conditions which can be fulfilled in a "slab" geometry. They constitute an important mechanism inducing anomalous transport in tokamaks. The mechanism responsible for drift-waves can be detailed schematically in the following way [see figure 2.3]:

(1) A periodic perturbation of the electric potential ϕ is assumed with positive $\delta\phi > 0$ and negative $\delta\phi < 0$ potential volumes (in red).

(2) Vertical electric fields appear between the positive and negative volumes.

(3) A periodic perturbation of the electron density δn_e is assumed (in blue), thus composed of the two following types of region:

- Around positive potential volumes, there are regions of super electron density ($\delta n_e > 0$) negatively charged with respect to the equilibrium.
- Around negative volumes, there are regions of sub electron density ($\delta n_e < 0$) positively charged with respect to the equilibrium.

(4) Due to the electric field created in (2), the electron regions described in (3) suffer an horizontal drift $\mathbf{v}_{E\times B}$ oriented toward the high or low n_e region.

In a stable drift-wave [see figure 2.3(a)], the electron response to an ϕ can be considered as instantaneous (i.e. adiabatic):

$$\frac{\delta n_e}{n_{eq}} = \frac{e\delta\phi}{T_e} \tag{2.9}$$

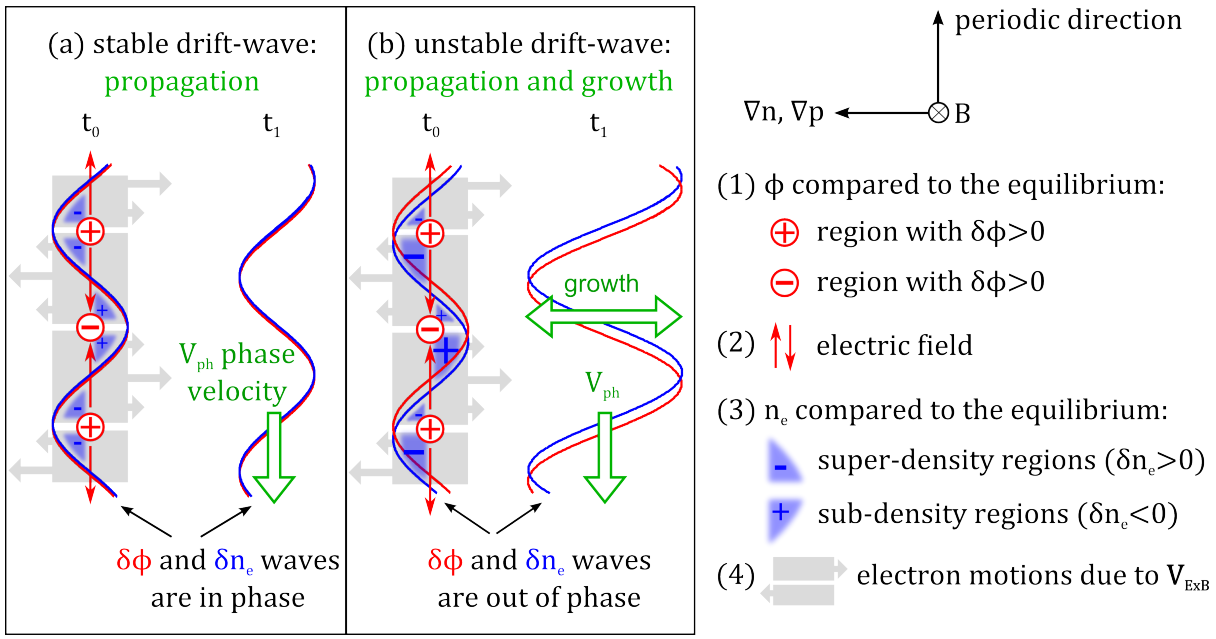

Figure 2.3: (a) principle of a stable drift wave and (b) of a unstable drift-wave.

Thus, both potential and electron density waves are considered in phase. In that case, $\mathbf{v}_{E\times B}$ only shifts the perturbed wave in the periodic direction i.e. inducing a phase velocity. Taking $v_{th,i}$ the ion thermal velocity, the drift-wave frequency produced by this mechanism is the electron diamagnetic frequency ω_e^* defined by:

$$\omega_{DW} = \omega_e^* = -\frac{k_\perp \rho_i}{v_{th,i}} \frac{\nabla n_e}{n_e} \tag{2.10}$$

A propagation of the drift-wave occurs in the periodic direction but this mechanism remains stable. In average the effects of $\mathbf{v}_{E\times B}$ do not make the wave grow. Indeed, the electrons which suffer the higher $\mathbf{v}_{E\times B}$ drift are at the equilibrium and by consequence half of each sub/super density region drifts toward the right side and the left side due to $\mathbf{v}_{E\times B}$.

The picture is different when δn_e and the $\delta\phi$ are out of phase [see figure 2.3(b)]. In that case, equation 2.9 is no longer valid and the drift-wave can be amplified. The higher $\mathbf{v}_{E\times B}$ does not act on the electrons which are at the equilibrium. In each sub/super density region, the part which drifts outward from n_{eq} is more important than the part which drifts toward n_{eq}. Thus the amplitude of the perturbation overall grows, and the wave becomes an instability.

This phase shift may originate from various phenomena but the underlying mechanism remains the one described above. Besides drift-waves, another mechanism described in the next section can induce turbulence: the interchange mode. Contrary to drift-waves which can appear in a slab geometry, the interchange modes require a toroidal geometry.

2.2.2.2 Interchange mechanism

In tokamaks, the second major type of turbulent mechanism is due to the combination of $\mathbf{v}_{\nabla B}$, $\mathbf{v}_c$ and the density or pressure gradient. This induces the so-called interchange mode that is illustrated in figure 2.4. On the LFS, its main principle can be explained schematically in the following way:

(1) Small positive (in blue) and negative (in red) equipotential convection cells are considered. They are assumed periodic in the poloidal direction.

(2) Between each positive and negative cells, a downward or a upward electric field is created.

(3) Due to the vertical $\boldsymbol{E}$, an horizontal $E\times B$ drift whose sign depends on the direction of $\boldsymbol{E}$ is induced. Due to the upward $\boldsymbol{E}$, few particles are carried from the low density region toward the cells. On the contrary due to the downward $\boldsymbol{E}$, many particles are carried from the high density region toward the cells.

(4) Then, electrons/ions suffer a vertical downward/upward force due to $\mathbf{v}_{\nabla B}$ and $\mathbf{v}_c$.

(5) The particle flux from the high density region is higher than from the low density region. Thus the already positive/negative cells receive on average even more ions/electron. This makes the initially small convection cells grow.

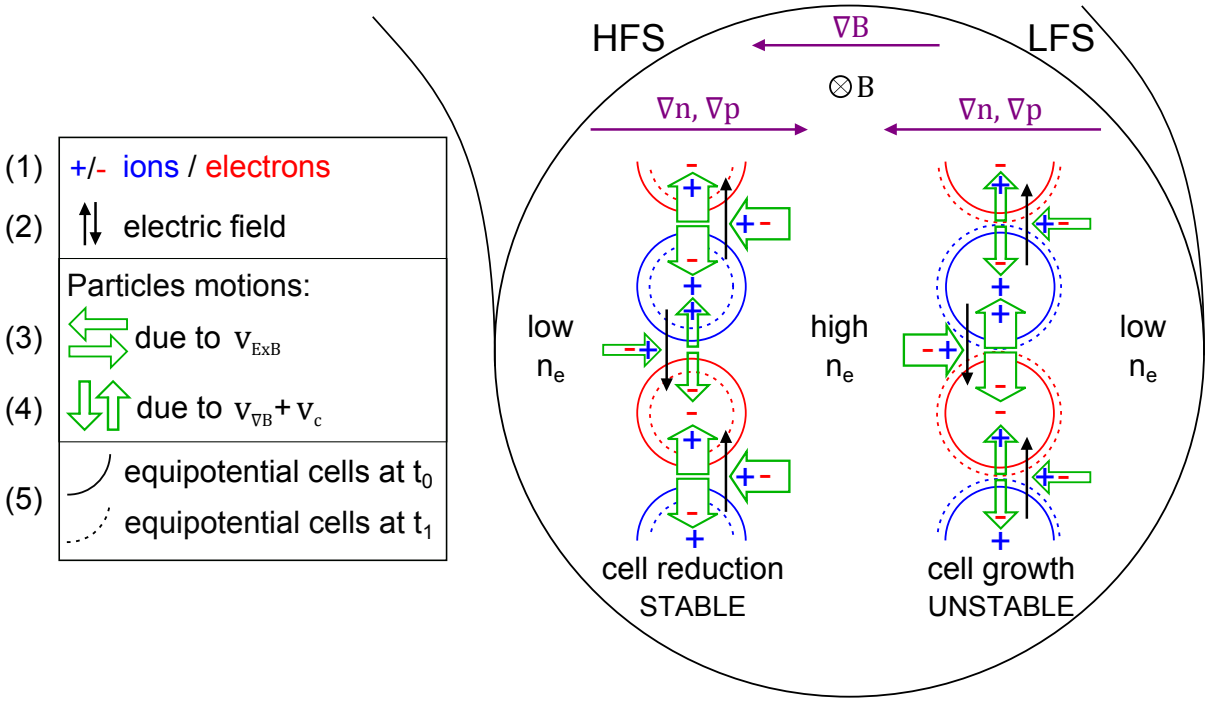

Figure 2.4: Schematic view of the interchange-like instability: equipotential convection cells grow on the LFS and decrease on the HFS.

The growth of equipotential convection cells on the LFS increases transport as they are vortices ($\mathbf{v}_{E\times B}$ being perpendicular to $\boldsymbol{B}$ and $\boldsymbol{\nabla}\phi$ see equation 2.8)

On the HFS, the positive/negative cells receive more electrons/ions which decreases their size and induces no instability. This is due to the fact that $\nabla p \cdot \nabla B < 0$ whereas an interchange mode requires both gradients to be oriented in the same direction to grow.

Thus the plasma is stable if the maximum pressure is in the same region of the minimum magnetic field. By definition, an interchange mode is therefore ballooned on the LFS of the tokamak where $\nabla p \cdot \nabla B > 0$.

Besides the charge separation required to create cells, interchange modes need that the particles stay long enough in the LFS region to affect them. Thus the parallel motion has a stabilizing effect on the passing particles by bringing them at the HFS and this way coupling the LFS and HFS regions. On the contrary, trapped particles are particularly inclined to suffer interchange modes because they are mainly located at the LFS.

It should be stressed that in reality these processes are more complicated than explained schematically in the present section. For example interchange modes can have a strong impact on drift-waves.

Now that the two main mechanisms responsible of turbulence have been introduced, the principal micro-instabilities they induce will be described in the next section.

2.2.3 Micro-instabilities: ETG, ITG, TEM and TIM

Before discussing the main micro-instabilities, it is necessary to introduce the following normalized quantities commonly used in turbulence analysis:

- R/L_{T_s}: The normalized logarithmic temperature gradient defined as the radio of R the major radius of the tokamak, with L_{T_s} the temperature gradient scale length ($L_{T_s} = -T_s/\nabla T_s$) of the species s (i and e for ions and electrons respectively).
- R/L_{n_s}: The normalized logarithmic density gradient defined similarly with the density gradient scale length $L_{n_s} = -n_s/\nabla n_s$.
- $k_\perp \rho_s$: The normalized scale of the instabilities, with $k_\perp$ the wavelength perpendicular to the magnetic field and ρ_s the Larmor radius of the species s [see equation 1.3].

In the following description, the fluctuations of the magnetic field $\widetilde{B}$ are not taken into account, only the perturbations of the electrostatic potential $\widetilde{\phi}$ are considered. Electromagnetic effects can be neglected only if β the ratio of the kinetic plasma pressure p over the magnetic pressure $B^2/2\mu_0$ is low enough [Garbet 2004]. Such an hypothesis is verified mainly in the core plasma region, where the investigations carried out in this thesis have been focused on.

Turbulence in magnetic fusion devices is attributed to micro-instabilities (drift-waves and interchanges instabilities) whose $k_\perp \rho_s$ ranges between 0.1 and a several tens as shown in figure 2.5.

The different scales of the main micro-instabilities can be inferred from their different characteristic lengths: the Larmor radius ρ_s [see equation 1.3] and the banana width δ_s [see equation 1.5] of the trapped particles. For the typical values of a tokamak we obtain the following ordering:

$$\delta_i < \rho_i \leq \delta_e < \rho_e \tag{2.11}$$

which correspond respectively to the characteristic lengths of the order of Trapped Ion Modes (TIM), Ion Temperature Gradients (ITG), Trapped Electron Modes (TEM) and Electron Temperature Gradient (ETG). It was discussed that the TIM instability ($k_\perp \rho_i < 0.1$) [Tang 1977, Tagger 1977, Depret 2000] could induce significant transport due to their large scales but the instabilities which are the most investigated are ITG, TEM and ETG:

- **ETG modes** [Drake 1988, Horton 1988, Dorland 2000] are large wavenumber instabilities $k_\perp \rho_i \approx 10$ which can arise from interchange-like instabilities due to the curvature or from drift-wave instabilities in a slab geometry. Despite their significant linear growth rate as shown in figure 2.5, ETG have generally a weak contribution to the transport because of their small scale. However they can have an important effect on electron transport in case of electron heating [Hoang 1998, Hoang 2001] or inside internal transport barriers [Hennequin 2004]. ETG were not studied as the experimental tool used (conventional reflectometers) is not sensitive to their large wavenumbers [see section 3.2 for more details on reflectometry].

- **TEM instabilities** [Kadomtsev 1967] have a phase velocity oriented in the electron diamagnetic direction. They can be driven by R/L_{T_e} or R/L_{n_e}. TEM are essentially driven by a resonant interaction of the modes with trapped electrons when their precession frequency is in the electron diamagnetic direction. Due to their localization on the bad curvature of the tokamaks (where ∇p and ∇B are aligned), trapped electrons are favorable to interchange modes driven instabilities which act in this region (see section 2.2.2.2). An important property of TEM is that they are usually damped by collisionality. Indeed, collisions induce a diffusion in the velocity space which tends to untrap particles (i.e. they go out of the trapped cone previously shown in figure 1.7). However, it has also been observed in low ν^* in case of steep density and temperature gradients that TEM may be destabilized [Connor 2006, Romanelli 2007]. Apart from collisionality, the magnetic shear can have a stabilizing effect on TEM at high values [Bonanomi 2015] but also at low or negative values (see section 6).

- **ITG modes** [Coppi 1967, Horton 1981] have a phase velocity oriented in the ion diamagnetic direction. These modes - usually the most important in tokamaks - are driven by R/L_{T_i} and stabilized by R/L_{n_i} [see figure 2.6]. They can arise from interchange-like instabilities due to the curvature or from drift-waves instabilities in a slab geometry. ITG can also be stabilized by dilution at high values of Z_{eff}, when there are less main ions in the plasma. As the impurity ions such as carbon have different characteristic frequencies due to their different mass and charge, they do not contribute to the same modes than the main ion ITG. This can even induce the so-called impurity-ITG.

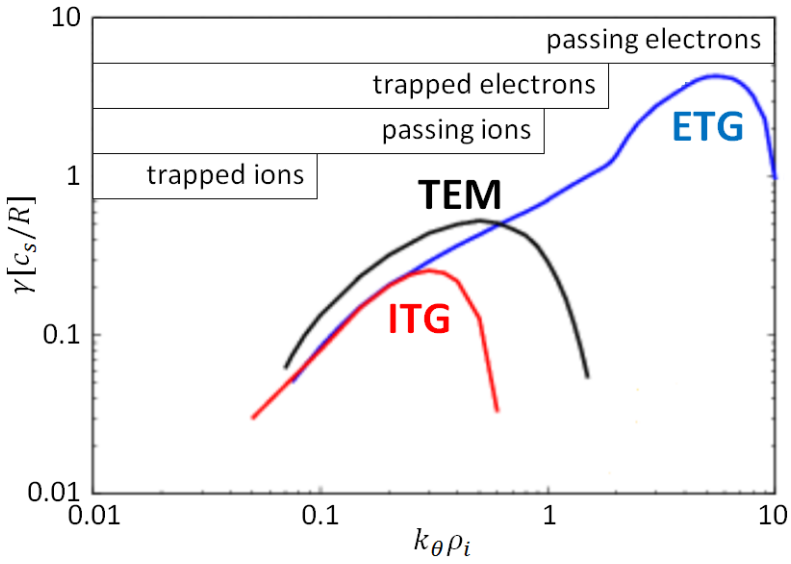

Figure 2.5: Typical linear growth rate γ as a function of the normalized scale $k_\theta \rho_i$ for the ITG, TEM and ETG instabilities, with the particles contributing to the instabilities [Casati 2012, Bourdelle 2015a].

This work focuses on ITG and TEM [Garbet 2004] which are micro-instabilities frequently dominant in the plasma core region. Even though TEM should be expected at a slightly higher $k_\perp \rho_i$ than ITG, they usually overlap at the same scale[3] $0.1 < k_\perp \rho_i < 1$ [see figure 2.5]. Therefore it is not possible to distinguish them experimentally by analyzing their normalized scale.

An important property of these two electrostatic modes is that they both exhibit a threshold above which they are unstable. These thresholds provide different instability domains for ITG and TEM, which can overlap or be distinct [see figure 2.6]. Their separation is usually an oversimplification[4] but it exists several plasma regimes in which one of the instabilities is dominant. In this work we will refer to them as ITG and TEM but one can note that several subtypes of ITG or TEM are sometimes distinguished in the literature.

As shown in figure 2.6, their stability domains depend on R/L_{T_s} and R/L_{n_s}. Their thresholds, i.e. the boundaries shown in figure 2.6 depend on plasma parameters such as T_i/T_e [Casati 2008], ν^*, s, Z_{eff}, etc. A complete review of the ITG and TEM dependency on these parameters is out of the scope of this description. Only the effects discussed later in the thesis have been described.

As it will be shown in the section 2.4.1, significant differences between the transport related to ITG and TEM are expected. This is one of the motivations which push physicists to attempt to distinguish ITG and TEM dominated regimes. In the following sections, it is described how ITG and TEM can be studied numerically [section 2.3] and experimentally [section 2.4].

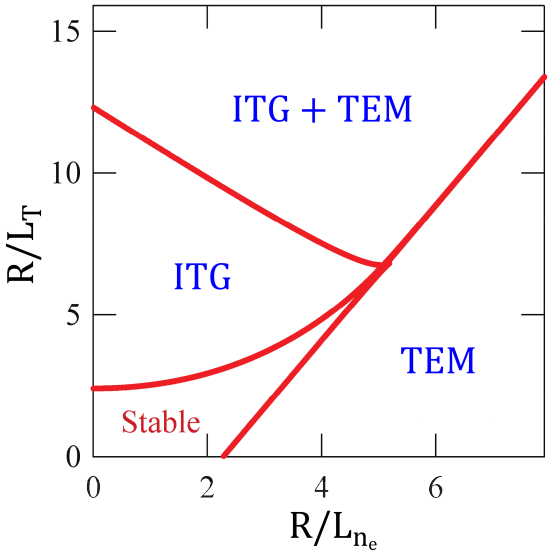

Figure 2.6: Example of a stability diagram of ITG and TEM (we consider $T_i = T_e$ and $L_{T_i} = L_{T_e}$) [Garbet 2009].

[3] The upper TEM branch can also overlap with the lower ETG range [Schmitz 2012]

[4] Instabilities can give hybrid modes [Malinov 2005] or be transformed into each other via continuous variations of the plasma parameters [Kammerer 2008]

2.3 Simulation of turbulence

Simulations of plasma dynamics allow to study the transport, to improve the understanding of the various phenomena occurring in fusion plasmas and to predict the performance of the futures devices.

2.3.1 Scope of the simulations

In the framework of this thesis, the simulations of turbulence are used to investigate and discriminate the dominant micro-instabilities among TEM and ITG modes. Indeed, both instabilities have a phase velocity in the opposite direction, which makes their differentiation straightforward. Thus their comparisons with measurements are of great interest to improve the interpretation of the experimental results.

To investigate the dynamics of a plasma, different approaches can be considered. The dynamics of each particle i could be described by $m_i d\boldsymbol{v_i}/dt = e_i(\boldsymbol{E} + \boldsymbol{v_i} \times \boldsymbol{B})$. This is not necessary and not feasible because the number of particles in a tokamak (on the order of $10 \times 10^{20}\,\mathrm{m}^{-3}$) would require too long computational times. Alternatively, two main descriptions exist:

- **The kinetic description**:

  A statistical approach is used to describe the dynamics of a plasma. A particle distribution function $f_s(\boldsymbol{x}, \boldsymbol{v}, t)$ gives the probability for a particle of the species s to have a velocity $\boldsymbol{v}$ at the position $\boldsymbol{x}$ at the time $\boldsymbol{t}$. In the simulations shown in this study, the kinetic approach has been used to investigate turbulence.

- **Fluid description**:

  A less time-consuming method considers the plasma as a fluid, using the distribution of the species considered. Some turbulence studies can be performed [Garbet 1996] with a fluid approach, but it is mainly used to study MHD instabilities. It does not properly describe the physics of interest in this work (weakly collisional plasmas, far from the equilibrium, resonant waves-particles interactions, etc.).

As mentioned above, kinetic models are used to investigate micro-turbulence in the plasma core. The motivation of this work being the comparison with fluctuation measurements, the simulations made are based on real plasma discharges performed on the Tore Supra tokamak.

We have seen in section 2.2.3 that the different turbulent modes are driven by different temperature and density gradients and that their thresholds depend on many plasma parameters (q, Z_{eff}, T_i/T_e, ν^*, etc.). Therefore, measurements of these parameters are necessary to properly model the discharges. Experimental data are used as an input of interpretative simulations[5]. Then experimental profiles fitted in that way are provided to predictive kinetic codes which model fluctuations as explained below.

[5] In all the simulations performed, the interpretative CRONOS suite of codes has performed this task [Artaud 2010]

For this study, kinetic simulations need to be run for $k_\perp$ values within the ITG/TEM range. The higher the maximum $k_\perp$ value, the longer the computing time. Thus an upper limit has to be settled (such as $k_\perp \rho_s \leq 1.5$ for instance). Additionally, to investigate TEM the simulations require non-adiabatic response of the electron to $\widetilde{\phi}$ (i.e. $\delta n_e/n_{eq} \neq e\delta\phi/T_e$). The aim of the next sections is to show the key features of the reduced kinetic model used, their output parameters and their link with the micro-instabilities.

2.3.2 From full-kinetic to gyrokinetic simulations

In the kinetic approach, the response of the distribution function to an electromagnetic field is computed by solving the Vlasov equation[6]:

$$\frac{\partial f_s}{\partial t} + \boldsymbol{v}\boldsymbol{\nabla}_x f_s + \frac{e_s}{m_s}(\boldsymbol{E} + \boldsymbol{v} \times \boldsymbol{B})\boldsymbol{\nabla}_v f_s = 0 \tag{2.12}$$

The modified distribution function will then perturb the electromagnetic fields. To compute the new electromagnetic fields, the particle density n_s and the current density j_s are calculated from the distribution function, and included in the Maxwell equations. The coupled equations lead to the dispersion relation whose solutions give the perturbation frequencies. We will see that this Vlasov–Maxwell system requires significant computing time.

A full-kinetic model gives a 6D problem which has to be solved in phase space (3 dimensions for $\boldsymbol{r}$ and 3 for $\boldsymbol{v}$). The large range of spatial-temporal scales involved [see figure 2.7(c)] makes difficult the simulations of the low frequency phenomena. To avoid this problem and hasten the computing time, the so-called gyrokinetic simulations are usually performed.

A gyrokinetic model gives a 5D problem which eliminates the fast periodic gyro-motion, keeping the slow guiding-center motion [see figure 2.7(a-b)]. A gyrokinetic description is valid if (i) the variations of the magnetic field are small during the cyclotron motion, and (ii) the fluctuation frequencies are small compared to the cyclotron frequencies. This is the case in most of the fusion devices.

Further reductions can be achieved to hasten simulations (local simulations, circular plasma shape, toroidal axisymmetry, $k_\parallel \ll k_\perp$, etc.). However, gyrokinetic simulations may still require high performance computing which run on parallelized computers. The ratio capabilities/computing time of each code depends on the number of assumptions made.

Among them the treatment of the distribution function is of great importance. It can use the so-called δf-scheme, where a scale-separation is made between the distribution function at the equilibrium f_{eq} (considered as constant) and its fluctuating part δf_s with $f_s = f_{s,eq} + \delta f_s$. The codes providing the simulations shown in this work use a δf-scheme which suppresses the impact that the fluctuations can have on the equilibrium but reduces the computational time compared to full–f codes which calculate f_s without a scale-separation between the background and the fluctuations.

[6] Or the Fokker-Planck equation if collisions are taken into account. For this a collisional operator such as $\sum_{s'} C(f_s, f'_s)$ has to be added on the right hand side of equation 2.12.

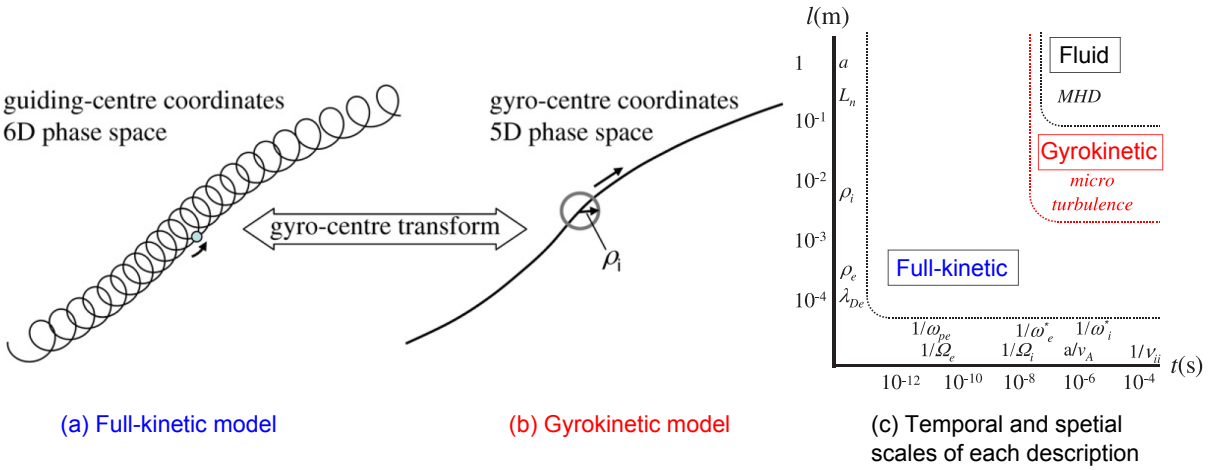

Figure 2.7: reduction from a 6D (a) to a 5D (b) problem by the gyro-center transform. (c) Different descriptions with their spatial-temporal scales. Reproduced from [Garbet 2010b].

2.3.3 Different types of gyrokinetic simulations used

One of the key features of gyrokinetic codes is the way they treat the interaction between the distribution function and the potential in the Vlasov–Maxwell system. Basically, gyrokinetic simulations can be linear, quasilinear or nonlinear. Results of the three types of simulations are shown in this work. Thus this section describes the main aspect of each of them. In addition, an illustration of the results in the case of linear theory is presented at the end of this section.

2.3.3.1 Linear simulations

Linear simulations use by definition a δf_s scheme, and neglect the quadratic terms of the fluctuating quantities $\delta f_s \times \delta\phi$. In other words, they consider only the linear response of the distribution function such as $\delta f_s = R_{lin,s}\delta\phi$. To be valid, the fluctuations have to be small compared to the equilibrium $\delta n \ll n$ which can be verified in the plasma core region but not at the edge where $\delta n/n$ can reach up to 50% [Casati 2009]. The advantage of neglecting the nonlinear coupling is to achieve simulations in a short time scale ($<$ 5min or even few seconds). Linear simulations provide ω such as:

$$\omega = \omega_r + i\gamma \tag{2.13}$$

where the imaginary part γ is the mode growth rate and the real part ω_r is the mode frequency. The sign of γ determines how the mode evolves. For $\gamma < 0$ the mode is damped and will disappear while for $\gamma > 0$ the mode will grow. The strength of γ indicates at which $k_\perp\rho_i$ are the dominant modes such as in figure 2.5. The sign of ω_r determines the nature of the mode (ion modes such as ITG or electron modes such as TEM). In the section 4.3.2.1, linear runs performed with the GENE code (Gyrokinetic Electromagnetic Numerical Experiment) have been compared with the measurements .

2.3.3.2 Quasi-linear simulations

In section 5.9, results from the QuaLiKiz code [Bourdelle 2007] are shown. This quasilinear code is based on the fast linear gyrokinetic code Kinezero [Bourdelle 2002] accounting for all the unstable modes and summing over a range of wavenumbers. Thus the Quasilinear codes also perform linear stability analysis, using a δf-scheme and providing ω_r and γ.

Additionally, QuaLiKiz gives the so-called quasilinear fluxes for the energy Q_s, the particles Γ_s (quantities discussed in section 2.1.1) and the parallel angular momentum $\Pi_{\|}$. These fluxes are computed using the mixing length rule [Kadomtsev 1965] and guided by parameters from measurements and nonlinear simulations (fluctuation intensity, spectral forms). Compared to linear simulations, they provide additional information of great interest for turbulence studies. A detailed explanation of the quasilinear theory can be found in [Bourdelle 2015a].

2.3.3.3 Non-linear simulations

They can use full-f or δf-schemes. By definition they take into account nonlinear terms $\delta f_s \times \delta\phi$ which allow to process the interactions between the different modes. This gives more realistic simulations than the linear ones, but has the drawback to require much more computational time.

Such simulations do not provide a single frequency of the most unstable mode per wavenumber k, but can give a frequency fluctuation spectrum for each k. The great advantage is that a full frequency spectrum can be obtained if the frequency spectra of all the k are added. It allows qualitative comparison with reflectometry spectra.

In the section 4.3.2.2, measured frequency spectra have been compared with frequency spectra obtained in nonlinear simulation performed by the Gene code[7]via a synthetic diagnostic [see section 3.3].

2.3.3.4 Illustration of the output of linear simulations

To illustrate the results of linear simulations described in equation 2.13, figure 2.8 shows an example of mode frequencies (left) and growth rates (right). In the two simulations presented in blue and red (not detailed here), different signs for the frequencies ω_r, and different values of the growth rates γ can be distinguished. This indicates that the nature of the dominant modes changes as a function of $k_\theta\rho_i$.

Ion modes (such as ITG) dominate in the red case for all the $k_\theta\rho_i$ values. In the blue case, electron modes such as TEM dominate for $k_\theta\rho_i < 1$ whereas ion modes dominate for $k_\theta\rho_i > 1$. The growth rate gives indications on the amplitude of the mode, maximum in both cases at $k_\theta\rho_i \approx 0.5$. These simulations will be analyzed in detail and compared with measurements in section 4.3.

Beside this illustration, in the framework of linear theory it is also possible for interchange instabilities to highlight the link between the properties of micro-instabilities

[7]The Gene code has been used in its local version.

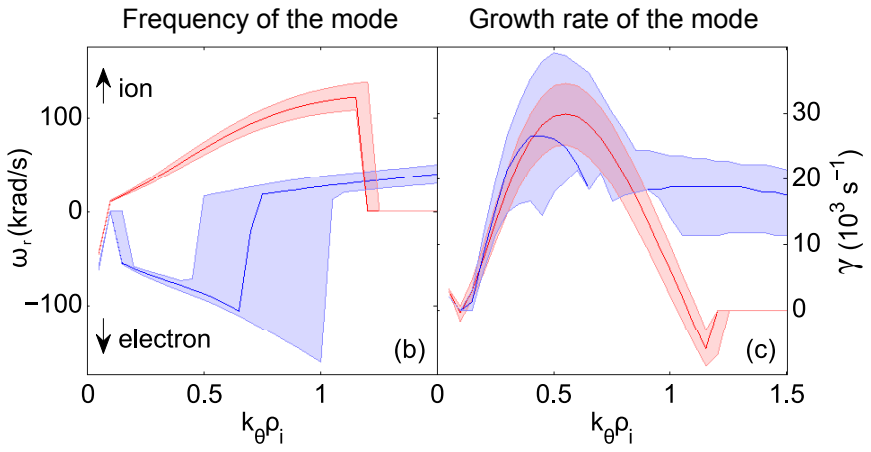

Figure 2.8: Example of the results of two different linear runs (red/blue) showing (left) the mode frequencies ω and (right) the mode growth rates γ.

introduced in section 2.2.3 and the results of gyrokinetic simulations. In the limit of long wavelength, far from the thresholds the simplified growth rate of TEM and ITG merge into:

$$\gamma^2 = \underbrace{f_t \omega_{de} \omega^*_{pe}}_{\text{TEM}} + \underbrace{\omega_{di} \omega^*_{pi}}_{\text{ITG}} \tag{2.14}$$

with f_t the trapped fraction defined in equation 1.7, and ω^*_{ds} and ω_{ps} being defined by:

$$\omega_{ds} = 2\lambda_s k_\theta V_{ds} = 2\lambda_s k_\theta \frac{-2T_s}{e_s B R} \tag{2.15}$$

$$\omega^*_{ps} = k_\theta V^*_{ps} = k_\theta \frac{B \times \nabla p_s}{n_s e_s B^2} \tag{2.16}$$

with k_θ the poloidal wavenumber, V_{ds} the vertical drift velocity due to the magnetic field curvature, $\lambda_e = 1/4 + 2s/3$ for the electrons and $\lambda_i = \langle cos(\theta) + s\theta sin(\theta) \rangle$ for the ions[8] (with $s = (r/a)(dq/dr)$ the magnetic shear), and V^*_{ps} the diamagnetic velocity.

From this simplified growth rate, we can deduce several properties of ITG and TEM discussed in sections 2.2.3. First, due to the charge e_s the diamagnetic velocities of ITG and TEM are in the opposite directions (the ion and electron directions respectively). On the LFS ($\theta = 0$) where interchange modes are the most unstable, λ_e shows the dependency of TEM on s (contrary to λ_i for ITG). Finally, when the trapped fraction $f_t \to 0$ at the plasma center, it shows that there TEM are stable.

[8] the bracket indicating an average over the mode poloidal structure

2.4 How to discriminate ITG & TEM experimentally?

Besides the gyrokinetic simulations introduced in the previous section, there are experimental techniques to get indications on the dominant instabilities. Two types of measurement can be used to discriminate ITG and TEM dominated regimes: the phase velocity estimations and the analysis of the turbulent transport. However, it should be stressed that they provide indications and not certainties.

2.4.1 Discriminating ITG and TEM with transport analysis

Different types of transport studies can be done to get indications on the dominant turbulent instability.

The first one described here is related to the particle pinch velocity (i.e. the convection introduced in section 2.1.1). To explain it, we decompose the turbulent particle flux in several terms[9]:

$$\Gamma_s(r) = \frac{n_s}{R}\Big(\underbrace{D_s(r)\frac{R}{L_{n_s}}}_{\text{Diffusion}} + \underbrace{C_s^{th}\frac{R}{L_{T_s}}}_{V_s^{th}} + \underbrace{RC_s^c}_{V_s^c} \Big) \tag{2.17}$$

where there are a diffusion term and a convection term, the later being divided between V_s^{th} and V_s^c the so-called the thermodiffusion and compressibility respectively. A more detailed description of each coefficient can be found in [Bourdelle 2007].

The diffusion is always opposite to the density gradient thus inducing a flux directed outward[10]. On the contrary, the sign of V_s^c is always directed inward. Thus the picture is already complex with a diffusion and a compressibility acting in the opposite directions. It becomes even more complicated due to the thermodiffusion (V_s^{th}) whose sign changes whether ITG or TEM dominate. As shown in table 2.2 it can be directed outward or inward, depending also on which particles it acts (electrons/ions).

	V_s^c		V_s^{th}	
	TEM	ITG	TEM	ITG
Pinch effects on the electrons	inward		outward	inward
Pinch effects on the ions			inward	outward

Table 2.2: Direction of the convective terms for ITG and TEM in the case where the curvature and ∇B are considered. Reproduced from [Bourdelle 2007] and [Angioni 2012]

Therefore the sign of the total flux exhibits a complex dependency on gradients as (i) it directly depends on R/L_{n_s} and R/L_{T_s} [see equation 2.17] and (ii) the turbulent

[9] This is one possible way to express the particle flux, but the roto-diffusion due to the presence of a toroidal angular velocity gradient can also be added [Angioni 2012] and V_s^c can be decomposed between the curvature pinch and the parallel compressibility.

[10] Except in case of hollow profiles where the gradients are reversed, and the diffusion can be directed inward.

modes which influence the thermodiffusion term are themselves dependent on R/L_{n_s} and R/L_{T_s}.

Since the first numerical evidence of the anomalous pinch due to the thermodiffusion [Garbet 2003], experimental studies have shown changes of the signs of the convective term due to transition from ITG and TEM [Xiao 2010, Zhong 2013].

Alternatively to the analysis of the pinch velocity, transport studies can look at the diffusion. The different parametric dependences of ITG and TEM can be investigated by scanning a plasma parameter and analyzing its effect on diffusion. These type of investigations [Villegas 2010b, Villegas 2014] will be shown in section 5.2.

One should note that a simple study of steady state profiles does not allow to separate the diffusive and convective terms. This can be done by perturbation experiments, i.e. modulations of ECRH or ICRH, or injection of a particle pulse.

2.4.2 Discriminating ITG and TEM with their phase velocity

Another way of investigating whether ITG or TEM dominates is to estimate the phase velocity $\mathbf{v}_{phase}$ of the turbulence. Indeed we have seen in the previous section that the phase velocity of both instabilities is in opposite directions:

- For TEM instabilities it is directed in the electron diamagnetic direction.
- For ITG modes it is oriented in the ion diamagnetic direction.

$\mathbf{v}_{phase}$ is one of the two components of the total perpendicular velocity $\mathbf{v}_{\perp}^{tot}$ of the density fluctuations:

$$\mathbf{v}_{\perp}^{tot} = \mathbf{v}_{E\times B} + \mathbf{v}_{phase} \tag{2.18}$$

with $\mathbf{v}_{E\times B}$ the $E \times B$ drift defined in equation 2.5 which is independent from the charge and therefore similar for any type of instability. It is not feasible to measure directly $\mathbf{v}_{phase}$ thus its value has to be deduced from the other velocity components. Indeed, it is in principle possible to approximate $\mathbf{v}_{phase}$ by estimating $\mathbf{v}_{E\times B}$ and $\mathbf{v}_{tot}$, and subtracting the first one from the second one. However, as we expect $\mathbf{v}_{E\times B} \gg \mathbf{v}_{phase}$, a precise and simultaneous measurement of $\mathbf{v}_{E\times B}$ and $\mathbf{v}_{tot}$ would be required. Additionally the velocity components can vary spatially, therefore local measurements are required.

In reality, it is possible to measure the total velocity of the electrons $\mathbf{v}_{tot}$ using for example Doppler Backscattered reflectometry discussed in section 3.2, but no direct local measurement of $\mathbf{v}_{E\times B}$ can be done in the plasma core[11]. Therefore $\mathbf{v}_{E\times B}$ has to be estimated using the radial force balance equation:

$$\mathbf{v}_{E\times B} = \underbrace{\frac{\nabla p_i}{eZ_i n_i B}}_{\substack{\text{(dia)}\\ \text{diamagnetic}\\ \text{velocity term}}} \underbrace{+ \; V_{\phi i}\frac{B_\theta}{B}}_{\substack{\text{(tor)}\\ \text{toroidal}\\ \text{velocity term}}} \underbrace{- \; V_{\theta i}\frac{B_\phi}{B}}_{\substack{\text{(pol)}\\ \text{poloidal}\\ \text{velocity term}}} \tag{2.19}$$

[11] In the literature estimations of $\mathbf{v}_{E\times B}$ using Doppler Backscattered reflectometry can be found, but in fact they interpret $\mathbf{v}_{tot}$ as $\mathbf{v}_{E\times B}$ assuming $\mathbf{v}_{E\times B} \gg \mathbf{v}_{phase}$.

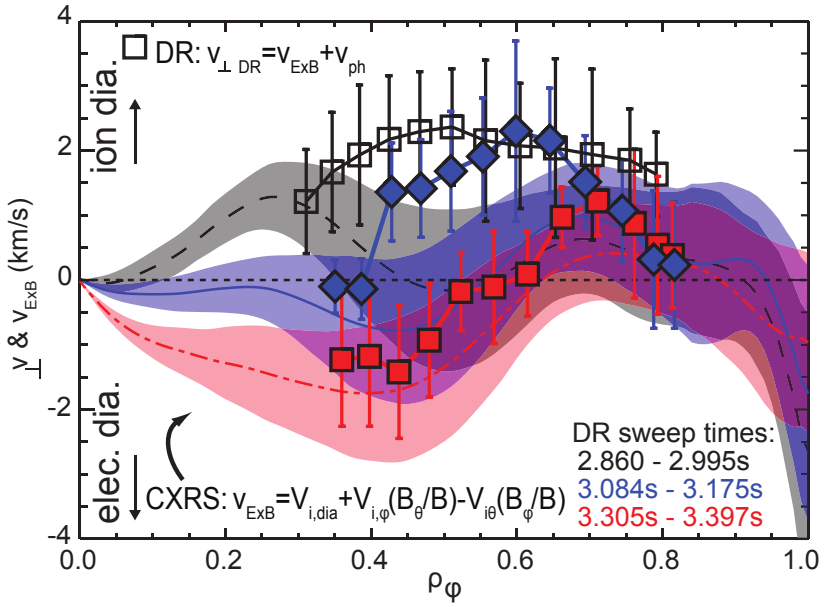

Figure 2.9: Radial evolution in AUG of (i) $\mathbf{v}_{E\times B}$ obtained by an estimation of each components described in equation 2.19 using CXRS and (ii) $\mathbf{v}_{\perp}^{tot}$ obtained by Doppler Backscattered reflectometry. Reproduced from [McDermott 2014].

with B_θ and B_ϕ the poloidal and toroidal components of the magnetic field respectively. For the main ion, p_i is the pressure, eZ_i the electric charge, n_i the density, $V_{\phi i}$ and $V_{\theta i}$ the toroidal and poloidal velocities. $V_{\phi i}$ and $V_{\theta i}$ can be obtained with measurements performed by charge exchange recombination spectroscopy (CXRS).

These measurements are complicated as they require several diagnostics (poloidal and toroidal CXRS, Doppler Backscattered reflectometry, etc.) able to measure with high accuracy. As shown in figure 2.9, even recent studies obtain large error bars. Therefore, estimation of $\mathbf{v}_{phase}$ remains challenging.

One can note that it is also possible to have some experimental indication of v_{phase} bu measuring the perpendicular velocity for different wavenumbers of the density fluctuations. This method can for instance be applied with Doppler Backscattered reflectometry [Happel 2015].

2.4.3 Motivation of this work: a new way to discriminate TEM from ITG

The two main techniques used to distinguish experimentally TEM from ITG dominated regimes (phase velocity estimation and transport analysis) are complicated. Moreover they are not always feasible as they require either advanced diagnostics or specific perturbation experiments.

The identification of a signature of these instabilities in the turbulent signals would help to directly investigate them in fluctuation measurements. This thesis will show that an additional and rather simple experimental indication can be used to investigate whether ITG or TEM dominate.

Chapter 3

Reflectometry

Contents

Reflectometry is a radar-like diagnostic which is sensitive to density fluctuations δn_e. Thus it can be used to investigate experimentally turbulent instabilities such as ITG and TEM introduced in section 2.2.3. Indeed the following equation shows that δn_e is proportional to $\delta\phi$ the fluctuations of the electrostatic potential:

$$\frac{\delta n_e}{n_e} = \Lambda \frac{e\delta\phi}{T} \tag{3.1}$$

with Λ an operator on the order of unity. Reflectometry has the advantage to provide local measurements, to be rather small, simple to implement, and cheap to build. Nowadays, reflectometry is widely used to study turbulence in magnetically confined fusion plasmas. As reflectometers rely on the propagation of electromagnetic waves in plasmas, it will be introduced in the first section. The main principles and the characteristics of the different types of reflectometers used are detailed in section 3.2. Then the properties of the reflectometry spectra and their components are discussed in section 3.4. Finally, a description of the synthetic reflectometer diagnostic used in section 4.3.3 is made.

3.1 Electromagnetic waves in plasma

3.1.1 Propagation in a homogeneous plasma

Let us consider an electromagnetic wave characterized by λ its wavelength, $\boldsymbol{k}$ its wave number, T its period, ω its frequency and $\boldsymbol{z}$ its propagation direction. Several assumptions are made to introduce the notions useful to describe the main reflectometry properties. The wave considered for this analysis is monochromatic and plane ($\mathbf{E} = \mathbf{E_0} e^{i\boldsymbol{kz} - i\omega t}$) with a high frequency thus only the electrons are not considered at rest ($\omega \gg \omega_{pi}$ and $\omega \gg \omega_{ci}$ as defined for electrons in equations 3.7 and 1.4) with a low power (in the order of the mW) not perturbing the plasma.

Such a plasma is considered as magnetized (smooth variation of the magnetic field with respect to the cyclotron motion), stationary (time scale of the plasma $\ll T$), homogeneous (scale length of the plasma $\ll \lambda$) and cold (electron motions due to the wave fields only). In this plasma, the following Maxwell equations are used to analyze the wave propagation:

$$\boldsymbol{\nabla} \times \mathbf{E} = -\frac{\partial \mathbf{B}}{\partial t} \tag{3.2}$$

$$\boldsymbol{\nabla} \times \mathbf{B} = \mu_0 \mathbf{J} + \mu_0 \varepsilon_0 \frac{\partial \mathbf{E}}{\partial t} \tag{3.3}$$

with $\mathbf{E}$ and $\mathbf{B}$ the electric and the magnetic fields respectively, $\mathbf{J}$ the current density, ε_0 the dielectric constant into vacuum and μ_0 the vacuum permeability. The propagation of an electromagnetic wave in a plasma is then obtained taking equation 3.2 in 3.3, using the Ohm's law $\mathbf{J} = \bar{\boldsymbol{\sigma}}\mathbf{E}$ and replacing $\boldsymbol{\nabla}$ by $i\mathbf{k}$ and ∂t by $i\omega$:

$$\mathbf{k} \times \mathbf{k} \times \mathbf{E} + \bar{\boldsymbol{\varepsilon}} \frac{\omega^2}{c^2} \mathbf{E} = 0 \tag{3.4}$$

with the dielectric tensor:

$$\bar{\boldsymbol{\varepsilon}} = \bar{\boldsymbol{I}} + \frac{i\bar{\boldsymbol{\sigma}}}{\varepsilon_0 \omega} \tag{3.5}$$

where $\bar{\boldsymbol{I}}$ is the unit tensor. If we define $\bar{\boldsymbol{M}}$ such as the operator $\mathbf{k} \times \mathbf{k} \times \cdot + \bar{\boldsymbol{\varepsilon}}\omega^2/c^2 \cdot$ we can write equation 3.4 as $\bar{\boldsymbol{M}}\mathbf{E} = 0$ which has non-trivial solutions only if $\det(\bar{\boldsymbol{M}}) = 0$. The latter equation provides $\mathbf{k} = \mathbf{k}(\omega)$, in other words the dispersion relation. The calculation not done here can lead to the *Appleton-Hartree* equation, which gives for the refractive index $\eta = ck/\omega$ of a wave propagating with an angle θ to the ambient magnetic field B_0:

$$\eta^2 = 1 - \frac{X}{1 - \frac{Y^2 sin^2\theta}{2(1-X)} \pm \left[\frac{Y^4 sin^4\theta}{4(1-X)^2} + Y^2 cos^2\theta\right]^{1/2}} \tag{3.6}$$

where $X = \omega_{pe}^2/\omega^2$ and $Y = \omega_{ce}/\omega$ with ω_{ce} the electron cyclotron frequency defined in equation 1.4 and ω_{pe} the plasma frequency defined by:

$$\omega_{pe} = \sqrt{\frac{n_e e^2}{\varepsilon_0 m_e}} \tag{3.7}$$

3.1.2 Propagation, absorption and reflection

In the previous section, the propagation equations in a homogeneous plasma have been described. In a tokamak, the plasma is in fact not homogeneous but these equations can provide useful reflectometer properties. The behavior of an electromagnetic wave in a plasma depends on the value of its refractive index η. Three cases can be considered:

- **Absorption or resonance** ($\eta \to \infty$) is avoided in reflectometry but used for ICRH or ECRH described in section 1.2.3.
- **Propagation in plasma** ($\eta finite$) occurs when the wave travels into the plasma before/after the reflection. In a tokamak, the reflectometer wave is launched radially thus its propagation direction is perpendicular to $\boldsymbol{B_0}$ ($\theta = 90°$ in equation 3.6).
- **Reflection or cut-off** ($\eta = 0$) happens to the reflectometer probing wave when it reaches the region of interest for the fluctuation measurements. In this case and for the propagation of a reflectometer wave in a tokamak ($\theta = 90°$), the equation 3.6 gives:

$$X\,(1-X) = 1 - X - \frac{1}{2}Y^2 \pm \frac{1}{2}Y^2 \tag{3.8}$$

The principle of all the reflectometers is to launch a wave, and to receive it back once it has propagated back and forth into the plasma.

3.1.3 Angle of propagation with respect to the reflection layer

All the reflectometers aim to reach the cut-off layer but there are two ways to probe the plasma, depending on the angle between the wave propagation and the cut-off layer. The origin of the received signal is significantly different between both cases:

- **A conventional reflectometer** probes perpendicularly to the cut-off layer ($\alpha = 90°$ in figure 3.1(a)). This is the case of the reflectometers used in this thesis which aim to analyze the reflected signal [Simonet 1985, Bottollier-Curtet 1987, Mazzucato 1991, Nazikian 1995]. As it will be explained in section 3.2.1, the two main ways to operate a conventional reflectometer allow to measure (i) local density fluctuations or (ii) density profiles. Nowadays, there are different types of conventional reflectometers able to provide additional information [see section 3.2.2].
- **A Doppler BackScattered (DBS) reflectometer** probes with an angle $\alpha < 90°$ with respect to the cut-off layer [see figure 3.1(b)]. They are not really reflectometers as they look for the backscattered wave [Zou 1999, Hennequin 1999, Hirsch 2001]. The capabilities of DBS reflectometry to measure perpendicular rotation, k-spectra were shown more than ten years ago [Hirsch 2004, Hennequin 2004, Conway 2004a, Conway 2005, Hennequin 2006]. They are also more suitable than conventional reflectometry to study radial correlation length [Blanco 2013]. As the DBS reflectometers have not been used in this thesis they will not be detailed.

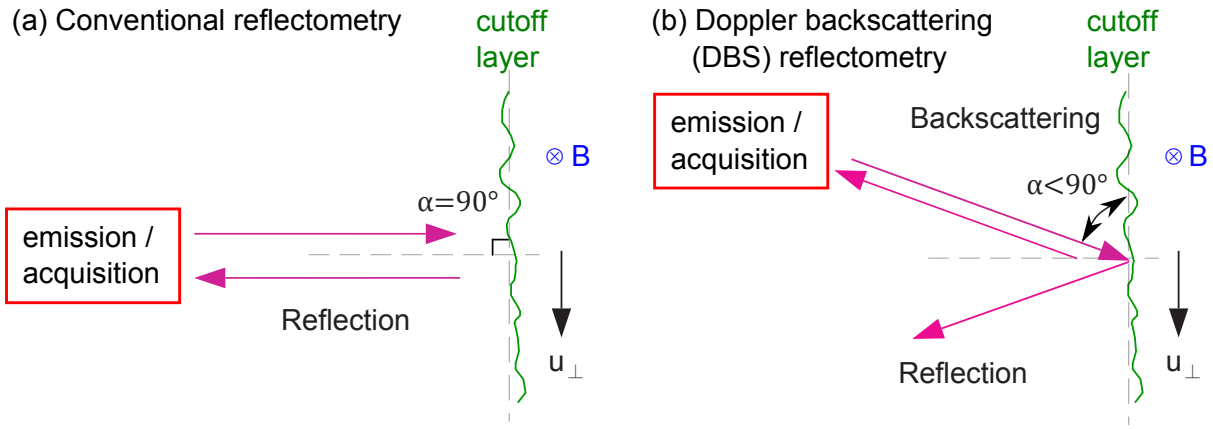

Figure 3.1: Schematic views of (a) conventional reflectometer and (b) DBS reflectometry. Adapted from [Conway 2004b].

All the data shown in this thesis come from conventional reflectometers ($\alpha = 90°$) which goal is to analyze the reflected signal. As they probe the plasma perpendicularly to the cut-off layer, the signal received is in principle not sensitive to any Doppler frequency shift $f_D \propto cos(\alpha)$. Indeed, generally speaking the Doppler effect does not act on the direction perpendicular to the propagation velocity. This is schematically shown in figure 3.2 where a receiver perpendicular to the direction of the motion detects the same wavelength as the one which is emitted at rest. Thus, only a source moving away or toward a receiver can show a Doppler effect.

However, we will discuss in section 3.4 that in some cases the backscattered signal may also influence the signal received by conventional reflectometers. Indeed, figure 3.1 shows a schematic view of both reflectometry systems but in reality DBS and conventional reflectometers can receive a part of the reflected and backscattered signal respectively[1].

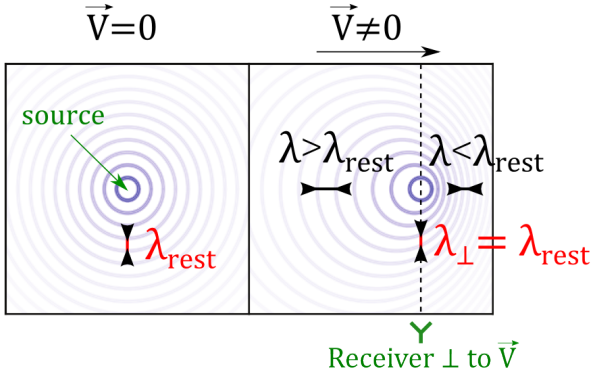

Figure 3.2: Schematic views of the Doppler effect due to a moving source showing that a receiver perpendicular to the direction of the motion is not sensitive to the Doppler effect.

[1] Conventional reflectometer can even be used as DBS reflectometers in some cases [Sirinelli 2013, Hillesheim 2015]

3.1.4 Polarization modes

At the reflection, equation 3.8 gives two solutions for the + and − signs. They correspond to the two possible polarizations of the wave for which different locations/accessibilities of the cut-off layer can be obtained:

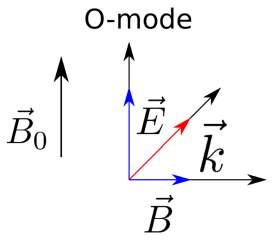

Figure 3.3: O-mode polarization, reproduced from [Hornung 2013a]

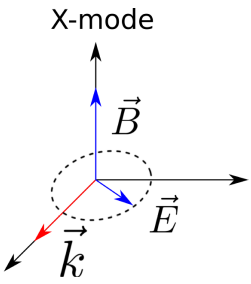

Figure 3.4: X-mode polarization, reproduced from [Hornung 2013a]

The ordinary mode (O-mode) occurs when the electric field of the launched wave **E** is parallel to the ambient magnetic field (**E** ∥ $\mathbf{B_0}$). It corresponds to the "+" of equation 3.8. In O-mode the cut-off frequency depends only on the plasma frequency (i.e. on n_e):

$$\omega_{cut-off}^{O-mode} = \omega_{pe} \tag{3.9}$$

The extraordinary mode (X-mode) occurs when the electric field of the launched wave **E** is perpendicular to the ambient magnetic field (**E** ⊥ $\mathbf{B_0}$). It corresponds to the "-" of equation 3.8. In X-mode, two solutions are possible, the "upper" and the "lower" cut-offs. Both depend on ω_{ec} and ω_p (i.e. on n_e and $\mathbf{B_0}$):

$$\omega_{Lower}^{X-mode} = \frac{\left(\sqrt{\omega_{ec}^2 + 4\omega_p} - \omega_{ec}\right)}{2} \tag{3.10}$$

$$\omega_{Upper}^{X-mode} = \frac{\left(\sqrt{\omega_{ec}^2 + 4\omega_p} + \omega_{ec}\right)}{2} \tag{3.11}$$

For these two polarization modes, the higher the probing frequency the deeper the cut-off layer. However, the cut-off frequencies of the O-mode depend only on n_e whereas the ones of the X-mode depend on n_e but also on B_0. In tokamaks, this implies that the radial profile of the cut-off frequencies is different for each polarization mode [see figure 3.5]. Indeed $B_0 \propto 1/R$ whereas n_e is usually peaked at the plasma center.

Consequently, the accessibility of the O and X-modes is noticeably different. O-mode and Upper X-mode polarizations have been used in this thesis. Only the upper X-mode polarization allows to get a reflection close to the center and on the HFS while probing the plasma from the LFS midplane. O-mode reflectometers installed on the LFS cannot access to the HFS, and a rather peaked density profile is required for them to measure close to the plasma center.

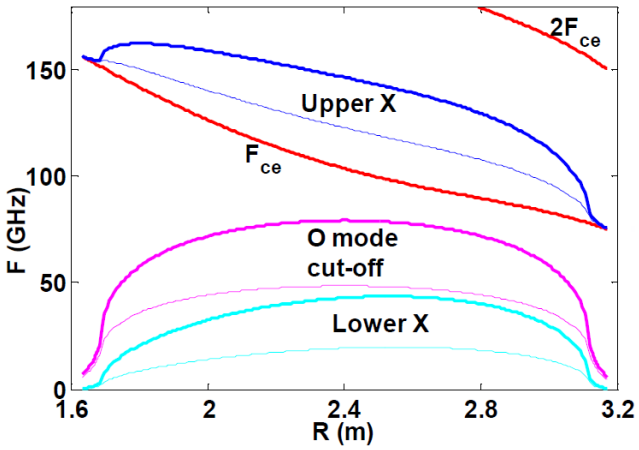

Figure 3.5: Radial profiles of the cut-off frequencies in the mid-plane of Tore Supra ($B_0 = 3.8$ T) at high density $n_e(0) = 8 \cdot 10^{19}\ m^{-3}$ (thick lines) and at low density $n_e(0) = 3 \cdot 10^{19}\ m^{-3}$ (thin lines).

3.2 Conventional reflectometer diagnostics

The working principle of two main types of reflectometers will first be introduced in section 3.2.1. Then the specificity of the three different types of reflectometers used are presented in section 3.2.2. Finally, the main characteristics of the seven reflectometers used in this thesis are summarized in section 3.2.3.

3.2.1 Working principle of reflectometers

As previously introduced, reflectometry is a technique based on the radar principle which uses the wave properties introduced in the section 3.1. As described in figure 3.6(a), a wave which is emitted from an antenna propagates into the plasma until it reaches the cut-off layer. Once the signal is reflected, it propagates back and at last, a receiving antenna collects the reflected signal after a time delay τ and a phase shift ϕ:

$$\phi(f) = \frac{4\pi}{c} f \int_{r_c}^{a} (f)\, \eta(f, r)\, dr - \frac{\pi}{2} \tag{3.12}$$

with r_c the radial position of the cut-off layer, a the minor radius of the tokamak and f the frequency of the wave. Equation 3.13 shows the time derivative of equation 3.12. It indicates that phase shifts can be due to either a change in the frequency of the probing wave (A) or a change in the optical path due to the density fluctuations (B)[2]:

$$\frac{\partial \phi}{\partial t} = \underbrace{\frac{4\pi}{c}\left(\frac{\partial f}{\partial t}\right)\int_{r_c}^{a} \eta(f, r)\, dr}_{\substack{\text{(A)} \\ \text{Changes in the frequency} \\ \text{of the probing wave}}} + \underbrace{\frac{4\pi}{c} f \frac{\partial}{\partial t}\left(\int_{r_c}^{a} \eta(f, r)\, dr\right)}_{\substack{\text{(B)} \\ \text{Changes in the optical path} \\ \text{due to the density fluctuations}}} \tag{3.13}$$

[2]Both A and B can contribute simultaneously to $\partial\phi/\partial t$ if their orders of magnitude are similar

Equation 3.13 implies that a reflectometer can operate in two different ways:

- **At a constant frequency** $A = 0$, the density fluctuations at a given reflection layer can be analyzed as shown in 3.6(a). Besides, it is possible to use an additional receiving antenna poloidally separated as described in 3.6(b). They allow to perform poloidal correlation and inferred additional fluctuation properties.

- **At a fast sweeping frequency** $A \gg B$, as (A) is of the order of the MHz whereas (B) is of the order of the kHz. In this case the turbulence can be considered as "frozen" during the frequency sweep [see figure 3.6(c)]. This allows (i) to measure electron density profiles and (ii) to study density fluctuations at each probing frequency in case of ultra-fast-swept frequencies.

In this thesis I have used three types of conventional reflectometers, namely fixed-frequency reflectometers, poloidal correlation reflectometers and ultra-fast-swept reflectometers. The working principle of each reflectometer used is shown schematically in figure 3.6 and will be described in the following section 3.2.2. The aim of these measurements was to investigate the density fluctuations and not the density profiles.

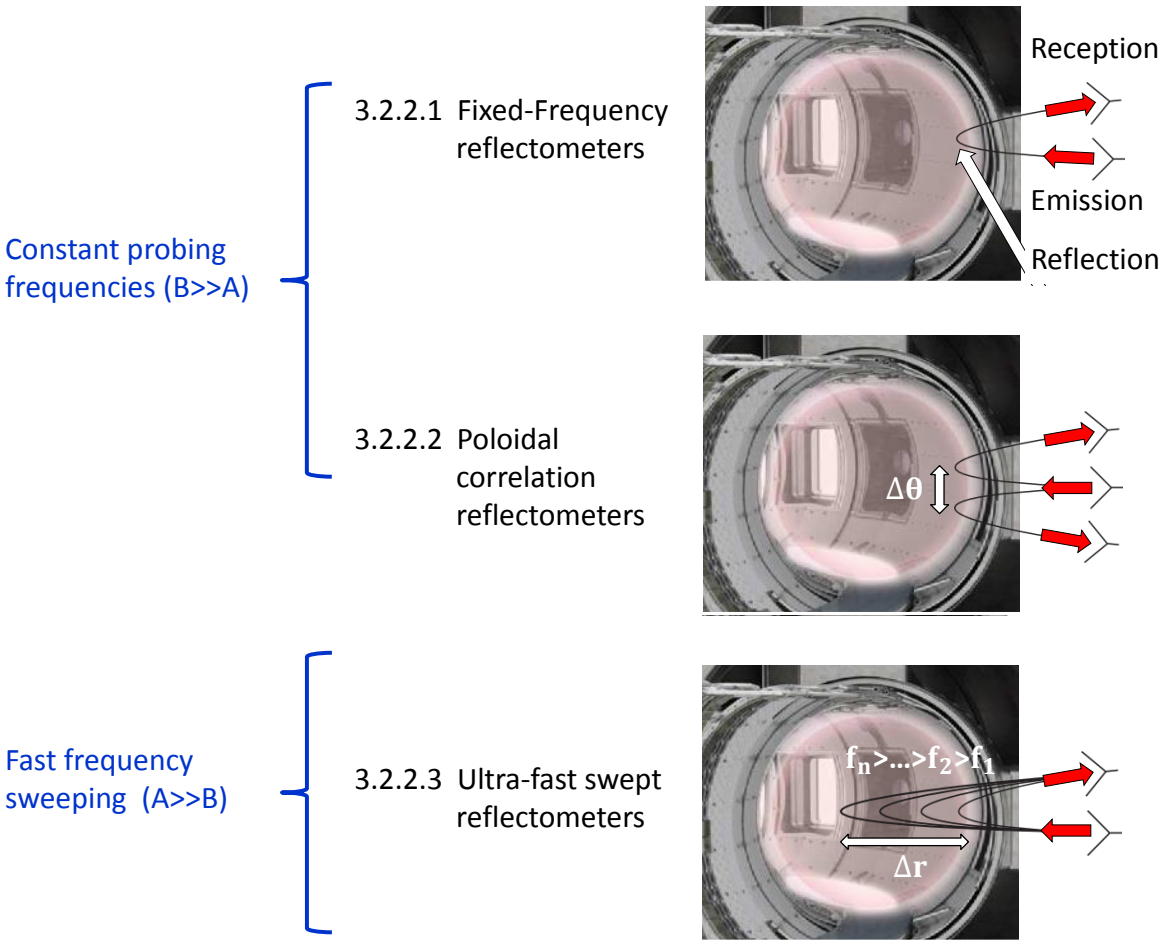

Figure 3.6: Schematic representations of the main types of reflectometer used

3.2.2 Types of reflectometers used

3.2.2.1 Fixed-frequency reflectometers

At a constant probing frequency ($B \gg A$) in equation 3.13, the location of the cut-off layer is rather stationary if the plasma parameters are constant [see figure 3.6(a)]. A simplified electronic diagram is shown in figure 3.7. When a fixed-frequency reflectometer operates, it describes the following steps:

(1) A wave is emitted by a source (a synthesizer) at a fixed frequency F_0. As the frequency[3] emitted by the synthesizer is very stable, it allows a good frequency dynamics required to analyze the frequency fluctuations coming from the plasma.

(2) For an heterodyne detection, a frequency F_m is added to this wave with a Single SideBand Modulator (SSBM). This frequency shift between the probing arm and the reference arm allows to have a wave carrier of the order of the hundred of MHz which decreases the electronic noise $\propto 1/F$. Heterodyne detection can be realized either by a single source as shown in figure 3.8 or by two separated sources.

(3) The frequency is multiplied by k to obtain a frequency able to measure at the desired cut-off layer, such as the one shown in figure 3.5.

(4) At such frequencies, a waveguide is required to carry a wave with the frequency of $k\,(F_0 + F_m)$ to the antenna.

(5) The wave goes back and forth into the plasma, suffering a phase shift φ.

(6) The frequency $kF_m + \varphi$ is obtained with a mixer (To compensate the time spent by the probing wave into the plasma, a delay line is added in the reference arm).

(7) A Low Noise Amplifier (LNA) allows to amplify the signal which is then filtered around kF_m.

(8) An I/Q demodulator provides the two signals $A(t)cos(\varphi(t))$ and $A(t)sin(\varphi(t))$ which are acquired at a frequency in the order of the MHz. $\varphi(t)$ is the phase of the signal and $A(t)$ is its amplitude. The received signal can be seen as a complex signal or electric field:

$$s(t) = A(t)cos(\varphi(t)) + iA(t)sin(\varphi(t)) = A(t)e^{i\varphi(t)} \tag{3.14}$$

The main processes described for the fixed-frequency reflectometers are common to the all types of conventional reflectometers. The characteristics proper to each other type of reflectometers used will be detailed.

[3] Even in "fixed-frequency" reflectometers, several frequency steps can be done by the synthesizer. This provides measurements at different radii in the plasma. Nevertheless, the velocity of the frequency scan is limited and consequently these measurements are well-separated in time, i.e. no simultaneous measurements can be done at different radial positions.

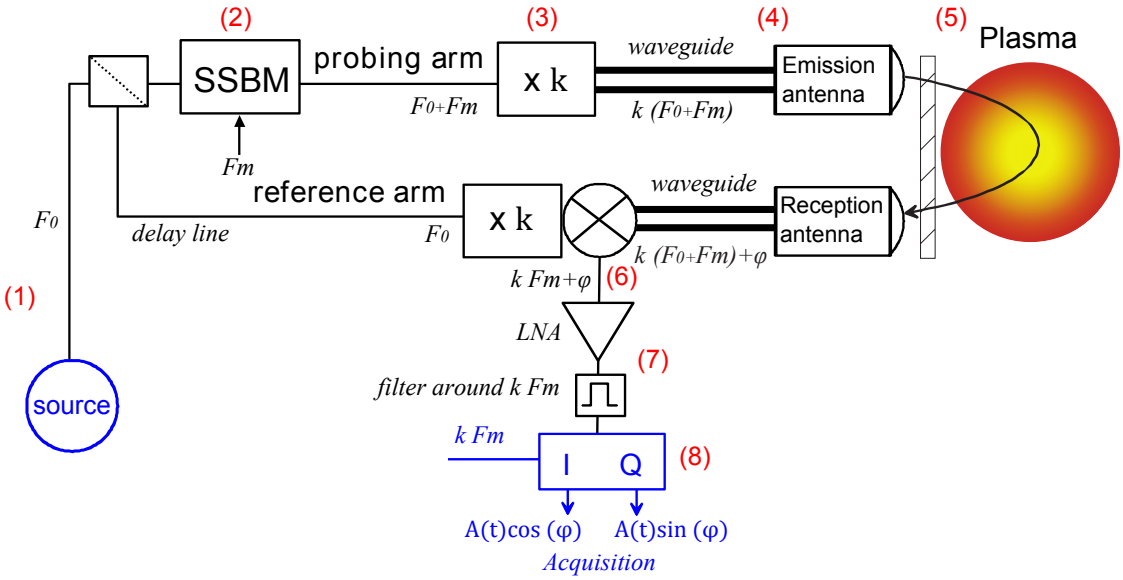

Figure 3.7: Simplified schematic reflectometer. The part common to fixed-frequency reflectometers and fast-swept reflectometers [see next section] are shown in black, whereas the main components which differ between fixed-frequency reflectometers and fast-swept reflectometers are shown in blue. Adapted from [Sabot 2006b].

3.2.2.2 Poloidal correlation reflectometry

Poloidal correlation reflectometry (PCR) [see figure 3.6(b)] works similarly to fixed-frequency reflectometry but it has the specificity to use several receiving antennas[4]. Therefore correlation can be performed between the different received signals which come from plasma locations poloidally separated [see figure 3.8(a)].

Many parameters can be inferred from such a system of antenna array [Krämer-Flecken 2011], this description is focused on the one used for this work.

A parameter of interest for this study is $v_\perp$ the perpendicular velocity of the density fluctuations. Indeed as shown schematically in figure 3.8(b), the eddies have a correlation length much higher in the parallel direction (on the order of 1-2 toroidal turns [Krämer-Flecken 2015]) than in the perpendicular direction. This makes the PCR sensitive to the perpendicular propagation only. Such a velocity is composed of a phase velocity in the plasma frame v_{phase} and the $E \times B$ drift $v_{E\times B}$:

$$v_\perp = v_{E\times B} + v_{phase} \tag{3.15}$$

The related angular velocity $\Omega_\perp = v_\perp / r$ can be estimated with the delay time Δt between two signals received by antennas separated in the perpendicular direction by an angle $\Delta\theta_\perp$:

$$\Omega_\perp = \frac{\Delta\theta_\perp}{\Delta t} \tag{3.16}$$

[4]Up to four receiving antennas are installed in the PCR systems used. It would be possible to design a PCR system with more receiving antennas.

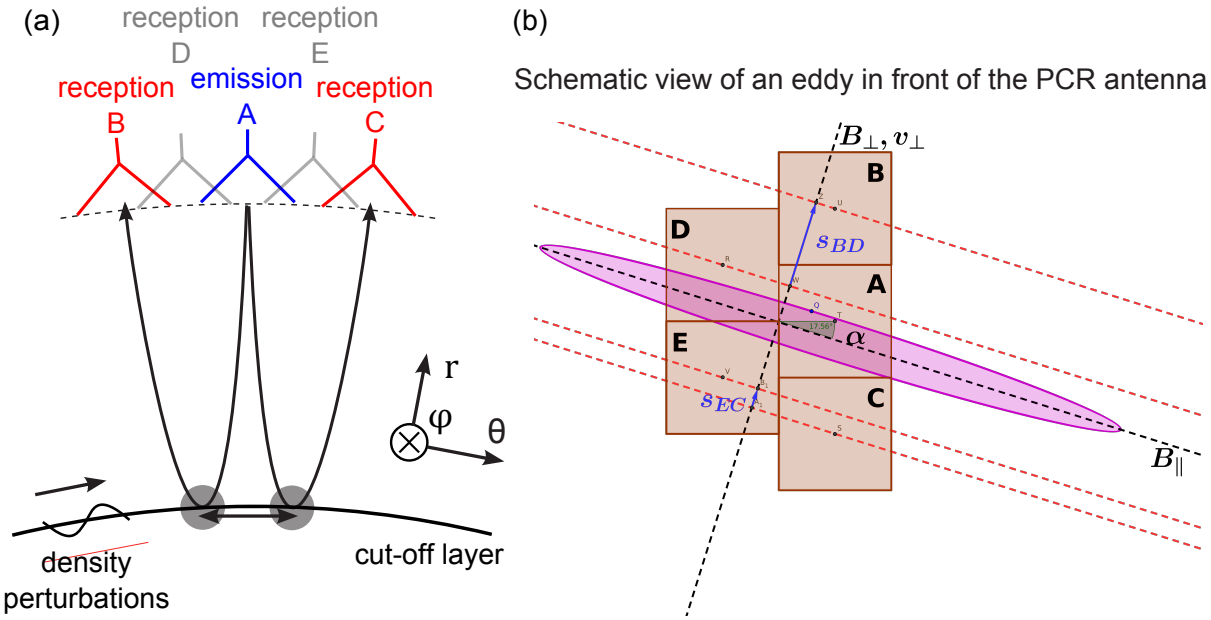

Figure 3.8: (a) schematic view of the PCR antennas in the poloidal plane, the antenna A is the a launcher, the others are the receivers. Adapted from [Meijere 2013]. (b) schematic view of an eddy elongated along a magnetic field line in front of the antennas of the AUG PCR [Prisiazhniuk 2015].

Therefore a precise estimation of $\Omega_\perp$ can be obtained if Δt is plotted for each antenna combination as a function of $\Delta\theta_\perp$. This is shown in figure 3.9(b) for the 6 combinations of the 4 receiving antennas in TEXTOR. For each combination, Δt is the time for which the signals of the two antennas s_1 and s_2 are the best correlated. As shown in figure 3.9(a), it can be estimated with a cross-correlation analysis, taking the delay time at the maximum of the cross-correlation coefficient written $\gamma(\Delta t)$:

$$\gamma(\tau) = (s_1 \star s_2)(\tau) = \int s_1^*(t) s_2(t+\tau) dt \tag{3.17}$$

$$\Delta t = \arg\max_t \left((|s_1 \star s_2|)(\tau) \right) \tag{3.18}$$

$$\gamma(\Delta t) = (|s_1 \star s_2|)(\Delta t) \tag{3.19}$$

From an estimation of $\Omega_\perp$, the perpendicular wavenumber $k_\perp$, the perpendicular mode number m and the perpendicular wave-length $\lambda_\perp$ can be calculated:

$$k_\perp = \frac{2\pi f_{turb}}{r\Omega_\perp} \tag{3.20}$$

$$m = k_\perp r \tag{3.21}$$

$$\lambda_\perp = \frac{2\pi}{k_\perp} \tag{3.22}$$

As shown in section 4.1 this allows to get useful information on the fluctuations measured.

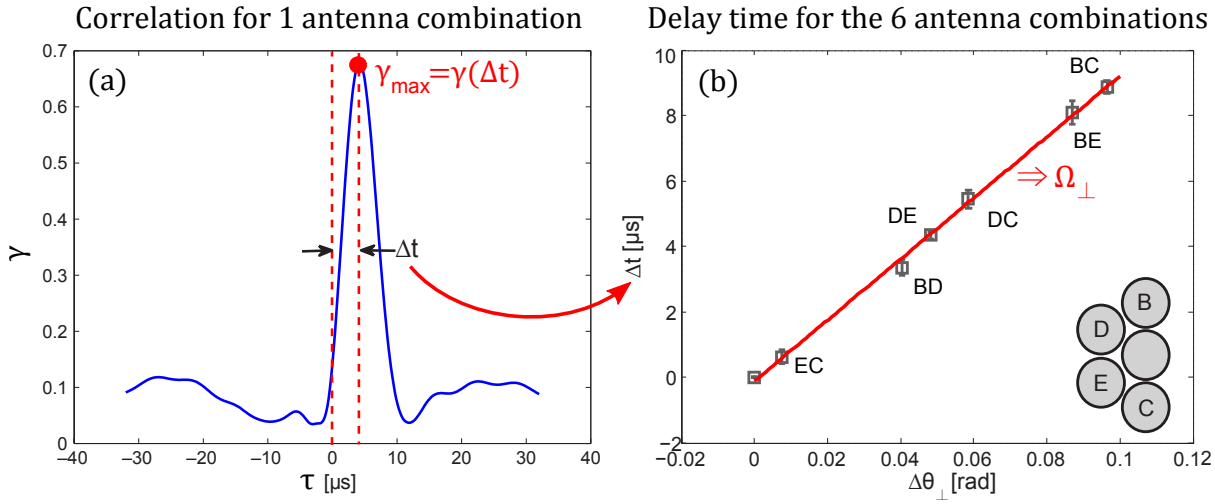

Figure 3.9: (a) example of a cross-correlation coefficient estimated for one pair of TEXTOR antennas. (b) example for all the antenna combinations of TEXTOR of the Δt the delay time as a function of $\Delta\theta_\perp$ the separation angle in the perpendicular direction. The perpendicular velocity $\Omega_\perp$ can be inferred from the slope $\propto 1/\Omega_\perp$. Reproduced form [Krämer-Flecken 2011].

3.2.2.3 Ultra-fast-swept reflectometers

This type of reflectometer scans the probing frequency with fast frequency sweeps to get $A \gg B$ in equation 3.13. The fluctuations are considered to be "frozen" during the frequency scan which induces a radial scan of the cut-off layer [see figure 3.6(c)]. Such a reflectometer can provide electron density profiles. Density profile reconstruction is not part of this work and will therefore not be detailed. A review is available in [Laviron 1996] and an example of the detailed profiles which can now be provided by this technique can be found in [Sabot 2006a] .

Recently, ultra-fast swept reflectometers have been developed [Clairet 2010]. They are able to achieve frequency scans in 2μs with a dead time between frequency sweeps of 1μs [see figure 3.10]. The main differences of ultra-fast swept reflectometers compared to fixed-frequency reflectometers are the much higher acquisition frequency (by a factor of 100) and the need of a source able to perform fast sweeping time (Voltage Controlled

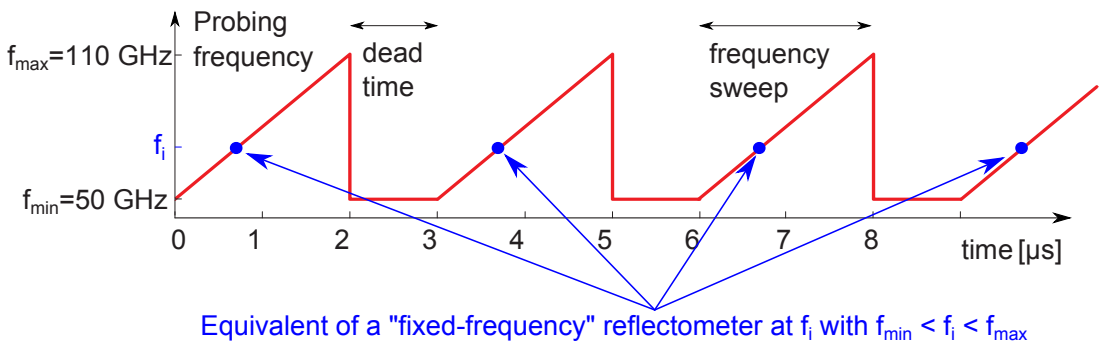

Figure 3.10: Frequency sweeps made by the ultra-fast-swept reflectometers used

Oscillator (VCO)).

With such reflectometers, fluctuation spectra analysis can also be done for each probing frequency. As shown in blue in figure 3.10, by taking the received signal for the same frequency f_i in each frequency sweep, the equivalent of a fixed-frequency measurement can be obtained. As a spectrum can be obtained for all the probing frequencies f_i between $f_{min} = 50$ and $f_{max} = 110$ GHz in that case, it has the great advantage to provide simultaneously fluctuation spectra at many different radial positions with an extremely good radial resolution, typically on the order of few tens of points per cm.

However, as the frequency emitted by the source is volatile the frequency dynamic is degraded compared to the fixed-frequency reflectometer. Additionally, the equivalent of the acquisition frequency for each probing frequency is ≤ 0.4 MHz therefore the fluctuation frequencies that can be analyzed are ≤ 200 kHz. Thus the quality of fluctuation spectra is overall reduced compared to a fixed-frequency reflectometer.

Two important parameters for ultra-fast-swept reflectometry are τ the propagation time of the probing wave and F_b the beat frequency such as:

$$F_b(F) = \frac{1}{2\pi}\frac{\partial\phi(F)}{\partial t} = \tau(F)V_s \tag{3.23}$$

V_s is the sweeping rate defined by $V_s = \Delta F/\Delta t$ with ΔF and Δt the frequency range and the duration of the frequency scan. In the ultra-fast-swept reflectometers used we have typically $V_s \approx 3 \times 10^{16}\,\mathrm{s}^{-2}$ so that the turbulence can be considered as "frozen".

3.2.3 Main properties of the reflectometers used

Table 3.1 shows the main properties of the seven reflectometers from four tokamaks used in this thesis. They belong to the three types of reflectometer described above.

	Fixed-frequency			Ultra-fast-swept	Poloidal correlation
Polarization	X-mode	X-mode	X-mode	X-mode	O-mode
$f_{probing}$[GHz]	75-110	92	105-150	50-110	24-40
$f_{Nyquist}$[kHz]	500	1000	500	≤ 200	1000
Quantities used/ possibly measurable	Frequency fluctuation spectra (FFS), spectrogram radial correlation length[5] (RCL), δn_e			Profiles of FFS, electron density, RCL, k_r-spectra δn_e	FFS, spectrogram, coherence spectra cross-phase spectra , $k_\perp$, m, $\lambda_\perp$, q, δn_e
Tokamaks	JET	Tore Supra		ASDEX-Upgrade	TEXTOR

Table 3.1: Reflectometers providing the data used in this thesis. References from the left to the right column are [Cupido 2013, Sirinelli 2013], [Hacquin 2004], [Sabot 2006b], [Clairet 2010], [Medvedeva 2015], [Prisiazhniuk 2015], [Krämer-Flecken 2010].

3.3 Synthetic reflectometer diagnostic

Besides the fluctuation data measured with the reflectometry systems described above, this thesis uses fluctuation data simulated by gyrokinetic codes such as the one shown in figure 3.11. They would be difficult to compare directly as the specificities of the reflectometers are not taken into account by the gyrokinetic simulations. A synthetic reflectometer diagnostic is therefore needed to properly compare them. Additionally, a synthetic diagnostic can help to interpret the reflectometry signal which is complicated as we will see in the next section. To reconstruct the reflectometry signal, gyrokinetic simulations provide the density fluctuations in which a wave propagation code computes the probing wave to obtain the reflected signal.

Synthetic diagnostics play an increasing role in many fields of plasma physics and fusion science, thus contributing to better interpretation of experimental results and validation of theoretical models [Coelho 2013]. This is particularly true for synthetic reflectometry diagnostics as the complexity of the physical processes taking place during the propagation of the reflectometry probing wave in turbulent fusion plasmas makes the data interpretation somewhat tricky.

Thanks to the continuing progress in processor speed the last two decades have seen the development of a large number of "full-wave" reflectometry codes, which rely on numerically solving Maxwell's equations in the presence of a plasma permittivity tensor [Hacquin 2013]. Reflectometry measurements in Tore Supra have been simulated using a synthetic reflectometry diagnostic, which relies on 2D full-wave computations of the following wave equation for the O-mode polarization [Hacquin 2015]:

$$\left[\frac{\partial^2}{\partial t^2} - c^2\nabla^2 + \omega_{pe}^2(\vec{r})\right] E(\vec{r},t) = 0 \tag{3.24}$$

A 2^{nd} order Finite Difference Time Domain (FDTD) scheme [Cohen 1998], combined with absorbing boundary conditions [Berenger 1994] and unidirectional signal emission [da Silva 2005], is used to solve equation 3.24, which allows for suitable accuracy and

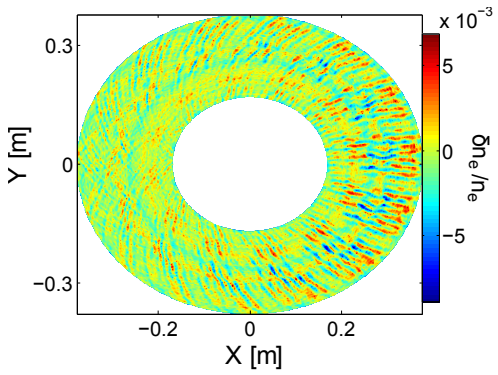

Figure 3.11: Example of a GENE map of $\delta n_e/n_e$ used as an input of the synthetic diagnostic.

[5] Conventional reflectometry always overestimates/underestimates the radial correlation length

acceptable computing times. Since usual times of the probing wave propagation in the plasma (up to a few ns) are much shorter than the typical time scales of the density fluctuations (on the order of magnitude of ms or μs at the maximum), the plasma frequency which is linearly proportional to n_e [see equation 3.7] is assumed to be motionless during all the time steps. The number of time iterations is optimized to ensure that the wave propagation has reached its stationary regime while keeping the computing time as low as possible.

The plasma density can be decomposed as the sum of the equilibrium profile $\langle n_e \rangle$ and density fluctuations δn_e due to turbulence, the latter being given by nonlinear gyrokinetic simulations from the GENE code [Jenko 2000]. Running the FDTD code for successive maps of δn_e, such as the one shown in figure 3.11 enables to reconstruct the synthetic reflectometer signal through the iteration of the following procedure:

For each GENE map of δn_e

(1) The incident probing wave is modeled by a Gaussian beam (with a width of 2 cm) at the reflectometer antenna aperture (shown in red in figure 3.12)

(2) The wave propagation is computed in the reflectometry code domain (depicted in black in figure 3.12) where the density fluctuations from GENE are taken into account for the whole spatial domain shown in the figure. It includes its propagation towards the reflecting cut-off layer (in blue in figure 3.12) up to its propagation back to the receiving antenna

(3) The reflected signal coming back to the antenna is stored in a similar way as done with a real reflectometer (i.e. the complex electric field is considered to allow for I/Q detection)

In this thesis the main goal of using a synthetic diagnostic is to compare the simulated fluctuation spectra with the measured ones. Thus once this process has been iterated for all the map of δn_e provided by the GENE code, a Fourier analysis of the recorded signal can provide the computed fluctuation spectra.

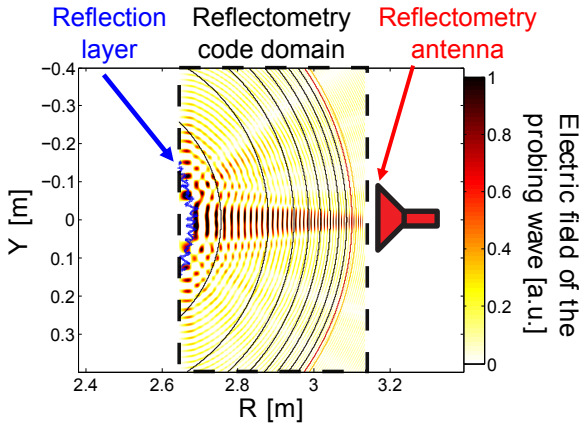

Figure 3.12: Electric field amplitude computed in the reflectometry code domain.

3.4 From reflectometry signal to fluctuation spectra components

3.4.1 Temporal reflectometry signal

As previously discussed, the goal of this analysis is to investigate the fluctuation of the reflectometry signal $s(t) = \widetilde{A}(t)e^{i\widetilde{\phi}(t)}$ with the fluctuating phase $\widetilde{\phi}(t)$ and amplitude $\widetilde{A}(t)$. $\widetilde{\phi}(t)$ and $\widetilde{A}(t)$ can account for different effects:

- **The phase fluctuations $\widetilde{\phi}(\mathbf{t})$** are due to the density fluctuations occurring mostly in the vicinity of the cut-off layer where η varies significantly ($\eta \to 0$). Thus the phase fluctuations mainly account for 1D radial effects.
- **The amplitude fluctuations $\widetilde{A}(t)$** better account for 3D effects. The amplitude is also affected by the variations of the cut-off layer but it can as well result from various processes (interference, dispersion, cut-off layer deformation, etc.).

It's important to stress that the reflectometry signal $s(t)$ used is not fully understood as its interpretation is complicated. Indeed several questions remain open: To what extent the fluctuations of the received signal and the real density fluctuations occurring in the plasma at the cut-off layer are linked (especially $\widetilde{\phi}(t) \overset{?}{\longleftrightarrow} \widetilde{\mathsf{n}}_e(t)$) ? What are the exact physical processes accounting for the amplitude and the phase ?

These fundamental issues linked to the interpretation of the reflectometry signal have not been investigated in this thesis. To improve the interpretation of the experimental signal, synthetic reflectometer diagnostics are developed such as the one previously introduced in section 3.3. In this work, the complex signal $s(t)$ is used for the analysis, thus both $A(t)$ and $\phi(t)$ are taken into account. As shown in figure 3.13(a), it is usually not possible to infer information from the temporal raw signal[6]. Fluctuation spectra are calculated for this purpose, their different types are presented in the following section.

3.4.2 Different types of reflectometry spectra

3.4.2.1 Spectra of the complex signal

All the conventional reflectometers can provide the spectra $S(f)$ obtained by probing the plasma at a fixed frequency. These spectra are the main tools of this thesis, one of them is shown as an example in figure 3.13(b). They are obtained with a discrete-time Fourier transform of the complex signal $s(t)$ recorded between the time t_0 and t_1:

$$S(f) = \sum_{t=t_0}^{t_1} s(t)e^{-i2\pi ft} \tag{3.25}$$

Before discussing the properties specific to the reflectometry spectra, some general comments can be made on the frequency spectra:

[6] One can note that in section 6.1.1, the temporal evolution of the phase of the signal will provide relevant information for the analysis.

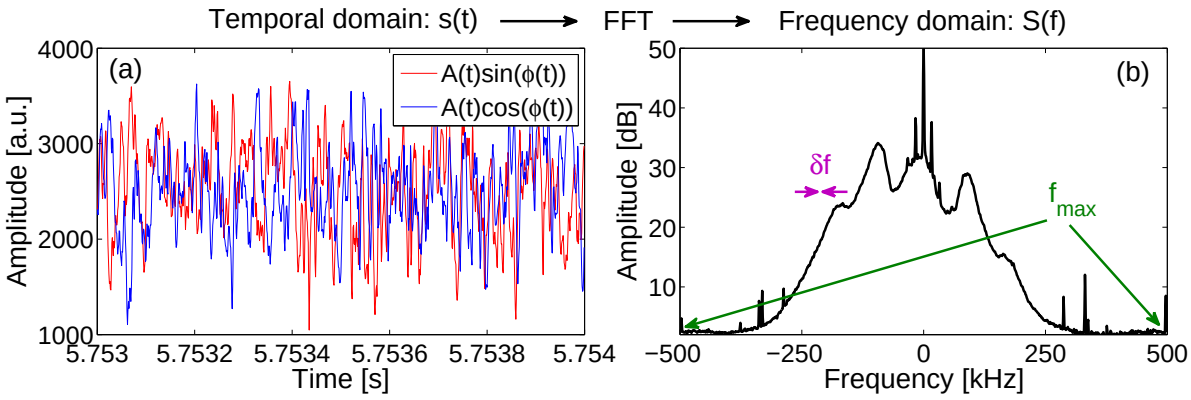

Figure 3.13: (a) example of a reflectometry temporal signal $s(t) = A(t)e^{i\phi(t)} = A(t)cos(\phi(t))+iA(t)sin(\phi(t))$ and (b) a reflectometry spectrum S(f) obtained by a Fourier analysis of the temporal signal as described in equation 3.25.

- **The maximum fluctuation frequency** f_{max} that can be analyzed in the spectra (the so-called Nyquist frequency) is by definition equal to half of the acquisition frequency. As the acquisition frequency varies between each reflectometer used, the Nyquist frequencies of the spectra analyzed range between 0.2 MHz and 1 MHz.
- **The frequency resolution** δf of the spectra is equal to the reciprocal of the length of the selected time window $t_1 - t_0$. Thus, the larger the time window is, the better the frequency resolution of the spectra. The time window of the reflectometry measurements has to be chosen long enough to provide a frequency resolution good enough to study the spectra obtained, but short enough to measure fluctuations in a "steady state" (i.e. in a regime not evolving in time). During this thesis, spectra from various reflectometers have been analyzed in different scenarios, thus the time windows can vary from a few ms to hundreds of ms. For the analysis of long time phenomena (typically in the order of s), spectrograms have been calculated (i.e. a series of spectra obtained for consecutive time windows).

Now that the general aspects of frequency spectra have been discussed, the properties of these spectra specific to reflectometry measurements can be discussed. Before it is important to stress that the interpretation of conventional reflectometry spectra is complicated and that they are not fully understood. In reality we will see that different mechanisms can induce different phase increments and decrements, explaining the asymmetric spectra obtained.

The first observations which come to mind by looking at the spectra shown in figure 3.13(b) is that (i) it shows different peaks and that (ii) it is asymmetric.

Regarding (i), the origins of all the different peaks (also named spectral components) are not known. Each type of spectral component will be discussed in section 3.4.3. Section 4 will show what is the underlying mechanism of one of them (the so-called Quasi-Coherent modes), whose finding has been one of the main results of this thesis.

The spectral asymmetry mentioned in (ii) is also not fully understood, and arises from different mechanisms which can coexist. The two main ones are:

1. **Differences in the phase increments and decrements at the reflection:**

   In the case of a reflected signal, the meaning of the positive and the negative frequencies can be inferred from its definition:

$$f = \frac{1}{2\pi}\frac{\partial \phi}{\partial t} \tag{3.26}$$

   As f is the derivative of the phase ϕ, the negative and the positive frequencies of the spectra correspond to the phase increments and the decrements respectively. This is schematically highlighted in figure 3.14(a) where the possible evolutions of the signal are shown in a complex plane at a constant value of the amplitude. In the case of a reflection layer oscillating sinusoidally shown in figure 3.14(b), the phase increment and decrement are identical and by consequence the spectra are symmetric. In reality this is never the case thus the spectra are always asymmetric.

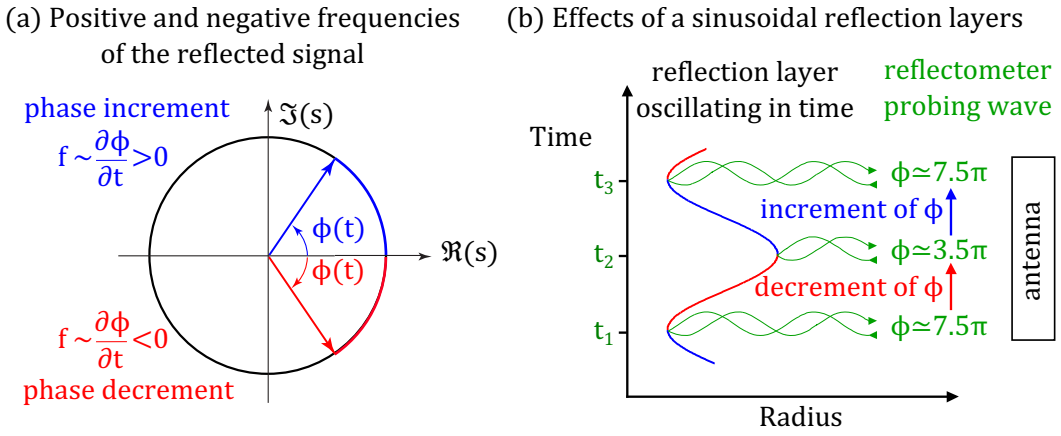

Figure 3.14: (a) evolution of the phase of the signal $\phi(t)$ in the complex plane with phase increment (blue) and phase decrement (red) corresponding to positive and negative frequencies respectively. (b) uses a similar color code to show the evolution of the reflectometer probing wave (green) due to a sinusoidal fluctuating cutoff layer.

2. **A Doppler shift acting on a fraction of the backscattered signal received:**

   It has been previously discussed in section 3.1.3 that the reflectometers probing the plasma perpendicularly to the cut-off layer should not be sensitive to the Doppler effect ($\alpha = 90°$ in figure 3.1 and the Doppler frequency shift $f_D \propto cos(\alpha)$). However, due to the divergence of the beam, the reflectometers measure over a small volume and not at a given point in the plasma. This can induce an inclination of a part of the probing wave with respect to the normal of the reflection layer ($\alpha < 90°$ in figure 3.1) and contribute to receive a part of the DBS signal. As the DBS signal is Doppler-shifted by the perpendicular velocity, its frequency spectra is strongly asymmetric, explaining a spectral asymmetry[7].

[7] The frequency shift of the conventional reflectometry spectra has already been used in that case to perform DBS reflectometry and estimate the perpendicular velocity [Sirinelli 2013, Hillesheim 2015].

In both cases, the spectral asymmetry can arise from various phenomena that are discussed in Appendix A (vertical plasma shift, tilted eddies, magnetic ripple, etc.).

3.4.2.2 Coherence spectra

The coherence spectrum $\gamma_{xy}(f)$ can be calculated with poloidal correlation reflectometers:

$$\gamma_{xy}(f) = \frac{G_{xy}(f)}{\sqrt{G_{xx}(f)G_{yy}(f)}} \tag{3.27}$$

with $G_{xy}(f)$ the cross spectral density[8] of two signals received with different antennas of the PCR, and $G_{xx}(f)$ and $G_{yy}(f)$ the auto-spectral density of each of the two received signals. Traditionally, the analysis uses the Magnitude Squared Coherence $MSC_{xy}(f)$:

$$MSC_{xy}(f) = |\gamma_{xy}(f)|^2 = \frac{|G_{xy}(f)|^2}{G_{xx}(f)G_{yy}(f)} \tag{3.28}$$

Estimating the coherence allows to get rid of most of the noise related to the reflectometry system. It also suppresses small scale phenomena whose lifetime is not long enough to be correlated between two separated antennas.

3.4.2.3 Cross-phase spectra

Parasitic noise can still induce coherent oscillations. In that case, the cross-phase spectra $\Delta\phi(f)$ allow to discriminate them from real fluctuations, which will be the only one to show a clear slope in the cross-phase spectra. It is the argument of the coherence $\gamma_{xy(f)}$:

$$\Delta\phi(f) = arctan\left[\frac{Im(\gamma_{xy(f)})}{Re(\gamma_{xy(f)})}\right] \tag{3.29}$$

From the slope of the cross-phase spectra $\Delta\phi(f)$, the angular perpendicular velocity $\Omega_\perp$ (or the perpendicular velocity $v_\perp = r\Omega_\perp$) can be estimated:

$$\Omega_\perp = \frac{2\pi\alpha}{\Delta\phi(f)} \tag{3.30}$$

with α the angle between the two separated antennas as discussed in section 3.2.2.2. If all the fluctuations frequencies rotate at the same $v_\perp$, then $v_\perp$ is better estimated by delay time calculations (which take into account all the antenna combinations) than the cross-phase slope (which comes from one pair of antennas). On the contrary, if there are different $v_\perp$ at different frequency ranges, the slopes of the cross-phase allow to visualize it contrary to delay time calculations. In this case, the latter can be used only once a filter on a frequency range of interest (provided by the cross-phase slope) is applied. Thus both approaches are complementary.

[8] $G_{xy}(f)$ is the Fourier transform of the cross-correlation function defined in equation 3.17.

3.4.3 Spectral components

Figure 3.15 shows in dotted black line the spectrum of a complex signal from one Tore Supra antenna (already shown in section 3.4.2.1). The measured spectra is decomposed in different curves, each spectral component being plotted with a different color. The curves composing the spectra have been chosen with a Gaussian shape because turbulence is assumed to be Gaussian distributed. The reconstructed spectrum shown in red is the sum of all the Gaussian components such as:

$$\text{Measured spectra} \approx \text{reconstructed spectra} = \sum \text{Gaussian components}$$

The Fytik software[9] is used to decompose the spectra in several Gaussian curves. The measured spectra is then fitted by automatic adjustments of each Gaussian property (amplitude, frequency and width (Full Width at Half of their Maximum (FWHM) written Δf). This process provides the reconstructed spectra shown in red in figure 3.15.

A quantification of the main characteristics of each spectral component can then be done with the properties of each Gaussian (amplitude, frequency and Δf). This can be used to investigate the origin of the spectral components which is not understood for all of them.

Some of them are always present whereas the appearance of others depends on the plasma scenarios and the measurement positions. The main properties of these spectral components are characterized in this section.

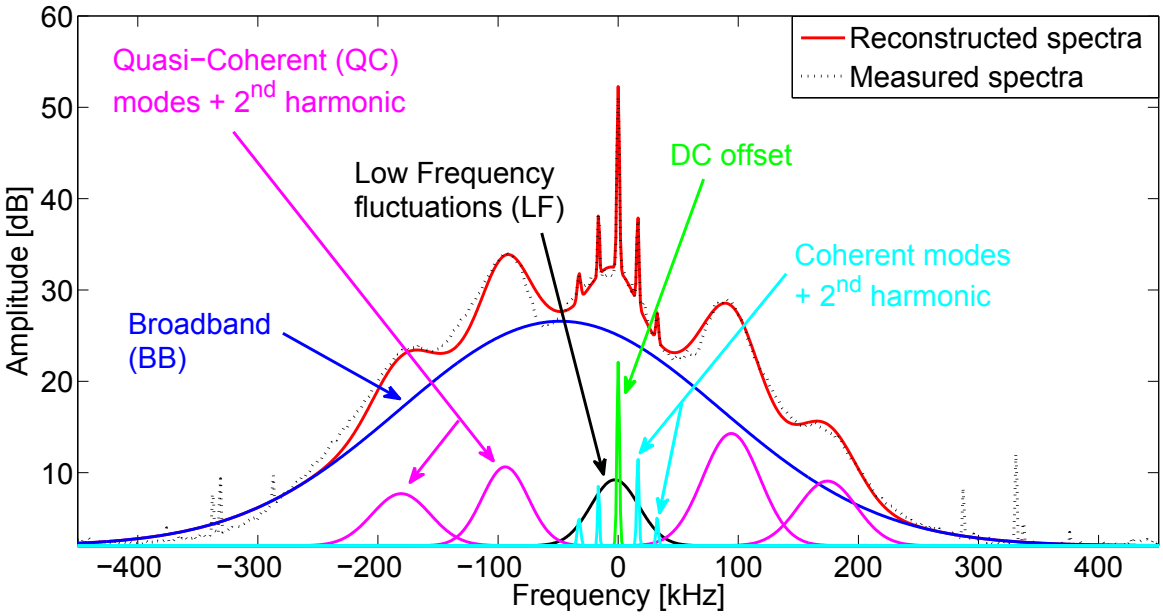

Figure 3.15: Example of a reflectometry spectra from Tore Supra #40806 (dotted black curve), with the reconstructed spectra (in red) and its different Gaussian components.

[9] http://fityk.nieto.pl/

3.4.3.1 Coherent modes

Coherent modes (see cyan curve in figure 3.15) represent oscillations at a well defined frequency, i.e. narrow frequency band fluctuations ($\Delta f \approx 1$ kHz). They can be due to different phenomena in fusion plasmas.

They are for example associated with MagnetoHydroDynamic (MHD) modes [Nave 2004, Sabot 2006a, Guimarães Filho 2012], Geodesic Acoustic Modes (GAMs) [Krämer-Flecken 2006, Fujisawa 2009, Krämer-Flecken 2009] or Alfvén instabilities [Sharapov 2004, Hacquin 2006]. Coherent modes have been studied in section 6, through the interplay they can show with the Quasi-Coherent modes that will be introduced in section 3.4.3.5.

3.4.3.2 Low Frequency (LF) fluctuations

LF fluctuations also named stochastic low frequency are represented by a small Gaussian on the top of the broadband (see black curve in figure 3.15). LF fluctuations are centered around zero kHz and never go up to more than a few tens of kHz.

They have not been studied during this thesis, but their origins will be discussed in the perspectives of this work.

3.4.3.3 Central spike at zero frequency (DC offset)

The zero frequency spike (see green curve in figure 3.15) is the reflectometer carrier wave, i.e. the DC offset or the mean value of the waveform [Conway 2002]. Its frequency is at zero because it comes from the mean amplitude and the FFT of a constant signal gives a spike at zero frequency. Its amplitude is indicative of the strength of the reflected power. If the mean value is subtracted before performing a sliding FFT, the amplitude of this spike decreases [see figure 3.16]. It does not provide indications on the physics.

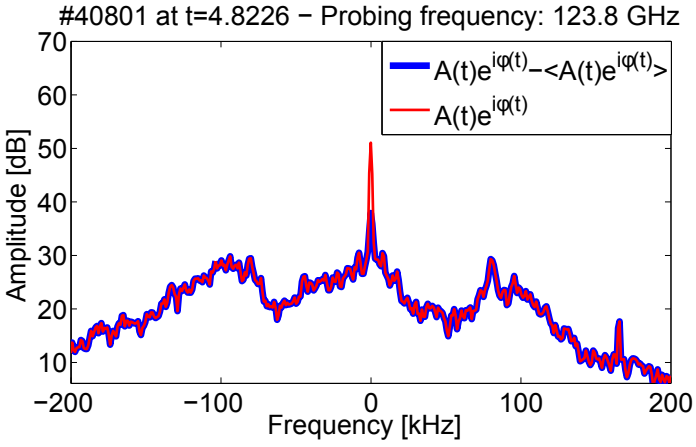

Figure 3.16: Effect of the subtraction of the mean values before the sliding FFT (Tore Supra data)

3.4.3.4 BroadBand (BB)

Broadband (BB) fluctuations (see blue curve in figure 3.15) are maximum at low frequencies and extend to much higher frequencies. A broadband spectral component is always observed in reflectometry spectra measured in tokamak plasmas.

- **The amplitude** of BB spectra is ballooned on the LFS as shown in [Vershkov 2011]. In other words, the amplitude is usually maximum at the LFS, decreases while increasing the poloidal angle, and is minimum on the HFS. Nevertheless, the BB spectra always make the main contribution to the fluctuation spectra.
- **The frequency** of the broadband spectra is expected to be centered at zero, but a small spectral asymmetry is always observed as discussed in section 3.4.2.1.
- **FWHM** of the broadband spectra depends on $v_\perp$, it is of the order of several hundred kHz. To highlight this dependency, $v_\perp$ is plotted as a function of the FWHM for a set of TEXTOR discharges including co and counter rotation NBI, ICRH and Ohmic discharges [see figure 3.17]. The link between $v_\perp$ and the spectra broadening is clearly observed. This comes from the fact that an oscillating system rotating faster will show higher oscillations frequencies. This is not strictly speaking due to a Doppler shift of the spectra which occur toward a single direction (positive or negative frequencies) but to a Doppler broadening which act symmetrically on both sides of the spectra.

Broadband spectra are generally attributed to turbulence [Frish 1995]. In section 4 some indication that ITG modes contribute to these fluctuations will be presented, and their origins will be discussed in the perspectives of this work.

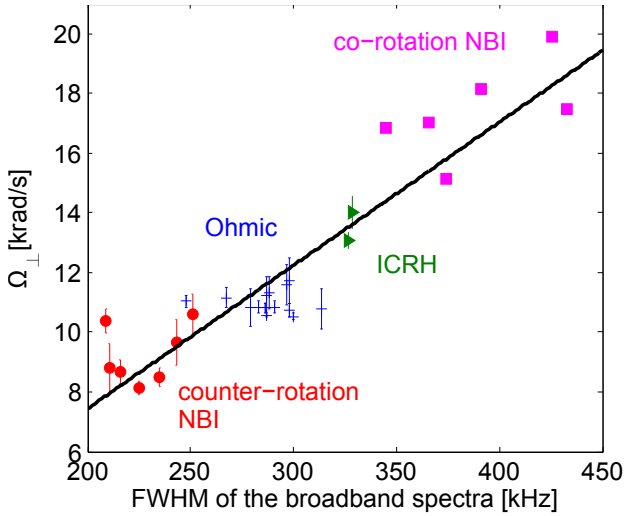

Figure 3.17: Effect of the perpendicular rotation on the spectra width in a set of TEXTOR discharges (#116494, #116495, #107985-7, #108012, #108824, 116518). These measurements were made from the LFS with a plasma current of $300 < I_p[\text{kA}] < 400$, a magnetic field $2.25 < B_t[\text{T}] < 2.5$, a central density of $1.5 < n_e[10^{19}\,\text{m}^{-3}] < 2.15$, $P_{co-NBI} = 400$ kW, $P_{counter-NBI} = 1300$ kW, $P_{ICRH} = 800$ kW.

3.4.3.5 Quasi-Coherent (QC) modes

QC modes (see magenta curves in figure 3.15) share characteristics of both coherent modes and broad-band fluctuations. Similarly to coherent modes they oscillate around a given frequency but their rather broad-band frequency ($\Delta f \approx$ tens of kHz) is reminiscent of broadband fluctuations which indicates that turbulence may play a role in these fluctuations. QC modes may possibly originate from various phenomena, the distinction is made between observations at the plasma edge and in the core region:

- **At the plasma edge (r/a>0.95)**, QC modes have been reported in several advanced regimes (H-modes [Da Graça 2013, Diallo 2014, Wang 2014, Zhong 2014], Enhanced D_α H-modes [Greenwald 1999, Snipes 2001, Terry 2005, Golfinopoulos 2014, LaBombard 2014], I-mode [Whyte 2010, White 2011, Cziegler 2013]). At the moment there is no unified explanation for these modes which present similar QC spectral signatures. None of them has been clearly identified regarding its underlying mechanism. Several instability mechanisms have been suggested, as for example the kinetic ballooning mode which limits the pedestal growth in H-mode [Diallo 2014]. They have not been investigated in this thesis.
- **In the plasma core (0.1<r/a<0.95)**, QC modes can be observed depending on the plasma scenario. They are the main topic of this work and their origin is investigated in detail in section 4. It is shown in this thesis that they arise from TEM instabilities and they have been named QC-TEM.

3.5 Which link between the spectral components and turbulence ?

Among the different spectral components, some have been identified to their underlying mechanism such as the coherent modes (GAMs, MHD). Other types of fluctuations such as Quasi-Coherent modes (QC), the low Frequency Fluctuation (LF) and the BroadBand spectra (BB) were not yet understood.

Previous studies [Vershkov 2005, Vershkov 2011] have shown that BB, LF and QC modes have different properties suggesting that they arise from different underlying mechanisms. Among them one can cite their poloidal ballooning as shown in figure 3.18 where we can observe that the BB and the QC modes are ballooned on the LFS contrary to LF fluctuations.

Investigations carried out during this thesis have been mainly focused on QC modes which can appear depending on the plasma scenario. However, in view of the results obtained, the role of LF fluctuations and of the BB will be discussed in the perspectives of this work in section 7.2.

QC modes were originally suspected to be due to ITG modes in previous studies [Vershkov 2005, Vershkov 2011, Vershkov 2013a]. During the first part of the thesis some contradictions with this interpretation of the observations have been highlighted. Indeed the dependency that QC modes shows with a density scan and ECRH were not

corresponding to what could be expected for ITG modes: QC modes were disappearing at high density and enhanced in ECRH plasmas.

Thus this interpretation of QC modes due to ITG has been questioned. We will show in the next section that this thesis has re-evaluated the origins of QC modes.

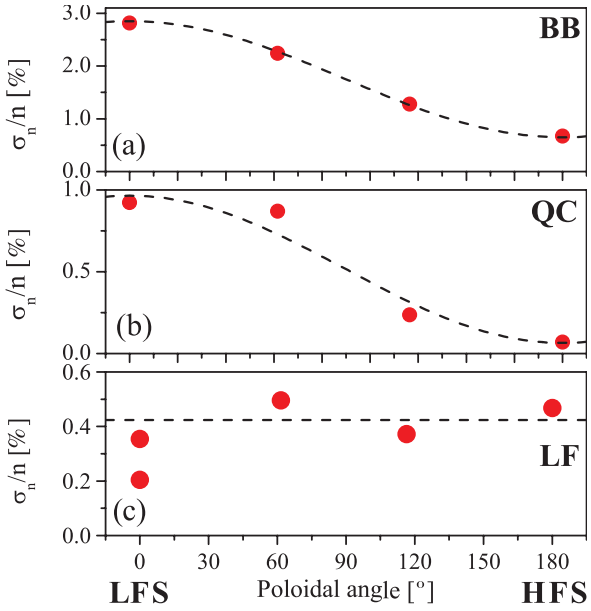

Figure 3.18: Amplitude of the broadband (BB), quasi-coherent modes (QC) and low frequency fluctuations (LF) as a function of the poloidal angle [Vershkov 2011].

Chapter 4

Quasi-Coherent modes, a signature of TEM instabilities

Contents

Following the inconsistencies highlighted in the interpretation of the origins of QC modes [see section 3.5] it has been decided to characterize them and to investigate their evolution during transitions of turbulent regimes.

To answer the question of the origin of QC modes, the computational (gyrokinetic simulations, synthetic reflectometer diagnostic) and the experimental tools (reflectometry spectra) described in the previous chapters have been used.

Their main properties are first characterized experimentally (normalized scale, location in the plasma, etc.) and discussed in the section 4.1. These general properties suggested that QC modes have a turbulent origin such as ITG or TEM, but deeper investigations were necessary to find the underlying mechanism of QC modes.

Thus, the evolution of QC modes in different plasma scenarios dominated by ITG or TEM has been investigated. One simple way to induce a TEM-ITG transition is to investigate the so-called LOC-SOC transition as described in section 4.2. Finally, the evidence

of the TEM origin of QC modes is shown by a comparison between reflectometry measurements and gyrokinetic simulations, including the results of a synthetic reflectometer diagnostic.

4.1 Main properties of QC modes

4.1.1 Oscillation frequency

To investigate the oscillation frequency of QC modes we analyze the same set of TEXTOR data as the one used in figure 3.17. Poloidal correlation reflectometry is used to measure $\Omega_\perp$ which includes the $E \times B$ drift component and the phase velocity of the mode in the plasma frame as described in section 2.4.2.

The different heating systems influence differently the perpendicular velocity. Thus a large range of perpendicular rotation values is provided by different types of heating schemes which include purely Ohmic discharges, Co-rotation NBI (1.3 MW), Counter-rotation NBI (400 kW) , and ICRH (800 kW).

These measurements were made from the LFS with a plasma current of $300 < I_p[\text{kA}] < 400$, a magnetic field of $2.25 < B_t[\text{T}] < 2.5$, and a central density of $1.5 < n_e[10^{19}\,\text{m}^{-3}] < 2.15$. As shown in figure 4.1(a), compared to Ohmic discharges the co-NBI increases the perpendicular rotation such as the IRCH (even though the acceleration is less pronounced). On the contrary, the counter-rotation NBI decreases the perpendicular velocity.

Compared to Ohmic discharges, the frequency of the QC modes increases in the ICRH and in the co-rotation NBI. This indicates that the QC mode frequency is proportional to the perpendicular velocity. Measurements in the counter-NBI case show a lower QC mode frequency supporting the link between QC mode frequency and perpendicular velocity.

The frequency of QC modes also scales with the perpendicular velocity in recent AUG observation made with correlation reflectometry [Prisiazhniuk 2015].

4.1.2 Frequency width

The same set of TEXTOR discharges is analyzed to highlight the effect of the perpendicular velocity on the frequency width (Δf) of QC modes. To quantify Δf_{QC}, the full width of the QC mode peak is estimated with the spectral decomposition previously explained in figure 3.15.

The perpendicular velocity is plotted as a function of the FWHM of the QC peak in figure 4.1(b) for the different heating schemes. As it can be seen, the FWHM of the QC modes peak is alway in the range:

$$20 < \Delta f_{QC}[\text{kHz}] < 100$$

This allows to distinguish QC modes from the coherent modes which usually have $\Delta f_{coherent} \approx 1$ kHz. The increase of Δf_{QC} with $\Omega_\perp$ is a typical broadening due to higher rotation velocity.

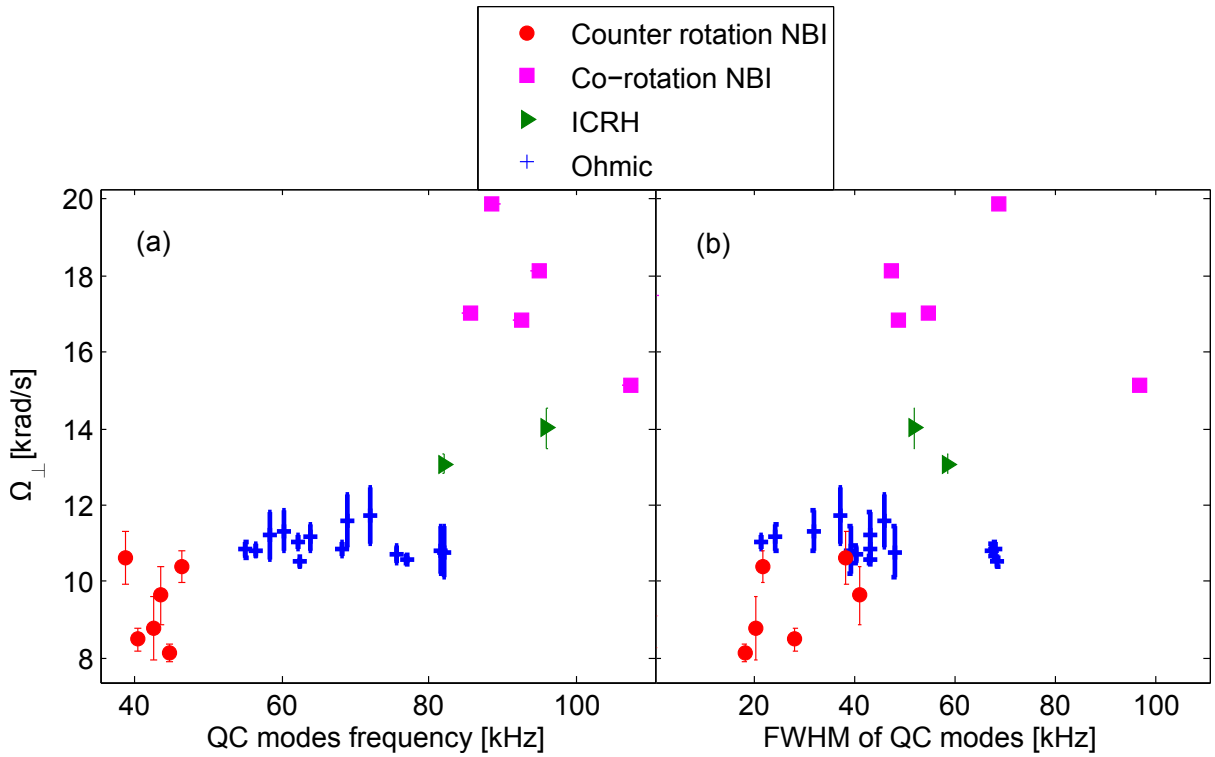

Figure 4.1: TEXTOR measurements of the perpendicular velocity $\Omega_\perp$ made at the LFS during the discharges #116494, #116495, #107985-7, #108012, #108824, 116518. (a) shows $\Omega_\perp$ as a function of the QC mode frequency and (b) shows $\Omega_\perp$ as a function of the frequency width of the QC mode peak.

4.1.3 Wavenumber, poloidal mode number and wavelength

As mentioned in section 3.2.2.2, poloidal correlation reflectometry can provide an estimation of $k_\perp$, $\lambda_\perp$ and m (assuming a constant wavelength across the poloidal wavelength). For QC modes, the following estimations have been obtained in a set of Ohmic discharges [Krämer-Flecken 2004]:

$$0.5 < k_\perp[\mathrm{cm}^{-1}] < 3$$
$$20 < m < 70$$
$$2 < \lambda_\perp[\mathrm{cm}] < 10$$

As expected for turbulent phenomena, the estimation of $k_\perp$, m and $\lambda_\perp$ are within a large range of values. Knowing $k_\perp$, an estimation of $\rho_i = V_{ti}/\omega_{ci}$ can provide their normalized scale $k_\perp\rho_i$. This will be done in the next section.

4.1.4 Normalized scale

$k_\perp \rho_i$ can be estimated taking $V_{ti} = \sqrt{2k_b T_i(r/a)/m_i}$ the ion thermal velocity (with k_b the Boltzmann constant, m_i the ion mass), and ω_{ci} the ion cyclotron frequency defined in equation 1.4. Due to the lack of T_i measurements in TEXTOR Ohmic plasmas, a typical ion temperature profile is assumed:

$$T_i\,(r/a) = T_i(0)\left[1 - (r/a)^2\right]^2 \tag{4.1}$$

with $T_i(0)$ [eV] the central ion temperature provided by the Artsimovich's formula valid for Ohmic plasmas [Gott 2007]:

$$T_i(0) = (1.29 \pm 0.11)\,\frac{(I_p \cdot B_t \cdot R^2 < n >)^{1/3}}{\sqrt{A_i}} \tag{4.2}$$

Where I_p $[kA]$ is the plasma current, B_t $[kG]$ is the toroidal magnetic field, R $[cm]$ is the tokamak major radius, $\langle n \rangle$ $[10^{13} cm^{-3}]$ is the line-averaged plasma density, and A_i is the atomic mass of the working gas (deuterium in that case). This scaling is deduced for T-10 plasmas which have large geometrical similarities with TEXTOR (size, circular shape).

Figure 4.2 shows the estimated values of the normalized scale of a set of Ohmic discharges of TEXTOR. It results that $0.35 \leq k_\perp \rho_i \leq 0.55$, in good agreement with previous observations always in the range $k_\perp \rho_i \leq 1$ [Krämer-Flecken 2004, Vershkov 2005, Krämer-Flecken 2015, Arnichand 2015b]. This is in the range of the normalized scale of micro-instabilities such as TEM and ITG. Several additional remarks can be done on these estimations.

As previously mentioned, the working gas in TEXTOR is deuterium. However, as there are always impurities in the plasma, A_i is in practice slightly higher than a pure deuterium plasma. It results that the values of $k_\perp \rho_i$ are overestimated and that they have to be taken as an upper limit.

The decrease of $k_\perp \rho_i$ observed when r/a increase is mainly due to ρ_i which decreases toward the edge due to the assumed ion temperature profile.

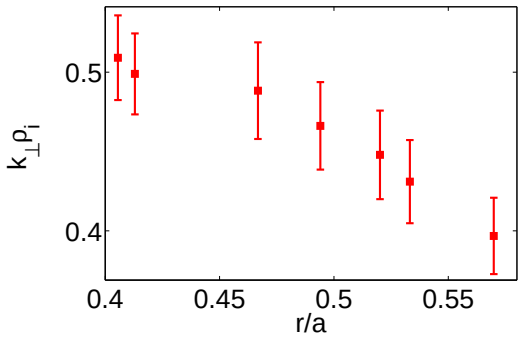

Figure 4.2: Normalized scale of QC modes estimated for a set of TEXTOR Ohmic plasmas (#113802-5,7) with $B_t = 1.9$ T, $I_p = 400$ kA and $1.33 < n_e[m^{-3}10^{19}] < 1.58$.

4.1.5 Radial and poloidal location

Combining the several reflectometers installed in different tokamaks, indications on the location of QC modes can be provided. From all the plasma scenarios investigated with different parameters, it generally results that:

- **Radially**, QC modes can appear at many different radial positions in the plasma core/edge region, depending on the plasma scenario. They do not depend on a specific location such as the rational surfaces or the separatrix. Observations of QC modes have been reported from $r/a \approx 0.1$ to $r/a \approx 0.8$ in Tore Supra [see section 5.1.1], and from $r/a \approx 0.25$ until $r/a \approx 0.7$ in AUG [see figure 5.2].
- **Poloidally**, in TEXTOR where reflectometers can probe the plasma from the LFS midplane and from the top of the torus, QC modes are usually more pronounced at the LFS than at the top [figure 4.3(a)]. In Tore Supra, where the reflectometers are able to measure on the LFS and on HFS, most of the time spectra can show QC modes on the LFS only [figure 4.3(b)]. Thus TEXTOR and Tore Supra spectra usually show that the amplitude of QC modes is ballooned on the LFS midplane, i.e. their amplitude is maximum at the LFS midplane, decreases with the poloidal angle, and is minimum on the HFS midplane. This confirms previous observations made in [Vershkov 2011] already mentioned in section 3.5.

Both poloidal and radial locations of QC modes are in agreement with expectations for micro-instabilities such as ITG or TEM. Indeed they are predicted to be unstable at many different radial positions, mainly on the LFS region of tokamaks.

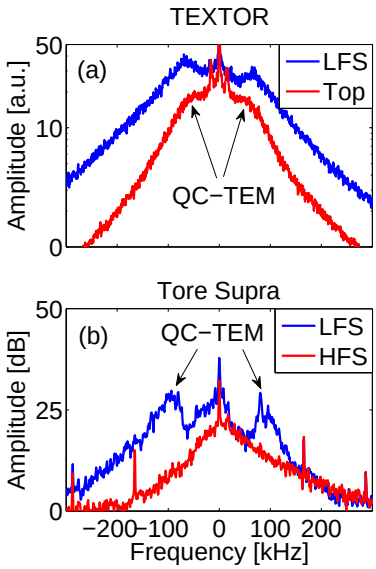

Figure 4.3: Poloidal ballooning of QC modes highlighted by reflectometry spectra from (a) TEXTOR at $r/a \approx 0.84$ between the LFS (#116492) and the top of the torus (#116495) (both taken from the antenna combination BC) and (b) Tore Supra between the LFS and the HFS (#40801 at $r/a \approx 0.11$).

4.2 Experimental evidence of the link between TEM and QC modes

Section 4.1 indicates that QC modes could arise from micro-instabilities such as TEM or ITG. Indeed ITG and TEM are expected to be unstable at many different radii, ballooned at the LFS midplane with a normalized scale in the range $k_\perp \rho_i \leq 1$.

In this section the aim is to determine if QC modes are linked to ITG or TEM. For this, Ohmic plasmas are analyzed because they provide a rather simple way to induce transitions from TEM toward ITG dominated regimes. As shown in figure 4.4, such a heating scheme shows mainly two regimes. In the framework of the ITG/TEM theory, they are usually dominated in the following way:

- At low density the confinement time τ_E increases linearly with n_e in the so-called Linear Ohmic Confinement (LOC) regime where TEM are expected to be dominant.
- Above a critical density, τ_E saturates in the so-called Saturated Ohmic Confinement (SOC) regime where ITG are expected to be dominant.

Therefore an analysis of the LOC-SOC transition can indicate whether QC modes could be linked to ITG or TEM. The LOC-SOC transition is predicted to occur at the transition density $n_{LOC-SOC}$ (in $10^{20} m^{-3}$) also called Shimomura density [Shimomura 1985]:

$$n_{LOC-SOC} \approx \frac{I_p \mu_0}{2\pi a^2} \sqrt{\frac{A_i \kappa}{2}} \tag{4.3}$$

where a is the minor radius of the tokamak, κ the plasma elongation, A_i the plasma atomic mass number, I_p the plasma current and μ_0 the vacuum permittivity. As shown by equation 4.3, $n_{LOC-SOC}$ is proportional to the plasma current. Thus a LOC-SOC transition can also be achieved at a constant n_e with a I_p ramp-down.

One can note that equation 4.3 provides the plasma parameters on which the transition density depends, but does not allow to predict the LOC-SOC transition. Indeed the

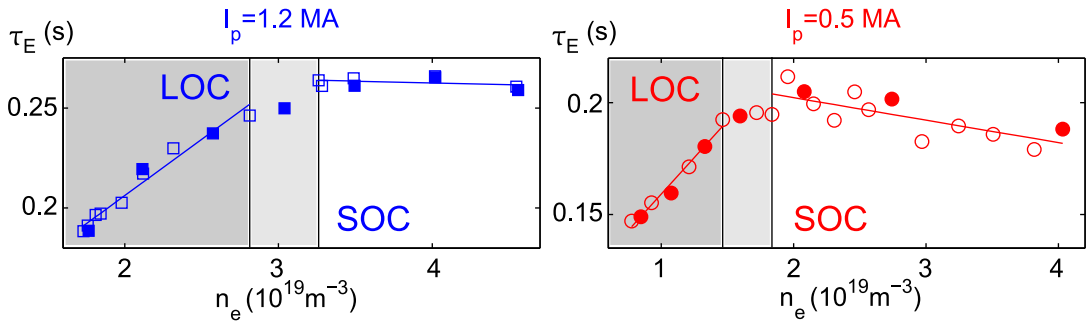

Figure 4.4: Tore Supra measurements of the energy confinement time τ_E during LOC-SOC transitions achieved at $B_t = 3.8$ T by scanning the central line averaged density n_e ($10^{19} m^{-3}$) at $I_p = 0.5$ MA ($\#41261 - 41272$) and $I_p \approx 1.2$ MA ($\#41003 - 41013$). Linear fits of the energy confinement time τ_E highlight the LOC and SOC regimes. The filled points correspond to the density for which spectra are shown in figure 4.5.

values of the transition density provided by equation 4.3 are not recovered experimentally. Hence it shows the parametric dependence of the transition but cannot be used to determine whether the plasma is in the LOC or the SOC regime. Recently, a more precise dependency of the transition on the collisionality has been highlighted [Rice 2012].

4.2.1 Disappearance of QC modes at the LOC-SOC transition

Performing density ramp-up to investigate Ohmic regimes has an important advantage: by looking at the evolution of τ_E as a function of the density the LOC-SOC transition can be rather well identified (even though it remains approximative) [see figure 4.4]. For reflectometry measurements, the drawback of such analysis is the modification of the cut-off layer locations during the density scan ($r/a_{\,cutoff} \propto n_e$). Thus to measure at a constant radial position requires different probing frequencies between each value of n_e.

As τ_E depends on $\partial W/\partial t$ [see equation 1.2], to obtain a precise estimation of the

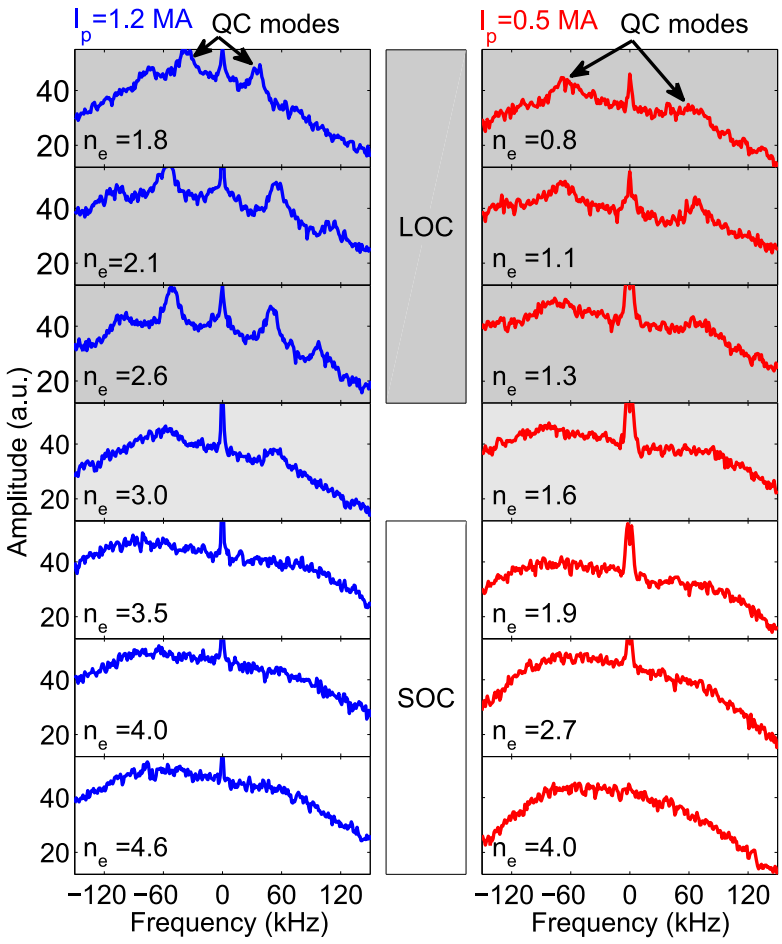

Figure 4.5: Tore Supra reflectometry spectra during the LOC-SOC transitions shown in figure 4.4. The measurements are performed at $r/a \approx 0.2$ for $I_p = 0.5$ MA and at $r/a \approx 0.3$ for $I_p \approx 1.2$ MA. The spectra correspond to the filled points shown in figure 4.4.

LOC-SOC transition instead of analyzing a current ramp-up it is preferable to analyze a density scan on a shot to shot basis (i.e. different discharges at different but constant density to get $\partial W/\partial t = 0$).

The evolution of the fluctuation spectra measured in Tore Supra during density scan performed in this way is shown in figure 4.5. The left-hand side column shows spectra measured in density scans performed at $I_p = 1.2$ MA and the right-hand side column at $I_p = 0.5$ MA. The reflectometry measurements were made at $r/a \approx 0.3$ and $r/a \approx 0.2$ respectively. The two different I_p provide a different $n_{LOC-SOC}$. Helium was used as the working gas, since it has a higher density limit than deuterium. For each of these density scans, QC modes are observed at around 30-80 kHz in the LOC regime and disappear in the SOC regime. Such QC modes behavior is usually observed above $r/a \approx 0.15$, but one can note that at $r/a \approx 0.2$ [figure 4.5(right)] the spectral changes are already less pronounced than at $r/a \approx 0.3$ [figure 4.5(left)].

Another way to visualize the stabilization of the QC modes at the LOC-SOC transition is the estimation of the "energy" of the mode. To calculate the QC mode energy, a decomposition of each spectrum is made as previously shown in figure 3.15 of section 3.4.2.1. The energy of the mode is then defined as the ratio of the amplitude [dB] over by the full width at half of its maximum [kHz] of the Gaussian curves fitting the peaks of the QC modes.

This analysis is performed for the n_e scan made at $I_p = 1.2$ MA presented in figure 4.5(left) where clear QC modes are observed in the LOC regime. Figure 4.6 shows that the energy of the QC modes decreases drastically between the LOC regime (≥ 1) and the SOC regime (≤ 0.3). The QC mode stabilization and the LOC-SOC transition are therefore highly correlated, which supports the long-standing hypothesis predicting the stabilization of TEM in the SOC regime.

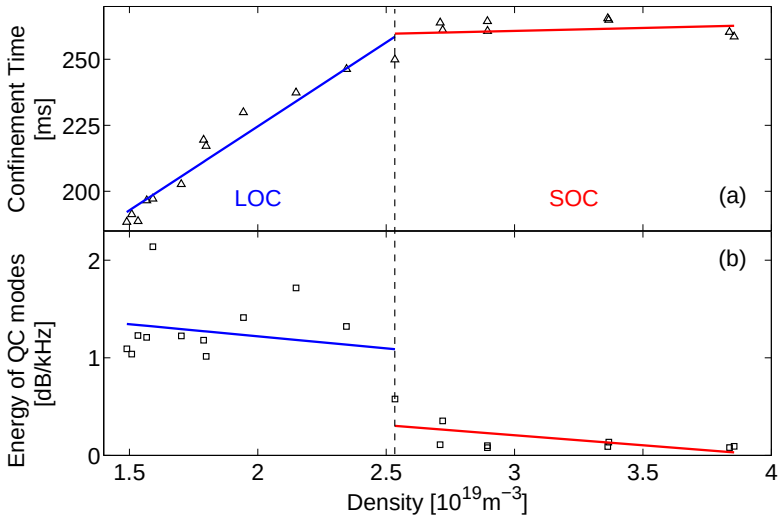

Figure 4.6: Tore Supra data showing (down) the evolution of the QC modes energy computed from the spectra presented in figure 4.5 as a function of the density, (up) the energy confinement time already shown in figure 4.4(left).

4.2.2 A phase velocity in the electron direction for QC modes ?

As previously mentioned, the TEXTOR poloidal correlation reflectometers can estimate the perpendicular rotation of electron density fluctuations $\Omega_{\perp}^{measured}$. In TEXTOR it is not possible to measure at a constant position during the LOC-SOC transitions achieved by density ramp-up. Indeed the maximum probing frequency (40 GHz) of the reflectometers cannot measure in the plasma core for high values of density. Therefore the SOC regime is not accessible by density ramp-up and LOC-SOC transitions have to be achieved by current ramp-down.

$\Omega_{\perp}^{measured}$ can be inferred from estimations of the delay time between each pair of antennas [see section 3.2.2.2], or can be visualized via the cross-phase slope [see section 3.4.2.3]. For the two Ohmic regimes, different observations of the cross-phase slopes $\Delta\phi(f)$ are made, they yield:

- **In the SOC regime**, figure 4.7(d) shows that only one slope is observed in the cross-phase spectra. It corresponds to Low Frequencies (LF) (< 50 kHz).
- **In the LOC regime**, figure 4.7(c) shows that excluding the GAM peaks which slightly deviate the cross-phase [Krämer-Flecken 2006, Krämer-Flecken 2009], two distinct slopes are observed. For LF ($f < 50$ kHz) the slope is steeper than for the QC modes frequencies ($f > 50$ kHz). These two cross-phase slopes (previously reported in [Krämer-Flecken 2012]) are seen in all the receiving antenna combinations on the top of the torus, they translate the faster rotation of the QC modes compared to LF.

Besides this qualitative indication, velocity estimations are made in the LOC regime via delay times calculation between the two selected antennas:

- **For the Low Frequencies** $\Delta t_{LF} = 5.4 \pm 0.6\ \mu s$ for $f < 50$ kHz, which corresponds to a velocities of 3.4 ± 0.4 km/s in the electron diamagnetic direction.
- **For the QC** $\Delta t_{QC-TEM} = 4.7 \pm 0.2\ \mu s$ for $f > 50$ kHz, which corresponds to a velocities of 3.8 ± 0.2 km/s in the electron diamagnetic direction.

There is an overlap of the absolute error-bars, but for each antenna combination calculations of Δt and observations of $\Delta\phi(f)$ always yield to $\mathbf{v}_{\perp}^{QC-TEM} > \mathbf{v}_{\perp}^{LF}$ in the LOC regime. As these measurements provide the total perpendicular velocity composed of $\mathbf{v}_{E\times B}$ and $\mathbf{v}_{phase}$ [see equation 3.15], $\mathbf{v}_{E\times B}$ can be canceled by subtracting the two measurements between the QC modes ($f > 50$ kHz) and LF ($f < 50$ kHz). Indeed $\mathbf{v}_{E\times B}$ at a given time and location in the plasma is similar for all the types of fluctuations. Hence $\mathbf{v}_{phase}$ is estimated ~ 400 m/s higher in the electron diamagnetic direction for the QC modes compared to the LF fluctuations.

This value is on the order of magnitude of previous $\mathbf{v}_{phase}$ estimations [Conway 2006]. It suggests that $\mathbf{v}_{phase}$ is oriented in the electron diamagnetic direction for the QC modes as expected for electron modes such as TEM and/or in the ion diamagnetic direction for the LF as expected for ion modes such as ITG.

More discharges than the two analyzed would be required to get more robust results but this was not possible as TEXTOR is not operating anymore. An analysis of the $\Omega_\perp$ of QC modes has been done in AUG for 17 L-mode discharges. An offset of ≈ 1 km/s was observed between correlation reflectometry and Doppler reflectometry measurements in the electron diamagnetic direction [Prisiazhniuk 2015], also suggesting that QC modes may have $\mathbf{v}_{phase}$ in the electron diamagnetic direction. However, these QC modes were measured at $\rho \approx 0.98$ and may therefore not come from TEM as the core QC modes.

One should note that the data reported here have been measured from the top of TEXTOR. From the LFS the velocity difference between QC modes and low frequencies is less/not observed.

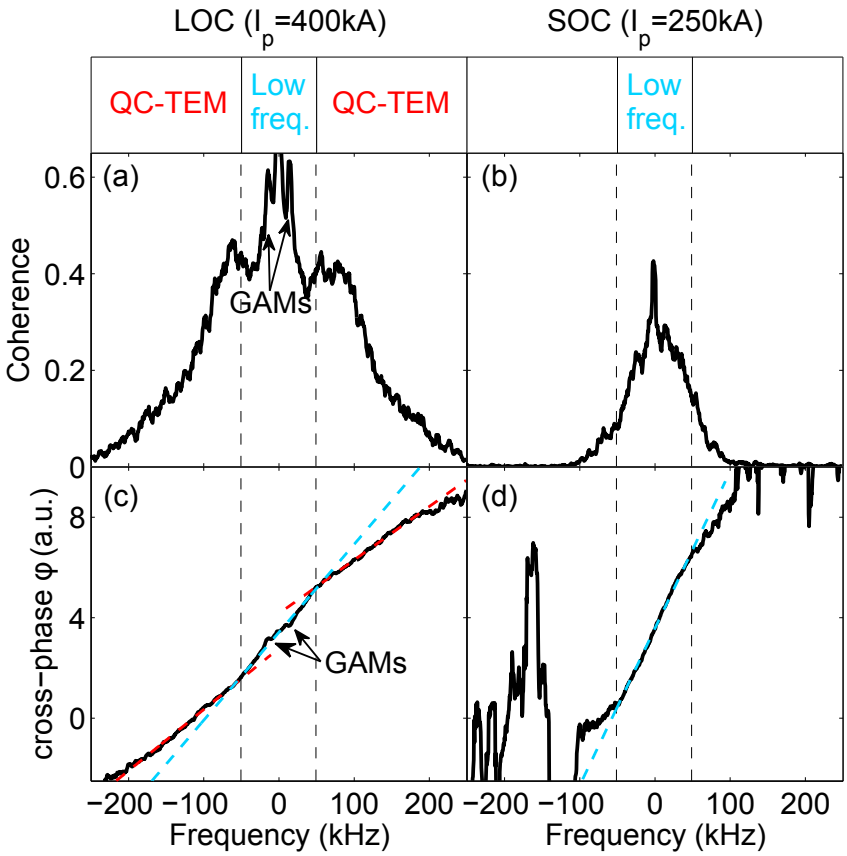

Figure 4.7: Reflectometry measurements made from the top of the TEXTOR torus, at $r/a \approx 0.91 \pm 0.01$ during the shot #117780 ($B_t = 1.9$ T and $3 \times 10^{19}\,\mathrm{m}^{-3}$). Spectra of coherence (a-b) and cross-phase (c-d) are obtained with a pair of antennas poloidally separated by $\alpha = 0.043$ rad. The left and right columns present the LOC ($I_p = 400$ kA) and SOC ($I_p = 250$ kA) regimes respectively. The cross-phase is linearly fitted for QC-TEM in red (50 kHz$< f <$ 200 kHz) and for LF fluctuations in blue ($f <$ 50 kHz).

4.3 Computational validation of the link between TEM and QC modes

After the first experimental indications of the link between QC modes and TEM, it was required to validate the measurements with simulations. This is done in this section for the Tore Supra discharge #48102 in which the LOC-SOC transition is investigated during a density ramp-up.

4.3.1 Experimental scenario

Figure 4.8(a) shows the main plasma parameters ($B_t = 3.7$ T). The two times considered for this analysis are indicated in black: $t_1 \approx 3s$ and $t_2 \approx 6s$. The behaviors of the density (green) and the energy confinement time (black) clearly show that t_1 is in the LOC regime whereas t_2 is in the SOC regime. The LOC-SOC transition occurs at around $n_e \approx 3.45 \cdot 10^{19} m^{-2}$ which corresponds to $t \approx 4.85s$.

Figures 4.8(b) shows fluctuation spectra obtained at t_1 (LOC) and t_2 (SOC) at $r/a \approx 0.18$ with the fixed-frequency reflectometer. QC modes are observed in the LOC regime around $25 < f_{QC}[kHz] < 75$ kHz. In the SOC case, only a broadband fluctuation spectrum remains.

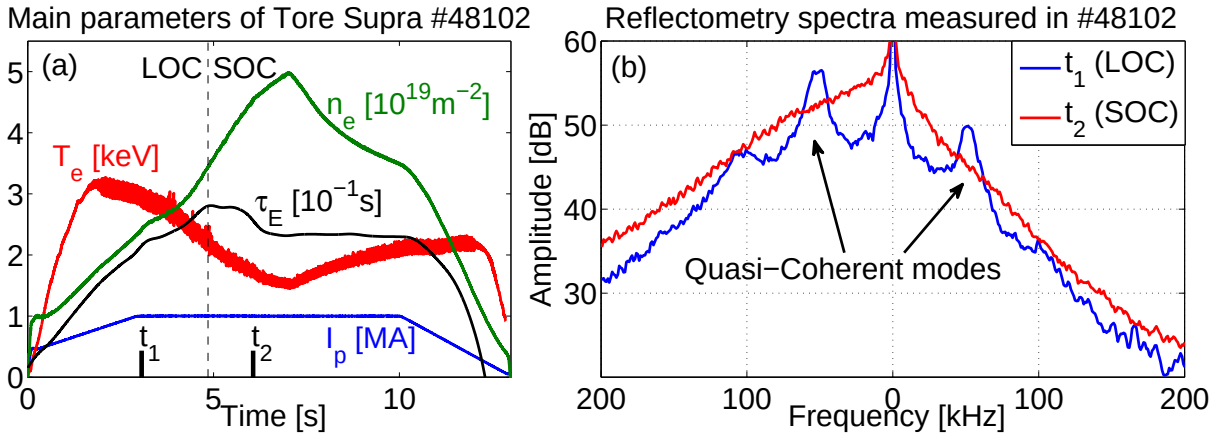

Figure 4.8: (a) Main parameters of the Tore Supra discharge #48102. I_p is the plasma current, T_e is the central temperature and n_e is the central line averaged density and τ_e the energy confinement time. The dotted line indicates the LOC-SOC transition and the two vertical black dashes show the two times investigated. (b) Reflectometry spectra measured at t_1 and t_2 around $r/a \approx 0.18$ taken from [Bernardo 2015].

4.3.2 Gyrokinetic simulations

4.3.2.1 Linear runs

For the discharge previously discussed, figure 4.9 presents GENE [Jenko 2000] linear simulations of mode frequencies (b) and growth rates (c) as a function of $k_\theta \rho_i$ in the

LOC (t_1) and SOC (t_2) phases [Citrin 2014]. The parameters displayed in figure 4.9(a) are calculated from the CRONOS [Artaud 2010] interpretative simulations which are used as an input of the gyrokinetic simulations. Z_{eff} is estimated from Bremsstrahlung measurements, q is the safety factor, $\hat{s}$ is the magnetic shear, and ν^* is the normalized collisionality defined in section 2.1.2.2.

In the LOC and the SOC phases, the most unstable modes are in the range $0.1 < k_\theta \rho_i < 1$ and a reversal of the frequency is observed from $\omega < 0$ (electron diamagnetic direction) as expected for TEM in the LOC regime toward $\omega > 0$ (ion diamagnetic direction) in the SOC regime. Thus suggests a transition from TEM toward ITG dominated regimes[1], supporting the previous analysis [Bernardo 2012, Bernardo 2015]. Therefore QC modes appear and disappear when TEM and ITG are respectively suspected to be unstable.

One can note that for $1 < k_\theta \rho_i < 1.5$ unstable modes are observed only in the LOC regime, with a frequency slightly oriented in the ion diamagnetic direction. Sensitivity test shows that a reduction of the normalized logarithmic temperature gradient R/L_{T_i} by 30% stabilizes these ion modes without affecting significantly the electron modes. They are most probably carbon ITG modes [see section 2.2.3].

(a)

Phase	R/L_{Ti}	R/L_{Te}	R/L_{ne}	T_i/T_e	β_e [%]	$\hat{s}$	q	ν^*	Z_{eff}
LOC	4.7±0.5	9.2±0.35	2.8±0.1	1.8±0.1	0.13	0.7	1.3	0.012	3.0±0.1
SOC	5.0±0.4	8.9±0.25	1.8±0.1	1.6±0.1	0.14	0.75	1.25	0.029	1.4±0.1

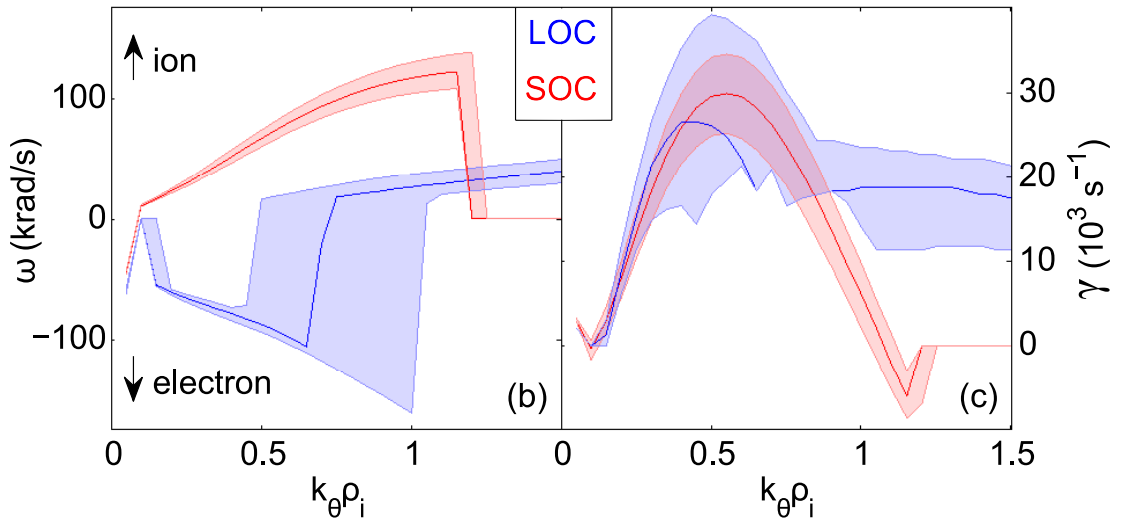

Figure 4.9: (a) input plasma parameters of the GENE linear stability analysis based on the Tore Supra discharge #48102 performed at r/a=0.37. This plasma region has been chosen because T_i measured by charge exchange recombination spectroscopy diagnostic has good resolution. Calculations are done at t_1 (LOC) and t_2 (SOC). (b) shows the mode frequencies ω and (c) the instability growth rates γ, the shaded regions represent uncertainties due to the gradients.

[1]Sensitivity tests show that the main parameters responsible for the turbulence transition are by decreasing order Z_{eff}, R/L_{n_e} and ν^*.

4.3.2.2 Nonlinear runs

Figure 4.10 shows frequency fluctuation spectra from GENE nonlinear simulations [Citrin 2014] performed at the same time and location as in the previous section. Simulated spectra of $\widetilde{n}_e$ can be compared qualitatively to the reflectometry spectra (sensitive to $\widetilde{n}_e$). Contrary to reflectometry spectra, the diamagnetic direction of the phase velocity (ion/electron) can be distinguished by looking at the sign of the frequency (+/-). Thus the spectra shown in figures 4.10 support the linear runs because the LOC and the SOC regimes are dominated by $f < 0$ (TEM) and $f > 0$ (ITG) respectively.

Additional crucial information provided by the nonlinear runs is the difference in the spectral shape. The ITG-dominated case shows a single broadband spectrum which mixes the turbulence and the density Zonal Flows (ZFs) (i.e. $k_y = 0$, $\omega = 0$), thus explains the broadband spectrum measured in figure 4.8(b). In the TEM-dominated spectra, the nonlinear frequency broadening of TEM is smaller which leads to a sharp peak separated from ZFs. As TEM instabilities coalesce in few wavenumbers, they induce a narrow frequency spectrum which explains the QC modes measured in figure 4.8(a).

The frequency of the TEM peak (≈ 12 kHz) is significantly lower than the frequency measured for QC modes (≈ 50 kHz). This is due to the fact that the GENE simulations do not take into account $v_{E\times B}$ but only v_{phase}. As the density fluctuations rotate with a total velocity $v_{tot} = v_{E\times B} + v_{phase}$, it makes their measured frequency higher than the one shown in the GENE spectra. In the next section, $v_{E\times B}$ is taken into account in the broadening of the spectra obtained with a synthetic reflectometer.

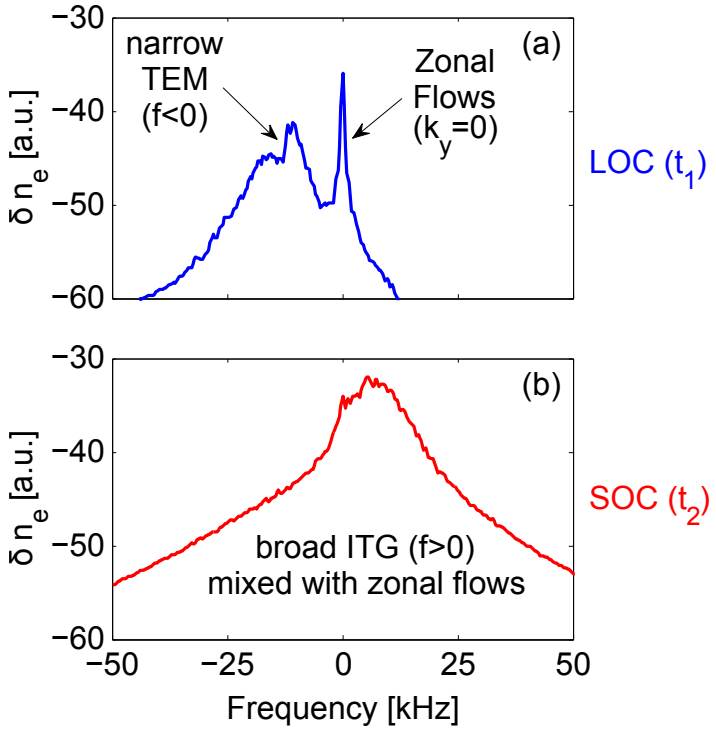

Figure 4.10: Fluctuation spectra from nonlinear gyrokinetic simulations computed at $r/a \approx 0.37$, in (a) the LOC (t_1) and (b) the SOC (t_2) regimes.

4.3.3 Synthetic reflectometer results

For a closer comparison with measurements, fluctuation spectra were simulated with a synthetic reflectometer diagnostic [Hacquin 2015]. The maps of density fluctuations from the GENE nonlinear gyrokinetic simulations were used as input in 2D full-wave computations. As described in section 3.3, an iteration for each map of δn_e is made by the synthetic diagnostic.

As the aim is to compare with the measured frequency spectra, once this process iteration has finished, a Fourier analysis of the recorded signal can provide the computed fluctuation spectra. However, the GENE simulations provide only the rotation due to v_{phase}, i.e. the fluctuations in the plasma frame [see equation 3.15]. Thus a correction has to be done to take into account $v_{E\times B}$ rotation, which affects the experimental data through an additional broadening of the fluctuation spectra.

4.3.3.1 Correction of the computed frequency fluctuation spectra

To address this issue and ensure an accurate comparison with the measured reflectometry spectra the $v_{E\times B}$ rotation velocity was deduced from the radial electric field, which can be estimated by thermal ripple losses in case of strong ripple such as in Tore Supra ($\delta = [B_{max} - B_{min}] / [B_{max} + B_{min}]$ up to 7%) [Connor 1973, Trier 2008, Garbet 2010a]:

$$E_r = \frac{T_i}{e}\left[\frac{\nabla n_i}{n_i} + 3.37\frac{\nabla T_i}{T_i}\right] \tag{4.4}$$

Then the $v_{E\times B}$ rotation velocity was included to artificially correct the time sampling of the reflectometry signal:

$$dt_{new} = \frac{dt}{|\frac{v_{E\times B}}{v_{phase}} \pm 1|} \tag{4.5}$$

As $v_{E\times B}$ is in the electron diamagnetic direction, the $\pm$ depends on the turbulence nature. "+" corresponds to the case of an electron turbulence (LOC) where the $v_{E\times B}$ is added to v_{phase} as they are in the same direction. On the contrary, "−" corresponds to the case of an ion turbulence (SOC) where the $v_{E\times B}$ is subtracted to v_{phase} as they are in opposite directions. The frequency spectra obtained after this correction are shown in figure 4.11(a-b).

4.3.3.2 Results

As shown in the fluctuation spectra of figure 4.11, QC modes appear in the LOC regime at around $\approx$ 75 kHz while the SOC regime shows only a broadband spectrum. This confirms the previous comparison between spectra from nonlinear simulations and measured fluctuation spectra, indicating that the ITG modes can have a broad-band spectrum while the TEM can induce QC modes. The present results prove that these QC modes measured in the plasma core region are due to TEM instability, and we will now refer to them as QC-TEM.

Several remarks can be done on the computed spectra. First the main parameters of

the simulation and the measurements are noticeably different as shown in the table 4.1. Indeed, nonlinear simulations require significant computing time and cannot be performed for a duration similar to measurements. The lower time length of the simulations induces a much lower frequency resolution in the spectra.

Second, the frequency of QC-TEM is slightly higher in the simulated than in the measured spectra. It may be explained by the fact that the position of the cutoff layer differs between the measurements (at $r/a \approx 0.18$) and the simulations (at $r/a \approx 0.37$)[2]. This could imply a higher $v_{E\times B}$ and therefore a higher QC-TEM frequency. One should note that this would be consistent with the increase of the QC-TEM frequency width observed from the measured toward the simulated spectra. As we have seen that Δf is proportional to the perpendicular velocity, a higher $v_{E\times B}$ at $r/a \approx 0.37$ would also explain the larger QC peak in the simulated spectra.

A last remark on the simulated spectra can be made on its asymmetry. It has been previously discussed that several phenomena can induce spectral asymmetry [see figure

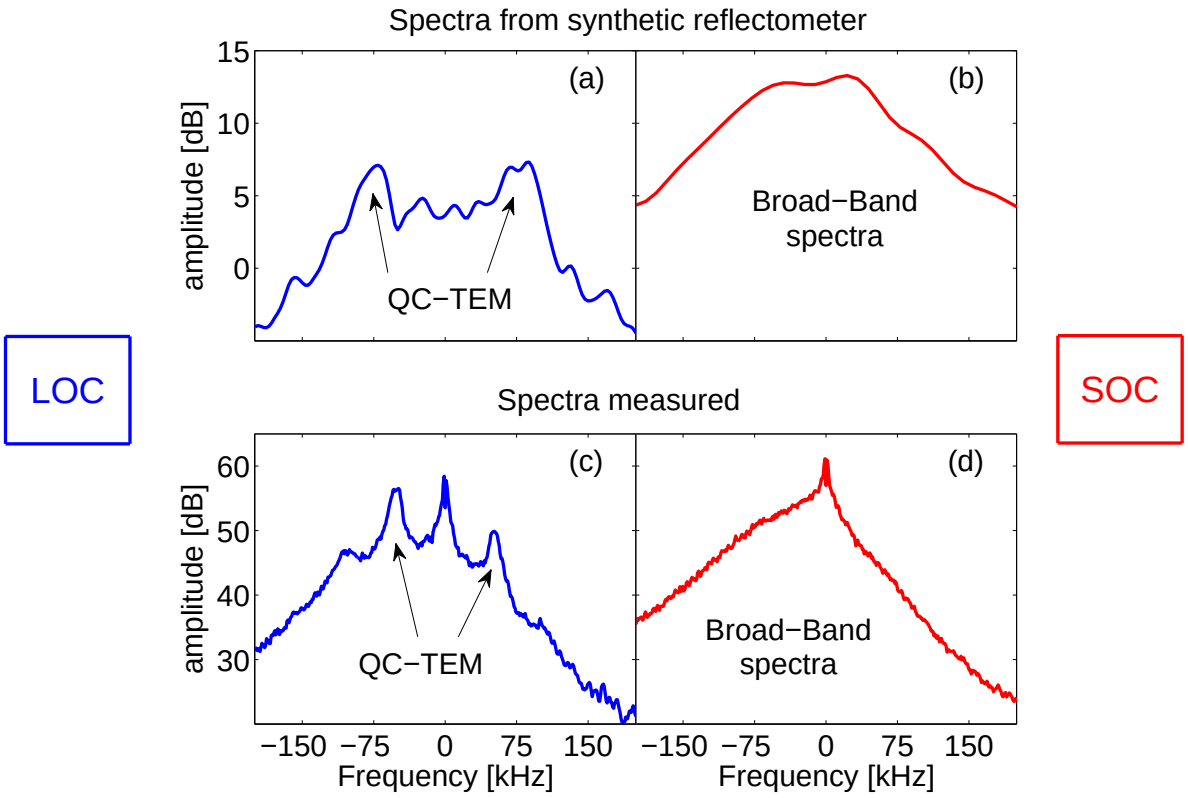

Figure 4.11: (a-b) Fluctuation spectra from a synthetic diagnostic using nonlinear gyrokinetic simulations as an input ($r/a \approx 0.37$) (a) in the LOC (t_1) and (b) the SOC (t_2) regimes. (c-d) are the spectra measured for $r/a \approx 0.18$ at the corresponding times (already shown in figure 4.8).

[2]The location of the measurements was fixed during the experiment made previously to this thesis and it was decided to perform the simulations slightly further out from the center to get a better estimation of the ion temperature gradient, a crucial input parameter for the gyrokinetic simulations

	Simulations		Measurements
	LOC	SOC	LOC and SOC
Duration	0.34 ms	0.12 ms	123 ms
Number of points	1200	1200	123000
Frequency resolution δf	2.9 kHz	8.3 kHz	8 Hz

Table 4.1: Main parameters of the simulations and the measurements of figure 4.11.

3.4.2.1]. A probing wave non-perpendicular to the cutoff layer is excluded in that case. Indeed the plasma is not vertically shifted and the launching/receiving antennas are perfectly aligned in the LFS midplane in the synthetic diagnostic. This means that the structure of the turbulence itself contributes to the spectral asymmetry observed in that case, possibly via the tilt of its eddies.

4.4 Conclusion: core QC modes are due to TEM

Besides the main properties of QC modes, this section has shown that they come from the TEM instabilities, and have thus been renamed QC-TEM. It supports the first indication of "features" suggested to be linked with TEM in PCI spectra measured in Alcator C-Mod [Rice 2011a].

In the present study, the experimental indications of the link between QC modes and TEM were first provided by the disappearance of QC modes at the LOC-SOC transition in Tore Supra. Additionally, TEXTOR measurements suggest that QC modes could have a $\mathbf{v}_{phase}$ oriented in the electron diamagnetic direction, which would support their link with TEM. Then the evidence that QC modes are indeed a signature of TEM have been shown by a comparison with frequency spectra of nonlinear gyrokinetic simulations via a synthetic reflectometer, the narrow frequency spectra of TEM being responsible of the QC modes.

An observation of QC modes can now be taken as an indication that TEM play a role in the plasma core region. Thus fluctuation spectra analysis can be applied to investigate phenomena suspected to be due to turbulence modification involving TEM. This is done in the following chapter: in Ohmic plasmas to investigate the role of TEM during the LOC-SOC transition, and in ECRH plasmas to study the role of TEM in the turbulent transport.

Chapter 5

Application to the study of TEM in Ohmic and ECRH plasmas

Contents

The aim of this chapter is to show the first applications of the results presented in the previous chapter. The identification of TEM through QC-TEM is used to study TEM instabilities. In the plasma core region, the observations of QC-TEM are thus taken as a signature of TEM and used as a tool to investigate issues related to TEM.

Thanks to the local measurements provided by reflectometers, the role of TEM is investigated locally in Ohmic and ECRH plasmas. This allows to study the changes of turbulence during the LOC-SOC transition in section 5.1 where measurements from Tore Supra, TEXTOR, AUG and JET are presented. Then Tore Supra ECRH plasmas are analyzed in section 5.2 to investigate the radial changes of turbulent impurity transport.

5.1 TEM instabilities and the LOC-SOC transition

Ohmic discharges have mainly two regimes (the LOC and the SOC regimes) which exhibit different dependencies of τ_E the energy confinement time on density (linear increase and saturation respectively) [see section 4.2].

Progress in the understanding of the LOC-SOC transition has been made since the first observations. The onset of an ion mode in the SOC regime was first proposed to explain the saturation of τ_E [Brower 1987, Rettig 2001]. Other measurements suggested that electron turbulence plays a major role in the change of behavior of τ_E [Garbet 1992, Simmet 1996]. In the LOC regime, the stabilization of electron modes would improve the confinement and increase τ_E, whereas in the SOC regime the full stabilization of electron turbulence would prevent any further increase in τ_E.

Over the last decade, the conventional understanding is that the LOC and the SOC regimes are dominated by TEM and ITG respectively [Angioni 2005, Conway 2006, Angioni 2011, Rice 2011a, Gao 2014], even though it is still under discussion [Sung 2013, McDermott 2014] and several questions remain on the link between the transition of turbulence regime and the saturation of τ_E:

- Is the LOC-SOC transition simultaneous to the TEM-ITG transition ?
- Which radial and poloidal region of the plasma does the TEM-ITG transition affect?
- Is this transition responsible for the reversal of the intrinsic toroidal rotation reported across the LOC-SOC transition ?

An analysis of QC-TEM across the LOC-SOC transition can then bring additional information and contribute to improve our understanding of the role of TEM in the transition of Ohmic regimes.

The simultaneity of the LOC-SOC transition with the stabilization of QC-TEM has already been reported in section 4.2.1. These sections report observations made in Tore Supra, TEXTOR, AUG and JET. Their aim is to show indications on the radial and poloidal extents of the stabilization of QC-TEM, and whether a link is observed with changes of intrinsic toroidal rotation.

5.1.1 Radial extent of the QC-TEM disappearance

As discussed in section 1.1.3, the confinement time is a global quantity. To investigate if its saturation at the LOC-SOC transition is linked to the disappearance of TEM, one can wonder which radius of the plasma is affected by the TEM stabilization.

This is investigated in this section, which shows reflectometry measurements obtained in both density and current scans. The results coming from several tokamaks, it has been decided to sort them as a function of the device.

5.1.1.1 Tore Supra measurements

A good indication on the radial location of the disappearance of QC-TEM can be obtained with two Tore Supra reflectometers. Indeed one of them is able to measure deep in the plasma core region whereas another one can measure simultaneously in the core/edge region.

During the plasma current scan performed in the discharge #47670, four measurements shown in figure 5.1 are made for both the fixed-frequency (a) and the ultra-fast-swept (b) reflectometers. The first one measuring at $r/a \approx 0.3$ and the second one at $0.71 < r/a < 0.84$. At $r/a \approx 0.3$ and for approximatively $0.71 < r/a < 0.8$, QC-TEM are observed in the LOC regime and disappear in the SOC regime.

Thus these measurements suggest that the stabilization of TEM occurs at two distinct radii, from a region close to the plasma center $r/a \approx 0.2$ out to $r/a \approx 0.8$.

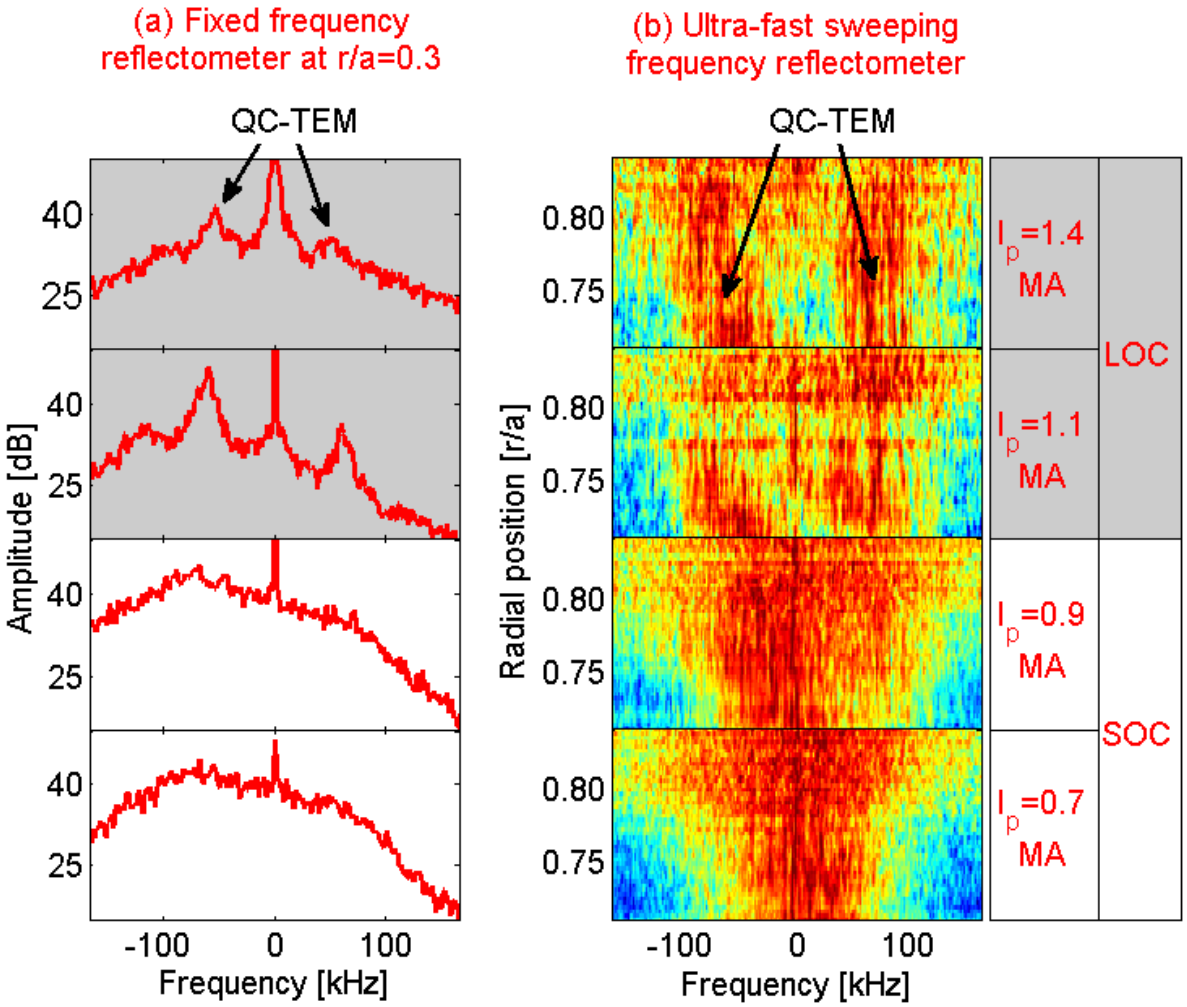

Figure 5.1: Spectra from (a) fixed-frequency reflectometer ($r/a \approx 0.3$) and (b) ultra-fast-swept reflectometer ($0.71 < r/a < 0.84$) during a LOC-SOC transition achieved by current scan in the Tore Supra discharge #47670.

5.1.1.2 ASDEX-Upgrade measurements

In AUG, the LOC-SOC transition is not investigated but the analysis is focused on the beginning of a density ramp-up (#31427 at $t \approx 1.4s$) in the LOC regime[1]. However, as it will be shown the radial extend of the QC-TEM can already be demonstrated in these LOC observations.

Figure 5.2(a) shows estimations of $v_{E\times B}$ performed with the NEOART code [Peeters 2000], for which all the components have been computed as previously shown in equation 2.19 (the diamagnetic, the toroidal velocity and the poloidal velocity terms). The negative/positive directions correspond to the electron/ion diamagnetic direction.

$V_{\phi i}$ is obtained with measurements performed by charge exchange recombination spectroscopy (CXRS) [Viezzer 2012, Lebschy 2015] and $V_{\theta i}$ is provided by a neoclassical formula of the same type as the Kim calculation given in [Meigs 1994]. It takes into account the gradients of the impurity density profile (carbon in that case) together with the main ion temperature and density profiles. The error bars of the $v_{E\times B}$ provided by the NEOART code are of the order of 0.5 to 1 km/s.

Figure 5.2(b) displays the radial evolution of the fluctuation spectra obtained by ultra-fast-swept reflectometry [Clairet 2010, Hornung 2013b, Medvedeva 2015]. We distinguish two regions along the plasma radius:

- For $0.25 < \rho < 0.4$, QC-TEM are clearly observed[2] while we expect $|v_{E\times B}| \geq 1$ km/s. From $\rho = 0.4$ toward $\rho = 0.25$ the increase of f_{QC-TEM} (up to ≈ 75 kHz) is due to the increase of $|v_{E\times B}|$ observed (up to ≈ 3 km/s).

- For $\rho > 0.4$, QC-TEM modes cannot be properly observed and NEOART estimations indicate $|v_{E\times B}| \leq 1$ km/s.

As f_{QC-TEM} depends on $v_{E\times B}$, a low $v_{E\times B}$ may induce a too low f_{QC-TEM}. Only weak QC-TEM are observed and they cannot be clearly distinguished in the conventional reflectometry spectra (i.e. where they merge into low frequency fluctuations).

Figure 5.2 shows for $\rho \approx 0.73$ spectra of the complex signal (c) and coherence (d) estimated with a poloidal correlation reflectometer (PCR)[3] [Prisiazhniuk 2015]. Even though QC modes are not very pronounced in the spectra of the complex signal, they are clearly seen in the coherence spectra. Therefore, in case of low $v_{E\times B}$, PCR can be used to highlight QC oscillations which occur at low frequency.

These results show that the QC-TEM can be observed in the LOC regime at very different radius in AUG ($0.25 < \rho < 0.4$ and $\rho \approx 0.73$).

[1] The investigation of the LOC-SOC transition in AUG is not performed in this thesis, but is an ongoing work [Prisiazhniuk 2015]

[2] In section 6.1.1 an analysis of the inner region of the plasma where TEM disappear is performed for the same AUG discharge.

[3] As an indication, the PCR estimates the perpendicular velocity to 0.7 ± 0.2 km/s in the ion diamagnetic direction, which should be compared with the ≈ 0.25 km/s in the ion diamagnetic direction of estimated by the NEOART code.

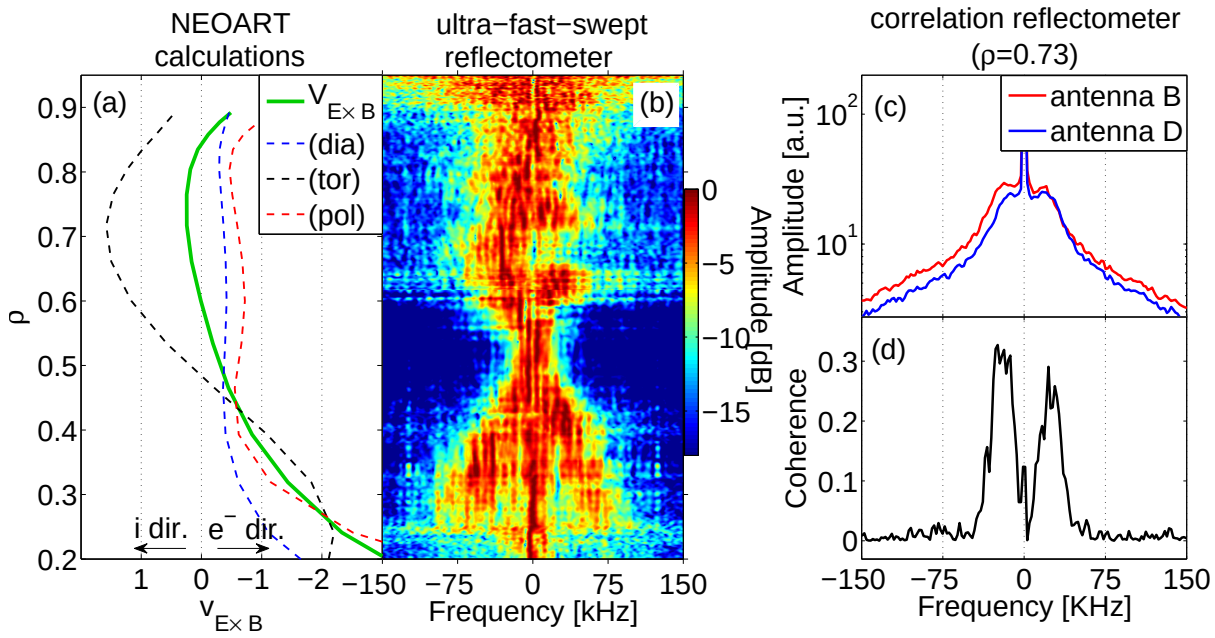

Figure 5.2: Data from the AUG discharge #31427 measured at $t \approx 1.4$s. In (a) the neoclassically predicted $V_{E\times B}$ provided by the NEOART code [Peeters 2000]. Fluctuation spectra from an ultra-fast swept reflectometer are shown in (b) for $0.2 < \rho < 0.95$ and from two antennas of a PCR (c) at $\rho = 0.73$. The coherence between the two antennas of the PCR is displayed in (d).

5.1.1.3 JET

To complete the previous observations, spectra measured during n_e and I_p scans performed in JET Ohmic plasmas are analyzed in this section. As it was unfortunately not possible to analyze discharges dedicated to the LOC-SOC transition in JET, the determination of the LOC-SOC transition were not possible for the following reasons:

- In the n_e scan, some parameters required to be constant in LOC-SOC experiments were varying (plasma volume, shape, etc.). Therefore we cannot determine if the evolution of τ_E arises from (i) a change of the plasma volume which modifies the stored energy W ($\tau_E \propto W$) [see equation 1.2], (ii) a change of the plasma shape which modifies $n_{LOC-SOC}$ [see equation 4.3] or (iii) the LOC-SOC transition itself.

- To identify the LOC-SOC transition during the I_p scan, several n_e scans at different I_p need to be analyzed to plot the transition density $n_{LOC-SOC}$ as a function of I_p (as shown in [Rice 2012]). This type of plot is required to estimate at which I_p the transition is expected for a given n_e. They were not obtainable in JET.

Therefore, the comparison with the measurements previously shown remains qualitative. Figure 5.3 presents the reflectometry spectra measured during (a) the n_e and (b) the I_p scans respectively. QC-TEM appear only at low n_e or high I_p. Thus a qualitative agreement is found with the results shown in the other tokamaks.

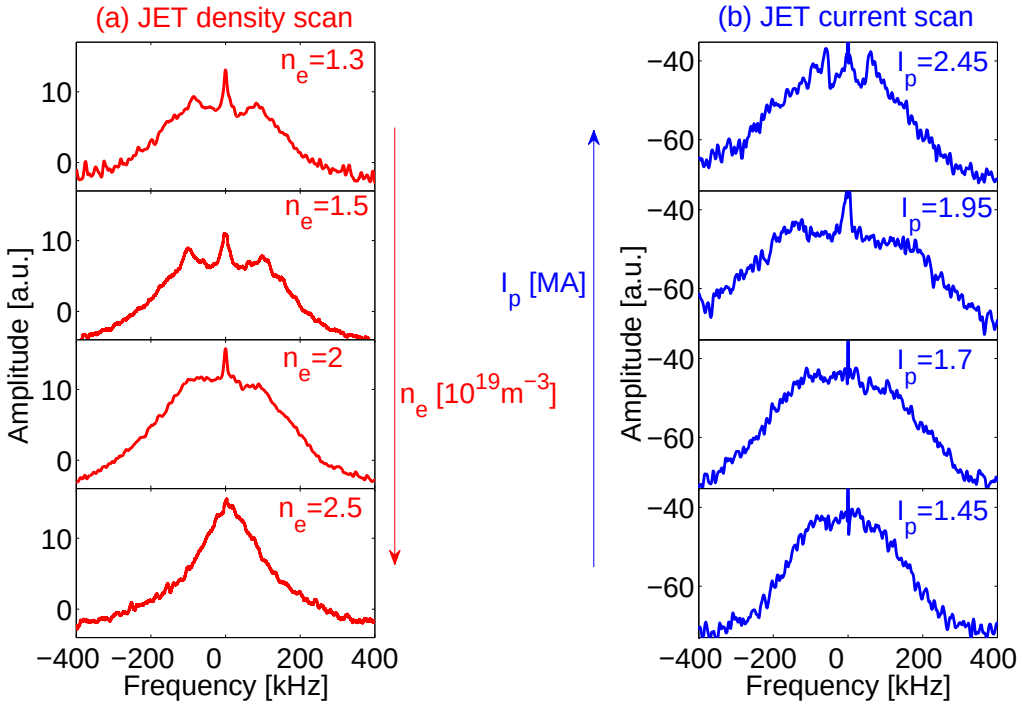

Figure 5.3: Fluctuation spectra from JET reflectometry. Spectra from the left-hand side column come from a n_e scan (#87756, $0.28 < r/a < 0.38$, $B_t = 1.8$ T, $I_p \approx 1.8$ MA, limiter plasma) and spectra from the right-hand side column come from a I_p scan (#87801,2,4,5, $0.32 < r/a < 0.44$, $B_t = 1.8$ T, $n_e = 1.65 \times 10^{19}\mathrm{m}^{-3}$, diverted plasma).

As summarized in table 5.1, the spectral measurements made in Ohmic regimes from various tokamaks report the disappearance of QC-TEM at many different radii. All the radii were not accessible in each device, but they indicate that the disappearance of QC-TEM can occur at many different radii. Combined with the simultaneity of the TEM stabilization with the LOC-SOC transition already presented in section 4.2.1, they are good indications of the important role of TEM in the LOC-SOC transition.

Tokamaks	Radius of the reflectometry observations across the LOC-SOC transition
Tore Supra	Disappearance of QC-TEM for $0.18 < r/a < 0.3$ and $0.71 < r/a < 0.8$
TEXTOR	Disappearance of QC-TEM at $r/a \approx 0.91$
JET	Disappearance of QC-TEM[4] for $0.28 < r/a < 0.44$
AUG	Observation of QC-TEM in LOC[5] for $0.25 < \rho < 0.4$ and $\rho \approx 0.73$

Table 5.1: Summary of the observations of QC-TEM across the LOC-SOC transition.

[4] As the LOC-SOC transition is not determined in JET we refer to n_e ramp-up and I_p ramp-down.

[5] The investigation of the LOC-SOC transition in AUG is not performed in this thesis, but is an ongoing work [Prisiazhniuk 2015].

5.1.2 Poloidal extent of the QC-TEM disappearance

After the observations described so-far at different radii, we can wonder which poloidal region of the plasma is affected by the stabilization of QC-TEM. As previously discussed, the QC-TEM are usually not observed on the HFS [see figure 4.3]. In TEXTOR, it has been possible to analyze the LOC-SOC transition by measuring from the top of the torus (shot #117780) and from the LFS (shot #117781) during two identical discharges. Four measurements have been made at a similar radial position ($r/a \approx 0.91$).

As shown in figure 5.4, in TEXTOR the QC-TEM are not pronounced in the frequency spectra of the complex signal[6] nevertheless spectral modifications are observed between the LOC and the SOC regimes as previously reported in other tokamaks. This indicates that the disappearance of TEM is also global in the sense that it affects different poloidal locations. One can note that QC-TEM seem to last longer on the LFS (i.e. down to lower I_p). Indeed at $I_p = 300$ kA, the QC-TEM are still slightingly visible on the LFS whereas the top measurements almost exhibit a broadband spectra. This would suggest that TEM could be first stabilized on the top before their complete disappearance occurs.

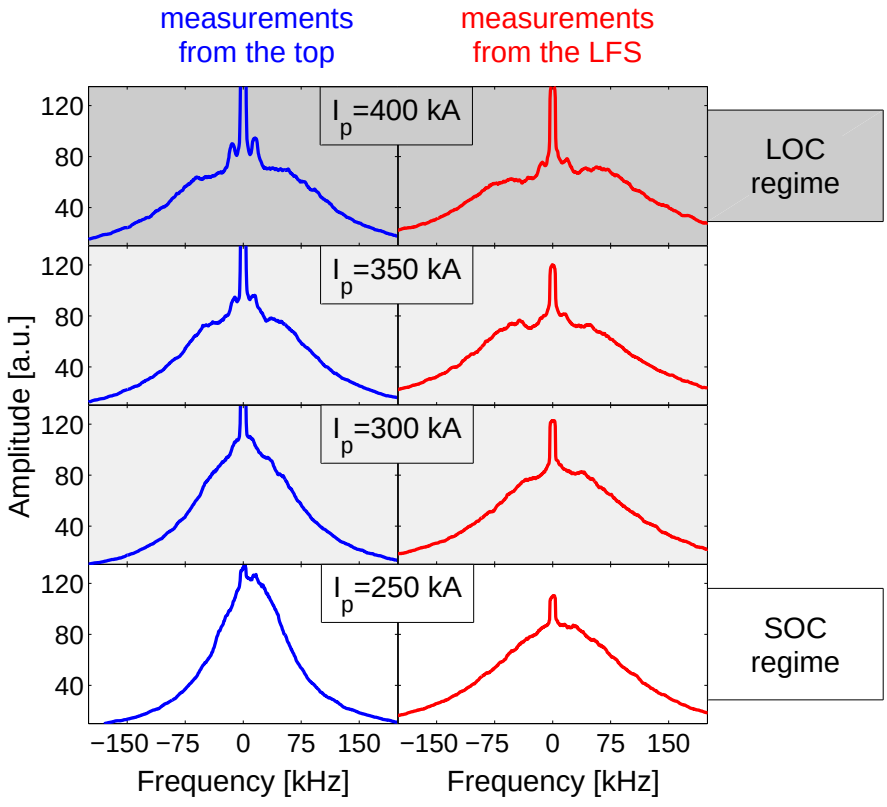

Figure 5.4: TEXTOR reflectometry spectra measured at $r/a \approx 0.91 \pm 0.01$ from the top of the torus (left hand side column #117780) and from the LFS midplane (right hand side column #117781) ($B_t = 1.9$ T and $3 \times 10^{19}\,\mathrm{m}^{-3}$).

[6] Coherence spectra can be used to highlight QC modes as shown in the previous chapter in figure 4.7, which corresponds to the left top and bottom spectra of figure 5.4.

5.1.3 QC-TEM and intrinsic toroidal rotation

Investigations of intrinsic toroidal rotation were previously made in several machines during the LOC-SOC transition. They have reported reversals of the intrinsic rotation [Bortolon 2006, Duval 2008, Rice 2011a, Rice 2011b, Angioni 2011, Rice 2012, Rice 2013, McDermott 2014]. The origin of these reversals is not fully understood, and the possibility for them to be due to transitions from TEM toward ITG dominated regimes has been discussed.

The knowledge of QC-TEM is used in this section to discuss the link between changes of turbulence and intrinsic rotation in the Tore Supra discharge #48102 [Bernardo 2015]. Reflectometry measurements from the two Tore Supra reflectometers are shown in figure 5.5 (a comparison with simulations has been presented in section 4.2). As previously discussed, QC-TEM are observed in the LOC regime only, here at $r/a \approx 0.18$ (left-hand side) and around $r/a \approx 0.7$ (right-hand side).

Beside these fluctuation measurements, an analysis of the intrinsic toroidal rotation across the LOC-SOC transition was made. Figure 5.6(a-c) shows the toroidal rotation amplitude measured by CXRS. The toroidal rotation amplitude is found to decrease as the electron density increases but no rotation reversal is observed. Contrary to observations reported in several machines, the intrinsic toroidal rotation remains in the counter-current direction.

As the ripple effect is pronounced in Tore Supra [Trier 2008], the lack of toroidal velocity reversal may be explained by the ripple-induced toroidal friction [Fenzi 2011]. In this case, according to the neoclassical predictions the intrinsic toroidal velocity is given

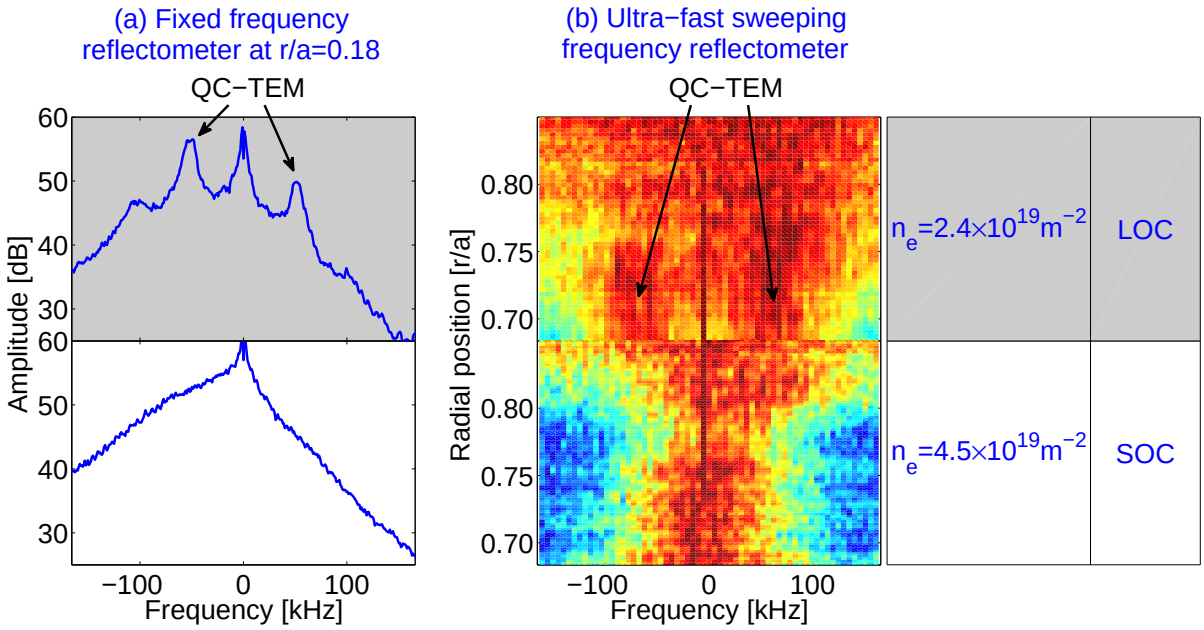

Figure 5.5: Spectra from (a) fixed-frequency reflectometer ($r/a \approx 0.18$) and (b) ultra-fast-swept reflectometer ($0.68 < r/a < 0.85$) during a LOC-SOC transition achieved by density scan in the Tore Supra discharge #48102.

by:

$$v_{tor} = \frac{k_T \nabla T_i}{e Z_i B_\theta} \tag{5.1}$$

with $k_T = 1.67$ in the regime predicted by the collisionality (ripple-plateau regime and collisional sub-regime); more details are provided in [Garbet 2010a]. During the density ramp-up, the measurements showing the overall reduction of the toroidal rotation velocity agree with the neoclassical predictions shown in figure 5.6(d-f), but the evolution of the core rotation ($r/a < 0.5$) is not reproduced by neoclassical predictions. Indeed, for an intermediate density ($3 < n_e[10^{19}\,\mathrm{m}^{-2}] < 3.5$), a transitory acceleration is observed in the plasma core region [see figure 5.6(a)]. This suggests that another mechanism such as turbulence can play a role in the intrinsic rotation.

The aim of this section is not to discuss the relation between ITG/TEM and the intrinsic rotation, but to present the observations deduced from the knowledge of QC-TEM combined with estimations of the intrinsic toroidal velocity. From reflectometry and CXRS data we can then deduce that:

- The transitory bifurcation of the toroidal velocity observed for $r/a < 0.5$ for the intermediate density is correlated to the disappearance of QC-TEM, which occurs between $n_e = 3.1$ and $3.8 \cdot 10^{19}\mathrm{m}^{-2}$.
- The stabilization of QC-TEM occurs also further out in the plasma ($0.6 < r/a < 0.75$) where no major change of intrinsic rotation is observed, and where the ripple effect is more pronounced.

Thus, a transition from TEM toward ITG occurs in the region where a transitory bifurcation of the toroidal velocity is observed, but such transition is also observed further out. More details on the toroidal rotation measurements are available in [Bernardo 2015].

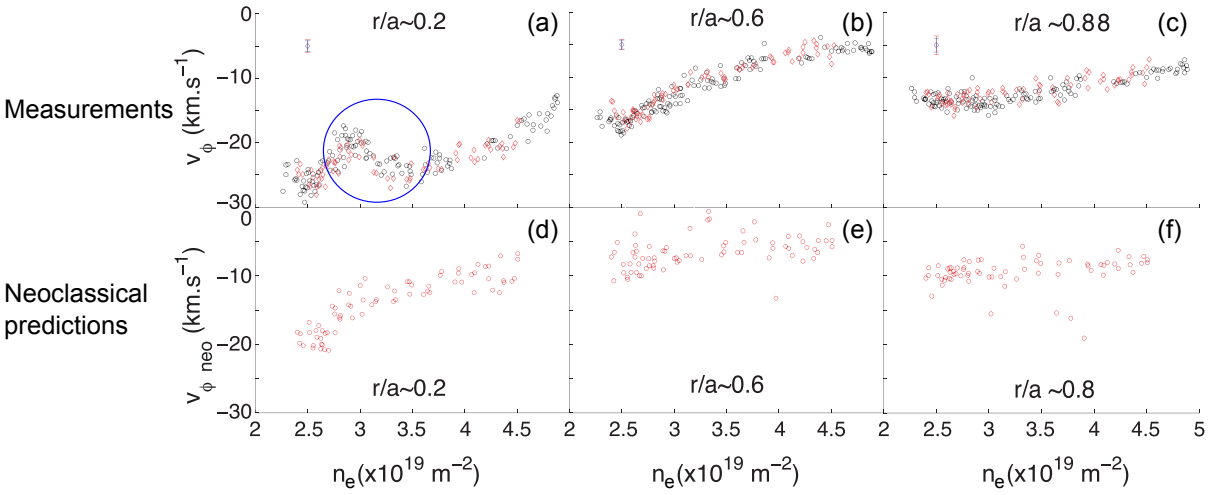

Figure 5.6: For three radial positions of the Tore Supra discharge #48102 and six similar discharges: (a-c) measurements of the intrinsic toroidal rotation (d-f) toroidal velocity from collisional ripple-plateau neoclassical predictions. Reproduced from [Bernardo 2015].

5.1.4 Summary of the Ohmic observations

Both I_p and n_e scans analyzed in Ohmic plasmas show that QC-TEM disappearance can affect a large part of the plasma (roughly from $r/a \approx 0.2$ until $r/a \approx 0.8$). The global and rather simultaneous aspect of the QC-TEM disappearance at the LOC-SOC transition supports the hypothesis that the TEM play an important role in the change of Ohmic regime. One can note that poloidally, the QC-TEM disappearance may start slightly before on the top of the torus compared to the LFS.

We have also reported that the disappearance of QC-TEM is correlated to a bifurcation of the intrinsic rotation that is not explained by neoclassical predictions. The QC-TEM stabilization also occurs in a region where no v_{tor} bifurcation is observed. All the observations related to the LOC-SOC transition are summarized in the table 5.2.

Tokamaks	Density scans	Current scans
Tore Supra	**QC-TEM ⇔ LOC** ▪ Disappearance of QC-TEM simultaneous to the LOC-SOC transition ▪ QC-TEM stabilization simultaneous to v_{tor} bifurcation observed in the core. QC-TEM stabilization also observed in a region where no v_{tor} bifurcation occurs.	**QC-TEM ⇔ LOC** Global stabilization of QC-TEM observed at the LOC-SOC transition.
TEXTOR	No measurements	**QC-TEM ⇔ LOC** ▪ Difference of $\mathbf{v}_{phase}$ between QC-TEM and low frequency fluctuations in the e^- direction ▪ Stabilization of QC-TEM at two poloidal locations (LFS and top)
JET	QC-TEM observed at low n_e	QC-TEM observed at high I_p
AUG	QC-TEM observed in the LOC regime[7]	No measurements

Table 5.2: Summary of the Ohmic observations made in Tore Supra, TEXTOR, JET and ASDEX-Upgrade tokamaks for two types of LOC-SOC transitions.

[7] The investigation of the LOC-SOC transition is an ongoing work [Prisiazhniuk 2015, Lebschy 2015]

5.2 TEM in Tore Supra ECRH plasmas

A study previously made to investigate impurity turbulent transport is used to apply the knowledge of QC-TEM to ECRH plasmas. After a presentation of the experimental scenario, the results previously obtained are described. Then they are compared to reflectometry measurements recently interpreted.

5.2.1 Experimental scenario

ECRH has been widely used to destabilize TEM in core tokamak plasmas [Angioni 2005, White 2010a, White 2010b, Shi 2013]. Here, its effect on nickel transport, linear gyrokinetic simulation and reflectometry fluctuation spectra is investigated in a set of Tore Supra discharges with $B_t = 3.8$ T and $I_p = 0.5$ MA. A power of 500 kW of ECRH was deposited by two gyrotrons. Keeping the total ECRH power constant, the deposition radii of the two gyrotrons were changed as indicated in table 5.3.

	Discharge number	1^{st} Gyrotron	2^{nd} Gyrotron
case n°1: outer deposition	#40807	$r/a = 0.58$	$r/a = 0.58$
case n°2: mixed deposition	#40805,#40806	$r/a = 0.58$	$r/a = 0.35$
case n°3: inner deposition	#40801	$r/a = 0.35$	$r/a = 0.35$

Table 5.3: Radii of the ECRH power deposition for the Tore Supra discharges analyzed

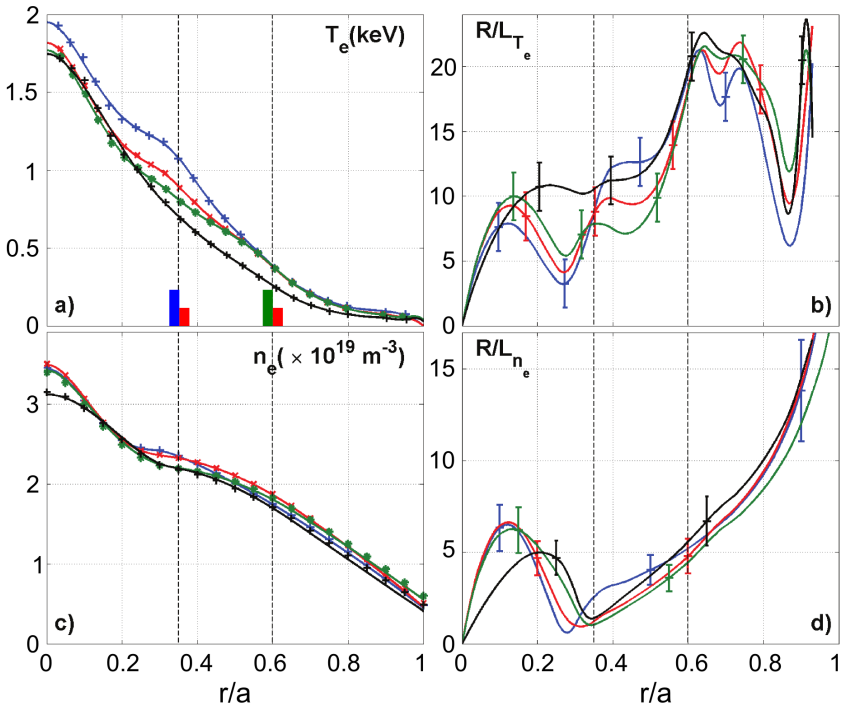

Figure 5.7: Profiles of the electron (a) temperature and (c) density, normalized (b) temperature and (d) density gradients for the discharges shown in table 5.3. These data are computed with CRONOS [Artaud 2010]. In black an Ohmic reference shot is shown.

Owing to this combination, we were able to modify the temperature gradient inside $r/a = 0.3$ while keeping the density profile almost constant [Villegas 2010b, Villegas 2014]. Switching ECRH on suppresses small saw-teeth observed in the Ohmic phase ($T_e < 100$ eV at the crash, inversion radius $(r/a)_{q=1} \approx 0.08$).

5.2.2 Previous work

5.2.2.1 Impurity transport study: R/L_{T_e} dependence of nickel diffusion

Nickel was injected as a trace by a laser blow-off system [Parisot 2008] during the ECRH phase. The impurity behavior was observed with a vacuum ultraviolet spectrometer consisting of a single line of sight in the plasma mid-plane. It measures the time evolution of the Ni XVII line at 24.92 nm, whose time evolution is used as the Ni source term in the transport simulations. Two soft-X-ray cameras with a 2 ms time resolution provide information on impurity radiation in the plasma core. Details on these diagnostics can be found in [Parisot 2008, Guirlet 2009].

The radial transport analysis of nickel was carried out using the ITC code [Parisot 2008]. It solves the system of continuity equations for all the ionization stages of the injected impurity. The impurity flux $\boldsymbol{\Gamma}_{Ni}(r)$ for each ionization stage results from diffusion $D_{Ni}(r)$ and convection $\boldsymbol{V}_{Ni}(r)$ as defined in equation 2.1. We assume that $D_{Ni}(r)$ and $\boldsymbol{V}_{Ni}(r)$ are independent of the ionization stage. Starting from an initial guess, ITC solves the system of continuity equations. It then reconstructs the VUV, bolometric and soft X-ray brightnesses. With the help of a genetic algorithm, the code converges towards the transport coefficient profiles best matching the measurements [Villegas 2014].

The analysis performed for the three different ECRH deposition schemes shows that the diffusion coefficient at $r/a = 0.1$ depends strongly on the normalized temperature gradient R/L_{T_e} [figure 5.8(a)]. On the contrary, at $r/a = 0.3$, the diffusion coefficient is almost independent of R/L_{T_e} [figure 5.8(b)].

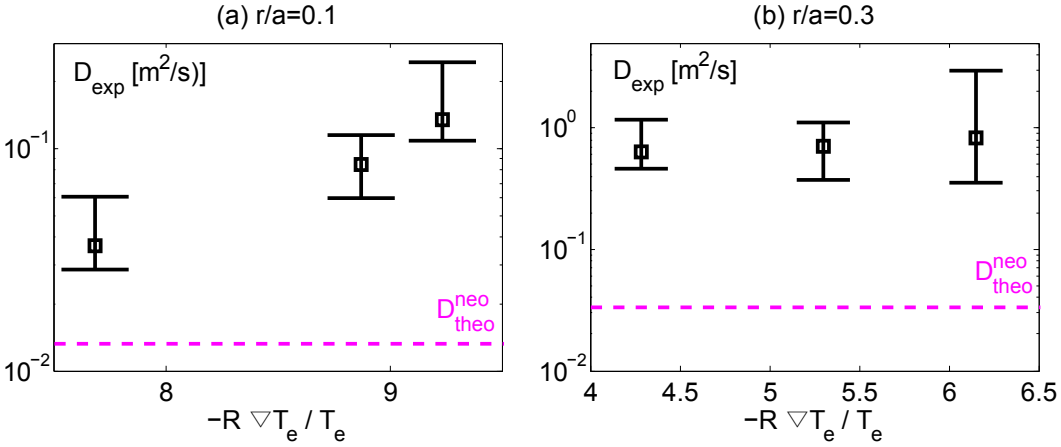

Figure 5.8: Experimental diffusion coefficient of nickel as a function of the normalized logarithmic electron temperature gradient at $r/a = 0.1$ (a) and $r/a = 0.3$ (b) in Tore Supra. The neoclassical diffusion coefficient is shown for both cases in dotted line

5.2.2.2 Linear gyrokinetic simulations

This difference is interpreted in the frame of the theory of turbulent transport. The existence of two regions [Villegas 2014] are observed in linear gyrokinetic simulations [see figure 5.9] performed with the QuaLiKiz code [Bourdelle 2007]:

- In the core ($r/a < 0.2$), turbulence is dominated by electron modes. Additionally, the values of the diffusion computed with QuaLiKiz (not shown here) versus the R/L_{T_e} also exhibit an increase as shown by the measurements. With TEM dominated turbulence, the transport characteristics are affected by the electron temperature hence explaining figure 5.8(a).

- Further out ($r/a > 0.2$), ions modes are found dominant. Additionally, the diffusion computed with Qualikiz (not shown here) is independent of R/L_{T_e}, supporting the measurements. The fact that ITG modes are independent of the electron temperature is consistent with diffusion coefficients independent of R/L_{T_e} [see figure 5.8(b)].

Thus the results of these gyrokinetic simulations support that the inner region ($r/a < 0.2$) is dominated by TEM whereas ITG dominate further out ($r/a > 0.2$).

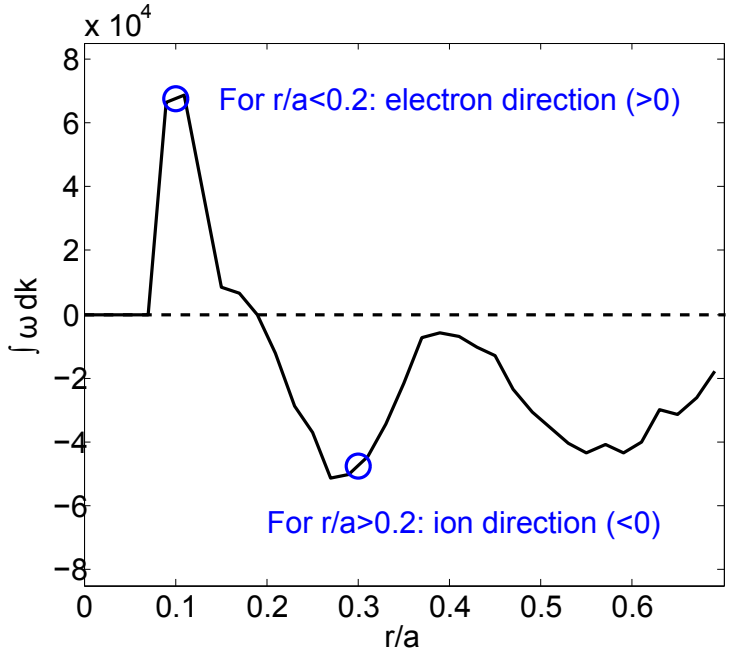

Figure 5.9: Radial profile of the integral over the wavenumber k of the spectrum of the most unstable mode frequency computed with the QuaLiKiz code for the Tore Supra discharge #40801. Circles correspond to the radii at which the diffusion coefficient is shown on figure 5.8

5.2.3 Spectral measurements

Figure 5.10 shows two sets of reflectometry spectra both measured within the radial range 0.15 (HFS) $< r/a <$ 0.35 (LFS) by changing the reflectometer probing frequency. The left and right columns correspond to the ECRH and Ohmic phases respectively.

In the ECRH phase, the radial scan shows that QC-TEM are pronounced for $0.1 < r/a < 0.2$, damped between $0.2 < r/a < 0.25$ and disappear further out for $r/a > 0.3$. One can note that QC-TEM are not observed on the HFS as previously discussed in section 4.1.5. Thus these observations give an experimental indication, which clearly supports the interpretation of a core dominated by TEM ($r/a < 0.2$) and an ITG dominated turbulence further out ($r/a > 0.2$).

Additionally, a comparison with the Ohmic phase shows that the QC-TEM amplitude is enhanced by the ECRH. This is what we could expect for TEM, and in agreement with the ECRH effects on QC modes reported in T-10 [Vershkov 2013b].

Thus both in terms of amplitude and radial location, the observations of QC-TEM coincide with the expectation for TEM deduced from the nickel transport analysis and the linear gyro-kinetic simulation. A summary of all the observations made in these Tore Supra ECRH plasmas can be found in the table 5.4.

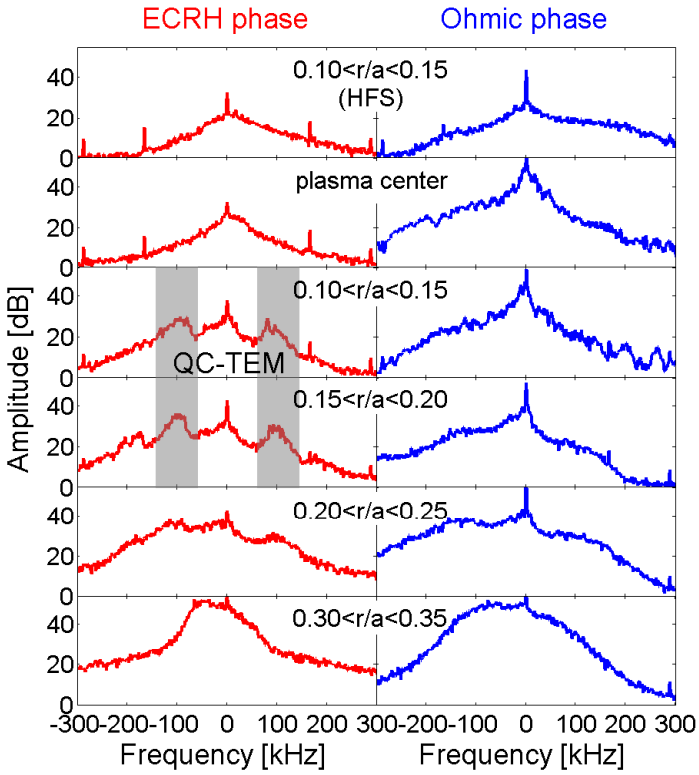

Figure 5.10: Fluctuation spectra of the discharge #40801 from Tore Supra reflectometry. (a) show the difference between ECRH and Ohmic phase and (b) show three different radial positions during the ECRH phase. QC-TEM are clearly destabilized only below $r/a \approx 0.2$ in the ECRH phase.

	$r/a < 0.2$	$r/a > 0.2$
Turbulence regime	TEM	ITG
Nickel diffusion [section 5.2.2.1]	increases with R/L_{T_e}	independent from R/L_{T_e}
Linear simulations [section 5.2.2.2]	electron mode	ion mode
Reflectometry spectra [section 5.2.3]	QC-TEM	broadband spectra

Table 5.4: Summary of the observations made in Tore Supra ECRH plasmas indicating a TEM dominated plasma for $r/a < 0.2$ and an ITG dominated plasma for $r/a > 0.2$.

One should note that the enhancement of QC-TEM amplitude while going from Ohmic toward ECRH plasmas is observed for three ECRH configurations shown in table 5.3 and in figure 5.7. It is not possible to conclude on the amplitude of QC-TEM during the scan of R/L_{T_e} because the reflectometer settings were not similar, therefore the noise level and the radial position slightly change between the three discharges. However we can notice that the QC-TEM energy as defined in section 3.1.1 remains high in the three ECRH cases for $0.1 < r/a < 0.2$. It is estimated to be between 1.73 and 1.88 dB/kHz, which corresponds to the high range of the values observed in the LOC regime shown in the previous section [see figure 4.6].

Chapter 6

Transitions between TEM and MHD modes

Contents

During the investigations of TEM such as the one reported in the previous sections, transitions/interplay between QC-TEM and MHD modes have been observed in several tokamaks. These types of observations appear to be of interest and will therefore be presented in the present section.

Direct interactions between MHD and turbulent instabilities are not well studied because (i) experimentally the identification of turbulent instabilities is so far limited and (ii) it is complicated for simulations to reproduce such a large range of fluctuation scales (from macro to micro-instabilities) involving electrostatic and electromagnetic fluctuations. The present section relates radial and temporal transitions between TEM and MHD modes.

The study of the MHD modes observed is out of the main scope of this thesis, therefore they will not be investigated in detail by comparing them with simulations for example.

6.1 Radial transitions between TEM and MHD modes

6.1.1 Radial transition in ASDEX-Upgrade Ohmic plasmas

The previous analysis of AUG data has shown that QC-TEM can be observed in the LOC regime at very distinct radii ($0.25 < r/a < 0.4$ and $r/a = 0.73$) [see figure 5.2]. In this section, a clear disappearance of QC-TEM close to the plasma center is reported in the same Ohmic discharge.

Close to the magnetic axis, TEM are expected to be stable as the fraction of trapped particles f_t is proportional to the radius ($f_t \approx \sqrt{2r/R_0}$). Figure 6.1(bottom) shows the set of reflectometry spectra measured by ultra-fast-swept reflectometry as a function of ρ (the color bar indicating the amplitude of the fluctuations). For $0.12 < \rho < 0.2$, QC-TEM are weaker than for $\rho > 0.25$. However the disappearance of the QC-TEM at $\rho \approx 0.12$ is rather sudden, suggesting that another mechanism than the decrease of f_t could be at play.

Figure 6.1(middle) shows the phase fluctuations $\delta\phi$ of the reflectometer signal as a function of ρ. The time evolution of the phase is usually hard to interpret, which justifies the use of Fourier analysis. Indeed, in most of the radii it is hard to extract information from the visualization of the phase fluctuations. However we can distinguish some clear slow oscillations of the phase at $\rho \approx 0.12$ which corresponds to the radius where QC-TEM disappear. Such fluctuations of the phase are a typical signature of MHD activity related to tearing modes [Vermare 2005, Hornung 2013b]. During the time interval of the measurement ($\delta t = 2.5$ ms) nine oscillations of the phase can be counted. It corresponds to an MHD mode frequency of ≈ 3.6 kHz.

One can note that these 3.6 kHz oscillations cannot be distinguished in the fluctuation spectra. Indeed ultra-fast swept reflectometers have the advantage to cover a wide radial region of the plasma, but at the price of a lower signal to noise ratio and a shorter acquisition duration. This usually makes impossible the analysis of MHD modes in frequency fluctuation spectra.

The q profile shown in figure 6.1(top) suggests that a m=3, n=2 tearing mode may be responsible of the sudden disappearance of QC-TEM observed at $r/a \approx 0.12$. Indeed, this q profile estimated with magnetic equilibrium indicates that the q=3/2 surface corresponds to the radius where the onset of the MHD mode occurs. There are no sawteeth during these measurements, in agreement with the estimated q profile (q>1).

This was the first example of pointing toward the complex relation between TEM and MHD modes. Beside these AUG observations, Tore Supra measurements have also shown a radial transition between MHD and TEM instabilities.

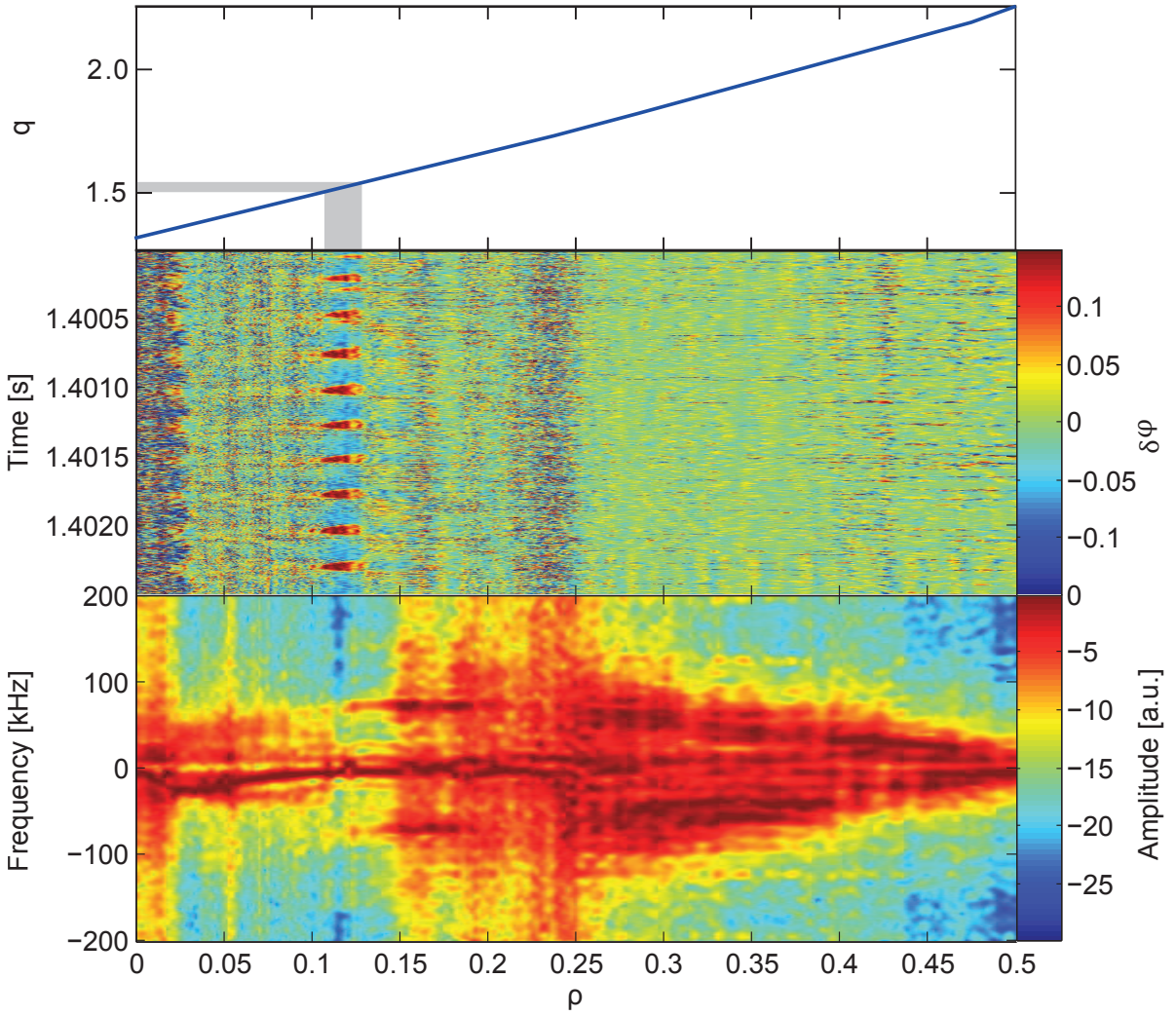

Figure 6.1: Data from the AUG discharge #31427 measured at $t \approx 1.4$s: (top) q-profile estimated from equilibrium reconstruction, (middle) phase fluctuations from the reflectometer measured during $1.4 < t[\text{s}] < 1.4025s$, (bottom) reflectometry spectra estimated at the same time.

6.1.2 Radial transition in Tore Supra LH heated plasmas

Another spatial transition between QC-TEM and MHD instabilities has been investigated in the Tore Supra shot #48220 heated by LH. This discharge is characterized by the following parameters: $P_{LHCD} = 1.25$ MW, $I_p = 0.6$ MA, $B_t = 3.66$ T and $n_e = 2.4 \times 10^{19}\,\text{m}^{-3}$.

Figure 6.2(a) shows reflectometry spectra measured at different radii. From the measurements obtained as far as possible from the plasma center ($r/a = 0.17$) we can observe that QC-TEM are detected at ≈ 50 KHz. Closer to the center, the amplitude of QC-TEM decreases and an MHD mode appears around $5 - 10$ kHz. This is somehow reminiscent of the observations made in the previous section.

These MHD modes were previously studied in Tore Supra LH heated plasmas with Electron Cyclotron Emission (ECE) data analysis [Maget 2006, Guimarães Filho 2011,

Guimarães Filho 2012]. They were identified as electron-fishbones (e-fishbones). E-fishbones [Zonca 2007, Merle 2012] are triggered by the interaction of fast electrons and internal kink mode, the frequency of the mode allowing a resonance with the energetic trapped electrons precessing in the ion diamagnetic direction. Therefore, the destabilization of e-fishbones requires (i) fast electrons which can be generated by ECRH or LH heating and (ii) trapped electrons with a toroidal precession velocity ω_d oriented in the ion diamagnetic direction [see figure 6.3]. As shown in figure 6.3, ω_d is a function of the magnetic shear s and the trapping parameter κ defined by:

$$s = \frac{r}{q}\frac{dq}{dr} \tag{6.1}$$

$$1 - 2\frac{r}{R_0}\kappa^2 = \frac{\mu B(r, \theta = 0)}{E} \tag{6.2}$$

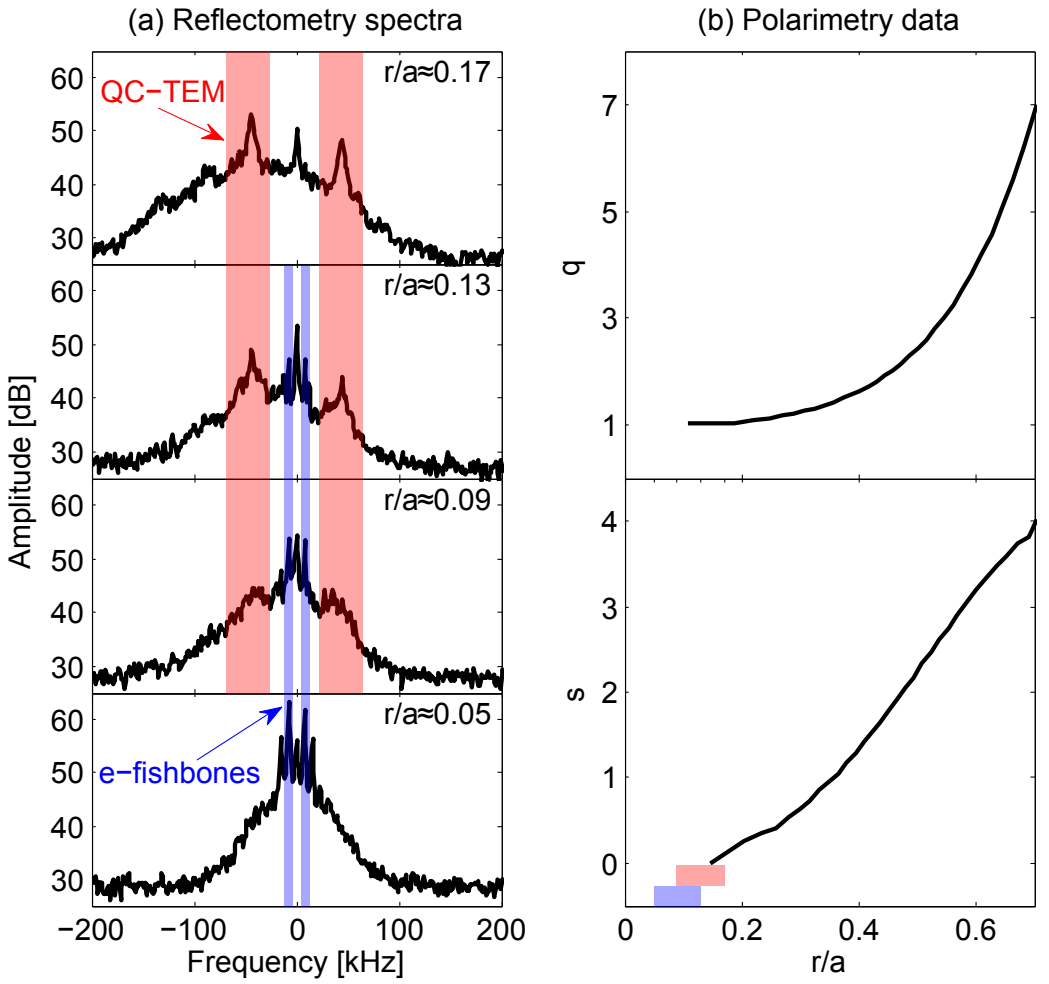

Figure 6.2: Data from the Tore Supra shot #48220 measured at $t = 14.5$ s: (a) reflectometry fluctuation spectra, and (b) profile of the safety factor (top) and the magnetic shear (bottom) estimated with polarimetry. The radial range corresponding to e-fishbones and QC-TEM are shown in blue and red respectively.

In a tokamak, the magnetic shear is usually positive $s > 0$, thus the trapped electrons such as the ones required to destabilized TEM rotate in the electron diamagnetic direction ($\omega_d > 0$). However, figure 6.3 shows that a reversal of ω_d can occur in the ion diamagnetic direction ($\omega_d < 0$) at low or negative magnetic shear. This reversal increases with the decrease of s and affects firstly the barely trapped electrons ($\kappa \to 1$) [Kadomtsev 1967]. As the barely trapped electrons are the most inclined to show $\omega_d < 0$, it makes them important for e-fishbones instabilities.

As shown in equation 6.2, the magnetic shear can be calculated from the safety factor profile. Unfortunately there is no estimation of q available below $r/a \approx 0.1$ thus s can be estimated the deepest at $r/a \approx 0.14$ [see figure 6.2(b)]. As the polarimetry data are not precise close to the plasma center, the analysis of the shear is restricted to qualitative observations.

Figure 6.2 indicates that the q-profile tends to flatten close to the magnetic axis. The shear could even be negative below $r/a \approx 0.15$, which corresponds to the radius where the e-fishbones appear. Many Tore Supra studies dedicated to LH heated discharges have indeed shown negative magnetic shear close to the plasma center [van Houtte 2004, Imbeaux 2005, Maget 2007, G. Giruzzi 2009, Goniche 2014, Dumont 2014].

Therefore a negative shear could increase the fraction of trapped electrons processing in the ion direction, and excite e-fishbones. Moreover, a negative shear and a decrease of trapped electron fraction close to the center ($f_t \underset{r\to 0}{\to} 0$) can both contribute to stabilize TEM.

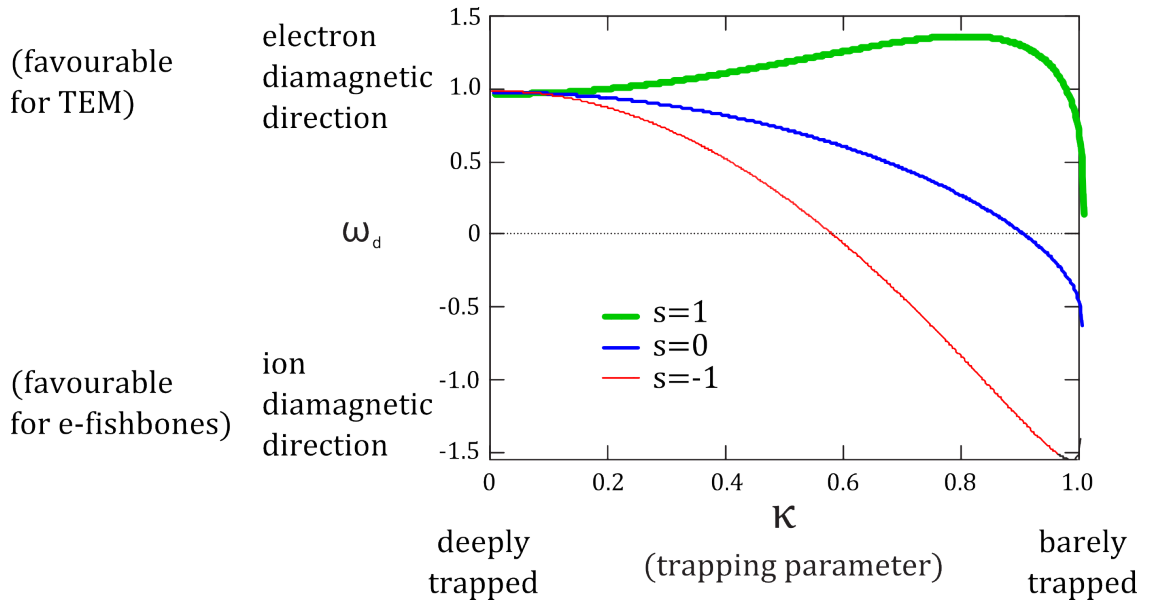

Figure 6.3: Normalized precession frequency of trapped particles ω_d as a function of the trapping parameter κ reproduced from [Garbet 2001]. $\omega_d > 0$ and $\omega_d < 0$ correspond to the electron and ion diamagnetic directions respectively. $\kappa > 1$ corresponds to the passing particles, close to $\kappa = 0$ the particles are deeply trapped and close to $\kappa = 1$ the particles are barely trapped.

6.2 Temporal interplay between TEM and MHD modes

In addition to the radial transitions between MHD and TEM reported in the previous section, some temporal interplay between MHD and TEM have also been observed.

6.2.1 Temporal MHD/TEM interplay in Tore Supra electron-heating

The Tore Supra tokamak allows two types of electron-heating: ECRH and LHCD. Both of them have shown temporal interplay between QC-TEM and MHD modes. They are described in this section.

6.2.1.1 Temporal e-fishbones/QC-TEM interplay in LH heated plasma

The observations of the Tore Supra discharge #48220 described in the previous section 6.1.2 have highlighted the spatial transition that can occur between e-fishbones and QC-TEM. In this discharge, we investigate the temporal evolution of both modes during the same discharge. Thanks to the 2^{nd} channel of the reflectometer which was settled at fixed frequency, a spectrogram at $r/a \approx 0.05$ can be analyzed. In this region e-fishbones are dominant as previously discussed in section 6.1.2.

Figure 6.4 shows the evolution of the normalized integrated power of two frequency ranges during 145 ms. They correspond to e-fishbones (5-10 kHz) and QC-TEM (35-55 kHz). E-fishbones seem erratic, indeed two short successive e-fishbones can be observed after t=14.51 and 14.52s, a more stationary one between t=14.53 and t=14.55s, and other oscillations thereafter.

Looking at the integrated power spectra of the frequency range corresponding to QC-TEM, the e-fishbones appearance/disappearance is anti-correlated with the amplitude of QC-TEM. A correlation analysis is made in figure 6.5. It shows the correlation coefficient of the two signals $\gamma(\tau)$ as a function of the delay time (as defined in section 3.2.2.2). The maximum of the correlation coefficient $\gamma(\Delta t) = -0.74$ shows that there is an anti-correlation. The value of the delay time $\Delta t = +0.9$ ms indicates that the QC-TEM are delayed compared to the e-fishbones.

As previously discussed, the trapped electrons contributing to TEM rotate in the electron direction via the banana toroidal precession velocity, while the trapped electrons contributing to e-fishbones rotate in the ion direction. Thus a temporal transfer of the trapped electrons contribution between e-fishbones and TEM could be a possible explanation of this anti-correlation. Figure 6.5 shows that the evolution of the correlation coefficient is periodic, with a periodicity of the order of 10 ms. Unfortunately it is not possible to get estimations of the magnetic shear precise enough to investigate its temporal evolution in such a short time-scale. This would allow to investigate if a periodic evolution of the magnetic shear could be responsible for the temporal interplay between QC-TEM and e-fishbones.

As the measurement location is sensitive to $\widetilde{n}_e$, small density variations can change the cutoff layer position and contribute to the variations of the QC-TEM and e-fishbones

amplitude. Indeed we have observed that further out the QC-TEM amplitude increases and that the e-fishbones disappear. We will see in the next section that such a spurious effect cannot explain the interplay observed between QC-TEM and MHD modes.

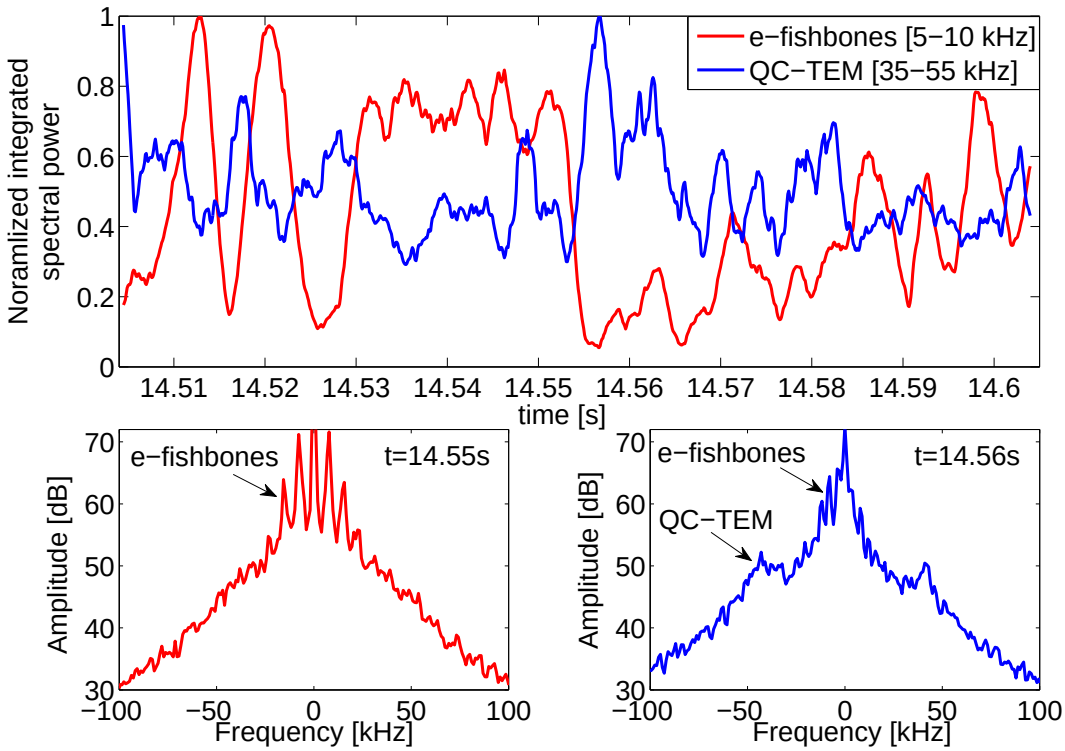

Figure 6.4: Reflectometry data from the Tore Supra discharge #48220 measured at $r/a \approx 0.05$. The top plot shows the time evolution of the normalized integrated spectral power for e-fishbones and QC-TEM. The bottom plots show spectra in which (left) only e-fishbones are observed and (right) weaker e-fishbones and QC-TEM are observed.

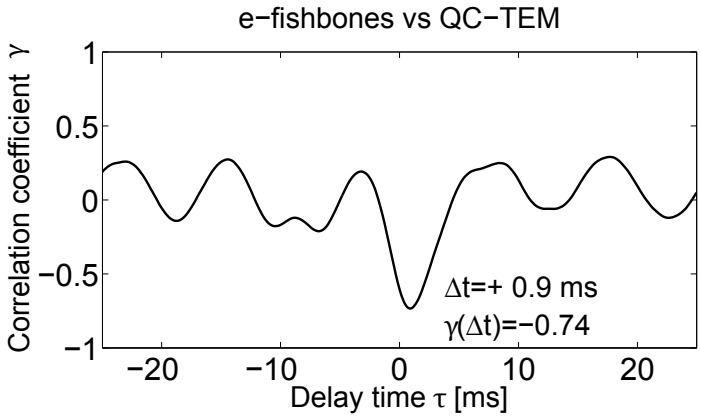

Figure 6.5: Correlation coefficient between the e-fishbone and the QC-TEM as a function of the delay time for the data shown in figure 6.4(bottom). The value of the correlation coefficient (<0) shows the anti-correlation and the sign of the delay time (>0) indicates that QC-TEM are delayed compared to the e-fishbones.

6.2.1.2 Temporal MHD/QC-TEM interplay in ECRH plasmas

In this section, the analysis focuses on the Tore Supra discharges already presented in section 5.2. As previously described, reflectometry measurements show QC-TEM in a region predicted to be TEM-dominated by linear gyrokinetic simulations and nickel transport analysis. In this set of discharges, an interplay is observed between turbulent fluctuations due to QC-TEM ($f \approx 100$ kHz and $\Delta f \approx 50$ kHz) and a coherent mode ($f \approx 15$ kHz and $\Delta f \approx 1$ kHz).

Among the ECRH configurations previously shown, we analyze the outer ECRH deposition (case n°1 in table 5.3) and the mixed ECRH deposition (case n°2 in table 5.3)[1].

The ECRH power starts to be deposited at $t = 9.5$ s, and an interesting observation is made when the QC-TEM are suddenly stabilized while a coherent mode appears. Such a transition is observed in the mixed ECRH deposition shown in figure 6.6(top,middle) but nothing happens in the case of outer deposition. This appears to be a cycle as it is observed at $t \approx 11.13$, ≈ 11.58, and ≈ 11.89 s (no fluctuation measurements are available later).

If the transition from the QC-TEM toward the coherent mode is very sudden (≤ 10 ms), a much slower recovering of QC-TEM occurs in-between each transition (until 300

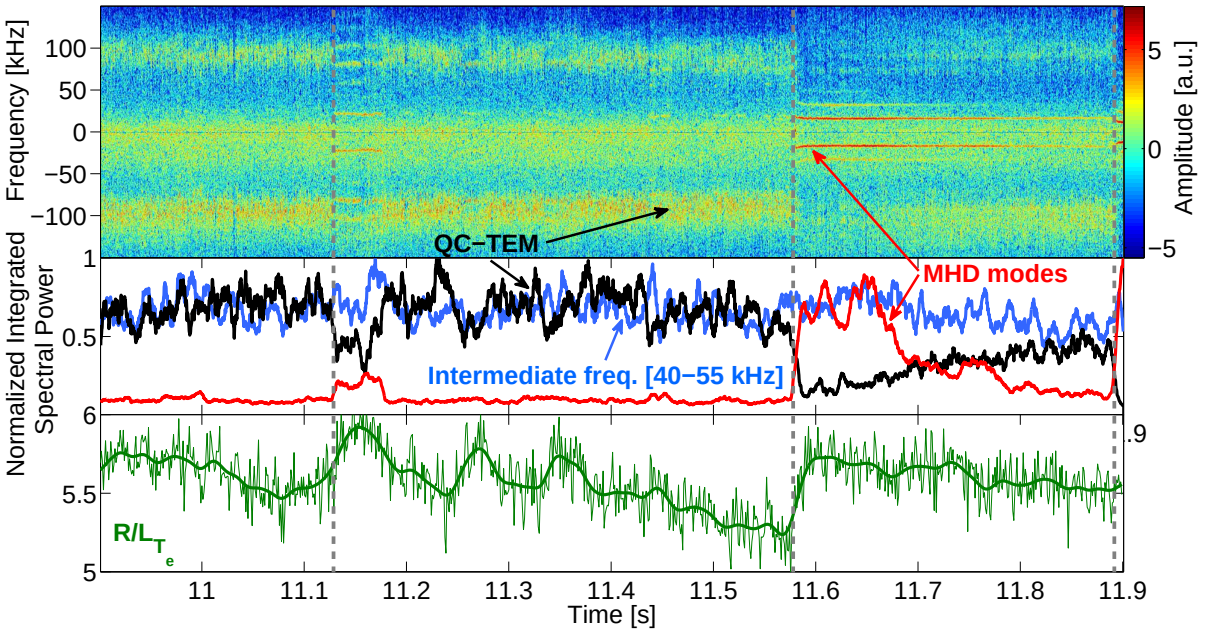

Figure 6.6: Data from the Tore Supra discharge #40806 measured at $0.15 < r/a < 0.2$: (top) reflectometry spectrogram, (middle) normalized integrated spectral power for the QC-TEM [70-120 kHz], the MHD mode [10-25 kHz] and an intermediate frequency band [40-55 kHz], (bottom) evolution of the normalized temperature gradient. The main transitions between QC-TEM and the MHD mode are shown by the vertical dashed lines (the three precursors within 11.1<t[s]<11.4 are not plotted to not overload the figure).

[1] There is no measurement allowing analysis of the temporal interplay for the inner deposition (i.e. case n°3).

ms for the main one). It suggests that a different mechanism is responsible for the two transitions (i.e. toward the coherent mode, and toward the QC-TEM). The spectral power of the intermediate frequency range selected $40 < f[kHz] < 55$ (plotted in blue in figure 6.6) shows no drastic change in time. This highlights the fact that the interplay occurs between the QC-TEM and the coherent mode.

A closer look at the QC-TEM shows that their peak can be modulated at the frequency of the MHD mode whereas the rest of the broadband spectrum is not, as previously reported in the Frascati Tokamak Upgrade (FTU) in LH heated plasmas [Vershkov 2001]. This indicates that the QC-TEM and the broadband fluctuations may not interact in the same way with the MHD instabilities, possibly due to their different underlying mechanisms.

A correlation analysis is made in figure 6.7. It shows the correlation coefficient $\gamma(\tau)$ of the two signals as a function of the delay time (as defined in section 3.2.2.2). The maximum of the correlation coefficient $\gamma(\Delta t) = -0.85$ shows that there is an anti-correlation. The value of the delay time $\Delta t = +0.3$ ms indicates that the QC-TEM are delayed compared to the e-fishbones. Figure 6.5 also shows that contrary to the LH heated case, the evolution of the amplitude of both modes is not clearly periodic.

Each time QC-TEM are damped, R/L_{T_e} rises. After the main transition shown at $t \approx 11.58$ s, R/L_{T_e} increases from ≈ 5.2 to ≈ 5.8 [see figure 6.6(bottom)]. This indicates that contrary to the LH heated case, the spurious effect of the measurement position can not be responsible for the transition observed. In this ECRH plasma, clear transitions occur, and they affect the surrounding plasma parameters as shown for the temperature. It could

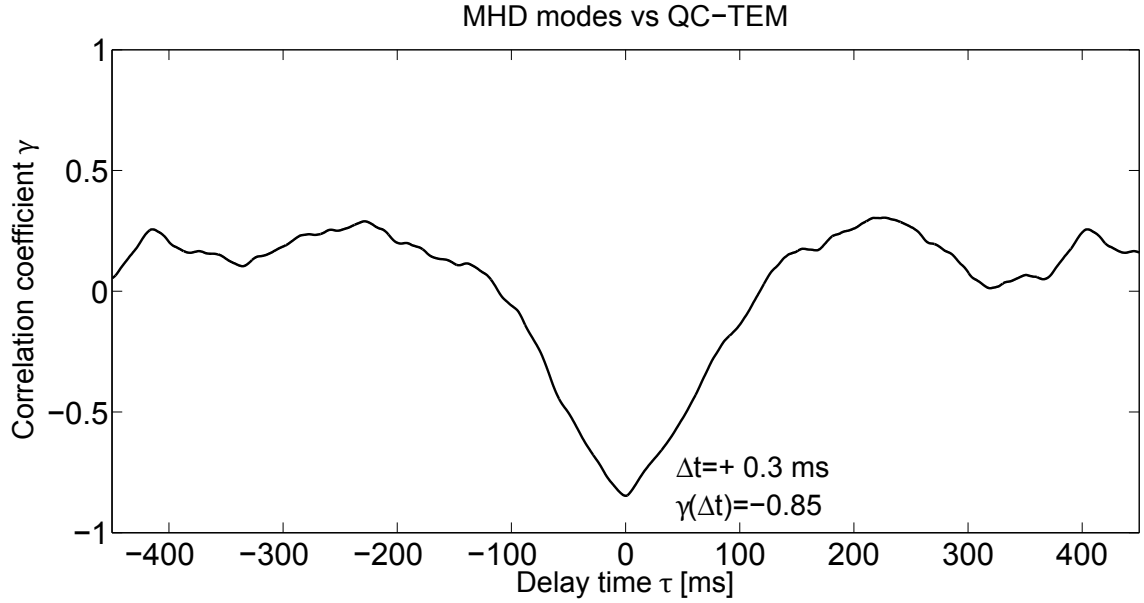

Figure 6.7: Correlation coefficient between the MHD mode and the QC-TEM as a function of the delay time for the data shown in figure 6.6(middle). The value of the correlation coefficient (<0) shows the anti-correlation and the sign of the delay time (>0) indicates that the QC-TEM are delayed compared to the MHD modes.

be explained by a local improvement of the confinement. Thereafter, the upholding of R/L_{T_e} at a rather high value ($R/L_{T_e} > 5.5$) can progressively contribute to drive TEM unstable again.

Regarding the identification of the MHD modes, several modes showing a coherent signature are unlikely responsible for the oscillations observed at $\approx 15kHz$:

- Geodesic acoustic modes (GAM) [Diamond 2005] are improbable because the density fluctuations they induce are weak in the mid-plane and they are usually damped in the deep plasma core region.
- Energetic GAM (eGAM) [Zarzoso 2012, Girardo 2014] could be unstable at this radial position, but the heating system (ECRH) does not produce the required fast ions.
- Other acoustic frequency range modes such as the toroidal Alfvén eigenmodes (TAEs) [Nazikian 1998] or the beta-induced Alfvén eigenmodes (BAEs) [Nguyen 2009] cannot explain these oscillations at $\approx$ 15 kHz because they are expected at much higher frequencies.

As this coherent mode (also observed on the HFS) does not present the characteristics of turbulent oscillations, it is attributed to MHD fluctuations, even though their origin is not clearly identified. Two candidates considered to be possibly responsible for the MHD mode are discussed in the following subsections: the e-fishbones and the tearing modes.

1^{st} hypothesis: Interplay between TEM and e-fishbones

E-fishbone is a potential candidate to explain the MHD mode. Indeed, some indications of an e-fishbone mode have been noticed in these observations:

- The MHD mode exhibits a frequency chirping-down [see figure 6.8]. Such behavior of the frequency at the onset of the mode is characteristic of e-fishbones.
- The power deposition region on the HFS is in favor of the destabilization of e-fishbones [Zonca 2007]. Indeed a HFS deposition can affect the barely trapped electrons more present in this plasma region as discussed in the introduction [see figure 1.8].

As previously highlighted in section 6.1.2, e-fishbones require fast electrons which can be generated by ECRH even though the deposition angle of 0.5^o is not very favorable for this. In Tore Supra, e-fishbones have not yet been reported in ECRH plasmas. This may come from the fact that they were investigated with the ECE system which becomes noisy in the presence of ECRH. Their study can be possible with reflectometers which are able to measure in ECRH plasmas[2].

[2]This is not always possible because the ECRH frequency (118 GHz) is in the range of the reflectometer frequency (105-155 GHz). A tiny fraction of the ECRH power ($P_{ECRH} \approx$ 500 kW) on the reflectometer mixer would damage it ($P_{reflecto} \approx$ 100 mW).

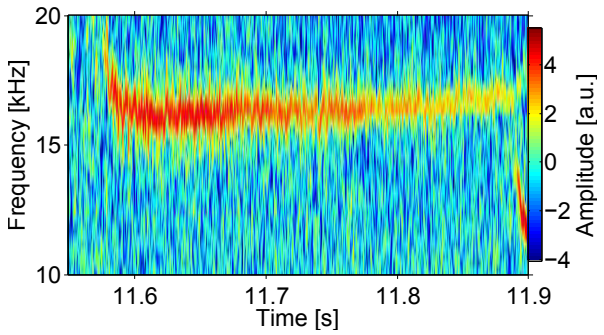

Figure 6.8: Zoom of the figure 6.6 to highlight the frequency chirping-down of the MHD mode (Tore Supra #40806).

Trapped electrons with a toroidal precession velocity ω_d oriented in the ion diamagnetic direction [see figure 6.3] are also required. Thus, in view of this e-fishbone hypothesis the analysis of the shear appears to be important. It is done in this section either by looking at the shear provided by the CRONOS suite of codes [Artaud 2010], or by polarimetry [Li 2011]. Unfortunately, none of these estimations is accurate in the plasma core of Tore Supra. We will therefore restrict our analysis to qualitative observations, and both estimations will be compared.

Figure 6.9(b) shows the estimations of the magnetic shear obtained with CRONOS at $r/a \approx 0.17$. The ECRH decreases significantly s only when one gyrotron power is deposited at $r/a_{ECRH} = 0.35$ (in green). One can note that the value of the shear remains significantly positive. Figure 6.9(c) shows the estimations of s made with polarimetry at $r/a \approx 0.17$. Here the shear is significantly reduced in both cases, reaching lower values in the case with $r/a_{ECRH} = 0.35$. One can note that s estimated with polarimetry decreases down to negative values.

Therefore, from both observations we deduce that the shear is reduced during the ECRH. In both CRONOS and polarimetry cases, s might decrease even more because they tend to produce a monotonic q profile ($s < 0$ is avoided).

Figure 6.9(a) shows the evolution of the normalized gradient for the two cases investigated. The small bumps in the R/L_{T_e} are observed only when the MHD mode appears for a mixed deposition (shown in red). In the case of an outer deposition, R/L_{T_e} remains higher (> 6) than in the case of mixed deposition where it goes below 5. Thus additionally to the magnetic shear, R/L_{T_e} probably plays a role in the interplay observed. A condition for the stabilization of TEM could be a value of R/L_{T_e} low enough. Indeed one can note that in both cases R/L_{T_e} decreases progressively during the ECRH deposition. This comes from the ECRH system, which always provides the maximum of its power at the beginning of the deposition[3].

The fact that QC-TEM and e-fishbones may be stabilized/destabilized by small changes of local plasma parameters (R/L_{T_e}, s) requires in any case that both instabilities remain marginally unstable/stable respectively.

[3]During the thermalization of the gyrotron cavity a frequency shift of the ECRH wave is induced, it is one of the reasons of the decrease of the ECRH power

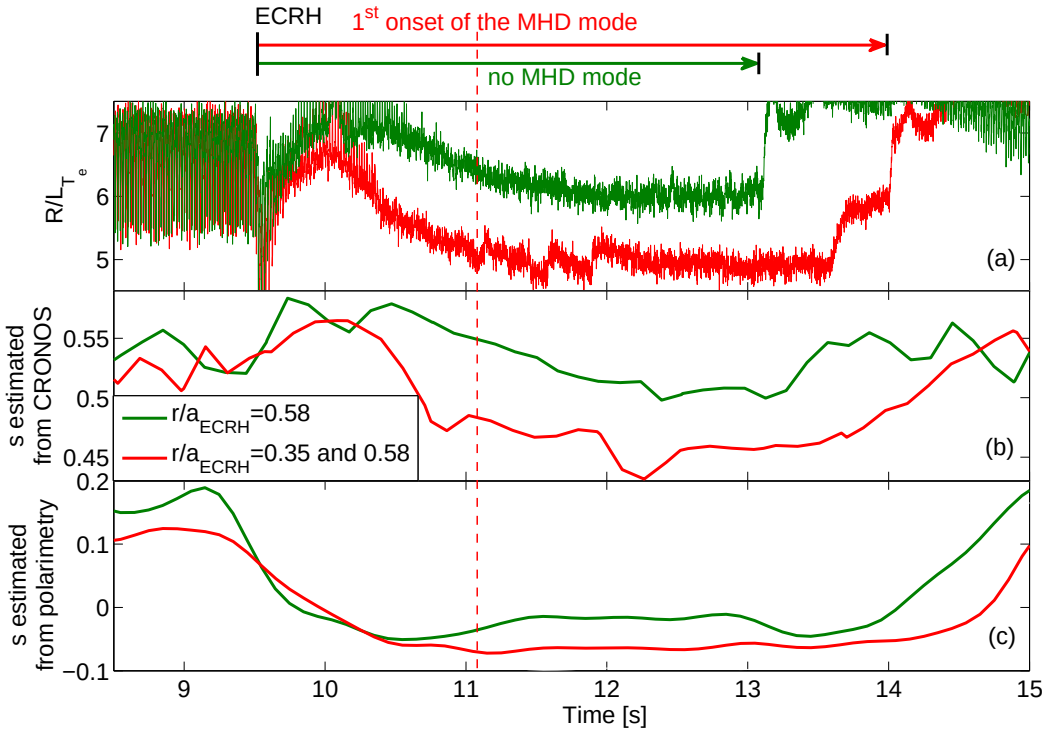

Figure 6.9: Tore Supra data showing (a) R/L_{T_e}, the magnetic shear from (b) CRONOS, (c) from polarimetry, estimated around $0.15 < r/a < 0.20$. Two configurations of ECRH deposition are shown [see table 5.3], the interplay with the MHD mode appearing only for $\rho = 0.35$ and $\rho = 0.58$.

2^{nd} hypothesis: Interplay between TEM and tearing modes

Another less probable possibility is that the MHD mode is a tearing mode, destabilized by the change of magnetic equilibrium induced by ECRH. Indeed, tearing modes become more unstable when the safety factor evolves towards a hollow profile [Zabiégo 2001], as it is the case here with the strong reduction of the magnetic shear indicated by the equilibrium reconstruction. This can be verified by computing the tearing parameter Δ' [Furth 1963] that measures the free energy available for developing a tearing mode:

$$\Delta' = \frac{\psi'_+(r_s+\delta) - \psi'_-(r_s-\delta)}{\psi(r_s)} \tag{6.3}$$

Δ' shows the difference of the slopes for the flux function ψ inside $(r_s-\delta)$ and outside $(r_s+\delta)$ the radius of the mode rational surface (r_s). In theory $\Delta' > 0$ implies an instability and $\Delta' < 0$ a stability.

In figure 6.10(a), Δ' is evaluated for the $(m = 3, n = 2)$ mode, since the reconstruction indicates a q-profile close to this value in the region probed by the reflectometer, and we use the safety factor profile from an integrated simulation with the CRONOS suite of codes [Artaud 2010]. We find that this mode becomes more unstable during the period of ECRH. Indeed we observe that even though Δ' remains negative, ECRH has

a destabilizing effect because Δ' increases progressively during the power deposition. Interestingly, the increase of Δ' is more pronounced when one ECRH gyrotron is deposited at $r/a = 0.35$, which would explain why the MHD mode appears only in this case.

It is also interesting to notice in figure 6.10(b) that when ECRH is applied, the radius of the resonance surface moves toward the location of the reflectometer measurements ($r/a \leq 0.2$). Again, this effect is more pronounced when one ECRH gyrotron is deposited at $r/a = 0.35$ where MHD activity is actually observed.

Note that the relatively large mode frequency could be an indication that higher harmonics could be involved (such as the 6/4 modes). This would be possible for a magnetic equilibrium slightly different from the one obtained by the equilibrium reconstruction, and possessing two close resonances: in such a case, high mode numbers could be more unstable that lower ones [Bierwage 2005].

As the MHD mode appears in reflectometry spectra after $\approx 1.5s$ of ECRH, it can be explained by the destabilization of the 3/2 tearing mode combined with the displacement of its rational surface. A local improvement of the confinement due to the stabilization of TEM could be responsible for the increase of temperature. This would tend to destabilize TEM again.

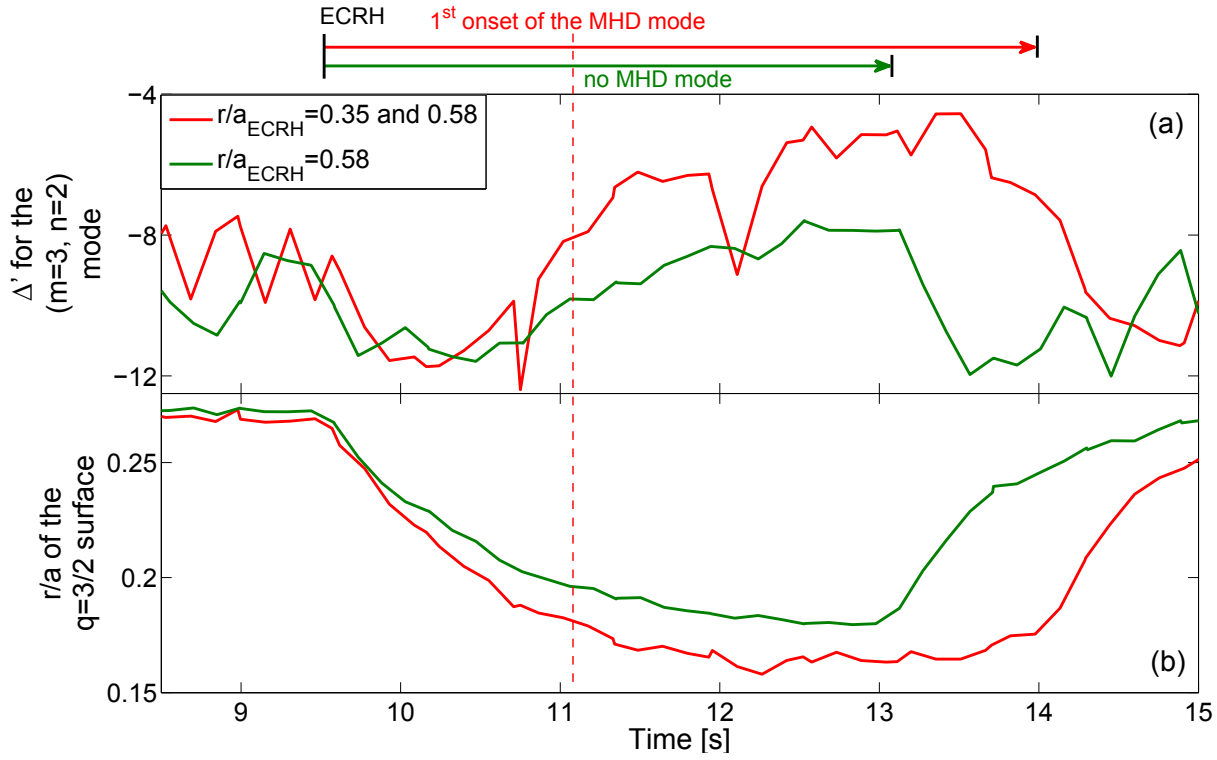

Figure 6.10: Tore Supra data showing (a) Δ' for the $(m = 3, n = 2)$ mode, and (b) the position of the q=3/2 resonance surface. Two configurations of ECRH deposition are shown [see table 5.3], the interplay with the MHD mode appearing only for $\rho = 0.35$ and $\rho = 0.58$.

6.2.2 Temporal MHD/TEM interplay during sawteeth in JET

Another type of interplay between turbulence and MHD modes has been observed in the deep plasma core of JET. These measurements were made across the transition from the L to the H-mode during sawtooth oscillations.

Before going in the details of the analysis, one should note that contrary to the previous observations discussed in ECRH sawtooth free plasmas, these measurements are performed during sawtooth crashes. The probing frequency is constant, as a result the measurement location oscillates during the sawtooth crashes. Hence, the reader has to keep in mind that the effects of this spatial change cannot be discriminated from the effect of the temporal changes.

Figure 6.11(top) shows the sawtooth effects on the central temperature. The D_α signal is also plotted to highlight the L to H transition. Around $t = 57.2$ s, the first L-H transition occurs, triggered by a sawtooth crash. Thereafter, an H-L transition is observed during the sawtooth build-up. These cycles last 1 s before the plasma fully enters H-mode. One can note that the small shift between the T_e and the D_α signal is due to the propagation time from the center where T_e is measured to the edge where the D_α signal originates.

Figure 6.11 presents the reflectometry spectrogram (middle) and the normalized integrated power spectra (bottom). They show significant changes of QC-TEM above 125 kHz and tearing MHD modes at $\approx$ 7 kHz. As one can see, their amplitude is driven by the sawtooth effects. The QC-TEM turbulent mode is observed before the crashes whereas the MHD modes is enhanced after the crashes. Even though the interaction

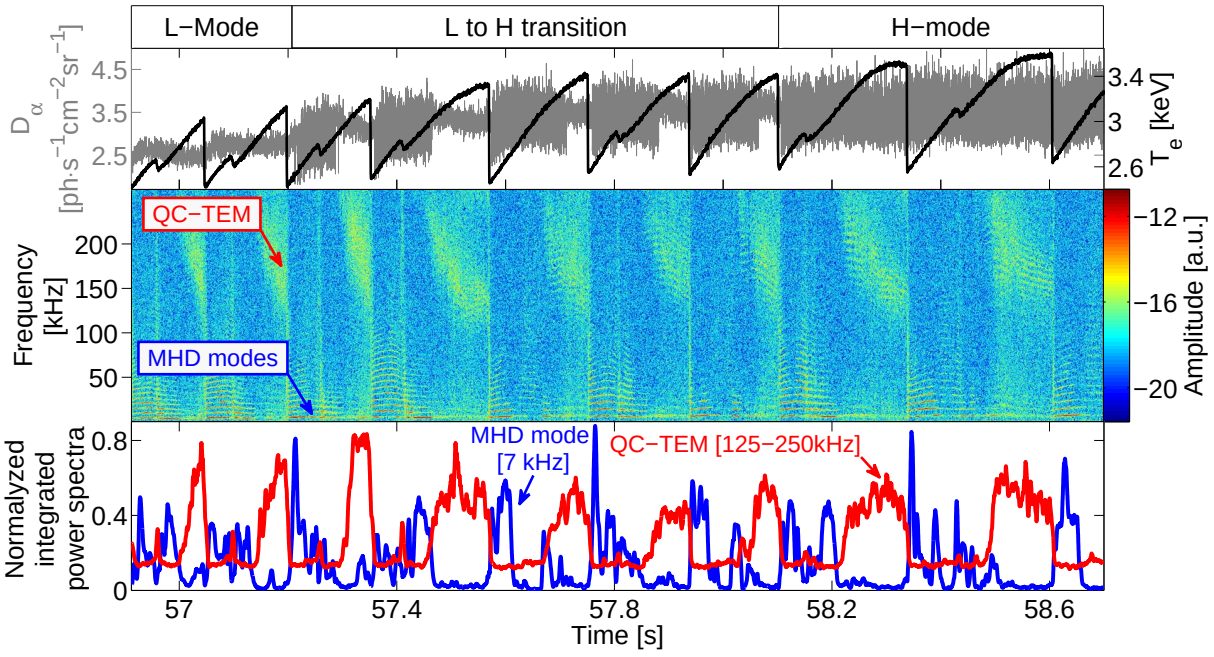

Figure 6.11: JET data showing (a) the electron temperature and the D_α signals, (b) the reflectometry spectrogram and (c) the normalized integrated power spectra.

is indirect (via the sawtooth effects), the amplitude of both instabilities is interestingly anti-correlated. As expected, the QC-TEM turbulence is driven by the temperature and density gradients and therefore appears when they are steeper. However, the reason which forces the turbulence to appear only once the MHD is stabilized remains an open question.

One can note that the maximum of the normalized integrated power spectra decreases from the H to the L mode. The core turbulence such as QC-TEM is not linked with the H-mode (it is observed before and after the transition), but this suggests that the H-mode could also reduce the turbulence in the deep plasma core region.

A correlation analysis is made in figure 6.12 which shows the correlation coefficient of the two signals $\gamma(\tau)$ as a function of the delay time (as defined in section 3.2.2.2). The maximum of the correlation coefficient $\gamma(\Delta t) = -0.5$ shows that there is an anti-correlation between the MHD modes and the QC-TEM. The value of the delay time $\Delta t = +0.64$ ms indicates that the QC-TEM are delayed compared to the MHD modes. As expected, figure 6.12 also shows that the strong periodicity of the two signals. It is of the order of ≈ 150 ms, which corresponds to the sawtooth period.

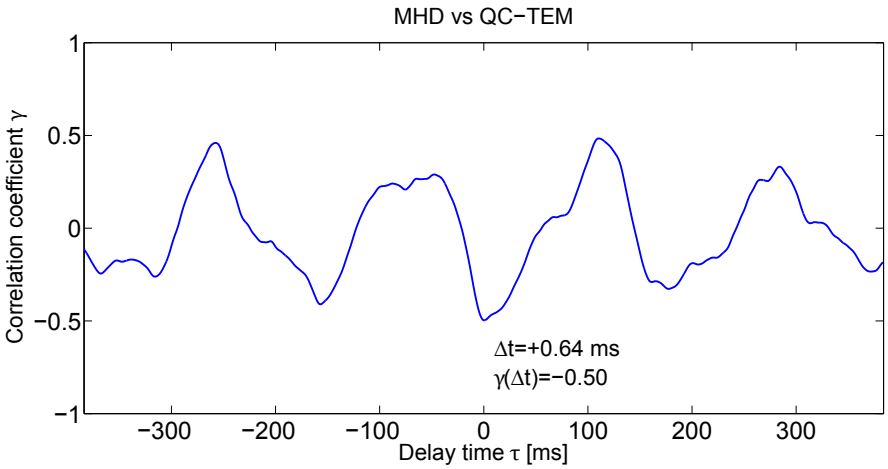

Figure 6.12: Correlation coefficient between the MHD mode and the QC-TEM as a function of the delay time for the data shown in figure 6.11(bottom). The value of the correlation coefficient (<0) shows the anti-correlation and the sign of the delay time (>0) indicates that the QC-TEM are delayed compared to the MHD modes.

As it can be seen in figure 6.13, a more detailed look at the QC-TEM peak allows to do several other observations on these measurements, in addition to the evolution of the amplitude of both instabilities:

- The QC-TEM frequency varies in time during the sawtooth crashes. It shows a decrease of the frequency peak from more than ≈ 200 kHz down to ≈ 150 kHz when it disappears at the sawtooth crash. This may be explained by (i) the decrease of the value of the $E \times B$ drift at the location of the measurements before the sawtooth crash, (ii) a slower phase velocity $v_{ph} \approx \omega / k_\theta$ of the turbulence which can come from a decrease of the mode frequency ω (in the plasma frame at $E = 0$) or an increase of the mode wavenumbers k_θ.

- The mode can be modulated at the frequency of the MHD mode, as previously reported in Tore Supra with ECRH [see section 6.2.1.2] or in [Vershkov 2001] with LH heating. Additionally, it seems that the modulation of QC-TEM is observed only in the H-mode [figure 6.13(right)].

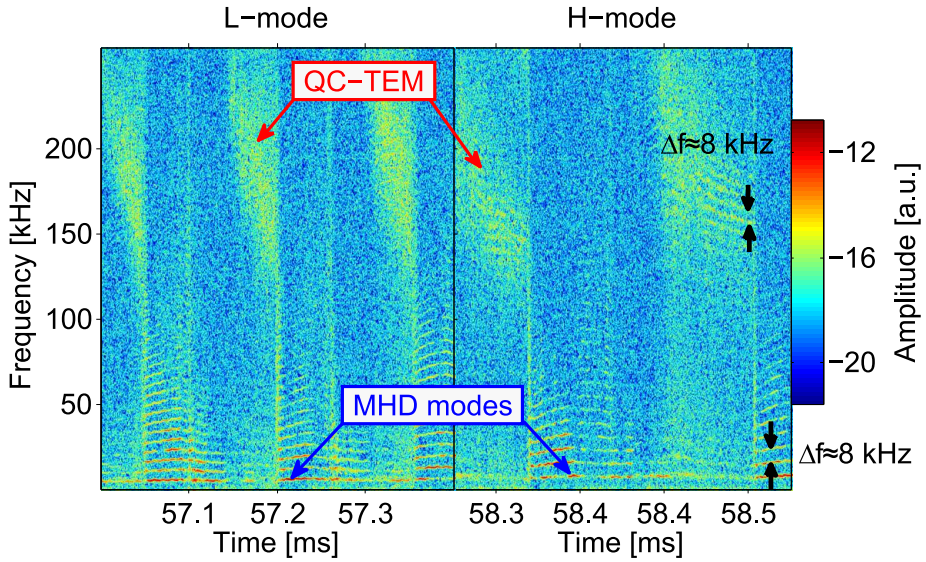

Figure 6.13: Zoom on the spectrogram shown in figure 6.11 for two time windows of 400 ms in L-mode (right) and H-mode (left).

6.3 Perspectives

These experimental observations indicate that interactions between MHD modes and turbulence (TEM) can occur in the plasma core region.

Toward the center of Tore Supra LH heated plasmas and AUG Ohmic plasmas, the amplitude of QC-TEM decreases while the onset of an MHD mode is observed. This radial transition suggests that the MHD activity may quench QC-TEM.

Temporally, observations in Tore Supra electron heated plasmas and JET NBI plasmas suggest that interplay between TEM and MHD modes can occur in the plasma core region. An anti-correlation is observed between the magnitude of the QC-TEM and the MHD modes. In all the cases QC-TEM shows a delay of the order of the 1 ms compared to the MHD modes.

Besides the numerical studies made in this domain [Ishizawa 2007, Waelbroeck 2009, Poyé 2015, Hornsby 2015], the measurements presented in this section give experimental indications that interactions between turbulence and MHD activity can occur in tokamak plasmas.

Chapter 7

Conclusion & Perspectives

Contents

7.1 Conclusion

This thesis was focused on frequency fluctuation spectral analysis provided by reflectometers in the plasma core region. In such spectra, so-called Quasi-Coherent (QC) modes can be observed, depending on the plasma scenario. Their origin, which was previously attributed to ITG in the reflectometry community [Vershkov 2005], has been re-evaluated. The present results have shown that QC fluctuations come from TEM instability.

To investigate the origins of QC modes, their general properties were first analyzed. They were found in agreement with a micro-instability-like signature such as ITG or TEM ($k_\perp \rho_i \leq 1$, can be observed at many different radii, amplitude ballooned on the LFS midplane). The LOC and the SOC regimes were then investigated to find whether QC modes were due to ITG or TEM. Experimentally, the QC modes were observed in the LOC regimes of different devices (Tore Supra, TEXTOR, JET and AUG) and at different radii (from $r/a \approx 0.15$ until $r/a \approx 0.9$). Their disappearance in the SOC regime were the first indication of their link with TEM. Additionally, the measurements of a different $v_\perp$ between QC modes and low frequencies fluctuations suggested that QC modes may rotate faster than low frequency fluctuations in the electron diamagnetic direction. Nonlinear simulations made showed that frequency fluctuation spectra of TEM are narrow whereas ITG have a broadband spectral signature. The cross-comparison with the measurements via the results of a synthetic reflectometer diagnostic have shown that QC modes are an experimental signature of TEM and subsequently they have been renamed QC-TEM.

Therefore it becomes possible to get indications on the turbulence regimes (ITG or TEM) by analyzing the fluctuation spectra.

The knowledge of QC-TEM was thus applied to investigate the role of TEM in the LOC-SOC transition. It shows that the disappearance of QC-TEM is (i) rather simultaneous to the LOC-SOC transition, (ii) rather global, i.e. it affects a large part of the plasma, (iii) it may occur first on the top of the torus before affecting the LFS, (iv) it can be correlated to intrinsic toroidal velocity bifurcation, which is not explained by neoclassical predictions. Another application using the QC signature of TEM was made

to study impurity transport in ECRH plasmas. The combination of results previously obtained with the one described in this thesis shows that the impurity diffusion depends on the electron temperature gradient only in a region dominated by TEM.

During these studies of TEM turbulence, transitions between QC-TEM and MHD modes have been observed in several tokamaks (Tore Supra, AUG, JET). It was shown that radial transition from QC-TEM toward MHD modes can occur while going toward the plasma center. Temporal interplay between QC-TEM and MHD modes have also been observed. They can be due to different drivers (sawtooth, magnetic shear) but they all indicate that QC-TEM and MHD are anti-correlated, and that QC-TEM fluctuations are delayed compared to MHD modes.

These multiple observations suggest that interactions between MHD and turbulent instabilities can be at play in the plasma core region.

7.2 Perspectives

Which limits for the QC signature of TEM instabilities ?

The comparison of frequency spectra from nonlinear simulations, reflectometry measurements and a synthetic diagnostic shows that TEM instability can have a QC signature contrary to ITG which show broadband spectra. This finding can then provide an additional indication on the dominant instability besides gyrokinetic simulations, transport analysis and phase velocity estimations. However, it has to be used cautiously for two reasons:

(i) the lack of QC-TEM does not necessarily imply that the TEM are stable as schematically shown in the figure below. First, the QC-TEM frequency depending on $v_{E\times B}$, if $v_{E\times B}$ is too low the QC-TEM peak may be close to zero frequency. Hence, the coherence spectra provided by poloidal correlation reflectometry can help discriminate QC-TEM in each low rotation plasma. Second, the QC signature of TEM may disappear in case of fully developed turbulence. In this case TEM would not remain oscillating at a rather well-defined frequency (i.e. with a narrow spectrum) but would become broad-band (such as ITG) as expected generally for a turbulent phenomena. Experimentally, the disappearance of QC-TEM has been observed while increasing ECRH power at high values [communication with V.A. Vershkov]. In gyrokinetic simulations, an artificial increase of R/L_{T_e} and R/L_{n_e} (with a constant gradient parameter $\eta_e = L_{n_e}/L_{T_e}$) in the LOC regime shows a broadening of the TEM spectra [Arnichand 2015a].

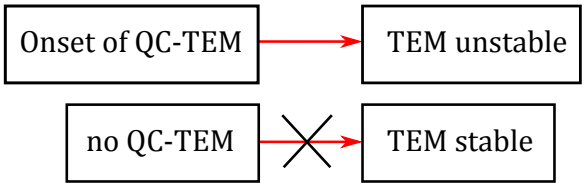

(ii) there are edge phenomena presently not attributed to TEM which can have a rather similar QC signature in H-mode [Diallo 2014, Wang 2014], enhanced D_α H-modes [Golfinopoulos 2014, LaBombard 2014] and I-mode [Cziegler 2013]. At the moment, there is no unified explanation for these modes which present rather similar QC spectral signatures. Several instabilities have been suggested to cause them but presently, none of these modes has been linked to TEM. Therefore, the observation of QC modes can be taken as an indication of TEM in the plasma core region only ($0.1 < r/a < 0.95$), where no other QC fluctuation phenomena have been reported.

Which diagnostics to observe QC-TEM ?

The diagnostics able to perform such a study require a sensitivity to low wavenumbers on the order of the ITG/TEM instabilities scale ($k_\theta \rho_i \leq 1$) and a capability to measure in the plasma core region. Apart from reflectometry [Krämer-Flecken 2004, Vershkov 2005, Arnichand 2014, Krämer-Flecken 2015], structures possibly similar to QC-TEM may have been observed in TEM-dominated regimes with phase contrast imaging (PCI), far infrared interferometry (FIR), beam emission spectroscopy (BES), Doppler backscattering (DBS) reflectometry, and correlation electron cyclotron emission (CECE) systems [White 2010b, White 2010a, Rice 2011a, Rice 2011b, Rice 2012, Rice 2013, Hillesheim 2013a, Hillesheim 2013b, Sarff 2015].

These studies have reported modifications of fluctuation spectra in TEM dominated regimes, without identifying a mode as being the signature of TEM. In view of the present results these spectral modifications could be revisited with dedicated studies to investigate whether BES, CECE, PCI, DBS and FIR can show similar QC-TEM phenomena.

In which fusion devices could QC-TEM be observed ?

This thesis reports observations of QC-TEM in Tore Supra, TEXTOR, JET and ASDEX-Upgrade but the onset of QC-TEM seems also possible in other fusion devices.

In stellarators, neoclassical effects represent a major transport mechanism. However, in modern stellarators the anomalous transport may be the primary cause of energy and particle losses. It has been suggested that TEM play a role [Guttenfelder 2008] in the Helically Symmetric eXperiment (HSX). Analytical studies [Proll 2012, Helander 2013] indicate that TEM can be stabilized in perfectly quasi-isodynamic stellarators, but it has been shown numerically [Proll 2013] that in Wendelstein 7-X (W7-X), a small fraction of the trapped orbits experiences bad average curvature, enhancing TEM. The finding of QC-TEM could indicate if TEM are unstable or not in W7-X and whether an optimized equilibrium stabilizes them [Proll 2015]. As in tokamaks, TEM should be located in the LFS region, but contrary to tokamaks the LFS regions of W7-X are toroidally shifted away from the regions of bad local curvature (where ITG modes should mainly be located) [see figure 7.1]. The turbulence regimes could thus be investigated with a PCR

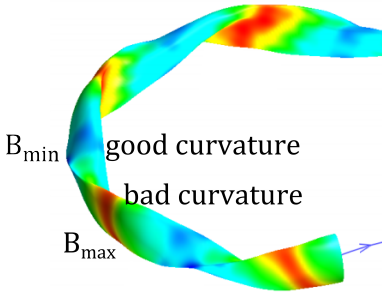

Figure 7.1: W7-X magnetic field with LFS in blue and HFS in red [Proll 2015].

system, which will operate in the bad curvature region of W7-X.

In Reversed field pinch (RFP), the recent measurements made in the Madison Symmetric Torus (MST) suggest that QC-TEM may also be observed. Indeed, they have shown a QC feature in fluctuation spectra [Sarff 2015] obtained by far infrared (FIR) interferometry at $r/a \approx 0.8$ and compared with gyrokinetic simulations. In the pulsed inductive current profile control (PPCD) where fluctuations similar to QC modes appear [see figure 7.2], gyrokinetic simulations predict the turbulence to be TEM-dominated, whereas in the standard plasmas, no QC-like feature appears. Therefore these observations are reminiscent of the ones related to QC-TEM.

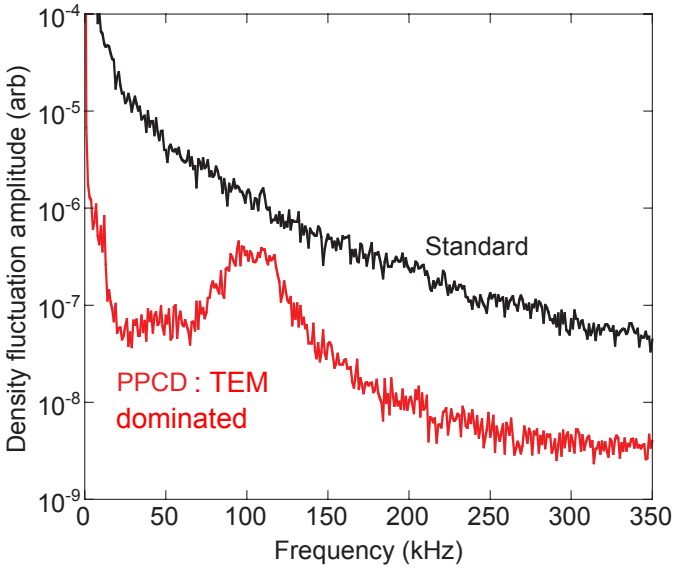

Figure 7.2: measurement made in the reversed field pinch MST in standard plasmas (black) and PPCD plasma dominated by TEM. Reproduced from [Sarff 2015].

The WEST project is a modification of the Tore Supra tokamak which will change the plasma from a circular to a D-shape. This will induce a reduction of the minor radius from 0.72 to 0.5 m in the equatorial plane, and an increase of the major radius from 2.4 until 2.5 m [see figure 7.3]. Thus the aspect ratio R_0/a will be increased from 3.3 up to ≈5 or 6, which is unusually high compared to present large tokamaks (to be compared

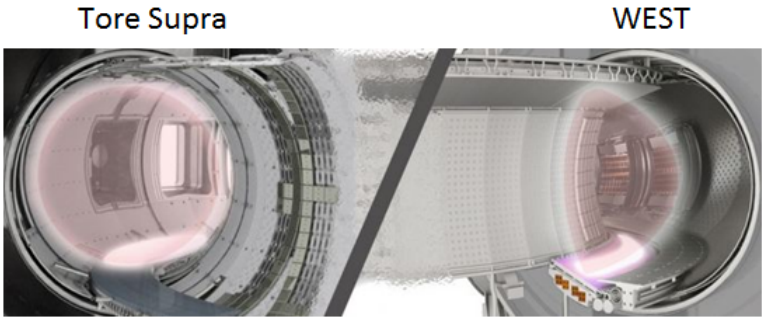

Figure 7.3: Tore Supra and the WEST configurations.

to ≈ 3 for AUG and JET). The trapped particles constitutes a $\sqrt{a/R_0}$ fraction of all particles, thus the amount of trapped particles should be substantially reduced in WEST.

As $\gamma_{TEM} \propto \sqrt{a/R_0}$, TEM are consequently expected to be more stable than in Tore Supra [Bourdelle 2015b]. This unique change of tokamak aspect ratio will allow to assess experimentally the geometric effects on confinement. The impact of the aspect ratio on the role of TEM could therefore be studied via an analysis including these results on QC-TEM.

In future tokamaks (Iter and beyond), a large amount of D-T fusion is expected to occur. Each reaction provides 17.6 MeV divided in 14.1 MeV for the neutrons and 3.5 MeV for the α-particles (producing P_α). Thus the fusion energy gain Q between the heat power P_{heat} and the fusion power becomes $Q = 5P_\alpha/P_{heat}$ which leads to the fraction of α-heating $f_\alpha = Q/(Q+5)$. Therefore f_α increases with the performance of the fusion devices. As the α particles lose their kinetic energy mainly by collisions with the electrons, the better the performance of a fusion device will be, the more the ratio T_i/T_e will decrease and the more the TEM could be unstable. Additionally the high temperatures required for fusion reactions will induce less collisional plasmas. Unlike the plasmas of the current devices which are often dominated by ITG modes, the plasma core region of the Iter tokamak could be more inclined to be dominated by TEM due to lower T_i/T_e and ν^*. These effects would be even more pronounced in a fusion reactor.

Toward the understanding of the other spectral components ?

As discussed in section 3.4.3, frequency fluctuation spectra show different types of components. The coherent modes are by far the most studied and understood (GAMs, MHD, etc.). This thesis has shown that QC modes observed in the plasma core region are a signature of TEM. From this study we can also learn some indications on other spectral components, namely the broadband fluctuations and the low frequency fluctuations.

Broadband fluctuation components are always observed in reflectometry measurements. Simulations have shown that frequency fluctuation spectra are broadband in case of ITG turbulence. However, as other instabilities may contribute to broadband spectra, which is usually taken as a signature of turbulence, a dedicated study is required. The indications obtained in this thesis could motivate future work to investigate the link be-

tween ITG and broadband spectra.

The low frequency fluctuations component has the following properties:

- Their amplitude is independent of the poloidal angle [see figure 3.18].
- Their radial delay time is zero and their radial correlation length is the longest of the spectral components [Vershkov 2005].

Additionally, during this thesis it has been noticed that low frequency fluctuations very often appear with QC-TEM. This can be seen in most of the spectra showing QC-TEM in this manuscript, but also for example in the spectra from an RFP device shown previously in figure 7.2. Frequency fluctuation spectra from nonlinear gyrokinetic simulations also show a Zonal Flow (ZF) peak around the zero frequency.

Regarding these findings and the properties listed above, the possibility for LF fluctuations to be due to ZFs [Diamond 2005] can be investigated in future studies. The two major issues which do not support a link between ZFs and low frequency fluctuations are that (i) ZFs are expected at zero frequency, therefore should in principle not be observed with reflectometry and (ii) ZFs are not seen in the fluctuation spectra of the synthetic diagnostic. However, their spectral signature is reminiscent of the ZFs reported with probes at the plasma edge [Xu 2003] [see figure 7.4].

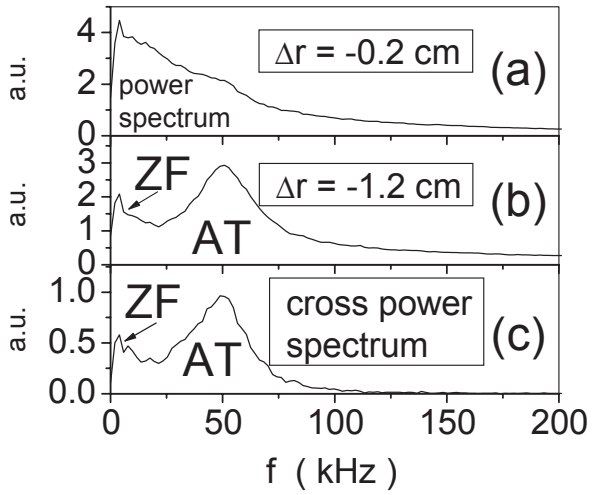

Figure 7.4: Measurement made in HT-7 Tokamak with Langmuir probes close to the separatrix. Reproduced from [Xu 2003].

Appendix A

Asymmetries of reflectometry frequency spectra

At least a small spectral asymmetry is always observed in reflectometry spectra. Their causes [Conway 1999] have already been discussed in the section 3.4.2.1. It has been described that they can arise either (i) from a Doppler effect acting on the backscattered signal or (ii) from a difference between the phase increment/decrement of the reflected signal. Note that they may also be due to other phenomena not discussed here such as the nonlinear response of the reflectometer.

Asymmetry due to a Doppler effect on the backscattered signal

This phenomena is well known and is at the origin of the DBS reflectometry discussed in section 3.1.3 which voluntary uses inclined antennas. Its effect on non-DBS reflectometry spectra was previously investigated in [Hornung 2013a]. It even allows to perform radial electric field estimations with conventional reflectometers used as a DBS reflectometers [Sirinelli 2013, Hillesheim 2015]. Thus a part of the received signal may come from the DBS signal, and be mixed with the reflected one.

Such a Doppler effects can very often be at play on the signal of a conventional reflectometer. However, its effect may be limited excepted if some conditions are fulfilled (i.e. Doppler effect are not expected to be pronounced for a normal operation of such a diagnostic). The following effects can contribute:

- **Vertical shift of the plasma**[1]: This is highlighted in figure A.1 between the red and the blue points measured for a plasma vertically shifted by 4 and 7 cm, respectively. The reflectometry spectra have been decomposed (as described in section 3.4.3) to plot the frequency center of the broadband as a function of the radius. The broadband spectra are usually centered at $f \approx 0$ kHz thus frequency center at $f >> 0$ or $f << 0$ is an indication of a spectral asymmetry. As shown in figure A.1, the higher the vertical displacement, the more pronounced the asymmetry.

[1] Note that a reflectometer antenna not properly aligned may produce an equivalent phenomena even for a well centered plasma.

- **Magnetic ripple on the LFS**: Figure A.1 also shows this effect which is always very pronounced on the LFS of the Tore Supra fixed-frequency reflectometer. While going toward the LFS, the asymmetry of the spectra always increases. In this case it can be observed for both values of the vertical displacements. Due to the ripple, the direction perpendicular to the magnetic flux may be inclined compared to the probing wave.

These two phenomena are reported in the present section because they have been observed during this thesis. However, the possible reasons for a Doppler effect on conventional reflectometry spectra may not be restricted to them and other phenomena may contribute to the spectral asymmetry such as the sawteeth effects.

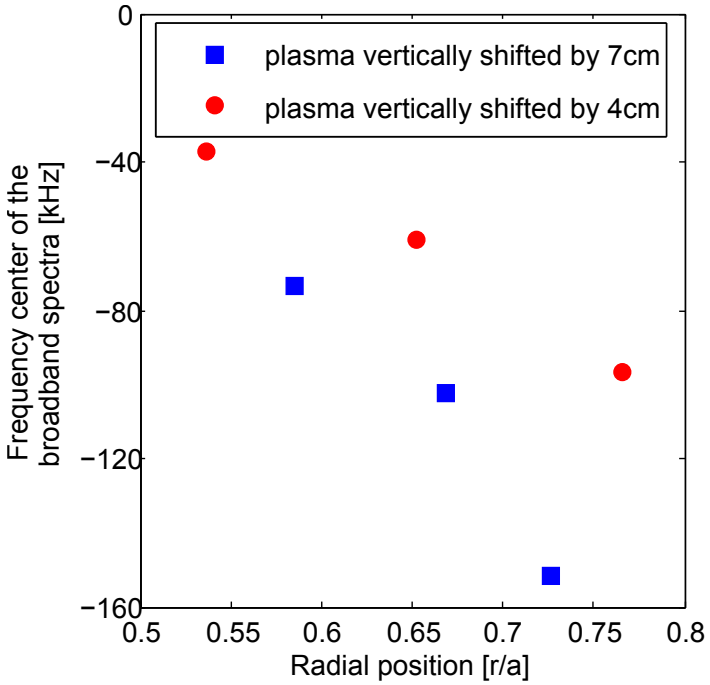

Figure A.1: Frequency center of the broadband spectra measured in Tore Supra for different radii and different vertical shifts of the plasma highlighting the asymmetry due to a Doppler effect, which increases while going toward the edge (due to the magnetic field ripple), and while changing the plasma position (vertical shift) in Tore Supra.

Interestingly, the spectral asymmetry often reverses at the plasma center. As shown in figure A.2 where two Tore Supra spectra measured at the same radius ($r/a \approx 0.3$) on the LFS and the HFS can be compared. The spectra measured on the LFS and the HFS have a more pronounced negative and positive frequencies, respectively.

Asymmetry due to a tilt of the eddies

The spectral asymmetries due to the Doppler effect have been studied, but from our knowledge the effects of a tilt of the eddies have not been demonstrated. It is illustrated in figure A.3 where the reflectometer antenna probing the plasma is on the right-hand side of

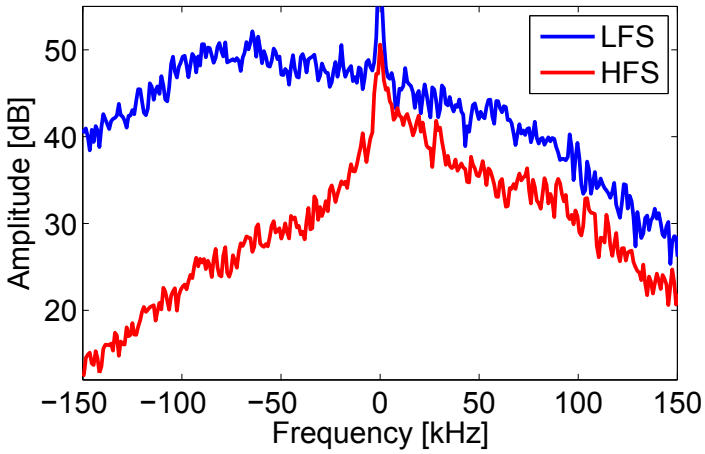

Figure A.2: Reflectometry spectra from the Tore Supra discharge #41012 measured at $r/a \approx 0.3$ on the LFS and the HFS.

the plot (similarly to figure 3.14). Due to the different eddies inclinations schematically shown, in (a) the spectral asymmetry would be expected in the positive frequencies, whereas in (b) it would be expected in the negative frequencies.

The tilt of the eddies could always be at play and thus explain the spectral asymmetry observed in the synthetic reflectometer diagnostic (see section 4.3.3.2). Indeed the latter probes the plasma perfectly perpendicularly to the reflection layer, thus a Doppler effect would not be expected. Note that in case of structure long enough, tilts of the eddies could also induce a Doppler effect via the deformation of the reflection layer they could produce (locally, the probing wave would not arrive perpendicularly to the cutoff layer).

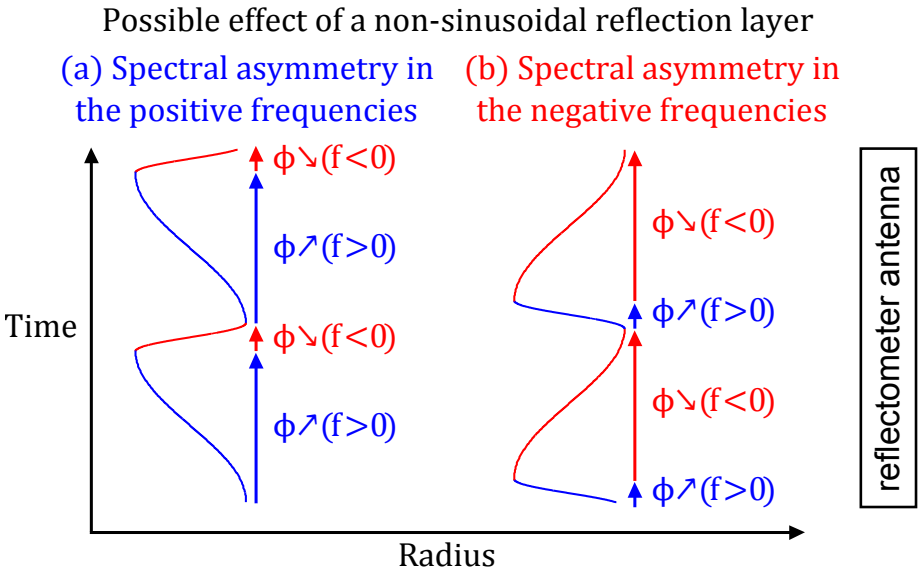

Figure A.3: Effects of a non sinusoidal reflection layer on the evolution of the phase inducing spectral asymmetries in (a) the positive frequencies and (b) the negative frequencies. Phase increments and decrements are shown in blue and red respectively.

Appendix B

Edge QC modes and Tungsten accumulation in JET hybrid scenarios

As previously discussed in the section 7.2, fluctuations rather similar to QC-TEM can be observed at the edge of several advanced regimes. These edge QC modes are not attributed to TEM, they are not understood at the moment and several instabilities have been suggested to cause them.

In JET, the performance of all the discharges are affected by the accumulation of tungsten in the plasma core. Radiations result from this accumulation, which decreases the plasma temperature and which can even lead to disruptions induced by a radiative collapse.

One of the current experimental technique to diagnose the tungsten accumulation is to measure the soft X-rays (SXR) emissions. Recently, simulations have identified neoclassical transport as the dominant mechanism responsible for tungsten accumulation in the plasma core region [Casson 2015].

This section reports reflectometry and SXR measurements made in the JET discharge (#84806). This discharge has been selected because it has reached the JET record of neutron rate in Iter-like wall, but note that similar observations have been made in the other discharges of this series and in other shots such as #82794 or #83533. Note that these discharges include high and low triangularity plasmas, and that they are always in the so-called hybrid scenario[1].

The behavior of the SXR emissions can be distinguished in two parts:

- During the first part (up to $t \approx 6.6$s), figures B.1 and B.2 show that the increase of the SXR amplitude is rather linear and remains maximum on the LFS (around the chord number 25).
- Then, figure B.1 shows that the increase of the SXR amplitude becomes non-linear. Additionally, for $t > 6.7$s the maximum of the SXR emission is observed on central chords (for the chord numbers 19-20) as shown in figures B.1 and B.2.

In the hybrid scenario, such abrupt change from a rather linear increase of the SXR emission toward a more chaotic one is very often observed. The central SXR emission is also common to most of the JET discharges.

[1] Hybrid scenario are characterized by high β plasmas, moderated magnetic fields and a flat q-profile in the inner part of the radius ($r/a < 0.5$)

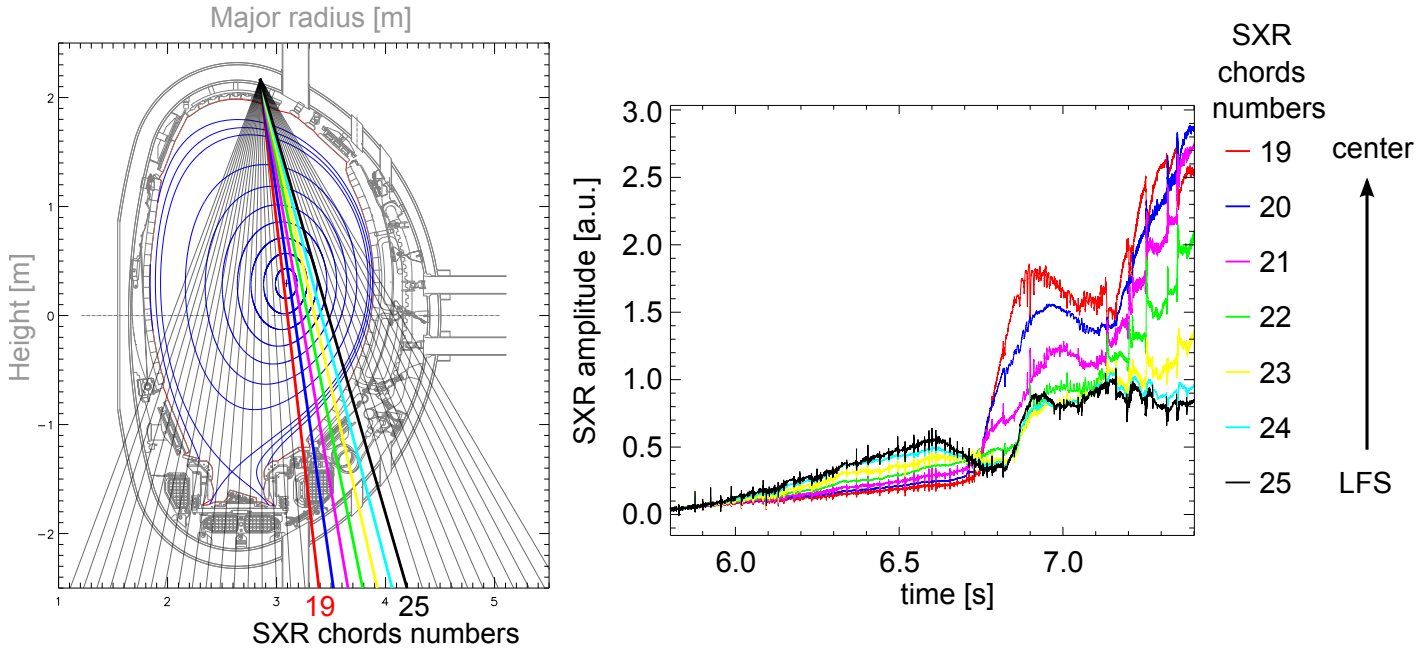

Figure B.1: Amplitude of the SXR signal in JET shot #84806 as a function of time for 6 SXR chords: 19 corresponds to the most central one, and 25 to the outer one.

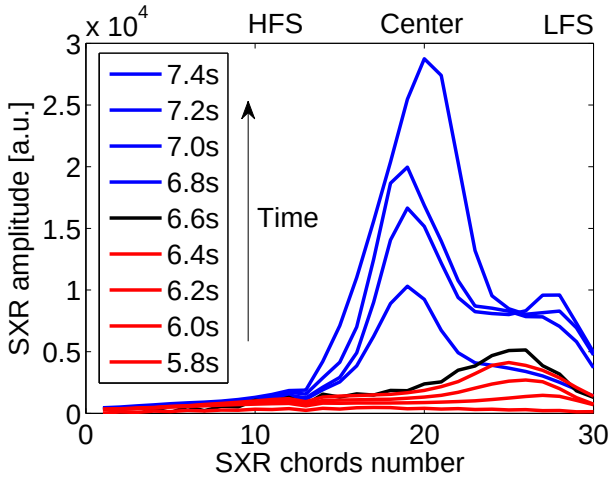

Figure B.2: Amplitude of SXR emissions for each SXR chord at different times of JET shot #84806.

Looking at the reflectometry spectra measured at $R \approx 3.8$ m, clear differences are observed between both time intervals. This is shown in figure B.3 where the following observations can be made:

- For $t \leq 6.6$s, clear QC modes are observed.
- At $t = 6.6$s, the QC modes become barely observable.
- For $t \geq 6.8$s, the spectra is broadband and additionally, some coherent modes which could be due to MHD activity are observed.

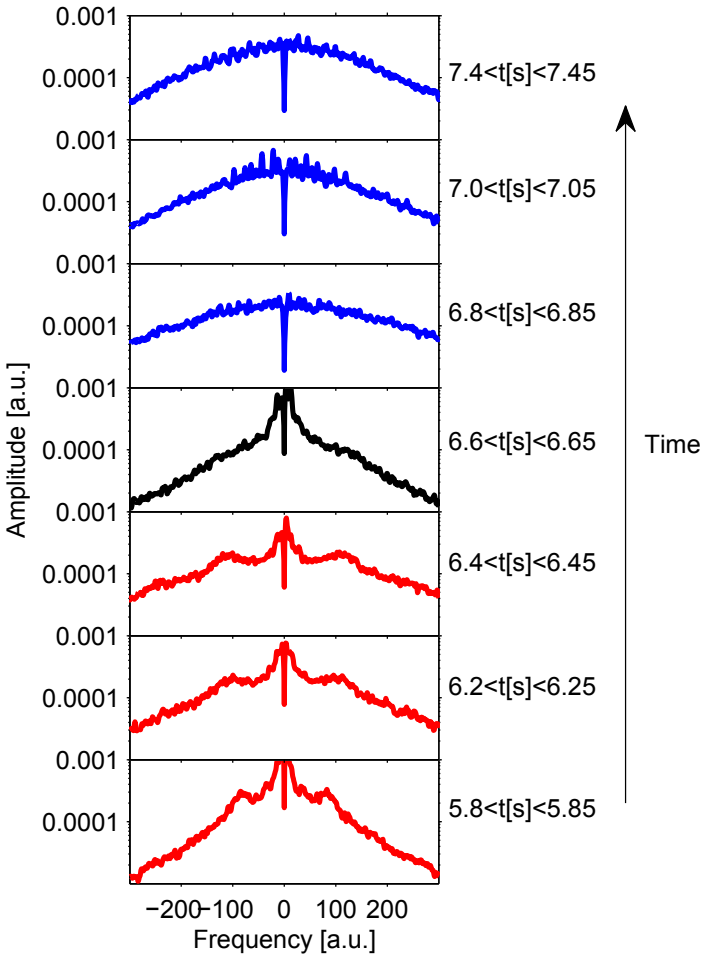

Figure B.3: Reflectometry spectra measured on the LFS in JET shot #84806 at $R \approx 3.8$ m for different times.

Thus in this type of discharges, the phase of low SXR emission - where the later increases rather linearly - is correlated to the observation of QC modes at the plasma edge. A change in the frequency spectra occurs for $6.4 < t[\mathrm{s}] < 6.6$, before that the SXR emission becomes peaked at the central lines ($t > 6.7$s). In this second phase, broadband spectra are observed (with possibly some MHD modes), and the increase of the SXR emissions becomes nonlinear.

These measurements suggest that changes of fluctuations occur prior to change of tungsten accumulation, but a more detailed study would be required to extract from the SXR emission a poloidal map of the tungsten concentration. Additionally, reflectometry measurements at different radii for a large set of JET discharges would be required to go deeper in the fluctuations analysis.

A hint of interpretation could be the following: it is known that the tungsten convection is very sensitive to the main ion gradients which can become inward under certain conditions. Therefore, a change of turbulence could indirectly influence the tungsten accumulation via modifications of the main ion density profiles acting on the neoclassical transport.

Bibliography

[Angioni 2005] C. Angioni, A. G. Peeters, F. Ryter, F. Jenko, G. D. Conway, T. Dannert, H. U. Fahrbach, M. Reich, W. Suttrop and L. Fattorini. *Relationship between density peaking, particle thermodiffusion, Ohmic confinement, and microinstabilities in ASDEX Upgrade L -mode plasmas.* Physics of Plasmas, vol. 12, page 040701, 2005.

[Angioni 2009] C Angioni, E Fable, M Greenwald, M Maslov, A G Peeters, H Takenaga and H Weisen. *Particle transport in tokamak plasmas, theory and experiment.* Plasma Physics and Controlled Fusion, vol. 51, page 124017, 2009.

[Angioni 2011] C. Angioni, R. M. McDermott, F. J. Casson, E. Fable, A. Bottino, R. Dux, R. Fischer, Y. Podoba, T. Pütterich, F. Ryter and E. Viezzer. *Intrinsic Toroidal Rotation, Density Peaking, and Turbulence Regimes in the Core of Tokamak Plasmas.* Phys. Rev. Lett., vol. 107, page 215003, 2011.

[Angioni 2012] C. Angioni, Y. Camenen, F.J. Casson, E. Fable, R.M. McDermott, A.G. Peeters and J.E. Rice. Nuclear Fusion, vol. 52, no. 11, page 114003, 2012.

[Arnichand 2014] H. Arnichand, R. Sabot, S. Hacquin, A. Krämer-Flecken, X. Garbet, J. Citrin, C. Bourdelle, G. Hornung, J. Bernardo, C. Bottereau, F. Clairet, G. Falchetto and J.C. Giacalone. *Quasi-coherent modes and electron-driven turbulence.* Nuclear Fusion, vol. 54, page 123017, 2014.

[Arnichand 2015a] H. Arnichand, J. Citrin, S. Hacquin, R. Sabot, A. Krämer-Flecken, X. Garbet, C. Bourdelle, C. Bottereau, F. Clairet, J.C. Giacalone, Z.O. Guimar aes Filho, R. Guirlet, G. Hornung, A. Lebschy, P. Lotte, P. Maget, A. Medvedeva, D. Molina, V. Nikolaeva, D. Prisiazhniuk, the Tore Supra team and the ASDEX Upgrade team. *Identification of Trapped Electron Modes in fluctuation spectra.* 42th European Physical Society Conference on Plasma Physics, Lisbon, Portugal, 2015.

[Arnichand 2015b] H. Arnichand, R. Sabot, S. Hacquin, A. Krämer-Flecken, C. Bourdelle, J. Citrin, X. Garbet, J.C. Giacalone, R. Guirlet, J.C. Hillesheim and L. Meneses. *Discriminating the trapped electron modes contribution in density fluctuation spectra.* Nuclear Fusion, vol. 55, no. 9, page 093021, 2015.

[Artaud 2010] J.F. Artaud, V. Basiuk, F. Imbeaux, M. Schneider, J. Garcia, G. Giruzzi, P. Huynh, T. Aniel, F. Albajar, J.M. Ané, A. Bécoulet, C. Bourdelle, A. Casati, L. Colas, J. Decker, R. Dumont, L.G. Eriksson, X. Garbet, R. Guirlet, P. Hertout, G.T. Hoang, W. Houlberg, G. Huysmans, E. Joffrin, S.H. Kim, F. Köchl, J. Lister, X. Litaudon, P. Maget, R. Masset, B. Pégourié, Y. Peysson, P. Thomas, E. Tsitrone and F. Turco. *The CRONOS suite of codes for integrated tokamak modelling.* Nuclear Fusion, vol. 50, no. 4, page 043001, 2010.

[Berenger 1994] Jean-Pierre Berenger. *A perfectly matched layer for the absorption of electromagnetic waves.* Journal of Computational Physics, vol. 114, page 185, 1994.

[Bernardo 2012] J. Bernardo, C. Fenzi, C. Bourdelle, T. Aniel, J.-F. Artaud, J. Gunn, F. Clairet, P. Lotte, S. Cortes, J. P. S. Bizarro and the Tore Supra team. *39th EPS Conference.* Stockholm, Sweden, 2012.

[Bernardo 2015] J Bernardo, C Fenzi, C Bourdelle, Y Camenen, H Arnichand, João P S Bizarro, S Cortes, X Garbet, Z O Guimarães-Filho, T Aniel, J-F Artaud, F Clairet, P Cottier, J Gunn, P Lotte and the Tore Supra Team. *Density impact on toroidal rotation in Tore Supra: experimental observations and theoretical investigation.* Plasma Physics and Controlled Fusion, vol. 57, page 035002, 2015.

[Besnard 2007] D. Besnard. *The megajoule laser program - ignition at hand.* The European Physical Journal D, vol. 44, page 207, 2007.

[Bierwage 2005] Andreas Bierwage, Sadruddin Benkadda, Satoshi Hamaguchi and Masahiro Wakatani. *Fast growing double tearing modes in a tokamak plasma.* Physics of Plasmas, vol. 12, page 082504, 2005.

[Blanco 2013] E Blanco and T Estrada. *Two-dimensional full-wave simulations of radial correlation Doppler reflectometry in linear and non-linear regimes.* Plasma Physics and Controlled Fusion, vol. 55, page 125006, 2013.

[Bonanomi 2015] N. Bonanomi, P Mantica and J. Citrin. *submitted to Nuclear Fusion.* 2015.

[Bortolon 2006] A. Bortolon, B. P. Duval, A. Pochelon and A. Scarabosio. *Observation of Spontaneous Toroidal Rotation Inversion in Ohmically Heated Tokamak Plasmas.* Phys. Rev. Lett., vol. 97, page 235003, 2006.

[Bottollier-Curtet 1987] H. Bottollier-Curtet and G. Ichtchenko. *Microwave reflectometry with the extraordinary mode on tokamaks: Determination of the electron density profile of Petula-B.* Review of Scientific Instruments, vol. 58, page 539, 1987.

[Bourdelle 2000] C Bourdelle. *Analyse de stabilité de plasmas de tokamak.* PhD thesis, 2000.

[Bourdelle 2002] C. Bourdelle, X. Garbet, G.T. Hoang, J. Ongena and R.V. Budny. *Stability analysis of improved confinement discharges: internal transport barriers in Tore Supra and radiative improved mode in TEXTOR.* Nuclear Fusion, vol. 42, page 892, 2002.

[Bourdelle 2005] C Bourdelle. *Turbulent particle transport in magnetized fusion plasma.* Plasma Physics and Controlled Fusion, vol. 47, page A317, 2005.

[Bourdelle 2007] C. Bourdelle, X. Garbet, F. Imbeaux, A. Casati, N. Dubuit, R. Guirlet and T. Parisot. *A new gyrokinetic quasilinear transport model applied to particle transport in tokamak plasmas.* Physics of Plasmas, vol. 14, page 112501, 2007.

[Bourdelle 2015a] C. Bourdelle. Hdr thesis: Turbulent transport in tokamak plasmas: bridging theory and experiment. Aix Marseille Université, 2015.

[Bourdelle 2015b] C. Bourdelle, J.F. Artaud, V. Basiuk, M. Bécoulet, S. Brémond, J. Bucalossi, H. Bufferand, G. Ciraolo, L. Colas, Y. Corre, X. Courtois, J. Decker, L. Delpech, P. Devynck, G. Dif-Pradalier, R.P. Doerner, D. Douai, R. Dumont, A. Ekedahl, N. Fedorczak, C. Fenzi, M. Firdaouss, J. Garcia, P. Ghendrih, C. Gil, G. Giruzzi, M. Goniche, C. Grisolia, A. Grosman, D. Guilhem, R. Guirlet, J. Gunn, P. Hennequin, J. Hillairet, T. Hoang, F. Imbeaux, I. Ivanova-Stanik, E. Joffrin, A. Kallenbach, J. Linke, T. Loarer, P. Lotte, P. Maget, Y. Marandet, M.L. Mayoral, O. Meyer, M. Missirlian, P. Mollard, P. Monier-Garbet, P. Moreau, E. Nardon, B. Pégourié, Y. Peysson, R. Sabot, F. Saint-Laurent, M. Schneider, J.M. Travère, E. Tsitrone, S. Vartanian, L. Vermare, M. Yoshida, R. Zagorski and JET Contributors. *WEST Physics Basis.* Nuclear Fusion, vol. 55, page 063017, 2015.

[BP 2014] Statistical review of world energy. British Petroleum, 2014.

[Brower 1987] D. L. Brower, W. A. Peebles, S. K. Kim, N. C. Luhmann, W. M. Tang and P. E. Phillips. *Observation of a high-density ion mode in tokamak microturbulence.* Phys. Rev. Lett., vol. 59, page 48, 1987.

[Casati 2008] Alessandro Casati, C. Bourdelle, X. Garbet and F. Imbeaux. *Temperature ratio dependence of ion temperature gradient and trapped electron mode instability thresholds.* Physics of Plasmas, vol. 15, page 042310, 2008.

[Casati 2009] A. Casati, T. Gerbaud, P. Hennequin, C. Bourdelle, J. Candy, F. Clairet, X. Garbet, V. Grandgirard, Ö. D. Gürcan, S. Heuraux, G. T. Hoang, C. Honoré, F. Imbeaux, R. Sabot, Y. Sarazin, L. Vermare and R. E. Waltz. *Turbulence in the TORE SUPRA Tokamak: Measurements and Validation of Nonlinear Simulations.* Phys. Rev. Lett., vol. 102, page 165005, Apr 2009.

[Casati 2012] A. Casati. *A quasi-linear gyrokinetic transport model for tokamak plasmas.* PhD thesis, 2012.

[Casson 2015] F J Casson, C Angioni, E A Belli, R Bilato, P Mantica, T Odstrcil, T Pütterich, M Valisa, L Garzotti, C Giroud, J Hobirk, C F Maggi, J Mlynar and M L Reinke. *Theoretical description of heavy impurity transport and its application to the modelling of tungsten in JET and ASDEX upgrade.* Plasma Physics and Controlled Fusion, vol. 57, page 014031, 2015.

[Citrin 2014] J. Citrin, H. Arnichand, C. Bourdelle, J. Bernardo, X. Garbet, S. Hacquin and R. Sabot. *Progress in understanding quasi-coherent modes through gyrokinetic simulation.* Joined US-EU TTF workshop, Culham, United Kingdom, 2014.

[Clairet 2010] F. Clairet, S. Heuraux, C. Bottereau, D. Molina, L. Ducobu, F. Leroux and A. Barbuti. Review of Scientific Instruments, vol. 81, no. 10, page 10D903, 2010.

[Coelho 2013] R. Coelho, S. Äkäslompolo, A. Dinklage, A. Kus, R. Reimer, E. Sundén, S. Conroy, E. Blanco, G. Conway, S. Hacquin, S. Heuraux, C. Lechte, F. Da Silva, A. Sirinelli and ITM-TF Contributors. *Synthetic Diagnostics in the European Union Integrated Tokamak Modelling Simulation Platform.* Fusion Science and Technology, vol. 63, page 1, 2013.

[Cohen 1998] Bruce I Cohen, Lynda L LoDestro, E Bickford Hooper and Thomas A Casper. *Simulations of broadband short-pulse reflectometry for diagnosing plasma density and magnetic-field profiles.* Plasma Physics and Controlled Fusion, vol. 40, page 75, 1998.

[Colas 1998] L. Colas, X.L. Zou, M. Paume, J.M. Chareau, L. Guiziou, G.T. Hoang, Y. Michelot and D. Grésillon. *Internal magnetic fluctuations and electron heat transport in the Tore Supra tokamak: Observation by cross-polarization scattering.* Nuclear Fusion, vol. 38, page 903, 1998.

[communication with V.A. Vershkov] Private communication with V.A. Vershkov.

[Connor 1973] J.W. Connor and R.J. Hastie. *Neoclassical diffusion arising from magnetic-field ripples in Tokamaks.* Nuclear Fusion, vol. 13, page 221, 1973.

[Connor 2006] J W Connor, R J Hastie and P Helander. *Stability of the trapped electron mode in steep density and temperature gradients.* Plasma Physics and Controlled Fusion, vol. 48, page 885, 2006.

[Conway 1999] G D Conway. *Effects of reflectometer asymmetries on fluctuation measurements.* Plasma Physics and Controlled Fusion, vol. 41, page 65, 1999.

[Conway 2002] G D Conway, G M D Hogeweij, M R de Baar, Yu Baranov, R Barnsley, N C Hawkes, X Litaudon, J Mailloux, E Righi, F G Rimini and K-D Zastrow. *Turbulence behaviour during electron heated reversed shear discharges in JET.* Plasma Physics and Controlled Fusion, vol. 44, page 1167, 2002.

[Conway 2004a] G D Conway, J Schirmer, S Klenge, W Suttrop, E Holzhauer and the ASDEX Upgrade Team. *Plasma rotation profile measurements using Doppler reflectometry.* Plasma Physics and Controlled Fusion, vol. 46, no. 6, page 951, 2004.

[Conway 2004b] G D Conway, J Schirmer, S Klenge, W Suttrop, E Holzhauer and the ASDEX Upgrade Team. *Plasma rotation profile measurements using Doppler reflectometry.* Plasma Physics and Controlled Fusion, vol. 46, page 951, 2004.

[Conway 2005] G D Conway, B Scott, J Schirmer, M Reich, A Kendl and the ASDEX Upgrade Team. *Direct measurement of zonal flows and geodesic acoustic mode oscillations in ASDEX Upgrade using Doppler reflectometry.* Plasma Physics and Controlled Fusion, vol. 47, no. 8, page 1165, 2005.

[Conway 2006] G.D. Conway, C. Angioni, R. Dux, F. Ryter, A.G. Peeters, J. Schirmer, C. Troester, CFN Reflectometry Group and the ASDEX Upgrade team. *Observations on core turbulence transitions in ASDEX Upgrade using Doppler reflectometry.* Nuclear Fusion, vol. 46, page S799, 2006.

[Coppi 1967] B. Coppi, M. N. Rosenbluth and R. Z. Sagdeev. *Instabilities due to Temperature Gradients in Complex Magnetic Field Configurations.* Physics of Fluids, vol. 10, no. 3, page 582, 1967.

[Cupido 2013] L. Cupido and L. Meneses. *Recent Hardware developments on synthetized sources for reflectometry hopping systems at IPFN.* 11th International Reflectometry Workshop (IRW11), Ecole Polytechnique, Palaiseau, France, 2013.

[Cziegler 2013] I. Cziegler, P. H. Diamond, N. Fedorczak, P. Manz, G. R. Tynan, M. Xu, R. M. Churchill, A. E. Hubbard, B. Lipschultz, J. M. Sierchio, J. L. Terry and C. Theiler. *Fluctuating zonal flows in the I-mode regime in Alcator C-Mod.* Physics of Plasmas, vol. 20, page 055904, 2013.

[Da Graça 2013] S. Da Graça, G.D. Conway, E. Viezzer, A. Silva, L Cupido, M E Manso and the ASDEX Upgrade Team. *Poloidal velocity of MHD modes at the edge of the ASDEX Upgrade tokamak.* 40th EPS Conference, Espoo, Finland, 2013.

[da Silva 2005] F. da Silva, S. Heuraux, S. Hacquin and M.E. Manso. *Unidirectional transparent signal injection in finite-difference time-domain electromagnetic codes - application to reflectometry simulations.* Journal of Computational Physics, vol. 203, page 467, 2005.

[Depret 2000] G Depret, X Garbet, P Bertrand and A Ghizzo. *Trapped-ion driven turbulence in tokamak plasmas.* Plasma Physics and Controlled Fusion, vol. 42, page 949, 2000.

[Diallo 2014] A. Diallo, W. Hughes J. M. Greenwald, B. LaBombard, E. Davis, S-G. Baek, C. Theiler, P. Snyder, J. Canik, J. Walk, T. Golfinopoulos, J. Terry, M. Churchill, A. Hubbard, M. Porkolab, L. Delgado-Aparicio, L. Reinke M. A. White and Alcator C-Mod team. *Observation of Edge Instability Limiting the Pedestal Growth in Tokamak Plasmas.* Phys. Rev. Lett., vol. 112, page 115001, 2014.

[Diamond 2005] P H Diamond, S-I Itoh, K Itoh and T S Hahm. Plasma Physics and Controlled Fusion, vol. 47, 2005.

[Dif-Pradalier 2008] G. Dif-Pradalier. *First-principle description of collisional gyrokinetic turbulence in tokamak plasmas.* PhD thesis, 2008.

[Dorland 2000] W. Dorland, F. Jenko, M. Kotschenreuther and B. N. Rogers. *Electron Temperature Gradient Turbulence.* Phys. Rev. Lett., vol. 85, page 5579, 2000.

[Drake 1988] J. F. Drake, P. N. Guzdar and A. B. Hassam. *Streamer Formation in Plasma with a Temperature Gradient.* Phys. Rev. Lett., vol. 61, page 2205, 1988.

[Dumont 2014] R J Dumont, M Goniche, A Ekedahl, B Saoutic, J-F Artaud, V Basiuk, C Bourdelle, Y Corre, J Decker, D Elbèze, G Giruzzi, G-T Hoang, F Imbeaux, E Joffrin, X Litaudon, Ph Lotte, P Maget, D Mazon, E Nilsson and The Tore Supra Team. *Multi-megawatt, gigajoule plasma operation in Tore Supra.* Plasma Physics and Controlled Fusion, vol. 56, page 075020, 2014.

[Duval 2008] B. P. Duval, A. Bortolon, A. Karpushov, R. A. Pitts, A. Pochelon, O. Sauter, A. Scarabosio, G. Turri and the TCV Team. *Spontaneous L-mode plasma rotation scaling in the TCV tokamak.* Physics of Plasmas, vol. 15, 2008.

[Efthimion 1999] P.C. Efthimion, S. Von Goeler, W.A. Houlberg, E.J. Synakowski, M.C. Zarnstorff, S.H. Batha, R.E. Bell, M. Bitter, C.E. Bush, F.M. Levinton, E. Mazzucato, D.C. McCune, D. Mueller, H.K. Park, A.T. Ramsey, A.L. Roquemore and G. Taylor. *Observation of neoclassical transport in reverse shear plasmas on TFTR.* Nuclear Fusion, vol. 39, no. 11Y, page 1905, 1999.

[Fenzi 2011] C. Fenzi, X. Garbet, E. Trier, P. Hennequin, C. Bourdelle, T. Aniel, G. Colledani, P. Devynck, C. Gil, Ö. Gürcan, L. Manenc, M. Schneider, J.-L. Segui and the Tore Supra team. *On plasma rotation with toroidal magnetic field ripple and no external momentum input.* Nuclear Fusion, vol. 51, no. 10, page 103038, 2011.

[Frish 1995] U. Frish. Turbulence: The legacy of a. n. kolmogorov. Cambridge University Press, 1995.

[Fujisawa 2009] Akihide Fujisawa. Nuclear Fusion, vol. 49, page 013001 (42pp), 2009.

[Furth 1963] H. P. Furth, J. Killeen and M. N. Rosenbluth. *Finite resistive instability of a sheet pinch.* Physics of Fluids, vol. 6, page 459, 1963.

[G. Giruzzi 2009] G. T. Hoang F. Imbeaux X. Litaudon P. Maget Y. Peysson G. Giruzzi C. Bourdelle. *Physics of Discharges with Vanishing Loop Voltage.* Fusion Science and Technology, vol. 56, page 1381, 2009.

[Gao 2014] C. Gao, J.E. Rice, H.J. Sun, M.L. Reinke, N.T. Howard, D. Mikkelson, A.E. Hubbard, M.A. Chilenski, J.R. Walk, J.W. Hughes, P.C. Ennever, M. Porkolab, A.E. White, C. Sung, L. Delgado-Aparicio, S.G. Baek, W.L. Rowan, M.W. Brookman, M.J. Greenwald, R.S. Granetz, S.W. Wolfe, E.S. Marmar and The Alcator C-Mod Team. *Non-local heat transport in Alcator C-Mod ohmic L-mode plasmas.* Nuclear Fusion, vol. 54, page 083025, 2014.

[Garbet 1992] X. Garbet, J. Payan, C. Laviron, P. Devynck, S.K. Saha, H. Capes, X.P. Chen, J.P. Coulon, C. Gil, G.R. Harris, T. Hutter, A.-L. Pecquet, A. Truc, P. Hennequin, F. Gervais and A. Quemeneur. *Turbulence and energy confinement in TORE SUPRA Ohmic discharges.* Nuclear Fusion, vol. 32, page 2147, 1992.

[Garbet 1996] X. Garbet and R. E. Waltz. *Action at distance and Bohm scaling of turbulence in tokamaks.* Physics of Plasmas, vol. 3, page 1898, 1996.

[Garbet 2001] X. Garbet. Instabilitiés, turbulence, et transport dans un plasma magnétisé. Aix Marseille Université, 2001.

[Garbet 2003] X. Garbet, L. Garzotti, P. Mantica, H. Nordman, M. Valovic, H. Weisen and C. Angioni. *Turbulent Particle Transport in Magnetized Plasmas.* Phys. Rev. Lett., vol. 91, page 035001, 2003.

[Garbet 2004] X Garbet, P Mantica, C Angioni, E Asp, Y Baranov, C Bourdelle, R Budny, F Crisanti, G Cordey, L Garzotti, N Kirneva, D Hogeweij, T Hoang, F Imbeaux, E Joffrin, X Litaudon, A Manini, C McDonald, H Nordman, V Parail, A Peeters, F Ryter, C Sozzi, M Valovic, T Tala, A Thyagaraja, I Voitsekhovitch, J Weiland, H Weisen and A Zabolotsky. *Physics of transport in tokamaks.* Plasma Physics and Controlled Fusion, vol. 46, page B557, 2004.

[Garbet 2009] X. Garbet. *Introduction to the Theory of Confinement.* ITER School, 2009.

[Garbet 2010a] X. Garbet, J. Abiteboul, E. Trier, Ö Gürcan, Y. Sarazin, A. Smolyakov, S. Allfrey, C. Bourdelle, C. Fenzi, V. Grandgirard, P. Ghendrih and P. Hennequin. *Entropy production rate in tokamaks with nonaxisymmetric magnetic fields.* Physics of Plasmas, vol. 17, no. 7, page 072505, 2010.

[Garbet 2010b] X. Garbet, Y. Idomura, L. Villard and T.H. Watanabe. *Gyrokinetic simulations of turbulent transport.* Nuclear Fusion, vol. 50, page 043002, 2010.

[George] William K. George. Lectures in turbulence for the 21st century.

[Gerbaud 2006] T Gerbaud. *Étude de la microturbulence par réflectométrie dans un plasma de fusion sur le tokamak Tore-Supra.* PhD thesis, 2006.

[Girardo 2014] Jean-Baptiste Girardo, David Zarzoso, Rémi Dumont, Xavier Garbet, Yanick Sarazin and Sergei Sharapov. *Relation between energetic and standard geodesic acoustic modes.* Physics of Plasmas, vol. 21, page 092507, 2014.

[Golfinopoulos 2014] T. Golfinopoulos, B. LaBombard, R. R. Parker, W. Burke, E. Davis, R. Granetz, M. Greenwald, J. Irby, R. Leccacorvi, E. Marmar, W. Parkin, M. Porkolab, J. Terry, R. Vieira, S. Wolfe and Alcator C-Mod team. *External excitation of a short-wavelength fluctuation in the Alcator C-Mod edge plasma and its relationship to the quasi-coherent mode.* Physics of Plasmas, vol. 21, page 056111, 2014.

[Goniche 2014] M. Goniche, R. Dumont, C. Bourdelle, J. Decker, L. Delpech, A. Ekedahl, D. Guilhem, Z. Guimarães Filho, X. Litaudon, Ph. Lotte, P. Maget, D. Mazon, B. Saoutic and Tore Supra Team. *Advances in long pulse operation at high radio frequency power in Tore Supra.* Physics of Plasmas, vol. 21, page 061515, 2014.

[Gott 2007] Yu. V. Gott. *On Artsimovich Formula.* Fizika Plazmy, vol. 33, page 958, 2007.

[Greenwald 1999] M. Greenwald, R. Boivin, P. Bonoli, R. Budny, C. Fiore, J. Goetz, R. Granetz, A. Hubbard, I. Hutchinson, J. Irby, B. LaBombard, Y. Lin, B. Lipschultz, E. Marmar, A. Mazurenko, D. Mossessian, T. Sunn Pedersen, C. S. Pitcher, M. Porkolab, J. Rice, W. Rowan, J. Snipes, G. Schilling, Y. Takase, J. Terry, S. Wolfe, J. Weaver, B. Welch and S. Wukitch. *Characterization of enhanced D high-confinement modes in Alcator C-Mod.* Physics of Plasmas, vol. 6, page 1943, 1999.

[Guimarães Filho 2011] Z.O. Guimarães Filho, D. Elbeze, R. Sabot, D. Molina, J.L. Segui, C. Nguyen, J. Decker, P. Maget, A. Merle, X. Garbet, N. Dubuit and S. Benkadda. *Energetic particle driven magnetohydrodynamic instabilities during relaxation cycles in Tore Supra.* Plasma Physics and Controlled Fusion, vol. 53, page 074012, 2011.

[Guimarães Filho 2012] Z.O. Guimarães Filho, S. Benkadda, D. Elbeze, A. Botrugno, P. Buratti, G. Calabró, J. Decker, N. Dubuit, X Garbet, P. Maget, A. Merle, R. Pucella G.and Sabot, A.A. Tuccillo and F. Zonca. *Electron fishbones in FTU and Tore Supra tokamaks.* Nuclear Fusion, vol. 52, page 094009, 2012.

[Guirlet] R. Guirlet. Transport in tokamak plasmas. Lecture given in the french master in fusion sciences.

[Guirlet 2009] R. Guirlet, D. Villegas, T. Parisot, C. Bourdelle, X. Garbet, F. Imbeaux, D. Mazon and D. Pacella. *Anomalous transport of light and heavy impurities in Tore Supra ohmic, weakly sawtoothing plasmas.* Nuclear Fusion, vol. 49, page 055007, 2009.

[Guttenfelder 2008] W. Guttenfelder, J. Lore, D. T. Anderson, F. S. B. Anderson, J. M. Canik, W. Dorland, K. M. Likin and J. N. Talmadge. *Effect of Quasihelical Symmetry on Trapped-Electron Mode Transport in the HSX Stellarator.* Phys. Rev. Lett., vol. 101, page 215002, 2008.

[Hacquin 2004] S. Hacquin, L. Meneses, L. Cupido, N. Cruz, L. Kokonchev, R. Prentice and C. Gowers. *Upgrade of the X-mode reflectometry diagnostic for radial correlation measurements in the Joint European Torus.* Review of Scientific Instruments, vol. 75, page 3834, 2004.

[Hacquin 2006] S. Hacquin, B. Alper, S. Sharapov, D. Borba, C. Boswell, J. Fessey, L. Meneses, M. Walsh and JET EFDA contributors. *Characterization of Alfvén*

cascades on the JET tokamak using a multi-channel O-mode reflectometer diagnostic. Nuclear Fusion, vol. 46, page S714, 2006.

[Hacquin 2013] S Hacquin. *Development of a European 3D full-wave reflectometer simulation code.* Communication at Journes scientifiques URSI-France, CNAM Paris, 2013.

[Hacquin 2015] S. Hacquin, J. Citrin, H. Arnichand, R. Sabot, C. Bourdelle, Garbet X. and the Tore Supra Team. *Reflectometry simulations using gyrokinetic code data or study of quasi-oherent modes.* 12th International Reflectometry Workshop (IRW12), FZ-Jülich, Germany, 2015.

[Happel 2015] T. Happel, A. Banón Navarro, G. D. Conway, C. Angioni, M. Bernert, M. Dunne, E. Fable, B. Geiger, T. Görler, F. Jenko, R. M. McDermott, F. Ryter, U. Stroth and the ASDEX Upgrade Team. *Core turbulence behavior moving from ion-temperature-gradient regime towards trapped-electron-mode regime in the ASDEX Upgrade tokamak and comparison with gyrokinetic simulation.* Physics of Plasma, vol. 22, page 032503, 2015.

[Helander] P. Helander. Classical and neoclassical transport in tokamaks. Lecture given in the carolus magnus summer school.

[Helander 2013] P. Helander, J. H. E. Proll and G. G. Plunk. *Collisionless microinstabilities in stellarators. I. Analytical theory of trapped-particle modes.* Physics of Plasmas, vol. 20, no. 12, 2013.

[Hennequin 1999] P. Hennequin, C. Honorë, A. Quéméneur, A. Truc, F. Gervais, C. Fenzi and R.Sabot. *Analysis of density fluctuation frequency spectra in Tore Supra as a tool for studying plasma motion and transport properties.* 26th EPS Conf. Controlled Fusion and Plasma Physics, Maastricht, The Netherlands, 1999.

[Hennequin 2004] P Hennequin, R Sabot, C Honoré, G T Hoang, X Garbet, A Truc, C Fenzi and A Quemenur. *Scaling laws of density fluctuations at high- k on Tore Supra.* Plasma Physics and Controlled Fusion, vol. 46, no. 12B, page B121, 2004.

[Hennequin 2006] P. Hennequin, C. Honoré, A. Truc, A. Quéméneur, C. Fenzi-Bonizec, C. Bourdelle, X. Garbet, G.T. Hoang and the Tore Supra team. *Fluctuation spectra and velocity profile from Doppler backscattering on Tore Supra.* Nuclear Fusion, vol. 46, no. 9, page S771, 2006.

[Hillesheim 2013a] J. C. Hillesheim, J. C. DeBoo, W. A. Peebles, T. A. Carter, G. Wang, T. L. Rhodes, L. Schmitz, G. R. McKee, Z. Yan, G. M. Staebler, K. H. Burrell, E. J. Doyle, C. Holland, C. C. Petty, S. P. Smith, A. E. White and L. Zeng. *Observation of a Critical Gradient Threshold for Electron Temperature Fluctuations in the DIII-D Tokamak.* Phys. Rev. Lett., vol. 110, page 045003, 2013.

[Hillesheim 2013b] J. C. Hillesheim, J. C. DeBoo, W. A. Peebles, T. A. Carter, G. Wang, T. L. Rhodes, L. Schmitz, G. R. McKee, Z. Yan, G. M. Staebler, K. H. Burrell, E. J. Doyle, C. Holland, C. C. Petty, S. P. Smith, A. E. White and L. Zeng. *Experimental characterization of multiscale and multifield turbulence as a critical gradient threshold is surpassed in the DIII-D tokamak.* Physics of Plasmas, vol. 20, page 056115, 2013.

[Hillesheim 2015] J. C. Hillesheim. *Radial electric field measurements with Doppler backscattering in JET.* 12th International Reflectometry Workshop (IRW12), FZ-Jülich, Germany, 2015.

[Hirsch 2001] M Hirsch, E Holzhauer, J Baldzuhn, B Kurzan and B Scott. *Doppler reflectometry for the investigation of propagating density perturbations.* Plasma Physics and Controlled Fusion, vol. 43, no. 12, page 1641, 2001.

[Hirsch 2004] M Hirsch and E Holzhauer. *Doppler reflectometry with optimized temporal resolution for the measurement of turbulence and its propagation velocity.* Plasma Physics and Controlled Fusion, vol. 46, page 593, 2004.

[Hoang 1998] G.T. Hoang, B. Saoutic, L. Guiziou, V. Basiuk, A. Bécoulet, R.V. Budny, F. Clairet, L. Colas, P. Devynck, C. Gil, E. Joffrin, X. Litaudon, J.-L. Ségui, I. Voitsekhovitch and X.L. Zou. *Magnetic shear effects on confinement and electron heat transport in Tore Supra discharges with electron heating.* Nuclear Fusion, vol. 38, no. 1, page 117, 1998.

[Hoang 2001] G. T. Hoang, C. Bourdelle, X. Garbet, G. Giruzzi, T. Aniel, M. Ottaviani, W. Horton, P. Zhu and R. V. Budny. *Experimental Determination of Critical Threshold in Electron Transport on Tore Supra.* Phys. Rev. Lett., vol. 87, page 125001, 2001.

[Hogeweij] G. M. D. Hogeweij. Degraded confinement and turbulence in tokamak experiments. Lecture given in the carolus magnus summer school.

[Hornsby 2015] W A Hornsby, P Migliano, R Buchholz, D Zarzoso, F J Casson, E Poli and A G Peeters. *On seed island generation and the non-linear self-consistent interaction of the tearing mode With electromagnetic gyro-kinetic turbulence.* Plasma Physics and Controlled Fusion, vol. 57, no. 5, page 054018, 2015.

[Hornung 2013a] G. Hornung. *Study of plasma turbulence by ultrafast sweeping reflectometry on the Tore Supra tokamak (Appendix C).* PhD thesis, 2013.

[Hornung 2013b] G Hornung, F Clairet, G L Falchetto, R Sabot, H Arnichand and L Vermare. *Turbulence correlation properties measured with ultrafast sweeping reflectometry on Tore Supra.* Plasma Physics and Controlled Fusion, vol. 55, page 125013, 2013.

[Horton 1981] Wendell Horton, Duk In Choi and W. M. Tang. *Toroidal drift modes driven by ion pressure gradients.* Physics of Fluids, vol. 24, page 1077, 1981.

[Horton 1988] W. Horton, B. G. Hong and W. M. Tang. *Toroidal electron temperature gradient driven drift modes.* Physics of Fluids, vol. 31, no. 10, pages 2971–2983, 1988.

[Hurricane 2014] O. A. Hurricane, D. A. Callahan, D. T. Casey, P. M. Celliers, C. Cerjan, E. L. Dewald, T. R. Dittrich, T. Doppner, D. E. Hinkel, L. F. Hopkins, J. L. BerzakKline, S. Le Pape, T. Ma, A. G. MacPhee, J. L. Milovich, A. Pak, H.-S. Park, P. K. Patel, B. A. Remington, J. D. Salmonson, P. T. Springer and R. Tommasini. *Fuel gain exceeding unity in an inertially confined fusion implosion.* Nature, vol. 506, page 343, 2014.

[IAE 2014] 25ˆth red book on uranium: Ressources, production and demand. International Atomic Energy Agency, 2014.

[Imbeaux 2005] F Imbeaux and Y Peysson. *Ray-tracing and Fokker–Planck modelling of the effect of plasma current on the propagation and absorption of lower hybrid waves.* Plasma Physics and Controlled Fusion, vol. 47, no. 11, page 2041, 2005.

[IPC 2014] Fifth assessment report (ar5). Intergovernmental Panel on Climate Change, 2014.

[Ishizawa 2007] A. Ishizawa and N. Nakajima. *Multi-scale-nonlinear interactions among micro-turbulence, double tearing instability and zonal flows.* Nuclear Fusion, vol. 47, no. 11, page 1540, 2007.

[Jenko 2000] F. Jenko, W. Dorland, M. Kotschenreuther and B. N. Rogers. *Electron temperature gradient driven turbulence.* Physics of Plasmas, vol. 7, no. 5, pages 1904–1910, 2000.

[Kadomtsev 1965] B.B. Kadomtsev. *Plasma Turbulence (translated by L.C. Ronson from the 1964 Russian edition, in: Leontovich, M.A., Rusbridge, M.C. (Eds.), Problems in Plasma Theory Trans.).* Academic Press, 1965.

[Kadomtsev 1967] B. B. Kadomtsev and O. P. Pogutse. *Plasma instability due to particle trapping in a toroidal geometry.* Soviet Physics JETP, vol. 24, page 1172, 1967.

[Kammerer 2008] M. Kammerer, F. Merz and F. Jenko. *Exceptional points in linear gyrokinetics.* Physics of Plasmas, vol. 15, page 052102, 2008.

[Keilhacker 2001] M. Keilhacker, A. Gibson, C. Gormezano and P.H. Rebut. *The scientific success of JET.* Nuclear Fusion, vol. 41, page 1925, 2001.

[Krämer-Flecken 2004] A. Krämer-Flecken, V. Dreval, S. Soldatov, A. Rogister, V. Vershkov and the TEXTOR-team. *Turbulence studies with means of reflectometry at TEXTOR.* Nuclear Fusion, vol. 44, page 1143, 2004.

[Krämer-Flecken 2006] A. Krämer-Flecken, S. Soldatov, H. R. Koslowski and O. Zimmermann. Phys. Rev. Lett., vol. 97, page 045006, 2006.

[Krämer-Flecken 2009] A Krämer-Flecken, S Soldatov, D Reiser, M Kantor and H R Koslowski. Plasma Physics and Controlled Fusion, vol. 51, no. 1, page 015001, 2009.

[Krämer-Flecken 2010] A. Krämer-Flecken, S. Soldatov, B. Vowinkel and P. Mueller. *Correlation reflectometry at TEXTOR.* Review of Scientific Instruments, vol. 81, page 113502, 2010.

[Krämer-Flecken 2011] A Krämer-Flecken, S Soldatov, Y Xu and T Zhang. *Correlation reflectometry in fusion plasmas, an application at TEXTOR.* Plasma Physics and Controlled Fusion, vol. 53, page 074020, 2011.

[Krämer-Flecken 2012] A. Krämer-Flecken, Y. Xu and S. Zoletnik. *Poloidal rotation asymmetry and relation to turbulence.* 39th EPS Conference, Stockholm, Sweden, 2012.

[Krämer-Flecken 2015] A Krämer-Flecken, S Soldatov, Y Xu, H Arnichand, S Hacquin, R Sabot and the TEXTOR team. *Long-range correlation properties of quasi-coherent modes at TEXTOR.* New Journal of Physics, vol. 17, page 073007, 2015.

[LaBombard 2014] B. LaBombard, T. Golfinopoulos, J. L. Terry, D. Brunner, E. Davis, M. Greenwald, J. W. Hughes and Alcator C-Mod Team. *New insights on boundary plasma turbulence and the quasi-coherent mode in Alcator C-Mod using a Mirror Langmuir Probe.* Physics of Plasmas, vol. 21, page 056108, 2014.

[Laviron 1996] C Laviron, A J H Donné, M E Manso and J Sanchez. *Reflectometry techniques for density profile measurements on fusion plasmas.* Plasma Physics and Controlled Fusion, vol. 38, no. 7, page 905, 1996.

[Lebschy 2015] A. Lebschy, R. M. McDermott, B. Geiger, M. Cavedon, M. G. Dunne, R. Dux, R. Fischer, E. Viezzer and the ASDEX Upgrade Team. *Indirect measurement of the poloidal rotation in the core of ASDEX Upgrade plasmas with CXRS.* 42nd EPS Conference on Plasma Physics, Lisbon, Portugal, 2015.

[Lerner 2012] Eric J. Lerner, S. Krupakar Murali, Derek Shannon, Aaron M. Blake and Fred Van Roessel. *Fusion reactions from $>$ 150 KeV ions in a dense plasma focus plasmoid.* Physics of Plasmas (1994-present), vol. 19, 2012.

[Li 2011] Y. G. Li, Ph. Lotte, W. Zwingmann, C. Gil and F. Imbeaux. *EFIT Equilibrium Reconstruction Including Polarimetry Measurements on Tore Supra.* Fusion Science and Technology, vol. 59, page 397, 2011.

[Maget 2006] P. Maget, F. Imbeaux, G. Giruzzi, V.S. Udintsev, G.T.A. Huysmans, J.-L. Ségui, M. Goniche, Ph. Moreau, R. Sabot and X. Garbet. *Temperature oscillating regimes in Tore Supra diagnosed by MHD activity.* Nuclear Fusion, vol. 46, 2006.

[Maget 2007] P. Maget, G. T. A. Huysmans, X. Garbet, M. Ottaviani, H. Lütjens and J.-F. Luciani. *Nonlinear magnetohydrodynamic simulation of Tore Supra hollow current profile discharges.* Physics of Plasmas, vol. 14, page 052509, 2007.

[Malinov 2005] P. Malinov and F. Zonca. *Ion temperature gradient modes and the fraction of trapped electrons.* Journal of Plasma Physics, vol. 71, page 301, 2005.

[Mazzucato 1991] E Mazzucato and R Nazikian. *Microwave reflectometry for the study of density fluctuations in tokamak plasmas.* Plasma Physics and Controlled Fusion, vol. 33, no. 3, page 261, 1991.

[McDermott 2014] R.M. McDermott, C. Angioni, G.D. Conway, R. Dux, E. Fable, R. Fischer, T. Pütterich, F. Ryter, E. Viezzer and the ASDEX Upgrade Team. Nuclear Fusion, vol. 54, no. 4, page 043009, 2014.

[Medvedeva 2015] A. Medvedeva, C. Bottereau C., F. Clairet, G.D. Conway, S. Heuraux, D. Molina, Stroth U. and the Asdex-upgrade Team. *Density fluctuation measurements with an ultra-fast-swept reflectometer in ASDEX-Upgrade.* 12th International Reflectometry Workshop (IRW12), FZ-Jülich, Germany, 2015.

[Meigs 1994] A. G. Meigs and William L. Rowan. *Impurity poloidal rotation velocity in tokamaks.* Physics of Plasmas, vol. 1, no. 4, pages 960–967, 1994.

[Meijere 2013] C. A. De Meijere. *An Experimental Study of Plasma Fluctuations in the TCV and TEXTOR Tokamaks.* PhD thesis, EPFL, 2013.

[Merle 2012] A. Merle, J. Decker, Xavier X. Garbet, R. Sabot, Z. Guimaraes-Filho and T. Nicolas. Physics of Plasma, vol. 19, 2012.

[Nave 2004] M. F. F. Nave, D. Borba, R. Galvão, S. Hacquin, B. Alper, C. Challis, S. Gerasimov, N. Hawkes, J. Mailloux, S. Sharapov, C. Boswell, M. Brix, E. Joffrin, E. de la Luna, P. Smeulders and EFDA-JET Contributors. Review of Scientific Instruments, vol. 75, no. 10, pages 4274–4277, 2004.

[Nazikian 1995] R. Nazikian and E. Mazzucato. *Reflectometer measurements of density fluctuations in tokamak plasmas (invited).* Review of Scientific Instruments, vol. 66, page 392, 1995.

[Nazikian 1998] R Nazikian, GY Fu, Z Chang, SH Batha, H Berk, RV Budny, Y Chen, CZ Cheng, DS Darrow, NN Gorelenkov, FM Levinton, S Medley, MP Petrov, M Redi, E Ruskov, DA Spong, RB White and SJ Zweben. Physics of Plasma, vol. 5, 1998.

[Nguyen 2009] C Nguyen, X Garbet, R Sabot, L-G Eriksson, M Goniche, P Maget, V Basiuk, J Decker, D Elbéze, G T A Huysmans, A Macor, J-L Ségui and M Schneider. Plasma Physics and Controlled Fusion, vol. 51, 2009.

[Parisot 2008] T Parisot, R Guirlet, C Bourdelle, X Garbet, N Dubuit, F Imbeaux and P R Thomas. *Experimental impurity transport and theoretical interpretation in a Tore Supra lower-hybrid heated plasma.* Plasma Physics and Controlled Fusion, vol. 50, page 055010, 2008.

[Peeters 2000] A. G. Peeters. *Reduced charge state equations that describe Pfirsch Schlüter impurity transport in tokamak plasma.* Physics of Plasmas, vol. 7, page 268, 2000.

[Poyé 2015] A. Poyé, O. Agullo, M. Muraglia, X. Garbet, S. Benkadda, A. Sen and N. Dubuit. *Generation of a magnetic island by edge turbulence in tokamak plasmas.* Physics of Plasmas, vol. 22, page 030704, 2015.

[Prisiazhniuk 2015] D. Prisiazhniuk, A. Krämer-Flecken, G. Conway, P. Manz, T. Happel, P. Simon, Stroth U. and the Asdex-upgrade Team. *Application of poloidal correlation reflectometry to study turbulence at ASDEX-Upgrade.* 12th International Reflectometry Workshop (IRW12), FZ-Jülich, Germany, 2015.

[Proll 2012] J. H. E. Proll, P. Helander, J. W. Connor and G. G. Plunk. *Resilience of Quasi-Isodynamic Stellarators against Trapped-Particle Instabilities.* Phys. Rev. Lett., vol. 108, page 245002, 2012.

[Proll 2013] J. H. E. Proll, P. Xanthopoulos and P. Helander. *Collisionless microinstabilities in stellarators. II. Numerical simulations.* Physics of Plasmas, vol. 20, page 122506, 2013.

[Proll 2015] J. H. E. Proll, B.J. Faber, P. Helander, S.A. Lazerson, H.E. Mynick and P. Xanthopoulos. *Microturbulence simulations in optimised stellarators.* 39th EPS Conference, Stockholm, Sweden, 2015.

[Rettig 2001] C. L. Rettig, T. L. Rhodes, J. N. Leboeuf, W. A. Peebles, E. J. Doyle, G. M. Staebler, K. H. Burrell and R. A. Moyer. *Search for the ion temperature gradient mode in a tokamak plasma and comparison with theoretical predictions.* Physics of Plasmas, vol. 8, page 2232, 2001.

[Rice 2011a] J. E. Rice, I. Cziegler, P. H. Diamond, B. P. Duval, Y. A. Podpaly, M. L. Reinke, P. C. Ennever, M. J. Greenwald, J. W. Hughes, Y. Ma, E. S. Marmar, M. Porkolab, N. Tsujii and S. M. Wolfe. *Rotation Reversal Bifurcation and Energy Confinement Saturation in Tokamak Ohmic L-Mode Plasmas.* Phys. Rev. Lett., vol. 107, page 265001, 2011.

[Rice 2011b] J.E. Rice, B.P. Duval, M.L. Reinke, Y.A. Podpaly, A. Bortolon, R.M. Churchill, I. Cziegler, P.H. Diamond, A. Dominguez, P.C. Ennever, C.L. Fiore, R.S. Granetz, M.J. Greenwald, A.E. Hubbard, J.W. Hughes, J.H. Irby, Y. Ma, E.S. Marmar, R.M. McDermott, M. Porkolab, N. Tsujii and S.M. Wolfe. *Observations of core toroidal rotation reversals in Alcator C-Mod ohmic L-mode plasmas.* Nuclear Fusion, vol. 51, page 083005, 2011.

[Rice 2012] J. E. Rice, M. J. Greenwald, Y. A. Podpaly, M. L. Reinke, P. H. Diamond, J. W. Hughes, N. T. Howard, Y. Ma, I. Cziegler, B. P. Duval, P. C. Ennever, D. Ernst, C. L. Fiore, C. Gao, J. H. Irby, E. S. Marmar, M. Porkolab, N. Tsujii and S. M. Wolfe. *Ohmic energy confinement saturation and core toroidal rotation reversal in Alcator C-Mod plasmas.* Physics of Plasmas, vol. 19, page 056106, 2012.

[Rice 2013] J.E. Rice, C. Gao, M.L. Reinke, P.H. Diamond, N.T. Howard, H.J. Sun, I. Cziegler, A.E. Hubbard, Y.A. Podpaly, W.L. Rowan, J.L. Terry, M.A. Chilenski, L. Delgado-Aparicio, P.C. Ennever, D. Ernst, M.J. Greenwald, J.W. Hughes, Y. Ma, E.S. Marmar, M. Porkolab, A.E. White and S.M. Wolfe. *Non-local heat transport, rotation reversals and up/down impurity density asymmetries in Alcator C-Mod ohmic L-mode plasmas.* Nuclear Fusion, vol. 53, page 033004, 2013.

[Ritz 1989] Ch. P. Ritz, R. V. Bravenec, P. M. Schoch, R. D. Bengtson, J. A. Boedo, J. C. Forster, K. W. Gentle, Y. He, R. L. Hickok, Y. J. Kim, H. Lin, P. E. Phillips, T. L. Rhodes, W. L. Rowan, P. M. Valanju and A. J. Wootton. *Fluctuation-Induced Energy Flux in the Tokamak Edge.* Phys. Rev. Lett., vol. 62, page 1844, 1989.

[Romanelli 2007] M. Romanelli, G. Regnoli and C. Bourdelle. *Numerical study of linear dissipative drift electrostatic modes in tokamaks.* Physics of Plasmas, vol. 14, page 082305, 2007.

[Sabot 2006a] R Sabot, F Clairet, G D Conway, L Cupido, X Garbet, G Falchetto, T Gerbaud, S Hacquin, P Hennequin, S Heuraux, C Honoré, G Leclert, L Meneses, A Sirinelli, L Vermare and A Truc. *Recent results on turbulence and MHD activity achieved by reflectometry.* Plasma Physics and Controlled Fusion, vol. 48, page B421, 2006.

[Sabot 2006b] R. Sabot, A. Sirinelli, J.-M. Chareau and J.-C. Giaccalone. *A dual source D-band reflectometer for density profile and fluctuations measurements in Tore-Supra.* Nuclear Fusion, vol. 46, page S685, 2006.

[Sarazin] Y. Sarazin. Turbulence and transport. Lecture given in the french master in fusion sciences.

[Sarff 2015] J.S. Sarff, A.F. Almagri, J.K. Anderson, M. Borchardt, W. Cappechi, D. Carmody, K. Caspary, B.E. Chapman, D.J. Den Hartog, J. Duff, S. Eilerman, A. Falkowski, C.B. Forest, M. Galante, J.A. Goetz, D.J. Holly, J. Koliner, S. Kumar, J.D. Lee, D. Liu, K.J. McCollam, M. McGarry, V.V. Mirnov, L. Morton, S. Munaretto, M.D. Nornberg, P.D. Nonn, S.P. Oliva, E. Parke, M.J. Pueschel, J.A. Reusch, J. Sauppe, A. Seltzman, C.R. Sovinec, D. Stone, D. Theucks, M. Thomas, J. Triana, P.W. Terry, J. Waksman, G.C. Whelan, D.L. Brower, W.X. Ding, L. Lin, D.R. Demers, P. Fimognari, J. Titus, F. Auriemma, S. Cappello, P. Franz, P. Innocente, R. Lorenzini, E. Martines, B. Momo, P. Piovesan, M. Puiatti, M. Spolaore, D. Terranova, P. Zanca, V.I. Davydenko, P. Deichuli,

A.A. Ivanov, S. Polosatkin, N.V. Stupishin, D. Spong, D. Craig, H. Stephens, R.W. Harvey, M. Cianciosa, J.D. Hanson, B.N. Breizman, M. Li and L.J. Zheng. *Overview of results from the MST reversed field pinch experiment.* Nuclear Fusion, vol. 55, page 104006, 2015.

[Schmitz 2012] L. Schmitz, C. Holland, T.L. Rhodes, G. Wang, L. Zeng, A.E. White, J.C. Hillesheim, W.A. Peebles, S.P. Smith, R. Prater, G.R. McKee, Z. Yan, W.M. Solomon, K.H. Burrell, C.T. Holcomb, E.J. Doyle, J.C. DeBoo, M.E. Austin, J.S. deGrassie and C.C. Petty. *Reduced electron thermal transport in low collisionality H-mode plasmas in DIII-D and the importance of TEM/ETG-scale turbulence.* Nuclear Fusion, vol. 52, no. 2, page 023003, 2012.

[Sharapov 2004] S. G. Sharapov, V. P. Gusynin and H. Beck. *Magnetic oscillations in planar systems with the Dirac-like spectrum of quasiparticle excitations.* Phys. Rev. B, vol. 69, page 075104, Feb 2004.

[Shi 2013] Y.J. Shi, W.H. Ko, J.M. Kwon, P.H. Diamond, S.G. Lee, S.H. Ko, L. Wang, S. Yi, K. Ida, L. Terzolo, S.W. Yoon, K.D. Lee, J.H. Lee, U.N. Nam, Y.S. Bae, Y.K. Oh, J.G. Kwak, M. Bitter, K. Hill, O.D. Gurcan and T.S. Hahm. *ECH effects on toroidal rotation: KSTAR experiments, intrinsic torque modelling and gyrokinetic stability analyses.* Nuclear Fusion, vol. 53, page 113031, 2013.

[Shimomura 1985] Y. Shimomura. *Empirical scaling of energy confinement time in L-mode plasma and optimised mode and some consideration of reactor core plasma in tokamak, Japanese Atomic Energy Research Institute (1985).* Report JAERI-M-85-080, 1985.

[Simmet 1996] E E Simmet and the ASDEX Team. *Statistical analysis of the global energy confinement time in ohmic discharges in the ASDEX tokamak.* Plasma Physics and Controlled Fusion, vol. 38, page 689, 1996.

[Simonet 1985] F. Simonet. *Measurement of electron density profile by microwave reflectometry on tokamaks.* Review of Scientific Instruments, vol. 56, no. 5, pages 664–669, 1985.

[Sirinelli 2013] A. Sirinelli, L. Meneses and JET-EFDA Contributors. *Density fluctuation measurements of JET H-mode plasmas using a radial correlation reflectometer.* 11th International Reflectometry Workshop (IRW11), Ecole Polytechnique, Palaiseau, France, 2013.

[Snipes 2001] J A Snipes, B LaBombard, M Greenwald, I H Hutchinson, J Irby, Y Lin, A Mazurenko and M Porkolab. *The quasi-coherent signature of enhanced D alpha H-mode in Alcator C-Mod.* Plasma Physics and Controlled Fusion, vol. 43, page L23, 2001.

[Sung 2013] C. Sung, A.E. White, N.T. Howard, C.Y. Oi, J.E. Rice, C. Gao, P. Ennever, M. Porkolab, F. Parra, D. Mikkelsen, D. Ernst, J. Walk, J.W. Hughes, J. Irby,

C. Kasten, A.E. Hubbard, M.J. Greenwald and the Alcator C-Mod Team. *Changes in core electron temperature fluctuations across the ohmic energy confinement transition in Alcator C-Mod plasmas.* Nuclear Fusion, vol. 53, page 083010, 2013.

[Tagger 1977] M. Tagger, G. Laval and R. Pellat. *Trapped ion mode driven by ion magnetic drift resonance in a fat torus.* Nuclear Fusion, vol. 17, page 109, 1977.

[Takenaga 2003] H. Takenaga, S. Higashijima, N. Oyama, L.G. Bruskin, Y. Koide, S. Ide, H. Shirai, Y. Sakamoto, T. Suzuki, K.W. Hill, G. Rewoldt, G.J. Kramer, R. Nazikian, T. Takizuka, T. Fujita, A. Sakasai, Y. Kamada, H. Kubo and the JT-60 Team. *Relationship between particle and heat transport in JT-60U plasmas with internal transport barrier.* Nuclear Fusion, vol. 43, no. 10, page 1235, 2003.

[Tang 1977] W. M. Tang, J. C. Adam and David W. Ross. *Residual trapped ion instabilities in tokamaks.* Physics of Fluids, vol. 20, page 430, 1977.

[Terry 2005] J.L. Terry, N.P. Basse, I. Cziegler, M. Greenwald, O. Grulke, B. LaBombard, S.J. Zweben, E.M. Edlund, J.W. Hughes, L. Lin, Y. Lin, M. Porkolab, M. Sampsell, B. Veto and S.J. Wukitch. *Transport phenomena in the edge of Alcator C-Mod plasmas.* Nuclear Fusion, vol. 45, page 1321, 2005.

[Trier 2008] E. Trier, L.-G. Eriksson, P. Hennequin, C. Fenzi, C. Bourdelle, G. Falchetto, X. Garbet, T. Aniel, F. Clairet and R. Sabot. *Radial electric field measurement in a tokamak with magnetic field ripple.* Nuclear Fusion, vol. 48, page 092001, 2008.

[UN 2003] World population in 2300, department of economic and social affairs, population division. United Nations, 2003.

[van Houtte 2004] D. van Houtte, G. Martin, A. Bécoulet, J. Bucalossi, G. Giruzzi, G.T. Hoang, Th. Loarer, B. Saoutic and the Tore Supra Team. *Recent fully non-inductive operation results in Tore Supra with 6 min, 1 GJ plasma discharges.* Nuclear Fusion, vol. 44, page L11, 2004.

[Vermare 2005] L Vermare, F Clairet, S Heuraux and G Leclert. *Rational surface localization and MHD activity measurements using fast sweep reflectometry on Tore Supra.* Plasma Physics and Controlled Fusion, vol. 47, no. 11, page 1895, 2005.

[Vershkov 2001] V. A. Vershkov, A. Tuccillo, O. Tudisco, M. De Benedetti, P. Buratti, P. Smeulders, D. A. Shelukhin, F. Zonca and FTU team. *Microturbulence simulations in optimised stellarators.* 28th EPS Conference on controlled fusion and plasma physics, Funchal, ECA Vol. 25A (2001) 65, 2001.

[Vershkov 2005] V.A. Vershkov, D.A. Shelukhin, S.V. Soldatov, A.O. Urazbaev, S.A. Grashin, L.G. Eliseev, A.V. Melnikov and the T-10 team. *Summary of experimental core turbulence characteristics in ohmic and electron cyclotron resonance heated discharges in T-10 tokamak plasmas.* Nuclear Fusion, vol. 45, page S203, 2005.

[Vershkov 2011] V.A. Vershkov, V.F. Andreev, A.A. Borschegovskiy, V.V. Chistyakov, M.M. Dremin, L.G. Eliseev, E.P. Gorbunov, S.A. Grashin, A.V. Khmara, A.Ya. Kislov, D.A. Kislov, A.D. Komarov, A.S. Kozachek, V.A. Krupin, L.I. Krupnik, S.V. Krylov, S.E. Lysenko, S.G. Maltsev, V.A. Mavrin, A.V. Melnikov, G.E. Notkin, A.Yu. Novikov, Yu.D. Pavlov, S.V. Perfilov, V.V. Piterskij, G.N. Ploskirev, V.I. Poznyak, K.A. Razumova, I.N. Roy, D.V. Ryzhakov, P.V. Savrukhin, E.A. Shestakov, D.A. Shelukhin, Yu.A. Skosyrev, R.V. Shurygin, G.N. Tilinin, E.V. Trukhina and V.M. Trukhin. *Recent results of the T-10 tokamak.* Nuclear Fusion, vol. 51, page 094019, 2011.

[Vershkov 2013a] V.A. Vershkov, M.A. Borisov, G.F Subbotin, D.A. Shelukhin, Yu.N. Dnestrovskii, A.V. Danilov, S.V. Cherkasov E.P. Gorbunov, D.S. Sergeev, S.A. Grashin, S.V. Krylov, E.O. Kuleshin, T.B. Myalton, Yu.V. Skosyrev and V.V. Chistiakov. Nuclear Fusion, vol. 53, page 083014, 2013.

[Vershkov 2013b] V.A. Vershkov, D.A. Shelukhin, M.A. Borisov, M.A. Buldakov, M.Yu. Isaev, V.P. Budaev, E.P. Gorbunov, D.S. Sergeev, T.B. Myalton and V.V. Chistiakov. *Turbulence poloidal distribution and long distance correlations along the magnetic field lines in T-10 tokamak.* 11th International Reflectometry Workshop (IRW11), Ecole Polytechnique, Palaiseau, France, 2013.

[Viezzer 2012] E. Viezzer, T. Pütterich, R. Dux, R. M. McDermott and ASDEX Upgrade Team. *High-resolution charge exchange measurements at ASDEX Upgrade.* Review of Scientific Instruments, vol. 83, page 103501, 2012.

[Villegas 2010a] D. Villegas. *Etude expérimentale de l'influence du gradient de température électronique sur le transport turbulent des impuretés dans un plasma de fusion.* PhD thesis, 2010.

[Villegas 2010b] D. Villegas, R. Guirlet, C. Bourdelle, G. T. Hoang, X. Garbet and R. Sabot. *Experimental Electron Temperature Gradient Dependence of Heavy Impurity Transport in Fusion Devices.* Phys. Rev. Lett., vol. 105, page 035002, 2010.

[Villegas 2014] D. Villegas, R. Guirlet, C. Bourdelle, X. Garbet, G.T. Hoang, R. Sabot, F. Imbeaux and J.L. Ségui. *Experimental and theoretical study of nickel transport dependence on gradients in Tore Supra.* Nuclear Fusion, vol. 54, page 073011, 2014.

[Waelbroeck 2009] F L Waelbroeck, F Militello, R Fitzpatrick and W Horton. *Effect of electrostatic turbulence on magnetic islands.* Plasma Physics and Controlled Fusion, vol. 51, no. 1, page 015015, 2009.

[Wang 2014] Q. Wang H. S. Xu G. N. Wan B. Y. Ding S. Y. Guo H. M. Shao L. C. Liu S. Q. Xu X. E. Wang, N. Yan, V. Naulin, H. Nielsen A. J. Juul Rasmussen, J. Candy, R. Bravenec, W. Sun Y. H. Shi T. F. Liang Y. R. Chen, W. Zhang,

L. Wang, L. Chen, N. Zhao, L. Li Y. L. Liu Y. H. Hu G. and Z Gong X.˙ *New Edge Coherent Mode Providing Continuous Transport in Long-Pulse H-mode Plasmas.* Phys. Rev. Lett., vol. 112, page 185004, 2014.

[WEC 2013] World energy resources. World Energy Council, 2013.

[White 2010a] A. E. White, W. A. Peebles, T. L. Rhodes, C. H. Holland, G. Wang, L. Schmitz, T. A. Carter, J. C. Hillesheim, E. J. Doyle, L. Zeng, G. R. McKee, G. M. Staebler, R. E. Waltz, J. C. DeBoo, C. C. Petty and K. H. Burrell. *Measurements of the cross-phase angle between density and electron temperature fluctuations and comparison with gyrokinetic simulations.* Physics of Plasmas, vol. 17, page 056103, 2010.

[White 2010b] A. E. White, L. Schmitz, W. A. Peebles, T. L. Rhodes, T. A. Carter, G. R. McKee, M. W. Shafer, G. M. Staebler, K. H. Burrell, J. C. DeBoo and R. Prater. *Simultaneous measurement of core electron temperature and density fluctuations during electron cyclotron heating on DIII-D.* Physics of Plasma, vol. 17, page 020701, 2010.

[White 2011] A.E. White, P. Phillips, D.G. Whyte, A.E. Hubbard, C. Sung, J.W. Hughes, A. Dominguez, J. Terry and I. Cziegler. *Electron temperature fluctuations associated with the weakly coherent mode in the edge of I-mode plasmas.* Nuclear Fusion, vol. 51, page 113005, 2011.

[Whyte 2010] D.G. Whyte, A.E. Hubbard, J.W. Hughes, B. Lipschultz, J.E. Rice, E.S. Marmar, M. Greenwald, I. Cziegler, A. Dominguez, T. Golfinopoulos, N. Howard, L. Lin, R.M. McDermott, M. Porkolab, M.L. Reinke, J. Terry, N. Tsujii, S. Wolfe, S. Wukitch, Y. Lin and the Alcator C-Mod Team. *I-mode: an H-mode energy confinement regime with L-mode particle transport in Alcator C-Mod.* Nuclear Fusion, vol. 50, page 105005, 2010.

[Xiao 2010] W. W. Xiao, X. L. Zou, X. T. Ding, L. H. Yao, B. B. Feng, X. M. Song, S. D. Song, Y. Zhou, Z. T. Liu, B. S. Yuan, H. J. Sun, X. Q. Ji, Y. D. Gao, Y. G. Li, L. W. Yan, Q. W. Yang, Yi Liu, J. Q. Dong, X. R. Duan, Yong Liu and C. H. Pan. *Observation of a Spontaneous Particle-Transport Barrier in the HL-2A Tokamak.* Phys. Rev. Lett., vol. 104, page 215001, 2010.

[Xu 2003] G. S. Xu, B. N. Wan, M. Song and J. Li. *Direct Measurement of Poloidal Long-Wavelength $E \times B$ Flows in the HT-7 Tokamak.* Phys. Rev. Lett., vol. 91, page 125001, Sep 2003.

[Zabiégo 2001] M Zabiégo, G Huysmans, Y Peysson, J F Artaud, F Imbeaux and X Litaudon. *MHD stability of lower hybrid enhanced performance discharges on the Tore Supra tokamak.* Plasma Physics and Controlled Fusion, vol. 43, page 1625, 2001.

[Zarzoso 2012] D. Zarzoso. *Kinetic description of the interaction between energetic particles and waves in fusion plasmas.* PhD thesis, 2012.

[Zhong 2013] W. L. Zhong, X. L. Zou, C. Bourdelle, S. D. Song, J. F. Artaud, T. Aniel and X. R. Duan. *Convective Velocity Reversal Caused by Turbulence Transition in Tokamak Plasma.* Phys. Rev. Lett., vol. 111, page 265001, 2013.

[Zhong 2014] Wulu Zhong. *The Role of Edge Plasma Instabilities in Dynamical Evolution of Pedestal in the HL-2A Tokamak.* 25th IAEA fusion energy conference, Saint Petersburg, Russia, 2014.

[Zonca 2007] F. Zonca, P. Buratti, A. Cardinali, L. Chen, J.-Q. Dong, Y.-X. Long, A.V. Milovanov, F. Romanelli, P. Smeulders, L. Wang, Z.-T. Wang, C. Castaldo, R. Cesario, E. Giovannozzi, M. Marinucci and V. Pericoli Ridolfini. Nuclear Fusion, vol. 47, 2007.

[Zou 1999] X. L. Zou, T. F. Seak, M. Paume, J. M. Chareau, C. Bottereau and G. Leclert. *Poloidal Rotation Measurement in Tore Supra by Reflectometry.* 26th EPS Conf. Controlled Fusion and Plasma Physics, Maastricht, The Netherlands, 1999.